The Dissertation Committee for Sahil Malhotra Certifies that this is the approved version of the following dissertation:

Role of Fluid Elasticity and Viscous Instabilities in Proppant Transport in Hydraulic Fractures

Committee:

Mukul M. Sharma, Supervisor

Larry Lake

Kishore K. Mohanty

Chun Huh

Roger T. Bonnecaze

David DiCarlo

Role of Fluid Elasticity and Viscous Instabilities in Proppant Transport in Hydraulic Fractures

by

Sahil Malhotra, B. Tech.; M.S.E.

Dissertation

Presented to the Faculty of the Graduate School of

The University of Texas at Austin

in Partial Fulfillment

of the Requirements

for the Degree of

Doctor of Philosophy

The University of Texas at Austin

May 2013

Dedication

To my grandmother for her love and blessings.

To my parents for their inspiration and support.

Acknowledgements

I would like to express my sincere gratitude to Dr. Mukul M. Sharma for his supervision and support throughout the duration of my research. He has been a great source of inspiration and has helped me with all aspects of graduate studies. He has helped me in cultivating independent and innovative thinking, which I believe will help me throughout my career. It has been my privilege to complete my graduate studies under his supervision. I would like to thank my dissertation committee members for their insights and feedback on the research.

I would like to thank Eric Lehman for his help in performing a lot of experiments. His input in designing the experimental setup and improving the experimental techniques has been invaluable. I would like to thank Glen Baum, Gary Miscoe, Rod Russell, Tony Bermudez, Harry Linnemeyer, Mark Smith and Daryl Nygaard for their help in building the experimental setup and procuring equipment. I am grateful to Dr. Do Hoon Kim for advising me on the using the rheometer. The day-to-day contributions of Jin Lee and Roger Terzian have been very valuable for the progress of my graduate studies.

I would like to acknowledge the effort put in by all the professors in the classrooms. The lessons learnt in the classroom have helped me in performing research and will be of great help for years to come. I would like to thank my colleagues in our research group: Somnath Mondal, Ripudaman Manchanda, Lionel Ribeiro, Karn

Agarwal, Bo Gao, Nicolas Roussel, Saptaswa Basu, Himanshu Yadav, Anand Nagoo, Trevor Pollock and Kyle Freihauf for their continuous feedback and insights into various aspects of research. I would like to thank Deepjyoti Deka for his recommendations and input in calculating the wave number distributions mentioned in Chapter 6. I am also indebted to my friends Divya, Abhishek, Abhinav, Pranav, Karun, Soumava, Lokendra, Sayantan for making the journey enjoyable. Finally I would like to thank my parents and my sister for their love, support and sacrifices, which have helped me in pursuit of my goals.

Role of Fluid Elasticity and Viscous Instabilities in Proppant Transport in Hydraulic Fractures

Sahil Malhotra, Ph.D.

The University of Texas at Austin, 2013

Supervisor: Mukul M. Sharma

This dissertation presents an experimental investigation of fluid flow, proppant settling and horizontal proppant transport in hydraulic fractures. The work is divided into two major sections: investigation of proppant settling in polymer-free surfactant-based viscoelastic (VES) fluids and development of a new method of proppant injection, referred to as Alternate-Slug fracturing.

VES fluid systems have been used to eliminate polymer-based damage and to efficiently transport proppant into the fracture. Current models and correlations neglect the important influence of fracture walls and fluid elasticity on proppant settling. Experimental data is presented to show that elastic effects can increase or decrease the settling velocity of particles, even in the creeping flow regime. Experimental data shows that significant drag reduction occurs at low Weissenberg number, followed by a transition to drag enhancement at higher Weissenberg numbers. A new correlation is presented for the sphere settling velocity in unbounded viscoelastic fluids as a function of the fluid rheology and the proppant properties.

The wall factors for sphere settling velocities in viscoelastic fluids confined between solid parallel plates (fracture walls) are calculated from experimental measurements made on these fluids over a range of Weissenberg numbers. Results indicate that elasticity reduces the retardation effect of the confining walls and this reduction is more pronounced at higher ratios of the particle diameter to spacing between the walls. Shear thinning behavior of fluids is also observed to reduce the retardation effect of the confining walls. A new empirical correlation for wall factors for spheres settling in a viscoelastic fluid confined between two parallel walls is presented.

An experimental study on proppant placement using a new method of fracturing referred to as Alternate-Slug fracturing is presented. This method involves alternate injection of low viscosity and high viscosity fluids into the fracture, with proppant pumped in the low viscosity fluid. Experiments are conducted in Hele-Shaw cells to study the growth of viscous fingers over a wide range of viscosity ratios. Data is presented to show that the viscous finger velocities and mixing zone velocities increase with viscosity ratio up to viscosity ratios of about 350 and the trend is consistent with Koval's theory. However, at higher viscosity ratios the mixing zone velocity values plateau signifying no further effect of viscosity contrast on the growth of fingers and mixing zone. The plateau in the velocities at high viscosity ratios is caused by an increase in the thickness of the displacing fluid and a reduction in the thin film of the displaced fluid on the walls of the Hele-Shaw cell.

Fluid elasticity is observed to retard the growth of fingers and leads to growth of multiple thin fingers as compared to a single thick dominant finger in less elastic fluids. Observations show the shielding effect is reduced by fluid elasticity. Elastic effects are observed to reduce the thickness of thin film of displaced fluid on the walls of Hele-Shaw cell. The dominant wave number for the growth of instabilities is observed to be higher in more elastic fluids. At the onset of instability, the interface breaks down into a greater number of fingers in more elastic fluids.

Experiments are performed in simulated fractures (slot cells) to show the proppant distribution using alternate-slug fracturing. Observations show alternate-slug fracturing ensures deeper placement of proppant through two primary mechanisms: (a) proppant transport in viscous fingers formed by the low viscosity fluid and (b) an increase in drag force in the polymer slug leading to better entrainment and displacement of any proppant banks that may have formed. The method offers advantages of lower polymer costs, lower pumping horsepower, smaller fracture widths, better control of fluid leak-off and less gel damage compared to conventional gel fracs.

Table of Contents

List of Tables xiii

List of Figures xv

Chapter 1: Introduction and Outline of Thesis 1

1.1 Introduction 1

1.2 Outline of Thesis 5

Chapter 2: Rheological Characterization of Fluids 8

2.1 Viscosity 8

2.1.1 Newtonian Fluids 8

2.1.2 Non-Newtonian Fluids 9

2.1.2.1 Shear Thinning or Pseudoplastic Fluids 10

2.1.3 Lab Measurement of Viscosity 11

2.2 Viscoelasticity 12

2.2.1 Maxwell Representation 12

2.2.2 Rheological Characterization 13

2.2.2.1 Stress Relaxation Test to Measure Relaxation Time 13

2.2.2.2 Dynamic Frequency Sweep Test to Measure Relaxation Time 14

Chapter 3: Settling of Spherical Particles in Unbounded VES Fluids 21

3.1 Past Work on Settling in Unbounded Viscoelastic Fluids 22

3.2 Description of Fluids 25

3.3 Rheological Measurements 26

3.4 Procedure For Measuring Settling Velocities in Unbounded Fluids 27

3.5 Results For Settling in Unbounded VES Fluids 28

3.5.1 Settling Velocities in Unbounded Fluids 28

3.5.2 Effect of shear thinning on drag reduction/increase 34

3.6 Conclusions 35

Chapter 4: Effect of Confining Walls on Settling of Spherical Particles in VES Fluids....57
4.1 Past Work on Effect of Confining Walls on Settling Velocities....58
4.2 Experimental Setup and Procedure....61
4.3 Description and Rheology for Fluids....62
4.4 Results for Particle Settling Between Parallel Walls....62
4.5 Effect of Shear Thinning on Wall Factors....65
4.6 Conclusions....66

Chapter 5: Growth of Mixing Zone in Miscible Viscous Fingering....77
5.1 Introduction and Past Work....77
5.2 Experimental Setup....80
5.3 Fluid Description....81
5.4 Observations and Results....82
5.4.1 Mixing Zone and Finger Tip Velocity....85
5.4.2 Relative Finger Width....88
5.5 Implications of Findings for Design of Fracture Treatments....92
5.6 Conclusions....94

Chapter 6: Impact of Fluid Elasticity on Miscible Viscous Fingering....131
6.1 Introduction and Past Work....131
6.2 Linear Stability Analysis....133
6.3 Experiments....138
6.3.1 Description and Characterization of Fluids....138
6.3.2 Experimental Setup....140
6.3.3 Observations and Results....141
6.3.3.1 Evolution of Finger Instability....144
6.3.3.2 Finger Tip Velocity....146
6.3.3.3 Relative Finger Width....147
6.4 Implications of Findings for Design of Fracture Treatments....152
6.5 Conclusions....154

Chapter 7: Alternate-Slug Fracturing....183
7.1 Introduction....183
7.2 Past Work on Proppant Placement Strategies....185
7.2.1 Slickwater Fracturing....185
7.2.2 Hybrid Fracturing....188
7.2.3 Reverse-Hybrid Fracturing....189
7.2.4 Channel Fracturing....192
7.3 Experimental Methods....194
7.4 Proppant Transport Experiments....195
7.4.1 Proppant Transport Experiments with Sand....198
7.4.1.1 Water Fracturing....198
7.4.1.2 Hybrid Fracturing....199
7.4.1.3 Reverse Hybrid Fracturing....200
7.4.1.4 Alternate-Slug Fracturing....200
7.4.2 Proppant Transport Experiments with Ceramic Proppants....202
7.4.2.1 Conventional Fracturing....202
7.4.2.2 Water Fracturing....203
7.4.2.3 Reverse Hybrid Fracturing Treatment....204
7.4.2.4 Alternate-Slug Fracturing....204
7.5 Design of Alternate-Slug Fracturing Treatments....205
7.6 Conclusions....210
Appendix A....233
Glossary....237
References....241

List of Tables

Table 3.1: Composition and rheological properties of the fluid mixtures along with the temperature at which experiment is performed. 37

Table 5.1: Weight percentage and viscosity of glycerol solutions. 97

Table 5.2: Mutual diffusion coefficients and Peclet numbers for injection of water into glycerol solutions at three injection rates. 97

Table 5.3: Fracture parameters, flow rate and fluid viscosities used for example calculation of design of reverse-hybrid treatment. 98

Table 6.1: Concentrations and viscosities of the PEG-PEO solutions used in the experiments. 156

Table 6.2: Concentrations and viscosities of glycerol solutions used in the experiments. 156

Table 6.3: Relaxation strengths, G_k and relaxation times, λ_k estimated using non-linear regression. 156

Table 6.4: Peclet numbers for injection of distilled water into glycerol solutions at different injection rates. 157

Table 6.5: Comparison of the dominant wave numbers in cm^{-1} at different injection rates in Liquids L1 and T1. 157

Table 6.6: Comparison of the dominant wave numbers in cm^{-1} at different injection rates in Liquids L2 and T2. 157

Table 6.7: Flow Deborah numbers based on fingertip velocities at different injection rates. 158

Table 7.1: Dimensions and flow rate comparison of field scale fracture and experimental fracture cell. 212

Table 7.2: Typical fracture parameters used for illustrating an example for design of Alternate-Slug fracture treatments.....213

List of Figures

Figure 2.1: Schematic representation of shearing flow between two parallel plates.17

Figure 2.2 ARES LS-1 Rheometer by TA Instruments with a double wall concentric cylinder fixture used for measuring fluid rheology.....17

Figure 2.3: Steady shear-viscosity measurement showing viscosity versus shear rate for a polymer sample. Power-law fit is also shown on the plot. 18

Figure 2.4: Maxwell representation of a viscoelastic material. 18

Figure 2.5: Demonstration of stress relaxation in a viscoelastic material. 18

Figure 2.6: Stress response of a viscoelastic material for a sinusoidal strain input.19

Figure 2.7: Dynamic oscillatory-shear measurements showing the elastic modulus, G' and viscous modulus, G'' as a function of the angular frequency, ω. 19

Figure 2.8: Ratio of storage modulus to elastic modulus as a function of angular frequency for a fluid sample. The Maxwell model fits to the data well. The relaxation time of the fluid sample is 0.175s. 20

Figure 3.1: Viscosity and shear stress as a function of shear rate for Fluid 1. 38

Figure 3.2: Viscosity and shear stress as a function of shear rate for Fluid 2. 38

Figure 3.3: Viscosity and shear stress as a function of shear rate for Fluid 3. 39

Figure 3.4: Viscosity and shear stress as a function of shear rate for Fluid 4. 39

Figure 3.5: Viscosity and shear stress as a function of shear rate for Fluid 5. 40

Figure 3.6: Viscosity and shear stress as a function of shear rate for Fluid 6. 40

Figure 3.7: Viscosity and shear stress as a function of shear rate for Fluid 7. 41

Figure 3.8: Viscosity as a function of shear rate along with the power law fit in the experimental range of shear rates for Fluid 1. 41

Figure 3.9: Viscosity as a function of shear rate along with the power law fit in the experimental range of shear rates for Fluid 2. 42
Figure 3.10: Elastic and viscous moduli as a function of angular frequency for Fluid 1. 42
Figure 3.11: Elastic and viscous moduli as a function of angular frequency for Fluid 2. 43
Figure 3.12: Elastic and viscous moduli as a function of angular frequency for Fluid 3. 43
Figure 3.13: Elastic and viscous moduli as a function of angular frequency for Fluid 4. 44
Figure 3.14: Elastic and viscous moduli as a function of angular frequency for Fluid 5. 44
Figure 3.15: Elastic and viscous moduli as a function of angular frequency for Fluid 6. 45
Figure 3.16: Elastic and viscous moduli as a function of angular frequency for Fluid 7. 45
Figure 3.17: Ratio of viscous to elastic modulus along with the Maxwell fit for Fluid 1. 46
Figure 3.18: Ratio of viscous to elastic modulus along with the Maxwell fit for Fluid 2. 46
Figure 3.19: Ratio of viscous to elastic modulus along with the Maxwell fit for Fluid 3. 47
Figure 3.20: Ratio of viscous to elastic modulus along with the Maxwell fit for Fluid 4. 47

Figure 3.21: Ratio of viscous to elastic modulus along with the Maxwell fit for Fluid 5. 48
Figure 3.22: Ratio of viscous to elastic modulus along with the Maxwell fit for Fluid 6. 48
Figure 3.23: Ratio of viscous to elastic modulus along with the Maxwell fit for Fluid 7. 49
Figure 3.24: Settling velocities in Fluid 1 under unbounded conditions. 49
Figure 3.25: Settling velocities in Fluid 2 under unbounded conditions. 50
Figure 3.26: Settling velocities in Fluid 3 under unbounded conditions. 50
Figure 3.27: Settling velocities in Fluid 4 under unbounded conditions. 51
Figure 3.28: Settling velocities in Fluid 5 under unbounded conditions. 51
Figure 3.29: Settling velocities in Fluid 6 under unbounded conditions. 52
Figure 3.30: Settling velocities in Fluid 7 under unbounded conditions. 52
Figure 3.31: Velocity ratio for different diameter particles in Fluids 1, 2 and 3. ..53
Figure 3.32: Velocity ratio for different diameter particles in Fluids 4, 5, 6 an7. .53
Figure 3.33: Velocity ratio as a function of the particle Weissenberg number. The plot shows the velocity increase followed by a velocity decrease with the increase in Weissenberg number. The error bars show the variance in the velocity ratio from repeated measurements.....54
Figure 3.34: Comparison of the experimental velocity ratios with those predicted using the correlation. The x-axis is $We_{\infty INEL}$ which is not the actual particle Weissenberg number.....55
Figure 3.35: Drag correction factor as a function of the particle Weissenberg number for fluids with different *n* values. 56

Figure 4.1: Schematic of the experimental cell for determining settling velocities between parallel walls (not to scale). 68
Figure 4.2: Schematic of the experimental cell illustrating the procedure for measuring the settling velocity of particles between the parallel walls. 68
Figure 4.3: Snapshot of particle settling in the experimental cell in the VES fluid.69
Figure 4.4: Snapshot of particle tracking in Tracker 2.0. 69
Figure 4.5: Wall factors for particles settling in Fluid 1. *r* is the ratio of particle diameter to slot width.....70
Figure 4.6: Wall factors for particles settling in Fluid 2. *r* is the ratio of particle diameter to slot width.....70
Figure 4.7: Wall factors for particles settling in Fluid 3. *r* is the ratio of particle diameter to slot width.....71
Figure 4.8: Wall factors for particles settling in Fluid 4. *r* is the ratio of particle diameter to slot width.....71
Figure 4.9: Wall factors for particles settling in Fluid 5. *r* is the ratio of particle diameter to slot width.....72
Figure 4.10: Wall factors for particles settling in Fluid 6. *r* is the ratio of particle diameter to slot width.....72
Figure 4.11: Wall factors for particles settling in Fluid 7. *r* is the ratio of particle diameter to slot width.....73
Figure 4.12: Experimentally measured wall factors against the particle Weissenberg number for three different fixed values of *r*. 74

Figure 4.13: Comparison of the experimental wall factors for particles settling in Fluids 4, 5, 6 and 7 with the correlation by Machac and Lecjaks (1995). 75

Figure 4.14: Wall factors in fluids with different *n* values predicted using the correlation in Equation 4.2. Wall factors decrease as the shear thinning behavior of the fluid increase. 76

Figure 5.1: Schematic of the mixing zone. A more viscous Fluid 1 is displaced by less viscous Fluid 2 leading to the development of fingers. 99

Figure 5.2: Schematic showing the injection of alternate slugs of Fluid 1 (more viscous) and Fluid 2 (less viscous) in rectilinear flow. The displacement of Fluid 2 by Fluid 1 is stable (piston-like). 99

Figure 5.3: Schematic of the Hele-Shaw cell (not to scale). 100

Figure 5.4: Schematic of the experimental setup. 100

Figure 5.5: Isco syringe pump used for the viscous fingering experiments. 101

Figure 5.6: Snapshot showing the Hele-Shaw cell kept in an inclined position. The pump pushes the glycerol solution through the accumulator against gravity. 102

Figure 5.7: Three-pronged manifold showing the inlet from the pump divided into three streams for inlet to the Hele-Shaw cell. 103

Figure 5.8: Snapshot showing the injection of dyed water into the Hele-Shaw cell from the three inlets. The experiment is recorded using a pair of tripods. 104

Figure 5.9: Steady shear-viscosity measurement for 97% Glycerol solution. 105

Figure 5.10: Sequential position of the interface between clear water and dyed water. Dyed water is injected into clear water at a rate of 12.35ml/min. (Viscosity Ratio, M = 1).....106

Figure 5.11: Sequential evolution of the interface between water and 79% glycerol solution. Dyed water is injected into glycerol solution at a rate of 4.69ml/min. (Viscosity Ratio, M = 50) 107

Figure 5.12: Sequential evolution of the interface between water and 83% glycerol solution. Dyed water is injected into glycerol solution at a rate of 4.69ml/min. (Viscosity Ratio, M = 79.5) 108

Figure 5.13: Sequential evolution of the interface between water and 89% glycerol solution. Dyed water is injected into glycerol solution at a rate of 4.69ml/min. (Viscosity Ratio, M = 177.5) 109

Figure 5.14: Sequential evolution of the interface between water and 95.5% glycerol solution. Dyed water is injected into glycerol solution at a rate of 4.69ml/min. (Viscosity Ratio, M = 463) 110

Figure 5.15: Sequential evolution of the interface between water and 97% glycerol solution. Dyed water is injected into glycerol solution at a rate of 4.69ml/min. (Viscosity Ratio, M = 665) 111

Figure 5.16: Sequential evolution of the interface between water and 100% glycerol. Dyed water is injected into glycerin at a rate of 4.69ml/min. (Viscosity Ratio, M = 1225) 112

Figure 5.17: Mixing zone length as a function of time for displacement of 97% Glycerol solution with water at 12.35 and 4.69 ml/min. (Viscosity Ratio, M = 665).....113

Figure 5.18: Mixing zone velocities at different viscosity ratios at an injection rate of 12.35ml/min. 114
Figure 5.19: Mixing zone velocities at different viscosity ratios at an injection rate of 4.69ml/min. 114
Figure 5.20: Mixing zone velocities at different viscosity ratios at an injection rate of 1.28ml/min. 115
Figure 5.21: Normalized mixing zone velocities at the three injection rates for different viscosity ratios. 115
Figure 5.22: Comparison of the Koval factor from the experimental data (using Equation 5.7) and the empirical fit with 0.22 as the fitting constant (Equation 5.2). 116
Figure 5.23: Viscosity of glycerol solutions at different concentrations. The fourth-root mixing rule (Equation 5.3) predicts the data well. 116
Figure 5.24: Comparison of the Koval factor from the experimental data (using Equation 5.7) with empirical fit with 0.094 as the fitting constant (Equation 5.8). 117
Figure 5.25: Fingertip velocities at different viscosity ratios at an injection rate of 12.34ml/min. 117
Figure 5.26: Fingertip velocities at different viscosity ratios at an injection rate of 4.69ml/min. 118
Figure 5.27: Fingertip velocities at different viscosity ratios at an injection rate of 1.28ml/min. 118
Figure 5.28: Relative front velocities in different viscosity glycerol solutions at three injection rates. 119

Figure 5.29: An illustration of the outlined interface between the injected dyed water and displaced glycerol solution. The area of the displacing water is calculated using ImageJ.....119
Figure 5.30: Relative finger width (RFW) as a function of time for injection of water at 12.35ml/min in different viscosity glycerol solutions.....120
Figure 5.31: Relative finger width (RFW) as a function of time for injection of water at 4.69ml/min in different viscosity glycerol solutions.....121
Figure 5.32: Schematic showing the symmetric tongue of the injected fluid. The thickness of the film of the displaced fluid on the walls is denoted by *t*. 122
Figure 5.33: Thickness of the thin film of the displaced fluid (glycerol solutions) on the walls of Hele-Shaw cells as a function of time. The injection rate of water is 12.35ml/min. 122
Figure 5.34: Thickness of the thin film of the displaced fluid (glycerol solutions) on the walls of Hele-Shaw cells as a function of time. The injection rate of water is 4.69ml/min. 123
Figure 5.35: Relative finger width as a function of dimensionless time for 100% glycerol solution at different injection rates of water. (Viscosity Ratio, M = 1225).....124
Figure 5.36: Relative finger width as a function of dimensionless time for 97% glycerol solution at different injection rates of water. (Viscosity Ratio, M = 665).....124
Figure 5.37: Relative finger width as a function of dimensionless time for 95.5% glycerol solution at different injection rates of water. (Viscosity ratio, M = 463) 125

Figure 5.38: Relative finger width as a function of dimensionless time for 94% glycerol solution at different injection rates of water. (Viscosity Ratio, M = 343).....125
Figure 5.39: Relative finger width as a function of dimensionless time for 89% glycerol solution at different injection rates of water. (Viscosity Ratio, M = 177.5).....126
Figure 5.40: Relative finger width as a function of dimensionless time for 88.3% glycerol solution at different injection rates of water. (Viscosity Ratio, M = 153).....126
Figure 5.41: Film thickness of the film of displaced fluid as a function of dimensionless time for 100% glycerol solution at different injection rates of water. (Viscosity Ratio, M = 1225).....127
Figure 5.42: Film thickness of the film of displaced fluid as a function of dimensionless time for 97% glycerol solution at different injection rates of water. (Viscosity Ratio, M = 665).....127
Figure 5.43: Film thickness of the film of displaced fluid as a function of dimensionless time for 95.5% glycerol solution at different injection rates of water. (Viscosity Ratio, M = 463).....128
Figure 5.44: Film thickness of the film of displaced fluid as a function of dimensionless time for 94% glycerol solution at different injection rates of water. (Viscosity Ratio, M = 343).....128
Figure 5.45: Film thickness of the film of displaced fluid as a function of dimensionless time for 89% glycerol solution at different injection rates of water. (Viscosity Ratio, M = 177.5).....129

Figure 5.46: Film thickness of the film of displaced fluid as a function of dimensionless time for 88.2% glycerol solution at different injection rates of water. (Viscosity Ratio, M = 153).....129

Figure 5.47: Schematic showing the viscous fingers of water in the polymer solution at the end of a reverse-hybrid fracture treatment for an example calculation. The volume of polymer slug is twice that of water. At the end of the treatment the mixing zone spreads from x=25.4m to x=152.4m in the fracture. The proppant is assumed to travel horizontally at the velocity of the fluid.....130

Figure 6.1: Steady shear viscosity as a function of shear rate for Liquids L1 and T1. 159

Figure 6.2: Dynamic oscillatory-shear properties of fluids L1 and T1.....159

Figure 6.3: Comparison of the measured dynamic moduli with that fitted using a 2 element series Maxwell model for liquid L1. 160

Figure 6.4: Comparison of the measured dynamic moduli with that fitted using a 1element Maxwell model for liquid T1. 160

Figure 6.5: Schematic of the Hele-Shaw cell (not to scale).....161

Figure 6.6: Sketch of the experimental setup showing the two pumps, with the accumulator and the Hele-Shaw cell.....162

Figure 6.7: Sequential position of the interface between clear water and dyed water. Dyed water is injected into clear water at a rate of 12.35ml/min. 163

Figure 6.8: Sequential evolution of the interface between water and 37.5%PEG 0.08%PEO solution (Liquid L1). Water is injected at a rate of 12.35ml/min. 164

Figure 6.9: Sequential evolution of the interface between water and 37.5%PEG 0.08%PEO solution (Liquid L1). Water is injected at a rate of 4.69ml/min. 165

Figure 6.10: Sequential evolution of the interface between water and 88.2% glycerol solution (Liquid T1). Water is injected at a rate of 12.35ml/min. 166

Figure 6.11: Sequential evolution of the interface between water and 88.2% glycerol solution (Liquid T1). Water is injected at a rate of 4.69ml/min. 167

Figure 6.12: Snapshot showing the evolution of the instability for injection of water in 37.5%PEG 0.08%PEO solution (Liquid L1) at a rate of 4.69ml/min. Snapshot is taken at 18.5 seconds after starting the injection.....168

Figure 6.13: Interface between the displaced and displacing fluid tracked from Figure 6.12 using 'Plot Digitizer'. 168

Figure 6.14: Modified profile of the interface between the two fluids to ensure that there is a unique value of A for every x. 169

Figure 6.15: The spectrum of the wave numbers for interface evolution between water and 37.5%PEG 0.08%PEO (Liquid L1) at an injection rate of 4.69ml/min. The dominant wave number is 20 cm^{-1}. 169

Figure 6.16: Relative front velocities (RFV) as a function of the injection rate in liquids L1 and T1. 170

Figure 6.17: Relative front velocities (RFV) as a function of the injection rate in liquids L2 and T2. 170

Figure 6.18: Snapshot of the outlined interface between the displacing and displaced fluid. The area covered by the displacing fluid is calculated using ImageJ. 171
Figure 6.19: Relative finger width as a function of time at an injection rate of 1.28ml/min for liquids L1 and T1.....172
Figure 6.20: Relative finger width as a function of time at an injection rate of 1.28ml/min for liquids L2 and T2.....172
Figure 6.21: Relative finger width as a function of time at an injection rate of 4.69ml/min for liquids L1 and T1.....173
Figure 6.22: Relative finger width as a function of time at an injection rate of 4.69ml/min for liquids L2 and T2.....173
Figure 6.23: Relative finger width as a function of time at an injection rate of 12.35ml/min for liquids L1 and T1.....174
Figure 6.24: Relative finger width as a function of time at an injection rate of 12.35ml/min for liquids L2 and T2.....174
Figure 6.25: Schematic showing the symmetric tongue of the injected fluid. *t* denotes the thickness of the film of the displaced fluid on the walls.175
Figure 6.26: Thickness of the displaced fluid film on the walls for Liquids L1 and T1 at an injection rate of 1.28ml/min.....175
Figure 6.27: Thickness of the displaced fluid film on the walls for Liquids L2 and T2 at an injection rate of 1.28ml/min.....176
Figure 6.28: Thickness of the displaced fluid film on the walls for Liquids L1 and T1 at an injection rate of 4.69ml/min.....176
Figure 6.29: Thickness of the displaced fluid film on the walls for Liquids L2 and T2 at an injection rate of 4.69ml/min.....177

Figure 6.30: Thickness of the displaced fluid film on the walls for Liquids L1 and T1 at an injection rate of 12.35ml/min.....177
Figure 6.31: Thickness of the displaced fluid film on the walls for Liquids L2 and T2 at an injection rate of 12.35ml/min.....178
Figure 6.32: Relative finger width as a function of dimensionless time for different injection rates of water in 88.2% glycerol (T1) solution. 178
Figure 6.33: Relative finger width as a function of dimensionless time for different injection rates of water in 89% glycerol (T2) solution. ...179
Figure 6.34: Relative finger width as a function of dimensionless time for different injection rates of water in 37.5%PEG 0.08%PEO (L1) solution.....179
Figure 6.35: Relative finger width as a function of dimensionless time for different injection rates of water in 37.5%PEG 0.14%PEO (L2) solution.....180
Figure 6.36: Film thickness versus dimensionless time in 88.2% glycerol (T1) solution at different injection rates. 180
Figure 6.37: Film thickness versus dimensionless time in 89% glycerol (T2) solution at different injection rates. 181
Figure 6.38: Film thickness versus dimensionless time in 37.5%PEG 0.08%PEO (L1) solution at different injection rates. 181
Figure 6.39: Film thickness versus dimensionless time in 37.5%PEG 0.14%PEO (L2) solution at different injection rates. 182
Figure 7.1: Schematic of sequence of proppant deposition in slickwater fracturing (after Kern et al. 1958).....214

Figure 7.2: Pumping schedule for conventional and channel fracturing treatments (from Gillard et al. 2010). 215
Figure 7.3: Schematic of the fracture cell. 215
Figure 7.4: Sketch of the experimental setup.....216
Figure 7.5: Snapshot showing the Moyno pump along with the water reservoir for the suction to the pump. 217
Figure 7.6: Illustration of the custom made blender for pumping proppant slurry. The blue arrow shows the direction of movement of the piston which is pushed by water. The red arrows show the direction of movement of proppant slurry through the hole in the piston and the tubing. ...218
Figure 7.7: Electric motor connected to the rotor on one side of the blender.....219
Figure 7.8: Illustration of the tubing connecting the piston to the end cap, transporting proppants along with liquid. 219
Figure 7.9: Snapshot showing the end cap connected to the PVC pipe with the tube curled in the chamber. 219
Figure 7.10: Illustration of the blender being used to pump proppants (black) in a polymer solution. The black arrow indicates the direction of injection of water from the pump pushing the piston upwards. White arrows shows the proppant slurry pumped our through the piston, tubing and the end cap. 220
Figure 7.11: Sequential snapshots showing the injection of water along with sand in the cell. The cell is initially filled with clear water and blue dyed water with white sand is injected. 221
Figure 7.12: Viscosity versus shear rate for 1 % polyethylene oxide (PEO) solution.....222

Figure 7.13: Sequential snapshots showing the injection of sand in 1% polyethylene oxide solution in the cell. The cell is initially filled with the blue dyed water and the injected polymer solution is clear. 223

Figure 7.14: Sequential snapshots illustrating the reverse-hybrid fracturing treatment. Dyed water along with land is injected into a cell containing 1% polymer (PEO) solution. 224

Figure 7.15: Sequential snapshots illustrating the alternate-slug fracturing treatment. Sand-laden water (dyed) and proppant-free 1% polyethylene oxide solution (clear) are injected alternately into the fracture cell. 225

Figure 7.16: Sequential snapshots showing the injection of 1% polyethylene oxide solution along with ceramic proppant in the cell. The cell is initially filled with the same polymer solution. 226

Figure 7.17: Sequential snapshots showing the injection of water along with ceramic proppant in the cell. The cell is initially filled with clear water and dyed water with proppant is injected. 227

Figure 7.18: Sequential snapshots illustrating the reverse-hybrid fracturing treatment. Water along with ceramic proppant is injected into a cell containing 1% polymer (PEO) solution. 228

Figure 7.19: Sequential snapshots illustrating the alternate-slug fracturing treatment. Proppant-laden water (dyed) and proppant-free 1% polyethylene oxide solution are injected alternately into the fracture cell. 229

Figure 7.20: Relative front velocity as a function of viscosity ratio. The figure is same as Figure 5.22 in Chapter 5. Relative front velocity is the velocity of the fingertip/finger front divided by the injection velocity.....230

Figure 7.21: Relative front velocity as a function of viscosity ratio. The figure is same as Figure 5.17 in Chapter 5. Normalized mixing zone velocity is the velocity of the mixing zone divided by the injection velocity.230

Figure 7.22: Schematic showing the movement of the fluid fronts in one wing of a vertical fracture. The more viscous fluid 1 is injected first at velocity, *U* followed by a less viscous fluid 2 at the same injection rate. The finger tip and the mixing zone move at different velocities. 231

Figure 7.23: Schematic showing the distances covered by the fingertip and mixing zone in one wing of the fracture at the end of the reverse-hybrid fracture treatment. The treatment consists of only one slug of polymer followed by one slug of water. The length of the mixing zone is 124.2m. 231

Figure 7.24: Schematic showing the distances covered by the fingertip and mixing zone in one wing of the fracture at the end of an alternate-slug fracture treatment. The treatment involves 3 slugs of polymer and water each. '1' denotes the polymer and '2' denotes water.....232

Chapter 1: Introduction and Outline of Thesis

1.1 INTRODUCTION

Hydraulic fractures are created in formations to increase the productivity of wells by increasing the surface area available for the flow of hydrocarbons and by providing a high permeability conduit for hydrocarbons to flow from the reservoir to the wellbore. The hydraulic fracturing treatments involve fracturing the formation by pumping fluids at high pressures, and placing proppant inside the fractures to maintain conductive conduits. Hydraulic fracturing along with horizontal drilling has made it possible to produce hydrocarbons from unconventional reservoirs including tight gas sandstones and shales.

In hydraulic fracturing treatments, proppants are placed in the fracture by mixing them with the fracturing fluid. Ideally this fluid is required to have excellent proppant carrying abilities so as to keep the proppant from settling and to distribute the proppant uniformly along the length of the fracture. The productivity of fractured wells is determined by two main factors, fracture conductivity and propped fracture length. In high permeability formations, fracture conductivity is more important to enhance productivity. In low permeability formations, propped fracture length is usually more important. Both these factors depend on the effective transport of proppant inside the fracture.

A typical hydraulic fracturing treatment consists of the following sequence of injection: (1) a fluid without any proppant, known as the pad, is pumped under high

pressure to initiate and extend the fracture. (2) The pad is followed by a high-viscosity fluid laden with proppant. The proppant is carried into the fracture because of the high viscosity of this fluid. (3) The third stage, or over-flush, consists of a fluid without the proppant. The function of the over-flush is to clear the wellbore of any proppant-slurry and displace it into the fracture.

Upon the cessation of pumping, the fracture closes on the proppant pack, which provides a highly conducive pathway for the hydrocarbons to flow from the reservoir to the wellbore. For efficient flow of the hydrocarbons the proppant must be carried far into the fracture, and distributed uniformly throughout the length of the fracture. The transport of proppant is thus key to well productivity and depends on many factors including fluid rheology and proppant size, density and concentration as well as fracture width.

In the oil industry, various types of fracturing fluids have been used for hydraulic fracturing. These range from conventional fracturing fluids, which include water-based and polymer-containing fluids, to energized fluids, foams and hydrocarbon-based fluids. Dantas et al. (2005) provides a thorough review of several types of conventional fracturing fluids and the methods applied for their design. The unconventional fracturing fluids include polymer-free fluids, methanol-containing fluids, liquid CO_2 based fluids and liquefied-petroleum based fluids. A review of unconventional fracturing fluids and their applications can be found in Gupta (2009).

The surfactant based viscoelastic (VES) fluid systems fall under the category of polymer-free fluids. They have been widely used for hydraulic fracturing (Samuel et al. 1997; Mathis et al. 2002; Leitzell 2007) over the past years. Free of polymers, these fluids leave very little residue and facilitate rapid flowback. The operational simplicity of these fluids also provides an advantage over conventional fracturing fluids (Gupta 2009). For VES fluids, elasticity plays an important role in suspending the proppant. It has been pointed out by Asadi et al. (2002) that the zero shear viscosity is an important parameter for evaluating proppant transport in these fluids. However, there is very little data that shows the influence of fluid elasticity on the settling velocity of proppant in VES fluids. This dissertation presents an experimental study to understand and quantify the settling velocity of proppant in VES fluids. Experimental data is presented to show the effect of fluid viscosity, elasticity and fracture walls on settling velocity.

Different types of fracturing and proppant injection strategies have been used in the industry. The strategies vary in the type of fluid used, and the sequence of fluid and proppant injection. The conventional method of fracturing involves the use of high viscosity cross-linked gels with large amounts of proppant (Gildey et al. 1989). High viscosity fluids lower the settling velocities of proppant and provide good proppant placement. However, cross-linked gel-based fluids may fully break or leave a residue upon breaking, which can cause severe damage to the proppant pack, lowering its conductivity and well productivity (Hawkins 1988; Pope et al. 1996). Gel damage is a major concern especially in low permeability formations. Over the past few years there

has been a shift in strategy towards use of low viscosity fluids such as uncross-linked linear gels and slick-water (Mayerhofer et al.1997; Walker et al. 1998; Palisch et al. 2010). Low viscosity fluids help in creating longer fractures and minimizing gel damage to the proppant pack. However, proppant transport is a major concern in low viscosity fluids.

Following the success of slickwater fracturing, a new type of treatment design, hybrid fracturing, was introduced (Sharma et al. 2004). This technique involves the use of water in the pad stage to create a long fracture. The water is followed by a cross-linked gel in the proppant stage. Hybrid fracturing, thus, takes advantage of the benefits of conventional fracturing as well as water fracturing. This method of fracturing has been observed to create longer propped fracture lengths and higher fracture conductivities (Sharma et al. 2004). However, this method still has the drawback of gel damage in the proppant pack as proppant are carried in the gel. Liu et al. (2007) presented a new method of fracturing, reverse-hybrid fracturing, to improve performance of fracturing treatments. This method involves the creation of the fracture with a high viscosity cross-linked fluid followed by proppant pumped in water. The water forms viscous fingers in the high viscosity fluid. Through the high velocity in the viscous fingers, water carries proppant deep into the fracture and places them heterogeneously in the fracture. However, there have been concerns of tip screen-outs using reverse-hybrid fracturing primarily because of the reduced width of the fracture when water is injected resulting in high leak-off into the matrix.

To improve the proppant transport and address concerns related to tip screen-outs, this work proposes a new method of fracturing, referred to as alternate-slug fracturing. The new method of proppant placement involves the injection of alternate slugs of high viscosity (cross-linked) fluid and low viscosity fluid in the fracture. The proppant is pumped in the low viscosity fluid. The method takes advantage of deeper proppant placement through viscous fingers of low viscosity fluid and viscous sweeps of proppant by the high viscosity fluid. The method reduces the risk of tip screen-outs because of the alternate slugs of high viscosity fluid.

1.2 Outline of Thesis

Chapter 2 provides an introduction to the rheological characterization of fluids. The rheological characterization involves measuring and quantifying the viscous and elastic properties of fluids. The experimental techniques and models discussed in this chapter are used for describing rheological properties of fluids in all the subsequent chapters.

Chapter 3 presents an experimental study to quantify settling velocities of spherical particles in unbounded, surfactant-based viscoelastic shear-thinning (VES) fluids. Experiments are performed to measure settling velocities of spherical particles in fluids of varying viscous and elastic properties. Results are presented to show that fluid elasticity reduces the settling velocity at low Weissenberg numbers, followed by an

increase in settling velocity at higher Weissenberg numbers. A new correlation is presented to quantify the settling velocity in unbounded VES fluids.

Chapter 4 presents an experimental study to quantify the effect of confining parallel (fracture) walls on settling velocities in VES fluids. Experiments are performed in cells with parallel walls and settling velocities are measured. Results show that fluid elasticity reduces the retardation effect of confining walls. A new correlation is presented to quantify the retardation effect of confining walls in VES fluids.

Chapter 5 focuses on the experimental measurement of the growth of the mixing zone and viscous finger velocities in Newtonian fluids over a wide range of viscosity ratios. Experiments are performed in rectilinear Hele-Shaw cells with water injected in glycerol solutions that have a wide range of viscosity. The mixing zone velocity is observed to increase with viscosity ratio up to ratios of 350, above which it plateaus. These measurements are critical for designing the alternate-slug fracturing treatments introduced in the previous section.

Chapter 6 aims to determine the effect of fluid elasticity on miscible viscous fingering. Rectilinear displacement experiments are performed in glycerol solutions and polymer based Boger fluids (constant-viscosity elastic fluids). Comparisons between the fluids show that fluid elasticity changes the viscous fingering patterns and leads to the formation of multiple thin fingers as compared to a single thick dominant finger in less

elastic fluids. Fluid elasticity is observed to retard the growth of fingers. Based on these observations, it is concluded that more elastic gels are more suitable for proppant placement using alternate-slug fracturing.

Chapter 7 discusses the proppant placement strategies used in hydraulic fracturing treatments in detail. A new method of proppant injection, alternate-slug fracturing, is introduced. This method involves the injection of proppant-free high viscosity fluid and proppant-laden low viscosity fluid alternately in the fracture. Experiments are performed in a fracture cell to demonstrate this method. The low viscosity fluid forms viscous fingers and transports proppant deep into the fracture. The trailing slug of high viscosity fluid sweeps the proppant banks into the fracture. Comparisons with experiments showing other proppant placement strategies show that alternate-slug fracturing leads to longer propped fracture lengths. This method has advantages over conventional methods of fracturing by reducing the gel damage as proppant are pumped in water. The method requires low pump horsepower, reduces leak-off and decreases the risk of tip screen outs as compared to slick-water and reverse-hybrid fracturing.

Chapter 2: Rheological Characterization of Fluids

Fluids of various rheological properties are used for hydraulic fracturing applications. These range from Newtonian fluids such as water (Palisch et al. 2010) and hydrocarbon based fluids, to non-Newtonian fluids including polymer gels (un-cross-linked and cross-linked guar-based gels) (Dantas et al. 2005), viscoelastic surfactant fluids (Leitzell 2007), liquid carbon dioxide based fluids (Gupta 2009) and energized fluids and foams (Ribeiro and Sharma 2012). The rheology of these fluids controls the flow behavior, proppant transport capabilities and leak-off. It is, therefore, important to characterize their rheology accurately. This chapter discusses the models and lab measurements used in the study for quantifying the rheological properties of fluids.

2.1 VISCOSITY

Viscosity is a measure of a fluid's internal resistance to flow. Viscosity is the most important rheological property for describing the fluid's flow and proppant suspension characteristics. Fluids are characterized as Newtonian or non-Newtonian depending upon how the viscosity behaves as a function of strain rate (or shear rate) or when they exhibit non-equal normal stresses in shearing flow.

2.1.1 Newtonian Fluids

Consider a layer of fluid confined between two parallel plates separated by a gap as shown in Figure 2.1. A constant force F is applied to the top plate. At steady state the applied force will be balanced by the internal frictional force of the fluid, resulting in a

velocity profile. For a Newtonian fluid, the shear stress is directly proportional to the shear strain,

$$\frac{F}{A} = \mu\left(-\frac{dV_x}{dy}\right) \tag{2.1}$$

$$\tau_{yx} = \mu\dot{\gamma}_{yx} \tag{2.2}$$

The proportionality constant μ is the viscosity of the Newtonian fluid. Therefore, a Newtonian fluid can be defined as a fluid whose stress versus strain rate is linear and passes through origin. For a Newtonian fluid, viscosity is the only property that characterizes the flow behavior at a constant pressure and temperature.

2.1.2 Non-Newtonian Fluids

A fluid is non-Newtonian when its shear stress versus shear rate curve is non-linear or the curve does not pass through origin. The value of the viscosity for these fluids not only depends upon pressure and temperature but also on flow geometry, shear rate, kinematic history. Non-Newtonian fluids can be divided into various classes such as shear thinning or pseudoplastic, shear thickening, viscoelastic etc. A detailed description of various classes of non-Newtonian fluids can be found in Chhabra (2007). In this thesis, we focus on shear thinning and viscoelastic fluids. All the fluids used in our experiments and in hydraulic fracturing applications fall into the categories of Newtonian, shear thinning or viscoelastic fluids.

2.1.2.1Shear Thinning or Pseudoplastic Fluids

A fluid whose apparent viscosity (shear stress divided by shear rate) decreases with an increase in shear rate is referred to as shear thinning. Most polymeric fluids exhibit a shear thinning behavior over a wide range of shear rates. The rate of decrease of viscosity with shear rate depends on many physiochemical factors such as polymer concentration and type, molecular weight distribution of polymer and type of solvent. Most polymeric solutions also have regions of constant viscosity at very low and very high shear rates. Numerical expressions of many forms and complexities are available in the literature for modeling shear thinning characteristics. These include models that involve curve fitting of the shear stress versus shear rate data and theoretical models based on statistical mechanics, kinetic theory of liquids etc. (Bird 1976; Bird et al. 1987; Carreau et al. 1997; Chhabra 2007).

In this work the Power-Law also known as Ostwald-De Waele Model, has been used to model the shear thinning behavior. For most fluids, the shear stress versus shear rate plot on a log-log plot exhibits a straight line over a limited range of shear rates. This model uses a power law expression to fit the straight line. The expression for the power law model is given by:

$$\tau_{yx} = K\left(\dot{\gamma}_{yx}\right)^{n} \tag{2.3}$$

or

$$\mu = K\left(\dot{\gamma}_{yx}\right)^{n-1} \tag{2.4}$$

n and *K* are referred to as the power-law index (or the flow behavior index) and flow consistency index respectively. The degree of shear thinning is determined by *n.* A lower *n* value indicates a higher degree of shear thinning. For a Newtonian fluid, *n* is equal to 1.

Viscoelastic fluids are described in the next section; however, it is important to mention that shear thinning and viscoelasticity are not mutually exclusive. Viscoelastic fluids have finite viscosity, and most viscoelastic fluids, being polymeric fluids, exhibit shear thinning characteristics. Special class of viscoelastic fluids that have a constant viscosity over a wide range of shear rates are called Boger fluids. These are discussed in more details in the next section.

2.1.3 Lab Measurement of Viscosity

In the lab, the viscosity of fluids is measured by performing steady shear-viscosity measurements. The steady shear-viscosity measurements involve the measurement of shear stress and viscosity as functions of shear rate. The ARES rheometer from TA instruments (Figure 2.2) with double wall geometry is used for performing the measurements. The dimensions of the double wall concentric cylinder fixture are: inside cup diameter-27.95mm, inside bob diameter-29.50mm, outside bob diameter-32.00mm, outside cup diameter-34.00mm, bob length-32.00mm.

The steady shear-viscosity measurement involves the ‘Step Rate Test’ for calibrating the measurement time in the rheometer and the ‘Steady Rate Sweep Test’ for

measuring the shear stress and torque as a function of shear rate. A constant shear strain is applied on the sample by rotating the outer cylinder. The torque on the inner cylinder is measured by the rheometer. The viscosity of the sample can be calculated from the torque generated at steady state. For all the fluid samples used in this study, the shear rate is varied from 0.1 to 800s^{-1} with 3 (up to 10) points per decade recorded. Figure 2.3 shows an example of a viscosity versus shear rate recorded for a polymer sample. The power–law model (Equation 2.4) is fitted between shear rates of 1 and 100s^{-1} as shown on the plot (K = 1.086Pa.s^n and n = 0.551).

2.2 VISCOELASTICITY

A material which regains its original configuration upon the removal of the stress is a perfectly elastic material. For a perfectly viscous material, shear stress is proportional to the shear strain. Viscoelastic fluids exhibit the properties of viscous as well as elastic substances.

2.2.1 Maxwell Representation

The most common representation of a viscoelastic fluid as proposed by Maxwell is shown in Figure 2.4. The figure shows a dashpot which represents the viscous component and a spring which represents the elastic component. The constitutive equation for the Maxwell model is given by:

$$\frac{d\varepsilon}{dt} = \frac{1}{k}\frac{d\tau}{dt} + \frac{\tau}{\eta} \qquad 2.5$$

In this equation τ is the stress in the Maxwell element, ε is the total strain, k is the spring constant of the spring and η is the viscosity of the dashpot. A characteristic relaxation time, λ of the Maxwell fluid, can be defined as:

$$\lambda = \frac{\eta}{k} \qquad 2.6$$

The relaxation time is the measure of the elasticity of the sample. The higher the relaxation time, more elastic the behavior of the material. A fluid with a zero relaxation time is a purely viscous (inelastic) fluid.

2.2.2 Rheological Characterization

The rheological characterization of viscoelastic fluids involves the measurement of the viscosity as well as the elasticity (relaxation time) of the fluid. Different kinds of experimental techniques have been used for the determination of the rheological properties of viscoelastic fluids (Ferry 1970). This section entails the theoretical basis behind the experimental techniques employed in this study.

2.2.2.1 Stress Relaxation Test to Measure Relaxation Time

The relaxation time of the fluid can be measured by performing either a stress relaxation test or a dynamic frequency sweep test. In a stress relaxation test, a constant strain is instantaneously applied to the sample, and the stress generated in the sample is measured as a function of time. For a Maxwell element, the stress generated for a

constant strain input ε_0 can be calculated from the constitutive equation (Equation 2.5) and is given by:

$$\sigma(t) = \varepsilon_0 k e^{-t/\lambda} \tag{2.7}$$

The relaxation modulus of the sample can thus be written as

$$E(t) = \frac{\sigma(t)}{\varepsilon_0} = k e^{-t/\lambda} \tag{2.8}$$

Figure 2.5 shows this stress output for a constant strain input for a viscoelastic material. The relaxation time, λ, of the sample can thus be calculated by fitting the experimental data for the stress output or the relaxation modulus data to Equation 2.7 or 2.8 respectively. However, it is important to mention that in fluids the stress decays very rapidly, and it can be challenging to measure the stress response accurately in the experiment. In order to avoid this inaccuracy, the relaxation time of fluids is generally measured using dynamic tests.

2.2.2.2Dynamic Frequency Sweep Test to Measure Relaxation Time

In a dynamic test, a sinusoidal shear strain of a particular angular frequency, ω, is applied to the sample and the stress generated in the sample. For a perfectly elastic material, the stress in completely in-phase with the strain, and in a perfectly viscous material, the stress is completely out-of –phase with the strain. In a viscoelastic material, the stress leads the strain by a phase angle, δ (less than 90°). Figure 2.6 shows the stress response for a sinusoidal strain input. The output stress, σ, can be resolved into two

components: a component in-phase with the strain, σ', and a component out-of-phase with strain, σ''. Thus, the dynamic modulus, G^* of the sample can be represented as

$$G^* = G' + iG'' \tag{2.9}$$

In this equation, $G' = \sigma'/\varepsilon$ is the in-phase component referred to as the elastic modulus or the storage modulus, and $G'' = \sigma''/\varepsilon$ is the out-of-phase component referred to as the viscous modulus or the loss modulus. For a Maxwell model, the stress output for a sinusoidal strain input can be calculated by solving the constitutive equation (Equation 2.5) and using the principle of superposition and linearity to arrive at the following expression for the dynamic modulus:

$$G^*(\omega) = \frac{k\omega^2}{\frac{1}{\lambda^2}+\omega^2} + i\frac{\frac{k\omega}{\lambda}}{\frac{1}{\lambda^2}+\omega^2} \tag{2.10}$$

Using Equations 2.9 and 2.10, we can write:

$$\frac{G''(\omega)}{G'(\omega)} = \frac{1}{\omega\lambda} \tag{2.11}$$

The dynamic test is performed over a range of frequencies, thus referred to as the Dynamic Frequency Sweep Test. The elastic and viscous moduli are measured as a function of the angular frequency. The double wall concentric cylinder fixture in the ARES rheometer is used to measure the moduli over a frequency range of 0.1 to 100rad/s. Figure 2.7 shows the moduli for a fluid sample. The Maxwellian relaxation time of the fluid sample can thus be calculated by fitting the experimental moduli, $G'(\omega)$ and $G''(\omega)$ to Equation 2.11. Figure 2.8 shows the $G''(\omega)/ G'(\omega)$ along with the fit. The

fitting is performed by minimizing the sum of the variance measure over the frequency range:

$$\sigma^2 = \left[1 - \frac{G'_{fit}(\omega)}{G'(\omega)}\right]^2 + \left[1 - \frac{G''_{fit}(\omega)}{G''(\omega)}\right]^2 \qquad 2.12$$

It is important to note that two methods of measuring the relaxation time of fluids shown above should be used only if the experimental data fits the Maxwell model. In case the Maxwell model is not fit to represent the experimental data, one relaxation time is not sufficient to quantify the elastic properties of the fluid, and a spectrum (multiple) of relaxations times using a Generalized Maxwell model is required (Ferry 1970; Delshad et al. 2008; Kim et al. 2010). The relaxation time which is comparable (in terms of the order of magnitude) to the experimental/process time should then be used for further analysis.

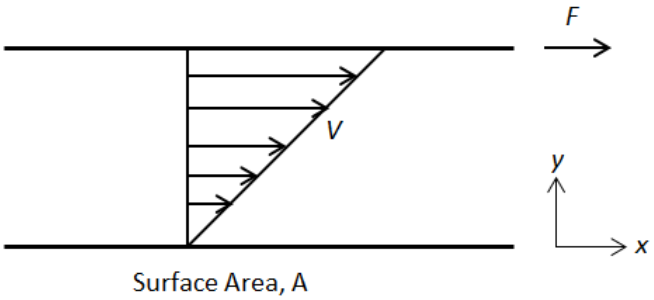

Figure 2.1: Schematic representation of shearing flow between two parallel plates.

Figure 2.2 ARES LS-1 Rheometer by TA Instruments with a double wall concentric cylinder fixture used for measuring fluid rheology.

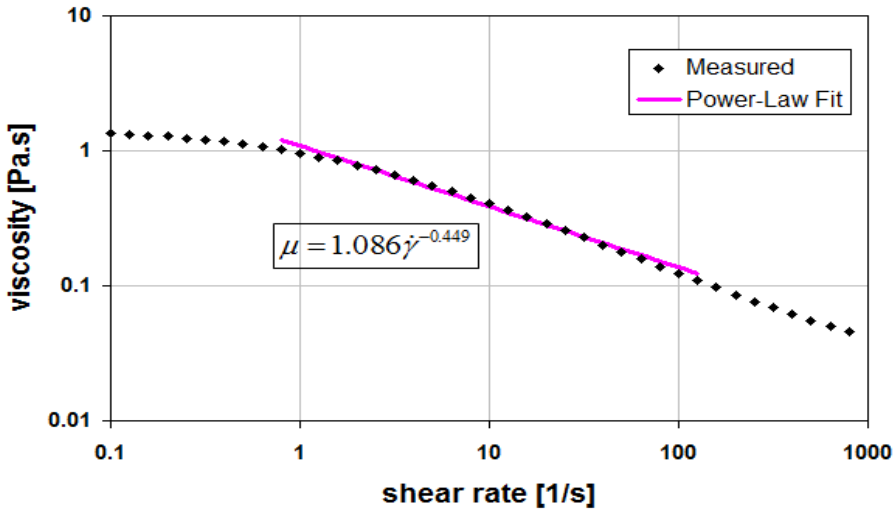

Figure 2.3: Steady shear-viscosity measurement showing viscosity versus shear rate for a polymer sample. Power-law fit is also shown on the plot.

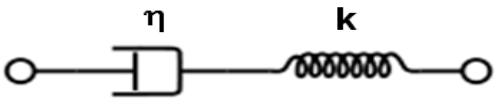

Figure 2.4: Maxwell representation of a viscoelastic material.

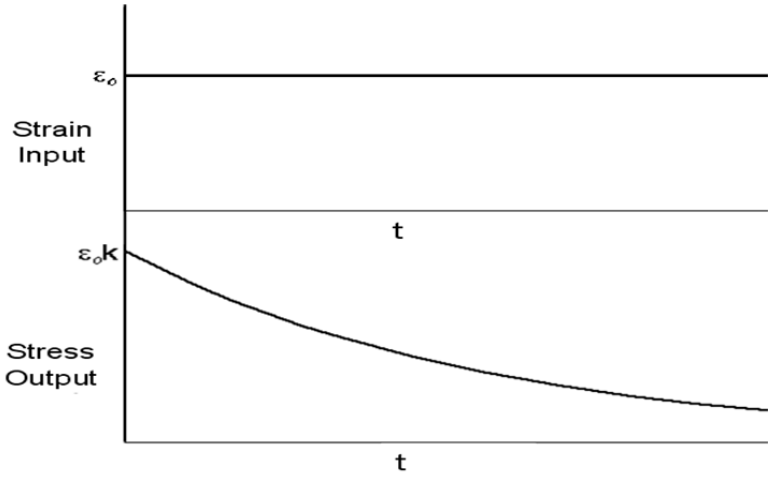

Figure 2.5: Demonstration of stress relaxation in a viscoelastic material.

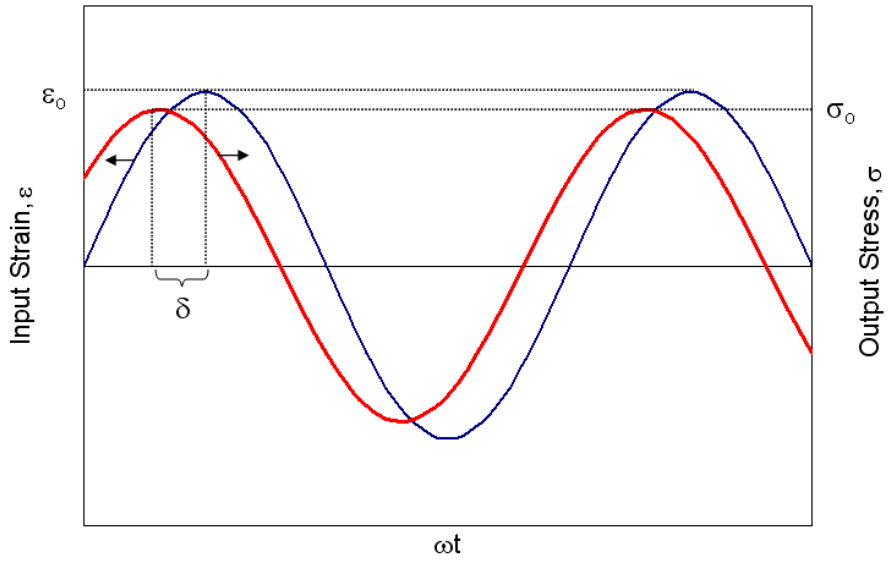

Figure 2.6: Stress response of a viscoelastic material for a sinusoidal strain input.

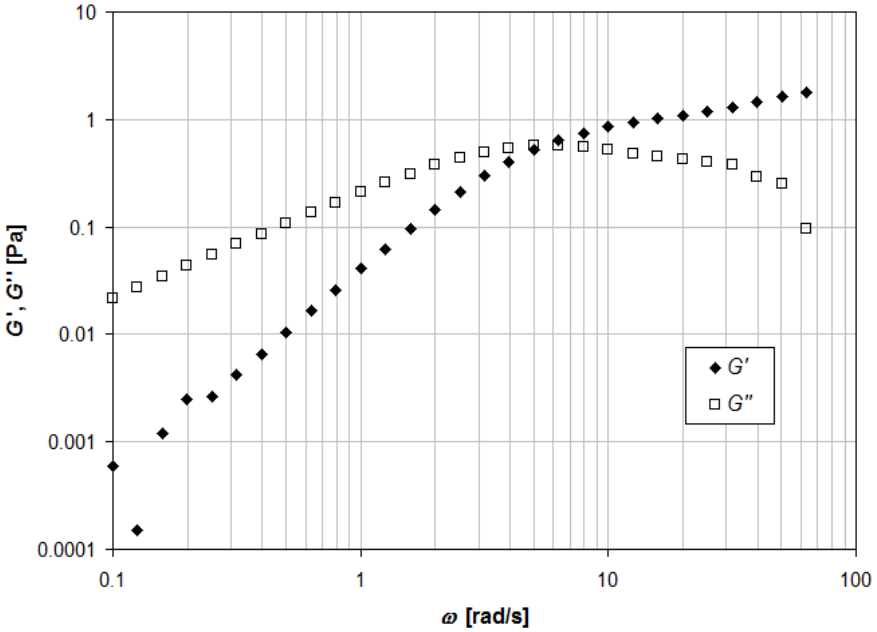

Figure 2.7: Dynamic oscillatory-shear measurements showing the elastic modulus, G' and viscous modulus, G'' as a function of the angular frequency, ω.

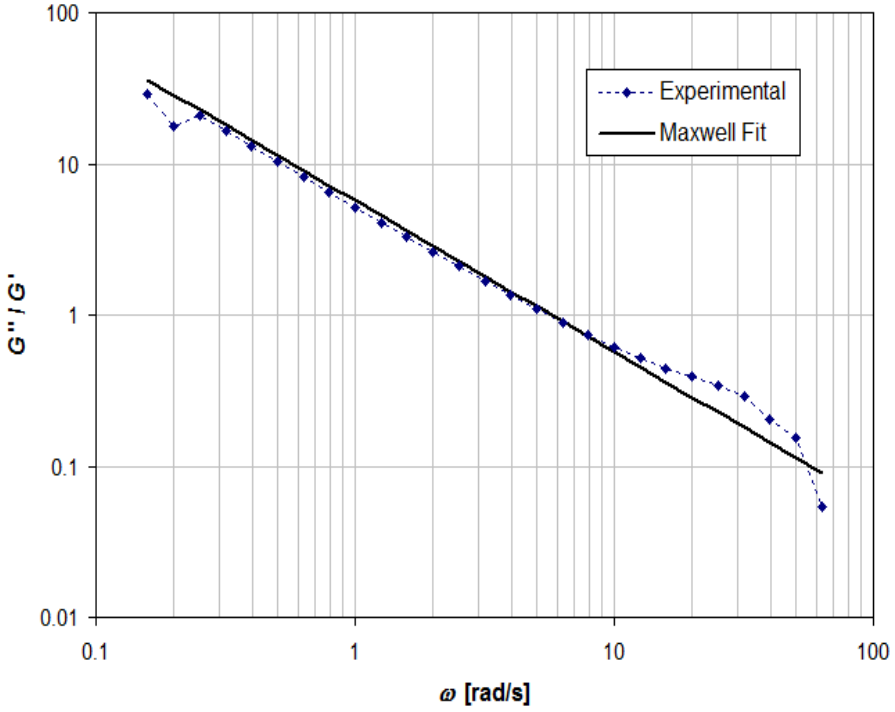

Figure 2.8: Ratio of storage modulus to elastic modulus as a function of angular frequency for a fluid sample. The Maxwell model fits to the data well. The relaxation time of the fluid sample is 0.175s.

Chapter 3: Settling of Spherical Particles in Unbounded VES Fluids

The free settling velocity of particles suspended in liquids is of importance in a wide variety of industrial applications. Slurries of solids suspended in fluids are widely used in a variety of applications including pharmaceutical manufacturing, wastewater treatment, space propellant reinjection, semiconductor processing, and liquid detergent manufacturing. In the oil industry, viscoelastic fracturing fluids are used to suspend proppant (typically sand) in hydraulic fractures. The proppant keep the created fracture open upon cessation of pumping. Settling of proppant is governed by the properties of proppant, rheology and density of fluid, and the retardation effect of confining fracture walls.

This chapter presents an experimental study to understand and quantify the settling velocity of spherical particles in unbounded surfactant-based shear thinning viscoelastic fluids. Experimental data are presented to show that elastic effects can increase or decrease the settling velocity of particles, even in the creeping flow regime. Experimental data shows that a significant drag reduction occurs with increase in Weissenberg number. This is followed by a transition to increasing drag at higher Weissenberg numbers. A new correlation is presented for the sphere settling velocity in unbounded viscoelastic fluids as a function of the fluid rheology and the proppant properties.

3.1 PAST WORK ON SETTLING IN UNBOUNDED VISCOELASTIC FLUIDS

The settling velocity of single spherical particle in a Newtonian fluid in the creeping flow regime was first derived by Stokes in 1851, commonly referred to as the Stokes equation. Subsequent researchers studied settling at higher Reynolds numbers and presented expressions to calculate the drag force (Clift et al. 1978; Khan and Richardson 1987; Zapryanov and Tabakova 1999; Michaelides 2002; Michaelides 2003). For bounded settling, the confining walls exert a retardation effect and reduce the settling velocities of particles. This effect is quantified in terms of a wall factor, $F_{w,}$ which is defined as the ratio of the settling velocity in the presence of confining walls to the unbounded settling velocity in the same fluid. Faxen (1922) pointed out that for Newtonian fluids, in the creeping flow regime, the wall factor depends only on the ratio of the particle diameter to the slot width irrespective of the viscosity of the fluid. Subsequently, many theoretical and experimental investigations determined the wall factors for spheres settling in different cross-section tubes over a wide range of Reynolds number (Bohlin 1960; Clift et al. 1978; Tullock et al. 1992; Chhabra 1996; Chhabra 2002; Chhabra 2007). While there is an extensive and a coherent body of information available for the calculation of drag on spheres settling in Newtonian fluid, the past work on the determination of settling velocity of particles in non-Newtonian fluids, particularly viscoelastic fluids, is not as complete.

Acharya et al. (1976, 1988) conducted experiments with shear-thinning viscoelastic fluids and concluded that in creeping flow regime, shear-thinning effects

completely overshadow the viscoelastic effects, and values of drag coefficient are in excellent agreement with the purely viscous theories (Chhabra and Uhlherr 1980; Bush and Phan-Thien 1984). However, other studies reported a drag reduction in the creeping flow regime (Broadbent and Mena 1974; Sigli and Coutanceau 1977). Acharya et al. (1976, 1988) also observed that at higher Reynolds numbers, the fluid elasticity causes the settling velocity to increase.

Chhabra et al. (1980) performed experiments in Boger fluids (constant viscosity elastic fluids) and observed a decrease in the drag coefficient with increasing values of Weissenberg number, until it reaches an asymptotic value at high Weissenberg numbers. The Weissenberg number is a dimensionless measure of the elastic effects, defined as follows:

$$\mathrm{We} = \frac{2\lambda V}{d_p} \tag{3.1}$$

where λ is the relaxation time of the fluid, V is the settling velocity in the fluid and d_p is the diameter of the spherical particle. The Weissenberg number can be understood as the ratio of the characteristic time of the fluid to the characteristic time of the process (settling in this case). For flow processes at steady state, the characteristic time is chosen as the inverse of the steady shear rate. For a sphere settling in a fluid, the characteristic steady shear rate is the surface averaged shear rate given by $2V/d_p$ (Uhlherr et al. 1976; Shah et al. 2007).

Brule and Gheissary (1993) performed experiments with Boger fluids as well as shear-thinning viscoelastic fluids, and observed that the settling velocity was reduced due to the elastic effects in the fluid rather than increased as reported by Chhabra et al. (1980). Walters and Tanner (1992) summarized that for Boger fluids, elasticity causes drag reduction with and increasing Weissenberg number which is followed by a drag increase at higher Weissenberg numbers. They also highlighted the other important effects such as the velocity overshoot effect (Jones et al., 1994) and the time effect (Bisgaard 1983; Cho et al. 1984; Jones et al. 1994).

Through an extensive review of the past experimental and numerical work, McKinley (2002) concluded that the observed drag increase at high Weissenberg numbers is due to the extensional effects in the wake of the settling sphere. Later, Chhabra (2007) provided another comprehensive review of past work and highlighted the gap between the theory and experimental results. Most experimental studies pertain to conditions where viscosity is a function of the shear rate whereas most theoretical developments model the effect of fluid viscoelasticity on spheres in the absence of shear thinning effects. Incorporating a realistic description of shear rate dependent viscosity together with fluid viscoelasticity has been a real challenge in theoretical developments. In the absence of a complete constitutive solution, one of the objectives of this work is to present an empirical relation that can quantify and capture the effect of both viscoelasticity and shear-thinning on particle settling in unbounded fluids.

3.2 DESCRIPTION OF FLUIDS

In this experimental study, a polymer-free, viscoelastic, two-component, surfactant-based fluid system (Zhang 2002; Gupta and Tudor 2005) is used for performing the settling experiments. The fluid system has been widely used for hydraulic fracturing treatments in oil and gas wells in many producing fields and formations (Gupta et al 2005). It consists of an anionic surfactant (such as sodium xylene sulfonate) as one component (commercially known as FAC-1) and a cationic surfactant (such as N,N,N, trimethyl-1-octadecamonium chloride) as the second component (commercially known as FAC2). The two components are diluted and mixed using an overhead mixer at high rpm to ensure proper mixing. Distilled water is mixed with the overhead mixer and a given amount of FAC-1 is added to it. The mixture is allowed to mix for 2-3 minutes. A given amount of FAC-2 is added to the mixture and allowed to mix for 2-3 more minutes. The mixture is then allowed to rest for 1-6 hours to vent out the air bubbles.

When the two components are mixed at different concentrations and in different proportions, the surfactant mixture forms wormlike micelles that yield a variety of different rheological properties. This fluid system was chosen for our study because it is optically transparent, and its rheology can be easily controlled by systematically varying the concentrations and proportions of the two components. Seven fluid mixtures of different concentrations labeled as Fluid 1 through 7 are used in this study. The concentrations are chosen to obtain fluid mixtures that cover a wide range of viscosities.

The K, n (power-law parameters) and relaxation time for the fluids are discussed in the next section.

3.3 RHEOLOGICAL MEASUREMENTS

Steady shear-viscosity measurements and dynamic oscillatory-shear measurements are made for all the fluid mixtures using the ARES rheometer according to the procedure described in Chapter 2. It is observed that the rheology of the fluids is very sensitive to temperature, and care is taken that the rheology of the fluid is measured at the same temperature at which the settling experiments are performed. It is observed that the fluids exhibit shear-thinning behavior. The power-law (K, n) model is fitted to the data in the range of the shear rates encountered by the particles during the settling experiments. The shear rate used is the surface averaged particle shear rate defined as ($2V/d_p$), where V and d_p are the settling velocity and particle diameter respectively. Figures 3.1 through 3.7 show the shear stress and viscosity data as a function of the shear rate for the fluid all the configurations mentioned in Table 3.1. Figure 3.8 and Figure 3.9 show the power-law model fit in the experimental range of shear rates for Fluids 1 and 2 respectively.

The dynamic oscillatory-shear measurements (explained in Chapter 2) are made in order to quantify the elasticity of the fluids. These measurements are made over a range of frequencies from 0.1 rad/s to 100 rad/s. The storage modulus, G' and the loss modulus, G'' are measured as a function of angular frequency, ω. Figures 3.10 through 3.16 show the moduli as functions of the angular frequency for all the fluid

configurations. The data is used to calculate the ratio of the viscous modulus to the elastic modulus (G''/G') as a function of the angular frequency.

Figures 3.17 through 3.23 show the plots for the ratio of the moduli against the angular frequency, for all the fluid configurations. It is observed that the ratio decreases with the increase in the angular frequency. The relaxation time, λ, of the fluid is calculated by fitting the data with Equation 2.11. It is observed that the dynamic modulus data fits the above equation very well for all the fluid samples used in the study. The relaxation times of all the fluid configurations are shown in Table 3.1.

3.4 Procedure For Measuring Settling Velocities in Unbounded Fluids

Glass spheres are used as proppant in the settling experiments. These spheres have smooth surfaces and have diameters ranging from 1mm to 5mm. The density of the glass spheres (measured using a weighing balance and displacement of water) is 2.52g/cc. The particles are selected such that they are near-perfect spheres, and their diameters are measured with a high resolution microscope. The settling experiments are performed in containers with diameters at least 25 times the diameter of the particles. This is done to ensure that there is no effect of the confining walls on the settling velocity of the particles. The containers are filled with the VES fluids, and a sphere is immersed in the fluid and allowed to settle.

A meter stick is placed alongside the cell, and the settling process is captured using a video camera. The recorded video is then used to track the position of the particle and to measure the terminal settling velocity. We use a software application called "Tracker 2.0" (http://www.cabrillo.edu/_dbrown/tracker/) to get accurate measurements of the settling velocities. The experiments are performed under a temperature controlled environment (oven). The temperature inside the oven is measured. The rheological properties of the fluid are measured at the same temperature as the experiments, and the density of the fluid is measured using an accurate weighing balance. Experiments are conducted with all the fluid mixtures mentioned in Table 3.1. It can be observed that the Fluids 4 & 5 and Fluids 6 & 7 have the same concentration of the two components. However, the experiments with these two mixtures were performed twice at different temperatures resulting in different rheologies. At least three measurements are made for each reported settling velocity under each unique set of conditions to ensure reproducibility. Error bars provided in the experimental results clearly show the reproducibility of the results and the possible variability in the experimental results.

3.5 Results For Settling in Unbounded VES Fluids

3.5.1 Settling Velocities in Unbounded Fluids

Settling velocities in unbounded viscoelastic fluids are experimentally measured for glass spheres of five different diameters in all the seven fluid mixtures mentioned in Table 3.1. Figure 3.24 through 3.30 show the settling velocities as a function of the particle diameter in the fluid mixtures. The experimentally measured settling velocity is

denoted with the symbol $V_{\infty VE}$ where '∞VE' refers to unconfined viscoelastic fluids. This settling velocity is compared with the settling velocity ($V_{\infty INEL}$) calculated on the basis of apparent viscosity data based on the power-law parameters. Here '∞*INEL*' refers to unconfined inelastic fluids. Vast amount of experimental studies (Dallon 1967; Uhlherr et al. 1976; Machac et al. 1987; Kelessidis and Mpandelis 2004; Shah et al. 2007 etc.) and numerical predictions (Dazhi and Tanner 1984; Tripathi et al. 1994; Graham and Jones 1994; Tripathi and Chhabra 1995; Missirlis et al. 2001) illustrating the drag force on a sphere in inelastic power-law liquids are available in the literature. Renaud et al. (2004) used the theoretical predictions of Tripathi et al. (1994) and Tripathi and Chhabra (1995), and developed the following expressions to calculate the drag coefficient (C_D):

For Re_{PL}≤0.1 (creeping flow regime)

$$C_{Do} = \frac{24X(n)}{\mathrm{Re}_{PL}} \tag{3.2}$$

where $X(n)$ is the drag correction factor (Chhabra 2007) and Re_{PL} is the Reynolds number for a sphere falling in a power law liquid defined as:

$$\mathrm{Re}_{PL} = \frac{\rho_f V^{2-n} d_p^n}{K} \tag{3.3}$$

where ρ_f is the density of the liquid. Based on the theoretical values, Renaud et al. (2004) fitted the drag correction factor with the following equation:

$$X(n) = 6^{\frac{n-1}{2}} \left(\frac{3}{n^2 + n + 1} \right)^{n+1} \tag{3.4}$$

Using the definition of drag coefficient the settling velocity is calculated as:

$$V_{\infty INEL} = \left[\frac{(\rho_p - \rho_f)\, g\, d_p^{\,n+1}}{18\, K\, X(n)} \right]^{\frac{1}{n}} \tag{3.5}$$

For $0.1 < Re_{PL} < 100$

$$C_D = C_{D0} + \chi C_{D\infty} C_{D0}^{2\beta} k \left(\frac{6X(n)b}{6X(n)b + C_{D0}} \right)^{\beta} + C_{D\infty} \left(\frac{6X(n)b}{6X(n)b + 128C_{D0}} \right)^{11/12} \tag{3.6}$$

where χ is the ratio of the surface area to the projected area of the particle and is equal to 4 for spheres. C_{D0} is the drag coefficient in the Stokes region ($Re_{PL} < 0.1$) given by Equation 3.2, $C_{D\infty}$ is the value of drag coefficient in the Newton's region ($Re_{PL} > 5\times10^2$) and is equal to 0.44 (Bird et al. 2007; Renuad et al. 2004). The parameters β, b, k are expressed as:

$$b = \exp\{3(\alpha - \ln 6)\} \tag{3.7}$$

$$k = \frac{\alpha_o - \alpha}{2\alpha_o \alpha} \exp\left\{ 3\left(\frac{\alpha_o - \alpha}{2\alpha_o \alpha} \right) \ln 3 \right\} \tag{3.8}$$

$$\beta = \frac{11}{48}\sqrt{6}\left[1 - \exp\left\{ \left(\frac{1}{\alpha} \frac{\alpha_o - \alpha}{\alpha_o - 1} \right)^2 \ln \frac{\sqrt{6}-1}{\sqrt{6}} \right\} \right] \tag{3.9}$$

$\alpha_o = 3$ and α is the correction for the average shear rate related to $X(n)$ as:

$$\alpha = \left\{ 6^{(1-n)/2} X(n) \right\}^{1/(n+1)} \tag{3.10}$$

To calculate the settling velocity, we use the dimensionless group N_d (Darby 2001) which is defined as:

$$N_d = C_D^{2-n}\left(\frac{\mathrm{Re}_{PL}}{X(n)}\right)^2 = \left(\frac{\rho_f}{X(n)K}\right)^2\left(\frac{4g\left(\rho_p-\rho_f\right)}{3\rho_f}\right)^{2-n} d_p^{n+2} \qquad 3.11$$

N_d is independent of the settling velocity and can be calculated explicitly. Using this value and the drag coefficient expression in Equation, Re_{PL} can be solved iteratively which is further solved to get the settling velocity using:

$$V_{\infty INEL} = \left(\frac{\mathrm{Re}_{PL}K}{\rho_f d_p^n}\right)^{1/(2-n)} \qquad 3.12$$

The expressions in Equations 3.4 through 3.10 were based on theoretical predictions that were obtained for the $1 \geq n \geq 0.4$. Chhabra (2007) showed that the expressions could be used to accurately predict the drag coefficients for fluids with lower n values by comparing them with the experimental results of Shah (1982, 1986) (n varied from 0.281-0.762) and Ford et al. (1994) (n varied from 0.06-0.29). Based on these comparisons, we have used these expressions to predict the inelastic settling velocity for the fluids mentioned in Table 3.1.

Any deviation of the experimental settling velocity ($V_{\infty \mathrm{EL}}$) from the inelastic settling velocity ($V_{\infty \mathrm{INEL}}$) is due to the influence of the elasticity of the fluid. This deviation from the inelastic settling velocity is expressed in terms of velocity ratio, which

is the ratio of the $V_{\infty EL}$ to $V_{\infty INEL}$. A ratio greater than 1 suggests an increase in settling velocity due to elasticity and vice versa.

Figure 3.31 shows the variation of velocity ratio as a function of the diameter for Fluids 1, 2 and 3. It is observed that in all the three fluids the smaller spheres experience drag reduction and larger spheres experience drag enhancement. The magnitude of the velocity ratio is different for the same size particles in fluids of different rheology. These results indicate that the settling velocity of particles in viscoelastic fluids is not determined by viscosity alone and elasticity plays a role on the drag force on the particle. It is also clear from the figure that elasticity of the fluid can increase as well as decrease the settling velocity. This clearly suggests that the increase as well as decrease in the settling velocities is a combined effect of the rheological properties of the fluid and the properties of the spherical particles.

Fluids 1, 2 and 3 have similar *K, n* values but different relaxation times as can be seen in Table 3.1. A comparison of the velocity ratios in the three fluids shows that for a fixed particle diameter, the velocity ratio is greater in a fluid of greater relaxation time. This suggests that for the particular range of *K, n* values and particle sizes, elasticity causes a drag reduction. Figure 3.32 shows the velocity ratios for particles settling in Fluids 4 through 7. The results for velocity ratios in all the fluids suggest that the increase as well as the decrease in the settling velocities is a combined effect of the rheological properties of the fluid and the properties of the spherical particles.

Figure 3.33 shows the velocity ratio as a function of the Weissenberg number of the particle ($We_{\infty EL}$) for all the fluids. The plot shows a drag reduction at lower Weissenberg numbers followed by a transition to drag increase at higher Weissenberg numbers. The plot is similar to the 'Overall Drag-Weissenberg number map' shown by Walters and Tanner (1992) and Chhabra (2007) for Boger fluids. The experimental data shows a similar trend for highly shear thinning viscoelastic fluids. The Reynolds number (Re_{PL}) for the particles in the experiments varies from 6×10^{-4} to 2.63. The range has been divided into creeping flow regime and intermediate flow regime as shown on the plot. The data shows that particles settling in the creeping flow regime also experience drag reduction or drag enhancement.

Based on a dimensional analysis, an attempt is made to correlate the velocity ratio, $V_{\infty EL}/V_{\infty INEL}$ as a function of the properties of the fluid and the properties of spherical particles. Using regression analysis, the following correlation is fitted to the experimental data.

$$\frac{V_{\infty EL}}{V_{\infty INEL}} = \frac{1 + \mathrm{We}_{\infty INEL}^{2.42}\, n^{-7.8}}{1 + \mathrm{We}_{\infty INEL}^{3.15}\, n^{-6.86}} \qquad 3.13$$

In the above equation $\mathrm{We}_{\infty INEL}$ is a dimensionless number similar to the Weissenberg number, relating the relaxation time of the fluid to the diameter of the particle and settling velocity based on apparent viscosity.

$$\mathrm{We}_{\infty INEL} = \frac{2\lambda V_{\infty INEL}}{d_p} \qquad 3.14$$

The correlation in Equation 3.13 is applicable in the following range of variables:

$$0.259 \leq n \leq 0.9;\ 0.15 \leq We_{\infty INEL} \leq 50;\ 3.8\times10^{-4} \leq Re_{\infty INEL} \leq 37$$

$Re_{\infty INEL}$ is the Reynolds number based on the inelastic settling velocity ($V_{\infty INEL}$) calculated using 3.3. Equation 3.13 is an explicit correlation which can be used to calculate the settling velocity in viscoelastic fluids using the properties of the fluid and the spherical particle. The coefficient of determination of the fit is 0.914. Figure 3.34 shows a comparison of the velocity ratio from all the experiments and the correlation. It is observed that the values from the correlation match well with the experimental results and important increasing and decreasing trends in the velocity ratio are captured by the correlation. It is important note that the dimensionless number $We_{\infty INEL}$ is different from the actual particle Weissenberg number. The quantity is used in order to get an explicit correlation between the settling velocity and the properties of the fluid and the particles.

3.5.2 Effect of shear thinning on drag reduction/increase

Let us assume a viscoelastic fluid of density 1000kg/m^3, K = 0.8Pa.s^n, n = 0.9 and λ = 0.3s. The settling velocities of spherical particles of density 2500 kg/m^3 and diameter varying from 0.5mm to 6mm in this fluid are calculated using the correlation in Equation 3.13. Figure 3.35 shows the variation of velocity ratio with the Weissenberg number. A drag reduction at lower Weissenberg numbers followed by a drag increase at higher Weissenberg numbers is observed. To illustrate the effect of shear thinning on the velocity ratios, let us vary n from 0.9 (less shear thinning) to 0.5 (more shear thinning). The velocity ratios for fluids with different n values are shown on the same plot. The

curves show that shear thinning behavior of the fluid causes a drag reduction causing the particles to settle faster. The results are consistent with the numerical simulations of Sugeng and Tanner (1986) and Huang and Feng (2005) who observed drag reduction with increased shear thinning.

3.6 CONCLUSIONS

This chapter summarizes the past work on the measurement of the drag force on particles settling in viscoelastic fluids and presents experimental results on rheological characterization of VES fluids and settling velocities of particles in unbounded VES fluids. The important conclusions from the experimental study are:

- The rheological properties (viscosity and elasticity) of the VES fluid system used in this experimental study are a strong function of the concentration of the two components of the system as well as the fluid temperature. The Maxwell model fits the dynamic modulus data accurately, and a Maxwellian relaxation time is sufficient to quantify the elastic properties of the fluid system.

- The viscous properties alone are insufficient to determine the drag force on spherical particles in viscoelastic fluids. Fluid elasticity can increase as well as decrease the settling velocity of particles, even in the creeping flow regime. The magnitude of the increase as well as decrease in the settling velocity depends on the diameter of the particle as well as the rheological properties of the fluid.

- Experimental results indicate that a significant drag reduction occurs at low Weissenberg numbers. This is followed by a transition to increased drag at higher Weissenberg numbers.

- A new correlation is presented to quantify the settling velocities of particles in unbounded VES fluids as a function of the properties of the fluid and the particles.

- Shear thinning effects are observed to reduce the drag on particle settling in unbounded VES fluids.

Table 3.1: Composition and rheological properties of the fluid mixtures along with the temperature at which experiment is performed.

Fluid #	Concentration of FAC1 (gallons per thousand gallons)	Concentration of FAC2 (gallons per thousand gallons)	Temperature at which fluid properties are measured (degrees C)	K (Pa.s^n)	n	Relaxation time, λ (s)
1	10	30	23	0.603	0.293	0.321
2	10	20	23.5	0.65	0.282	0.183
3	10	10	22	0.654	0.259	0.385
4	20	20	24	1.122	0.552	0.189
5	20	20	23	1.243	0.494	0.2
6	40	40	22.5	2.8258	0.876	0.189
7	40	40	22	2.8412	0.903	0.182

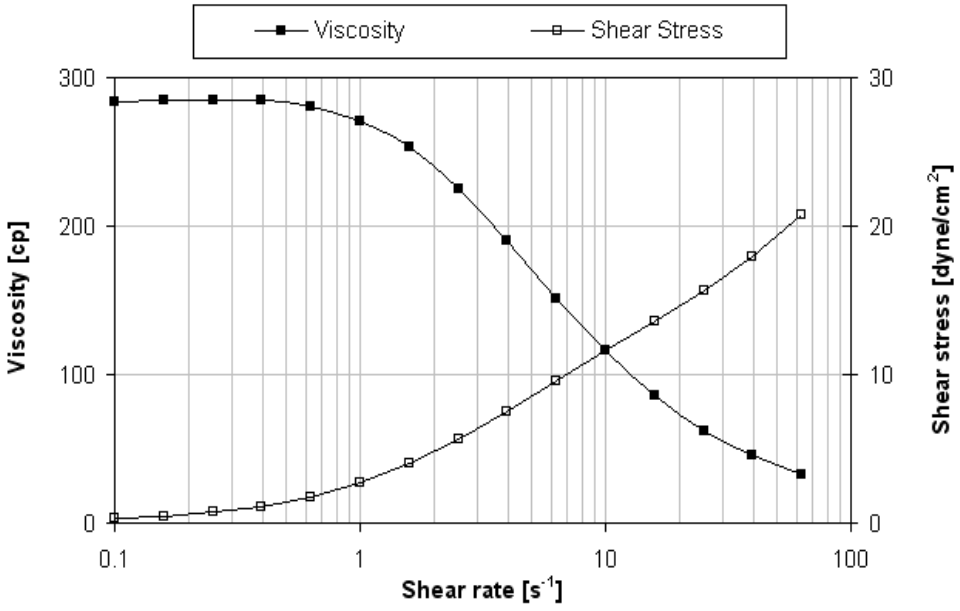

Figure 3.1: Viscosity and shear stress as a function of shear rate for Fluid 1.

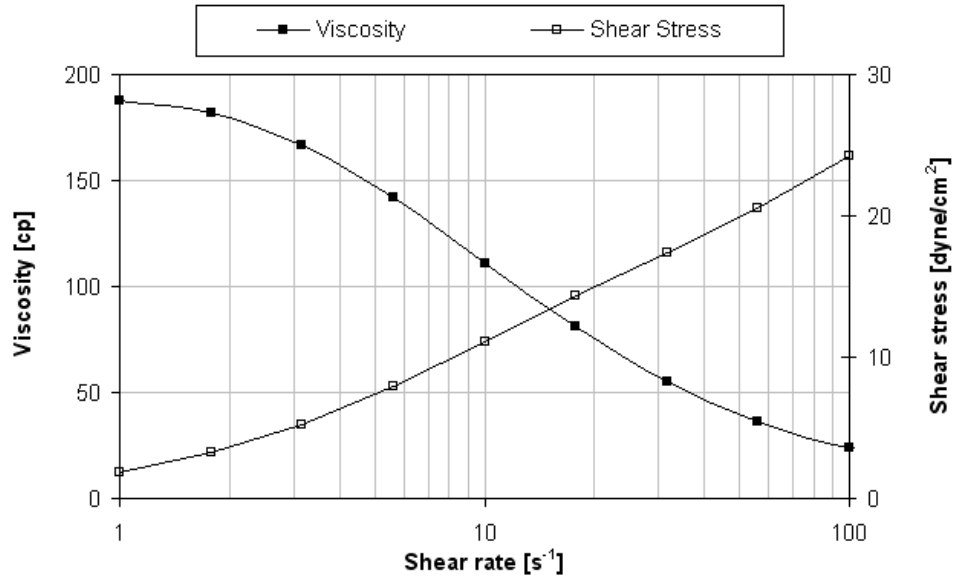

Figure 3.2: Viscosity and shear stress as a function of shear rate for Fluid 2.

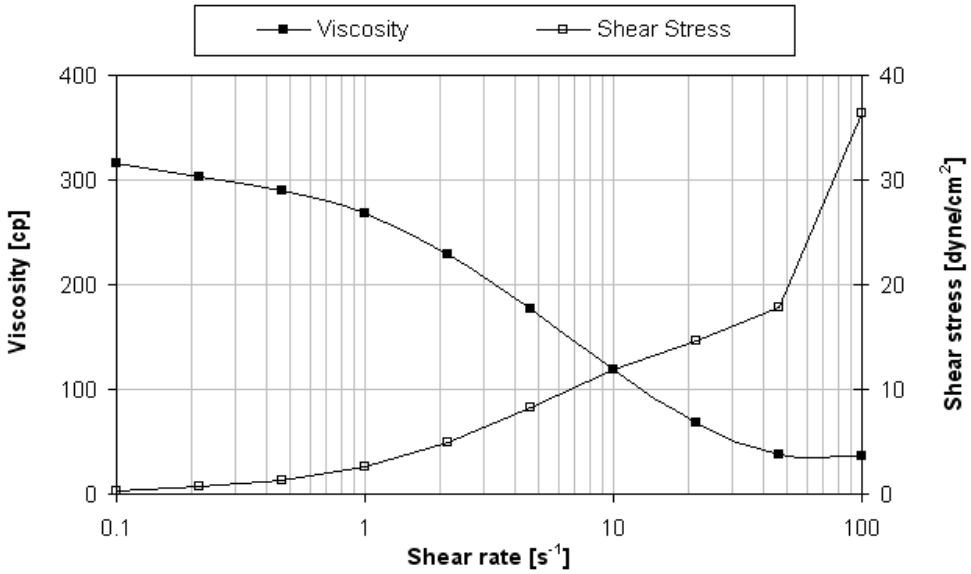

Figure 3.3: Viscosity and shear stress as a function of shear rate for Fluid 3.

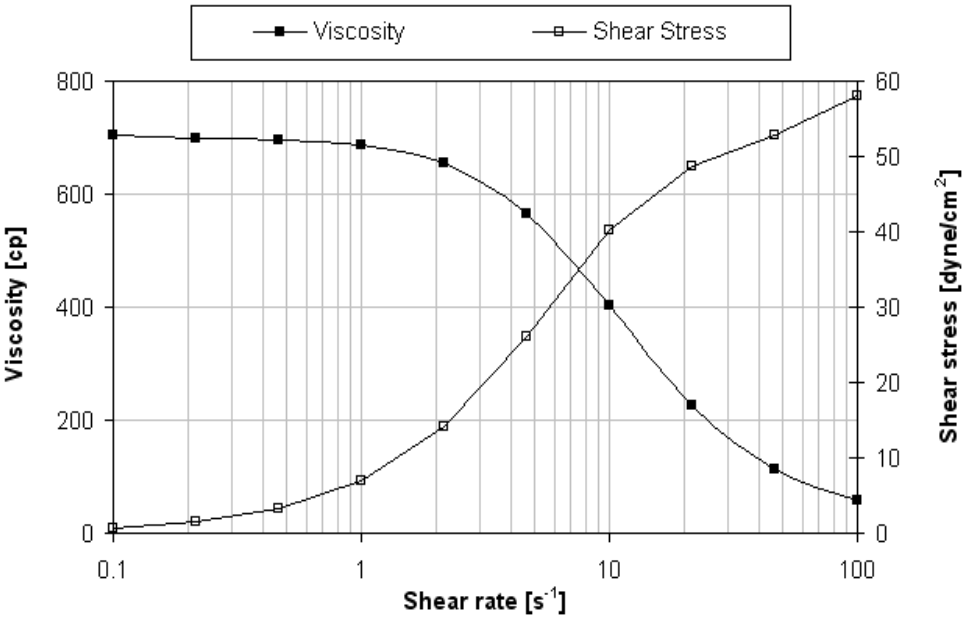

Figure 3.4: Viscosity and shear stress as a function of shear rate for Fluid 4.

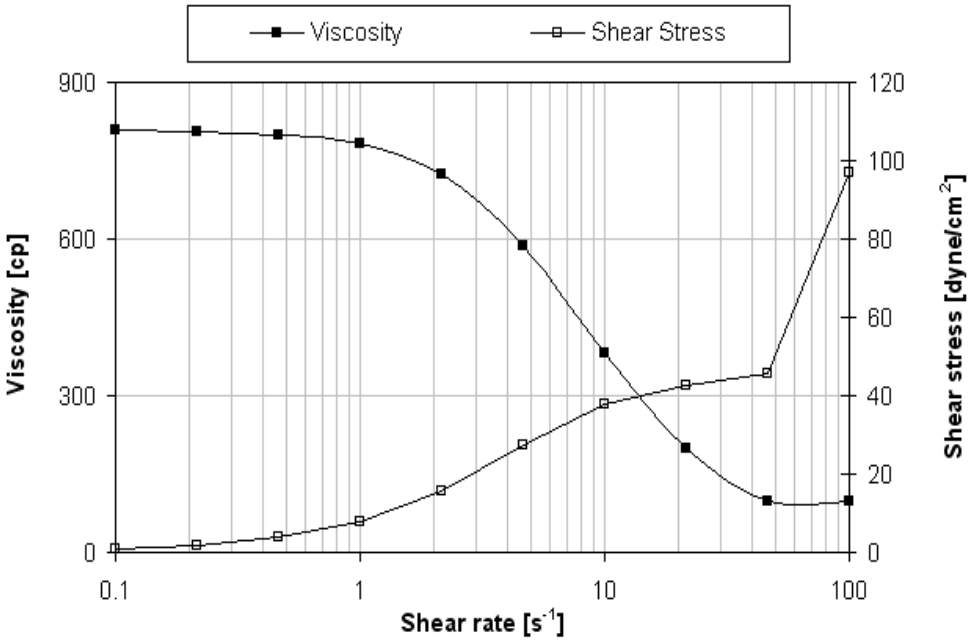

Figure 3.5: Viscosity and shear stress as a function of shear rate for Fluid 5.

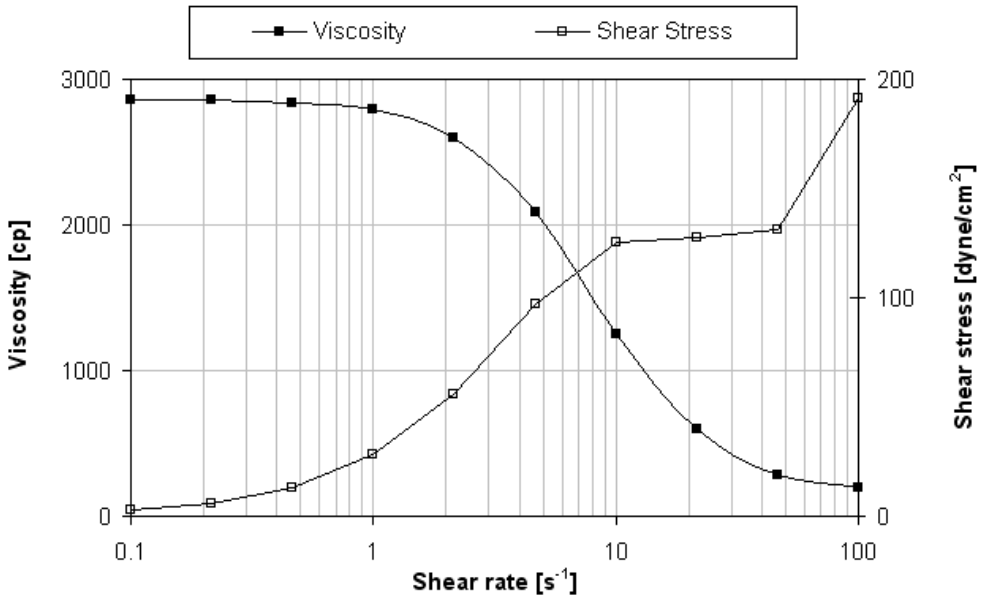

Figure 3.6: Viscosity and shear stress as a function of shear rate for Fluid 6.

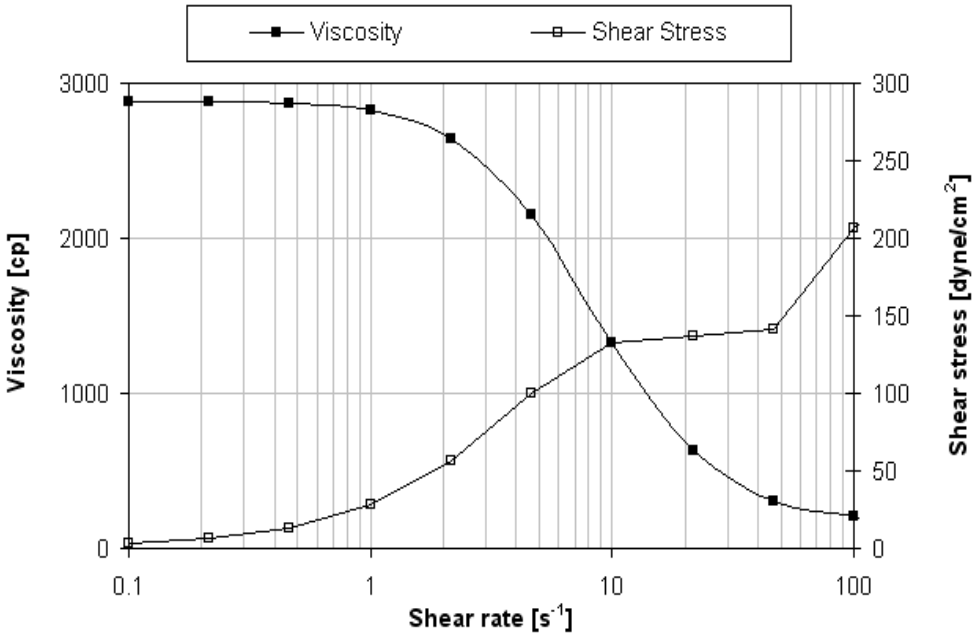

Figure 3.7: Viscosity and shear stress as a function of shear rate for Fluid 7.

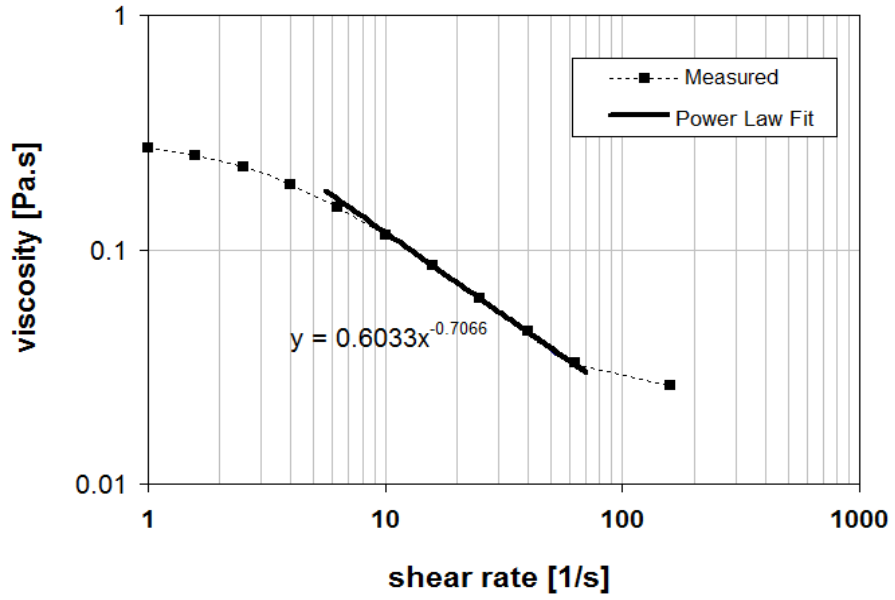

Figure 3.8: Viscosity as a function of shear rate along with the power law fit in the experimental range of shear rates for Fluid 1.

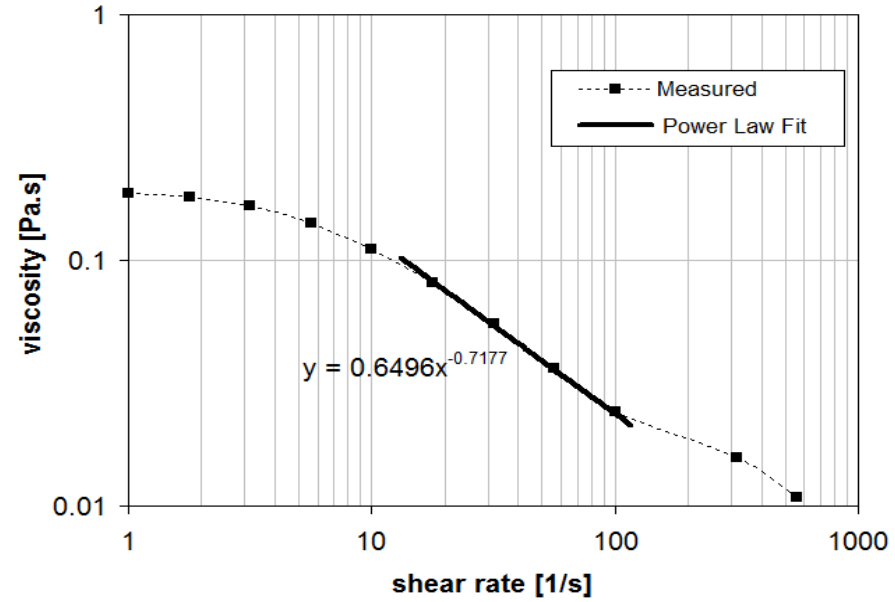

Figure 3.9: Viscosity as a function of shear rate along with the power law fit in the experimental range of shear rates for Fluid 2.

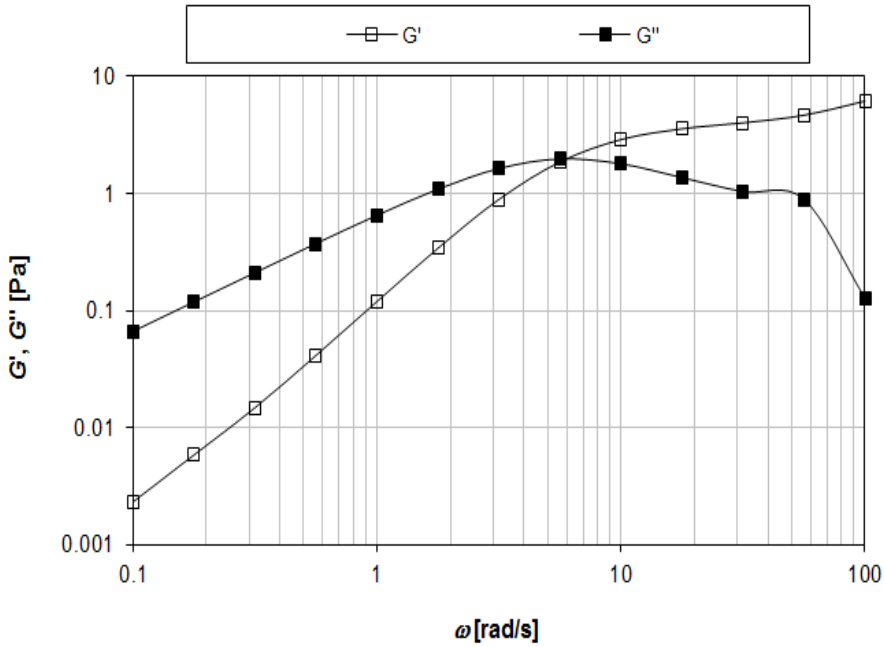

Figure 3.10: Elastic and viscous moduli as a function of angular frequency for Fluid 1.

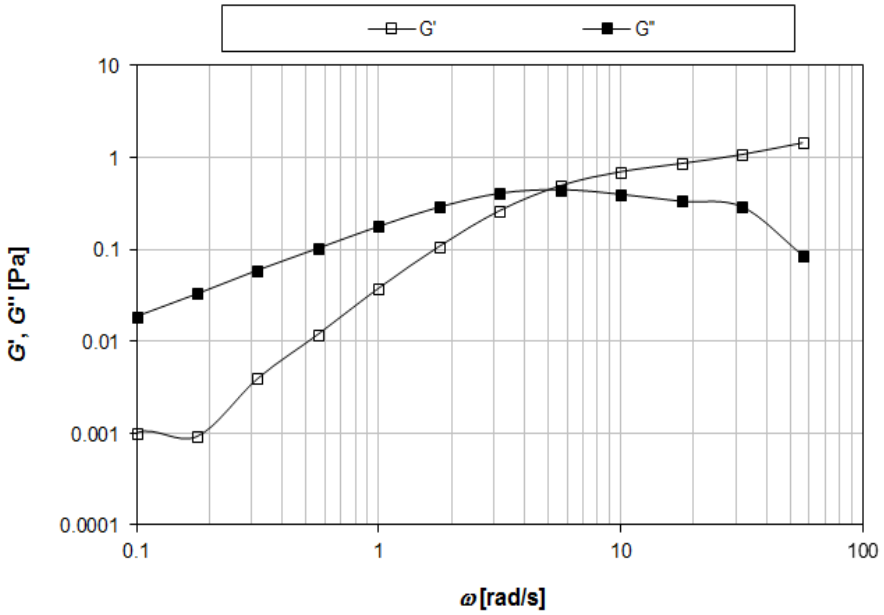

Figure 3.11: Elastic and viscous moduli as a function of angular frequency for Fluid 2.

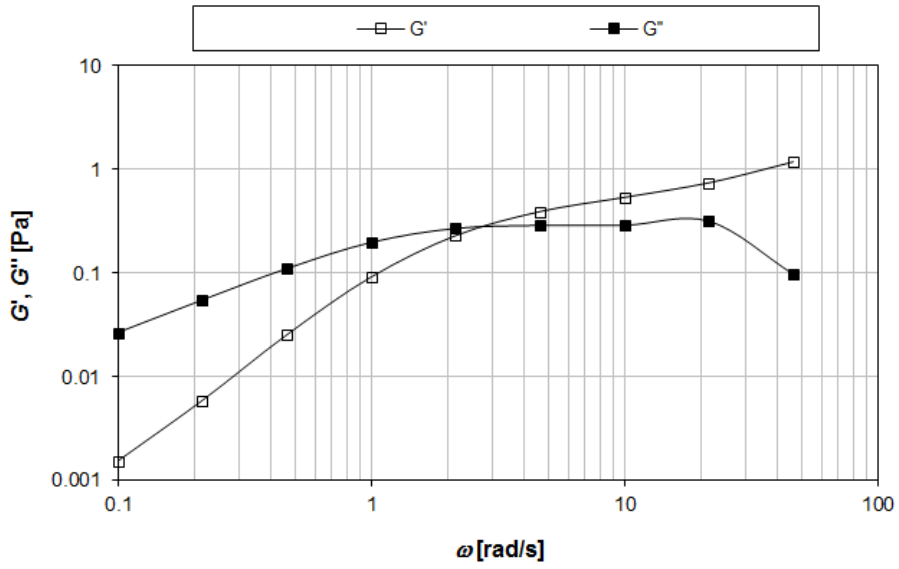

Figure 3.12: Elastic and viscous moduli as a function of angular frequency for Fluid 3.

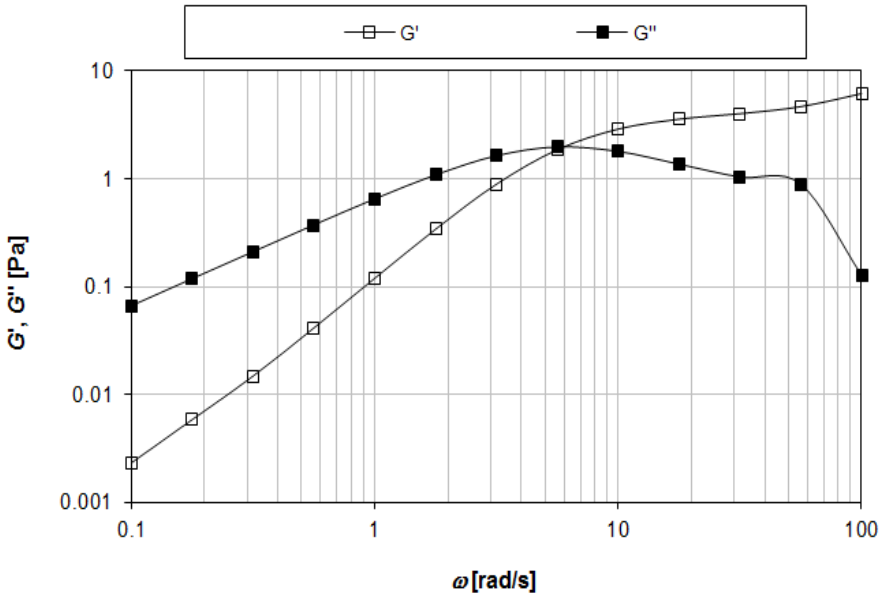

Figure 3.13: Elastic and viscous moduli as a function of angular frequency for Fluid 4.

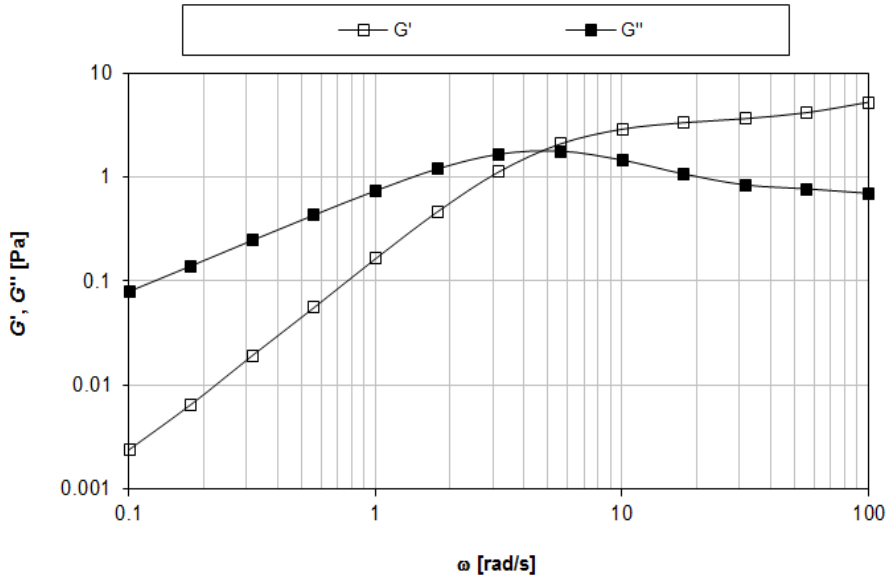

Figure 3.14: Elastic and viscous moduli as a function of angular frequency for Fluid 5.

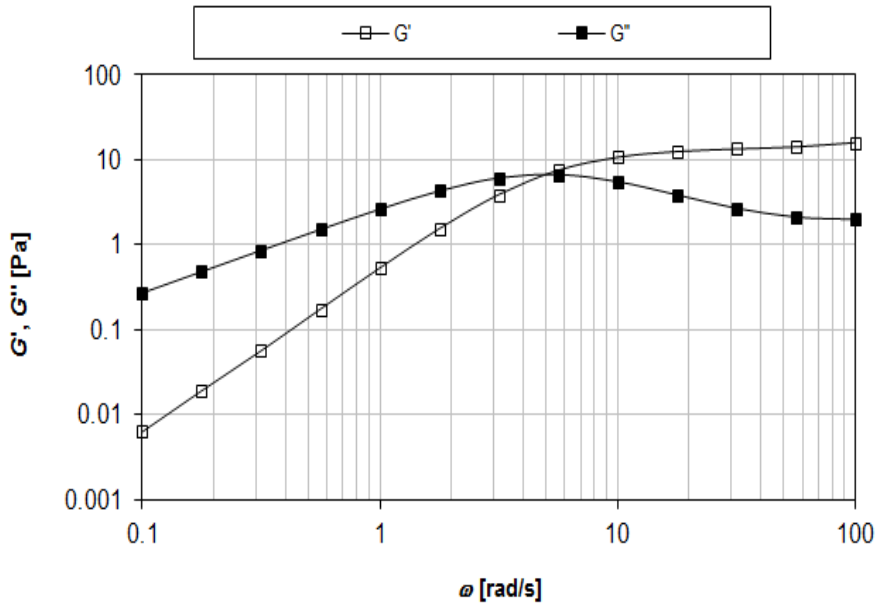

Figure 3.15: Elastic and viscous moduli as a function of angular frequency for Fluid 6.

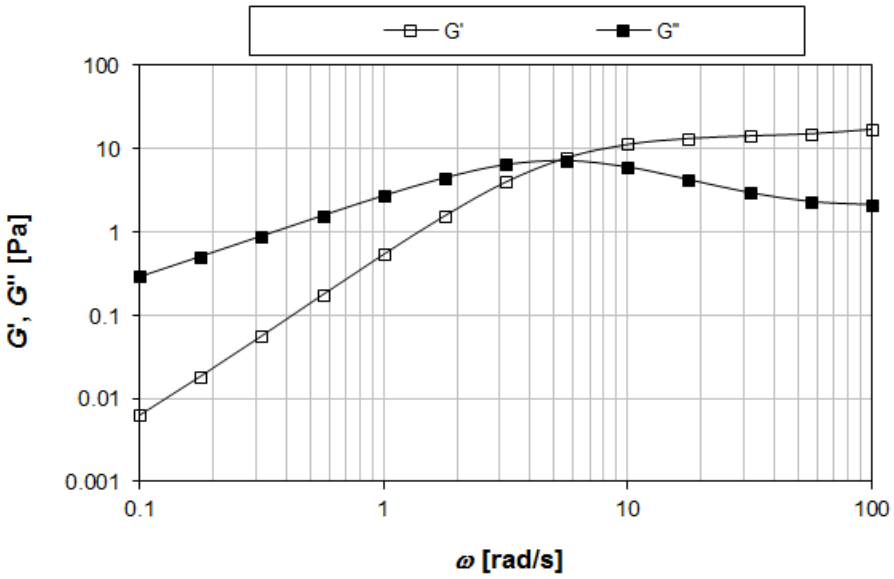

Figure 3.16: Elastic and viscous moduli as a function of angular frequency for Fluid 7.

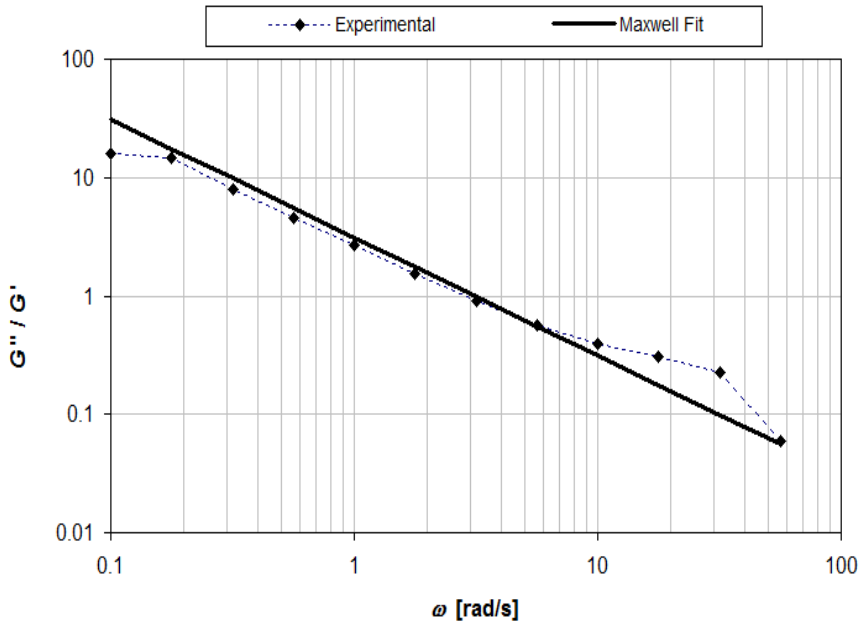

Figure 3.17: Ratio of viscous to elastic modulus along with the Maxwell fit for Fluid 1.

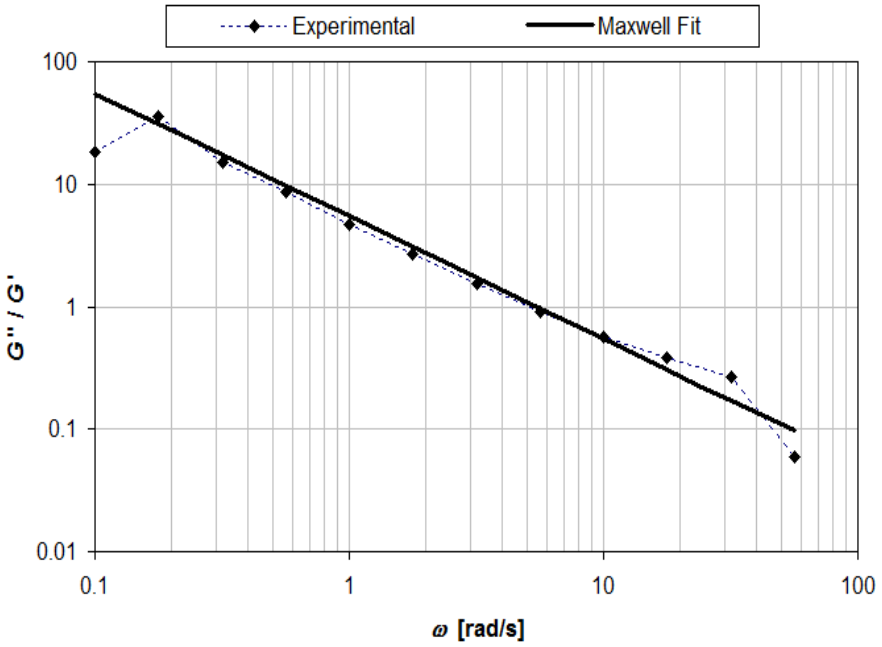

Figure 3.18: Ratio of viscous to elastic modulus along with the Maxwell fit for Fluid 2.

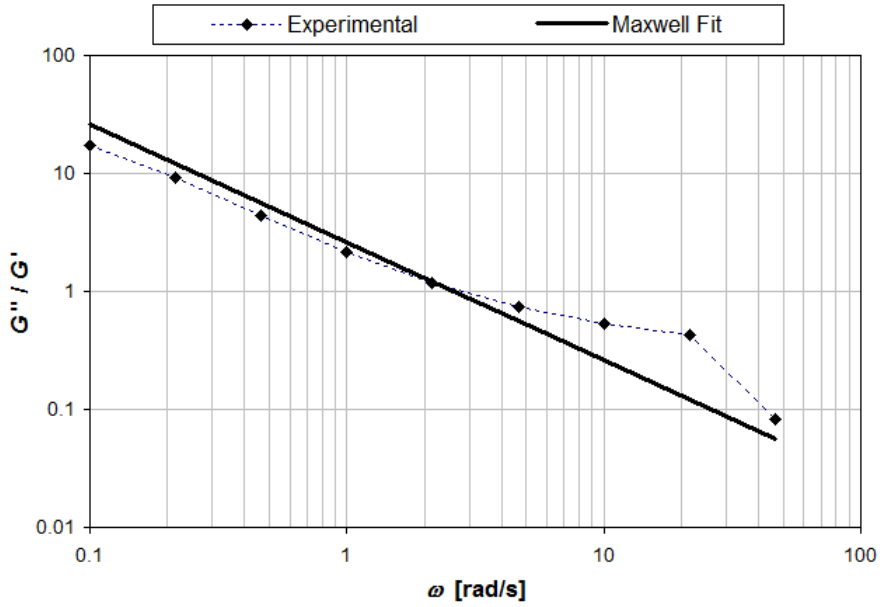

Figure 3.19: Ratio of viscous to elastic modulus along with the Maxwell fit for Fluid 3.

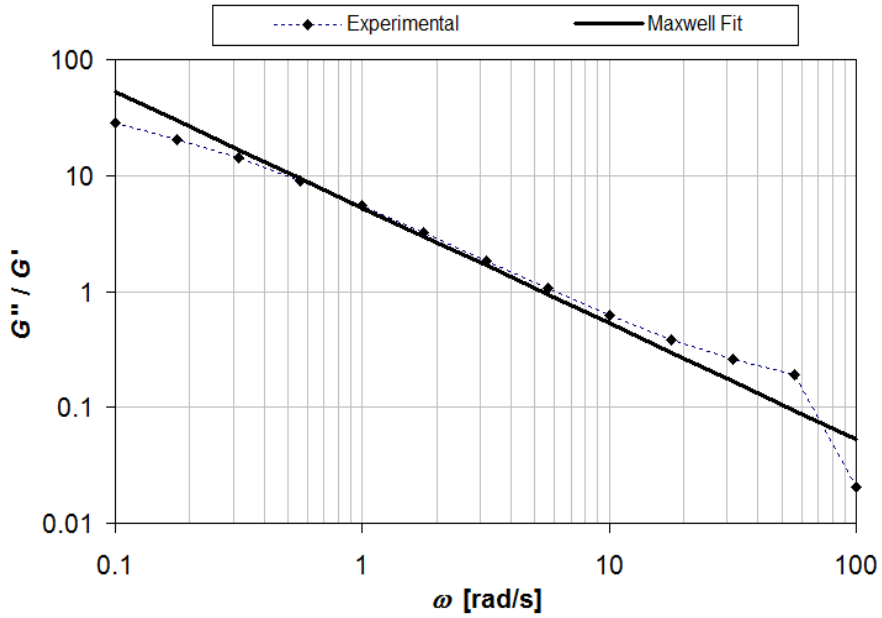

Figure 3.20: Ratio of viscous to elastic modulus along with the Maxwell fit for Fluid 4.

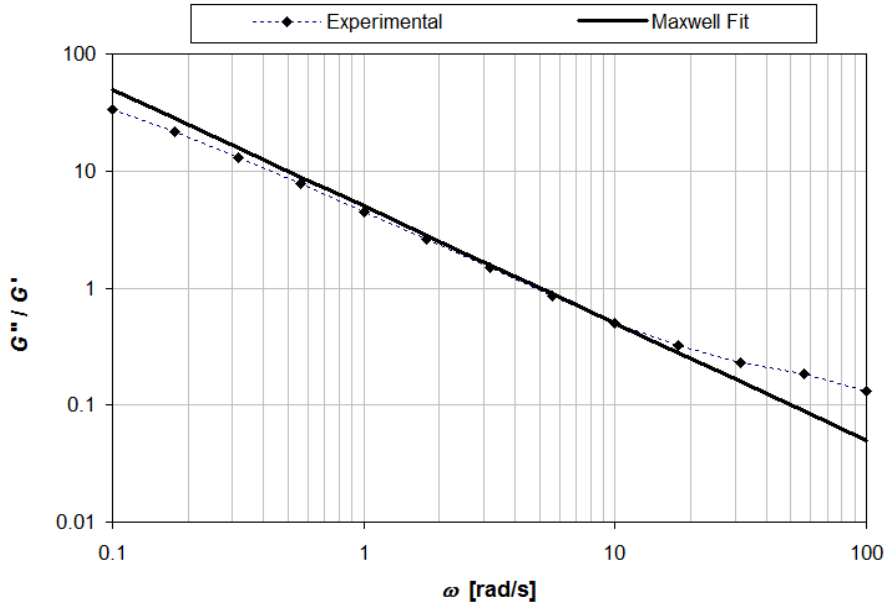

Figure 3.21: Ratio of viscous to elastic modulus along with the Maxwell fit for Fluid 5.

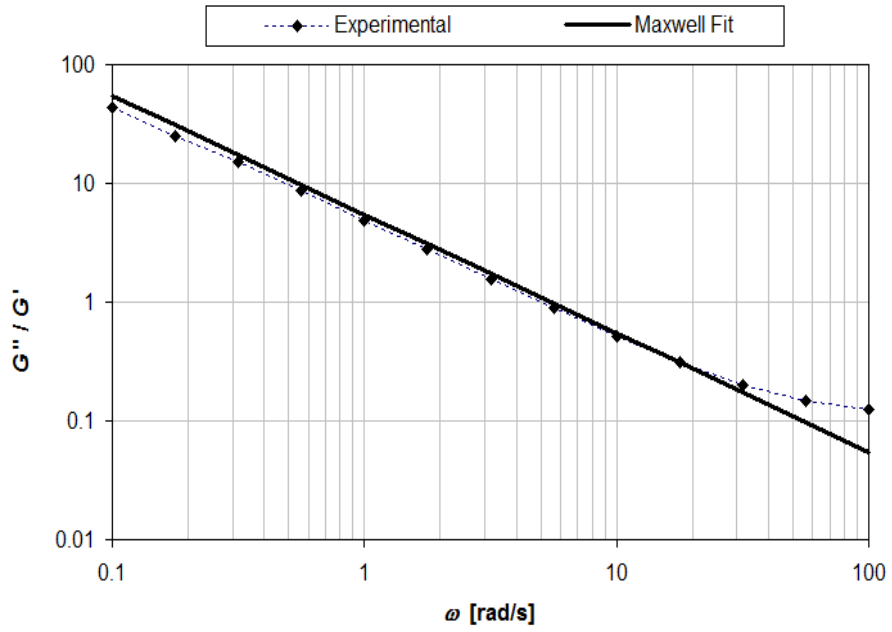

Figure 3.22: Ratio of viscous to elastic modulus along with the Maxwell fit for Fluid 6.

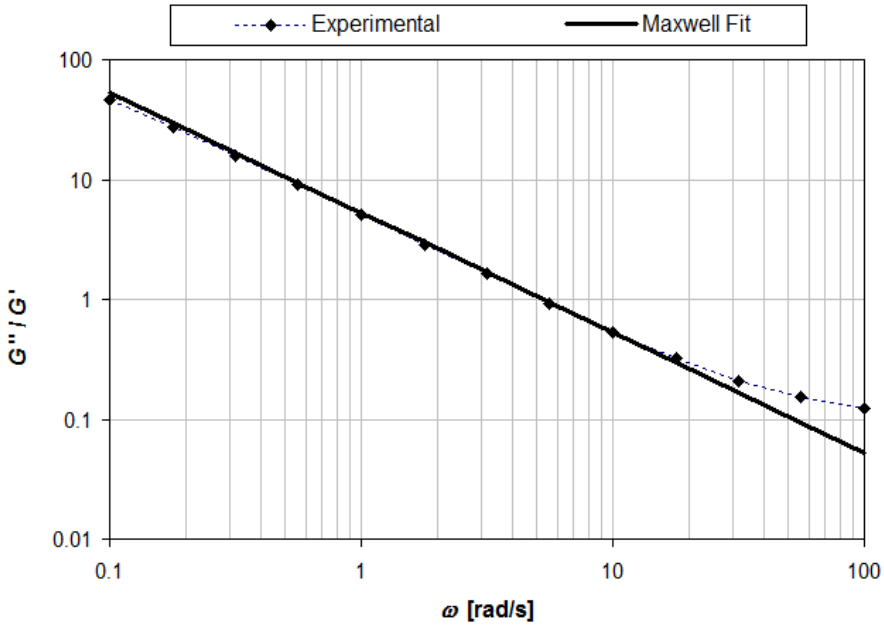

Figure 3.23: Ratio of viscous to elastic modulus along with the Maxwell fit for Fluid 7.

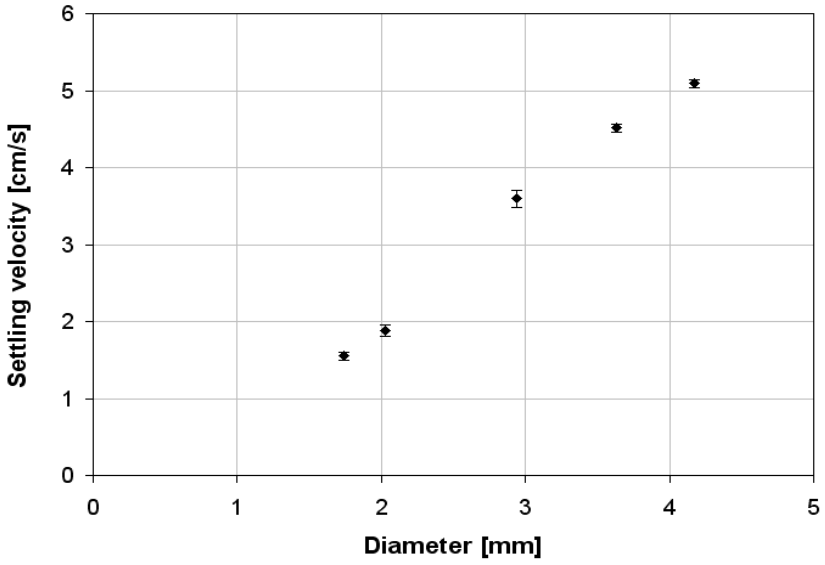

Figure 3.24: Settling velocities in Fluid 1 under unbounded conditions.

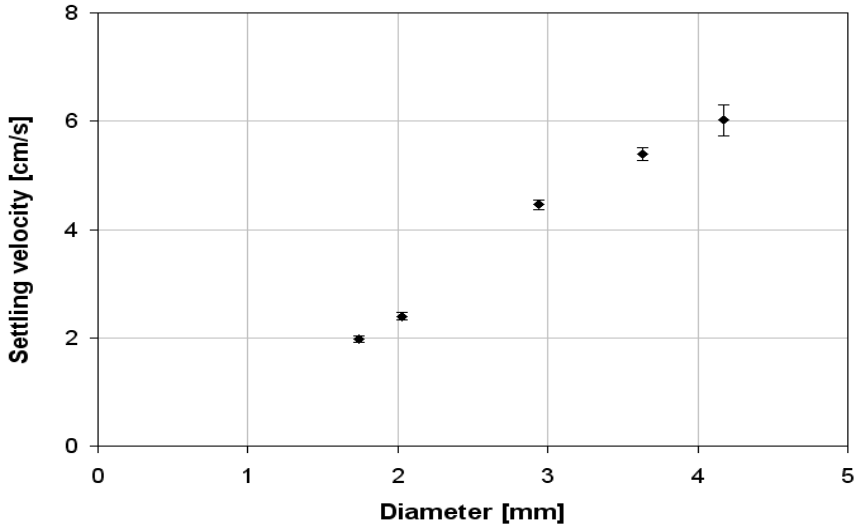

Figure 3.25: Settling velocities in Fluid 2 under unbounded conditions.

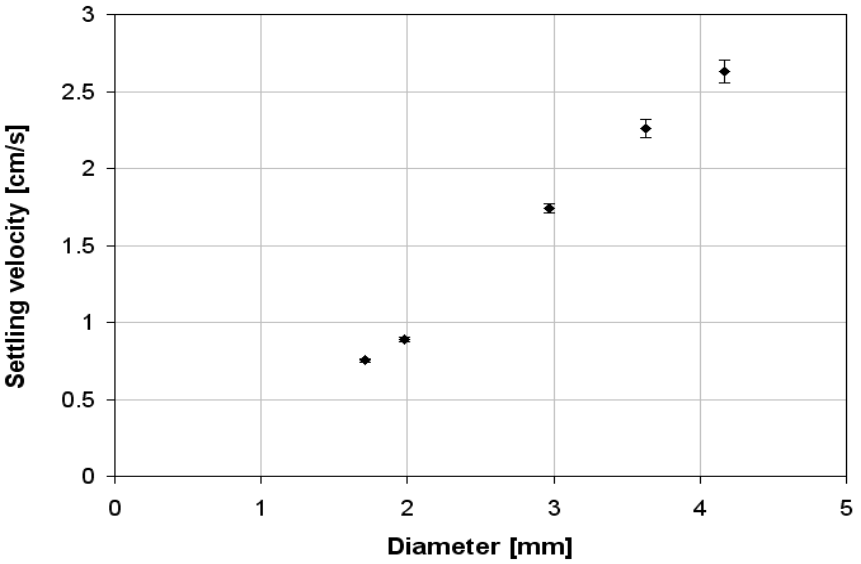

Figure 3.26: Settling velocities in Fluid 3 under unbounded conditions.

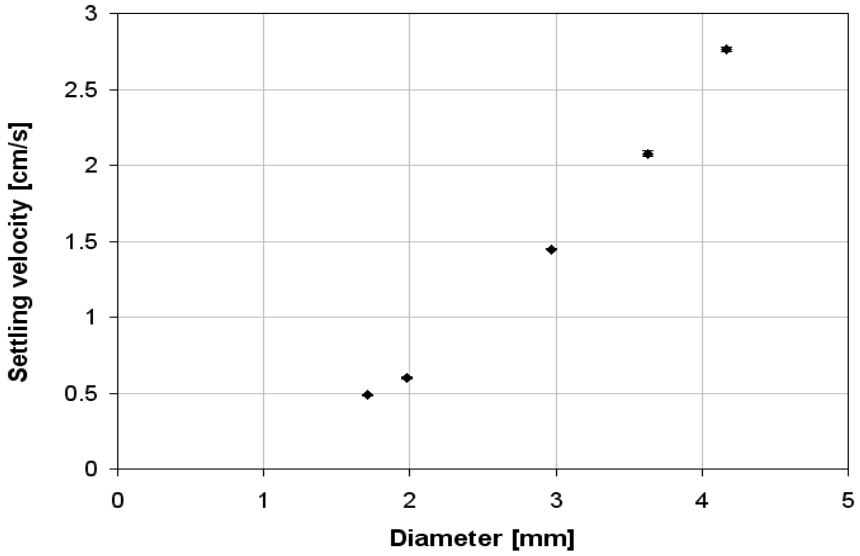

Figure 3.27: Settling velocities in Fluid 4 under unbounded conditions.

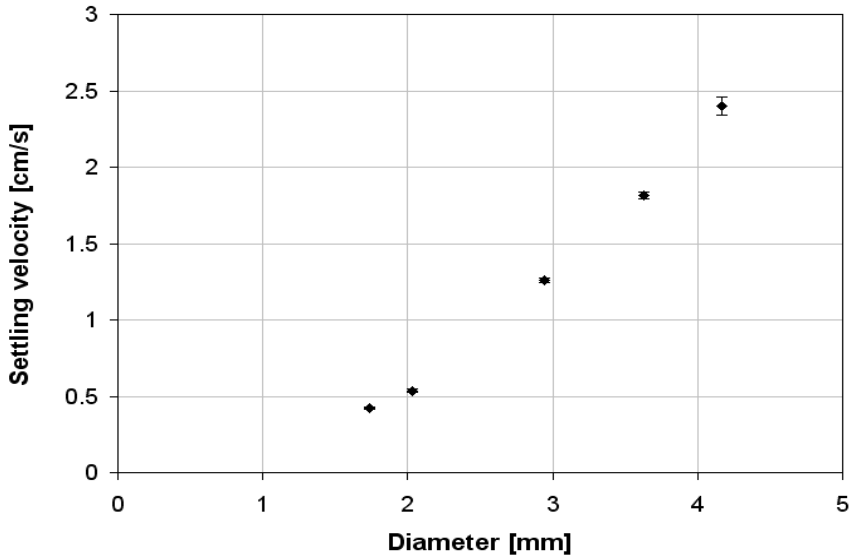

Figure 3.28: Settling velocities in Fluid 5 under unbounded conditions.

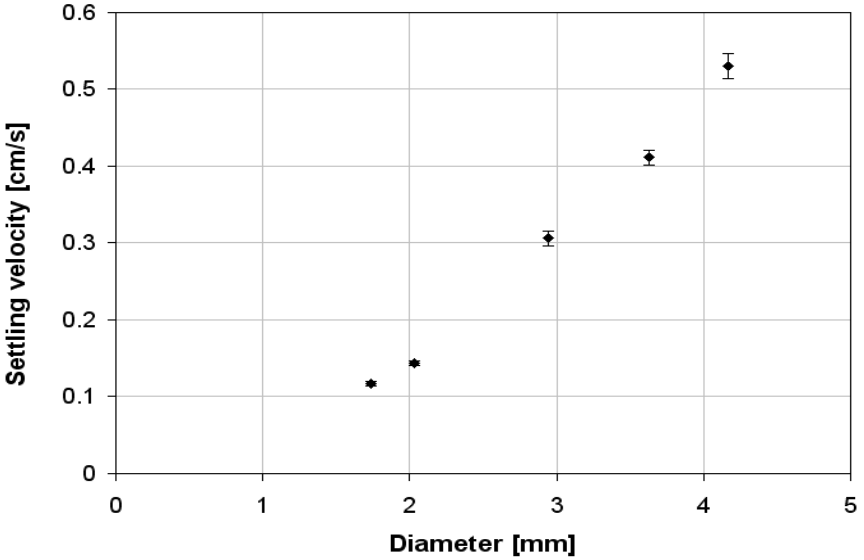

Figure 3.29: Settling velocities in Fluid 6 under unbounded conditions.

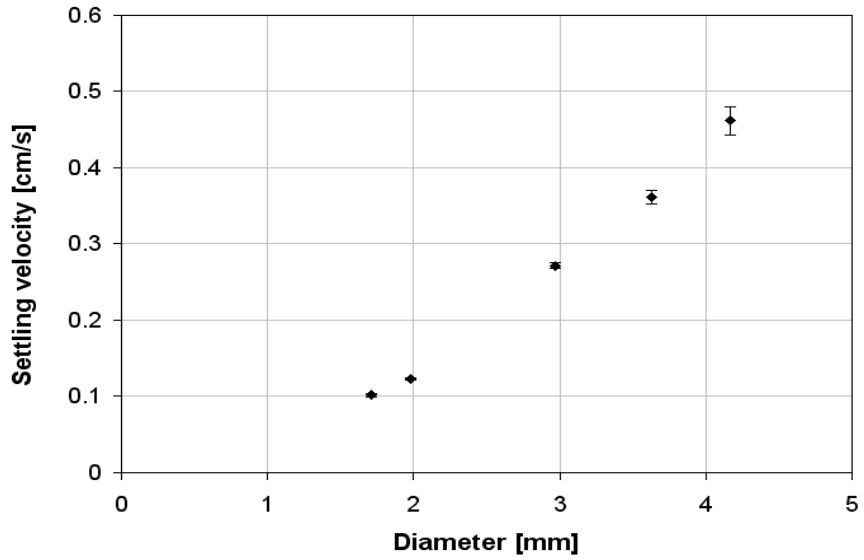

Figure 3.30: Settling velocities in Fluid 7 under unbounded conditions.

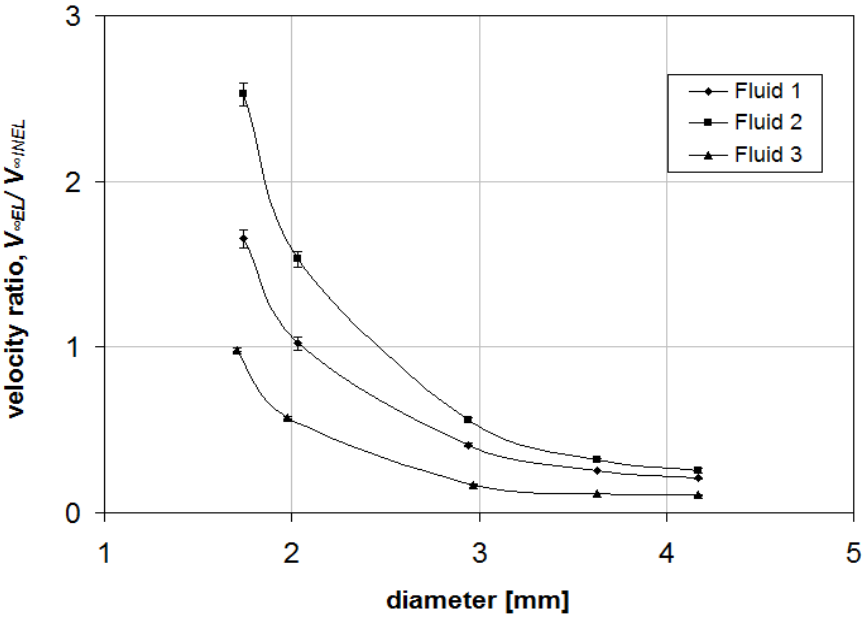

Figure 3.31: Velocity ratio for different diameter particles in Fluids 1, 2 and 3.

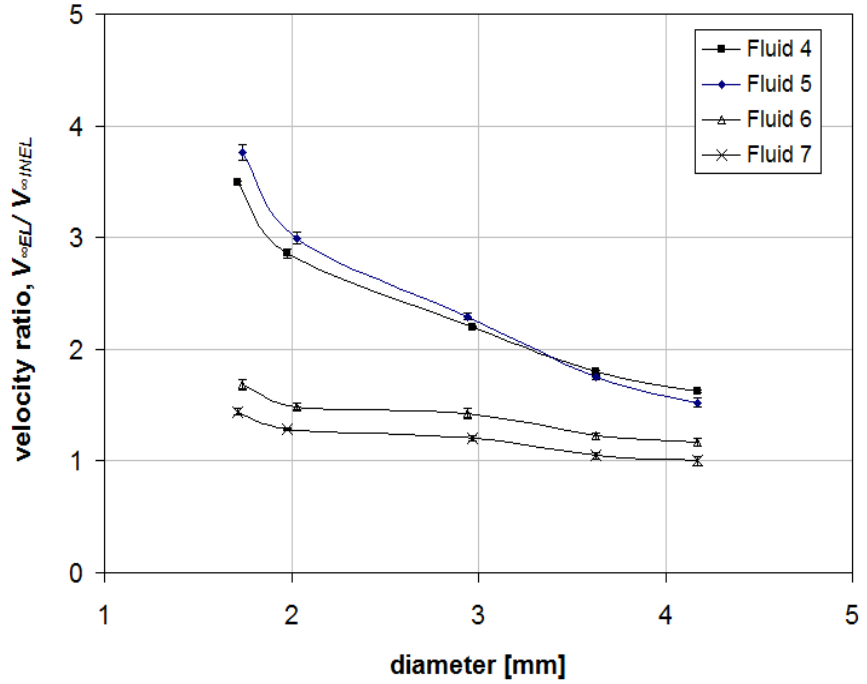

Figure 3.32: Velocity ratio for different diameter particles in Fluids 4, 5, 6 an7.

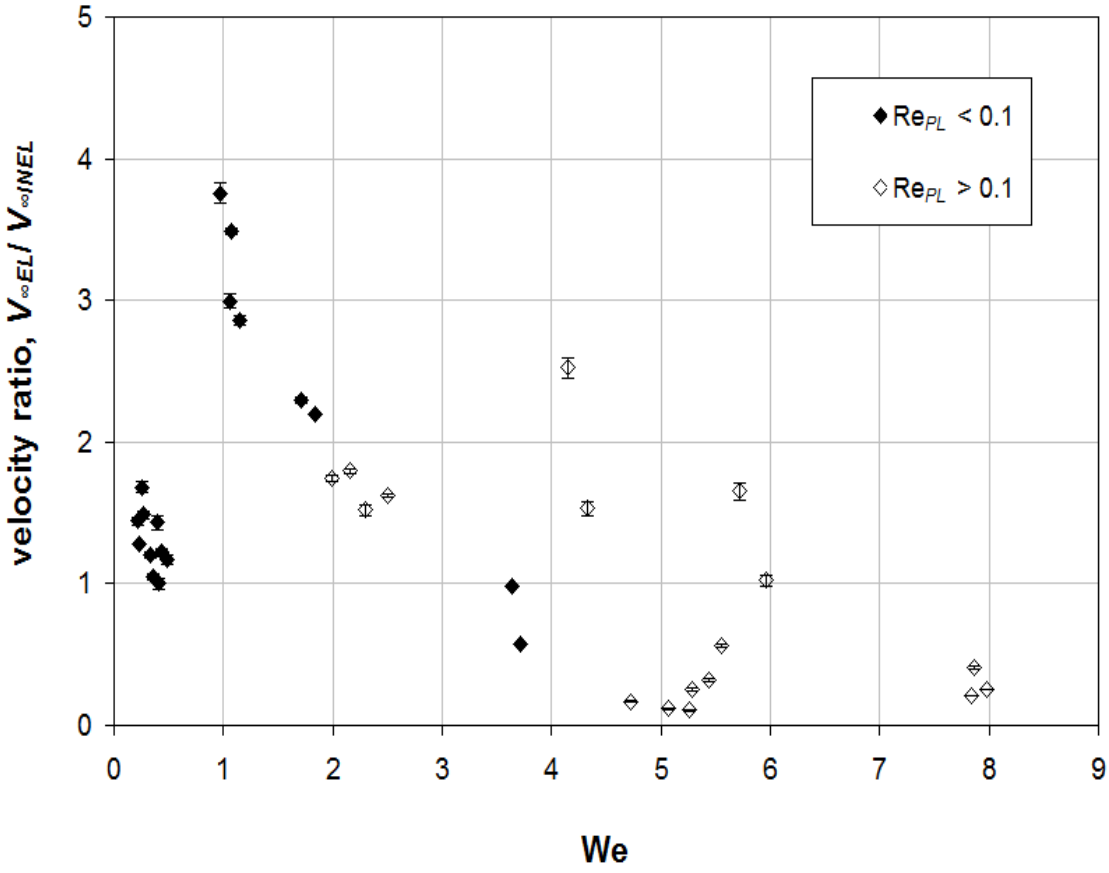

Figure 3.33: Velocity ratio as a function of the particle Weissenberg number. The plot shows the velocity increase followed by a velocity decrease with the increase in Weissenberg number. The error bars show the variance in the velocity ratio from repeated measurements.

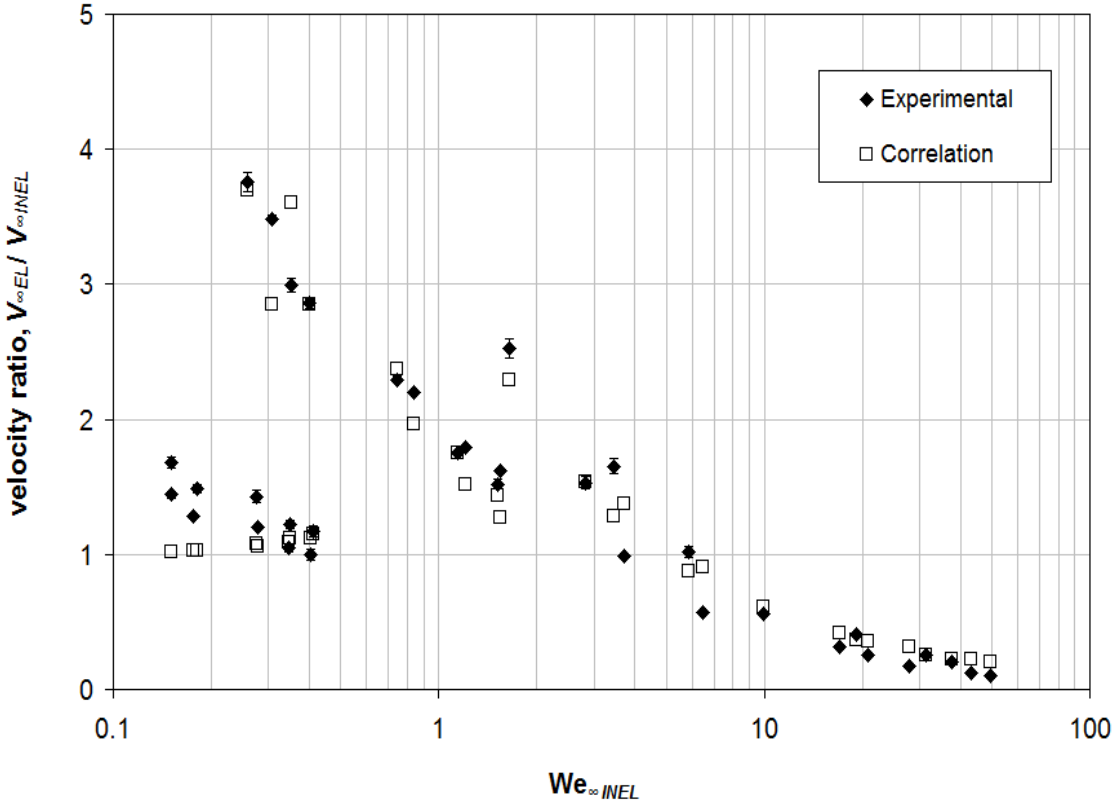

Figure 3.34: Comparison of the experimental velocity ratios with those predicted using the correlation. The x-axis is $We_{\infty INEL}$ which is not the actual particle Weissenberg number.

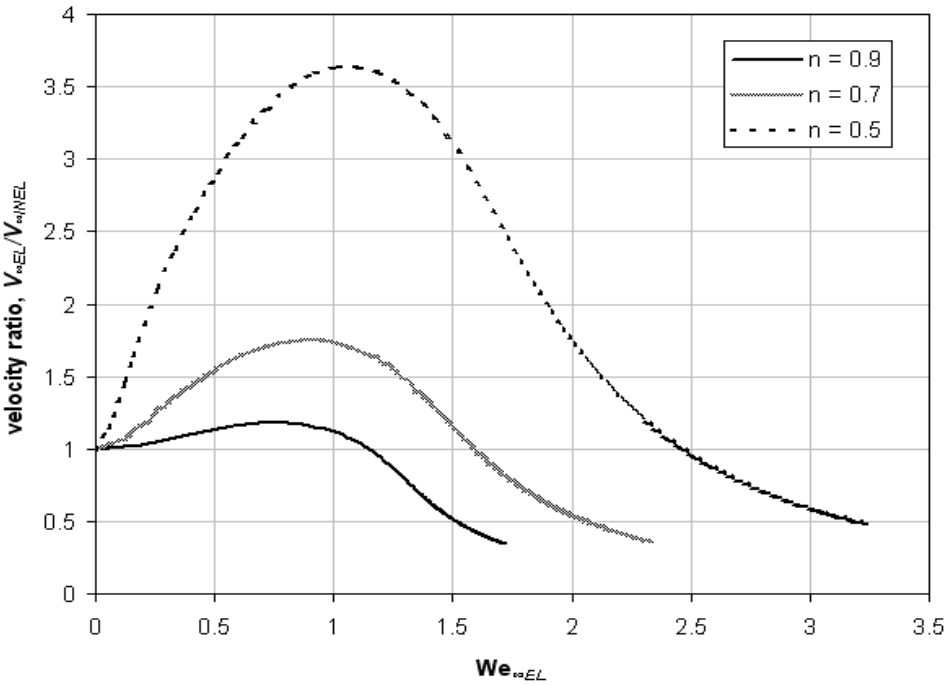

Figure 3.35: Drag correction factor as a function of the particle Weissenberg number for fluids with different *n* values.

Chapter 4: Effect of Confining Walls on Settling of Spherical Particles in VES Fluids

Chapter 3 described the settling of spherical particles in unbounded VES fluids. In practice, the finite size of vessels and presence of boundaries affect the settling velocity of particles. Examples include hydraulic and pneumatic transport of particles in pipes and falling ball viscometry. The boundaries exert a retardation effect on particles and reduce the settling velocities. The magnitude of the retardation effect depends on the shape and size of the confining walls i.e. circular or non-circular ducts (triangular, square, rectangular, planar slit etc.). This retardation effect is quantified in terms of a wall factor, $F_{w,}$ which is defined as:

$$F_w = \frac{\text{Settling Velocity in Presence of Confining Walls}}{\text{Unbounded Settling Velocity}} \qquad 4.1$$

In hydraulic fracturing, the surrounding fracture walls reduce the settling velocities of proppant. The fracture walls can be approximated by a planar slit (two parallel walls with a very low aspect ratio). Liu and Sharma (2005) showed that for Newtonian fluids the effect of the fracture walls in reducing the settling velocity of the proppant becomes significant as the ratio of the proppant diameter to the fracture width increases. This chapter focuses on the effect of parallel walls on settling velocities in VES fluids.

4.1 PAST WORK ON EFFECT OF CONFINING WALLS ON SETTLING VELOCITIES

Faxen (1922) stated that for Newtonian fluids, in the creeping flow regime, the wall factor depends only on the ratio of the particle diameter to the slot width, irrespective of the viscosity of the fluid. Subsequent studies presented theoretical expressions and experimental correlations to calculate the wall factors for spheres settling in cylindrical tubes in the creeping, intermediate and turbulent flow regime (Bohlin, 1960; Clift et al., 1978; Tullock et al., 1992; Chhabra et al., 1996; Chhabra, 2002). Detailed discussion of all the theoretical and experimental work for wall effects of spherical particles in cylindrical tubes can be found in Chhabra 2007. Miyamura et al. (1981) formulated a 19th order polynomial to determine the wall factors for spheres settling between two parallel plates in Newtonian fluids. Machac and Lecjaks (1995) conducted experiments with purely viscous shear-thinning (power-law) fluids and showed that the retardation effect of the walls decreases with the decreasing flow behavior index, n of the fluid. In other words, increased shear-thinning behavior reduces the retardation effect of the walls. They proposed a correlation to calculate the wall factors in terms of the diameter to wall spacing ratio and the flow behavior index, n. To summarize, there is a vast amount of coherent literature available to determine the wall effects for spheres settling in different cross-section tubes over a wide range of Reynolds numbers.

The determination of wall effects on settling in non-Newtonian fluids and particularly viscoelastic fluids is not as complete. Machac and Lecjaks (1995) conducted

experiments with purely viscous shear-thinning (power-law) fluids and showed that the wall retardation effect decreases with the decreasing power law index, *n* of the fluid. Missirlis et al. (2001) performed finite-element and finite-volume simulations for purely-viscous shear-thinning fluids and showed that the drag coefficient converges to a constant value as the power law index approaches zero, independent of the sphere-to-tube diameter ratio. Song et al. (2009) numerically investigated the drag force on spheres in cylindrical tubes and reported that the wall effects were less severe in power law fluids than in Newtonian fluids (in the range: Reynolds number 1-100; power law index 0.2-1 and sphere-to-tube diameter ratio 0-0.5).

Most of the work on determination of wall effects in viscoelastic fluids has been focused on spheres settling in cylindrical tubes. Chhabra et al. (1981) performed experiments with viscoelastic aqueous polymer solutions with different rheologies and determined wall factors for different ratios of particle diameter to cylinder diameter. They provided an empirical correlation to calculate the wall factors as a function of the diameter ratio and Weissenberg number. It was highlighted that the retardation effects due to the cylinder walls reduces with increasing levels of elasticity of the fluid.

Jones et al. (1994) conducted experiments for spheres settling inside cylinders in Boger fluids and observed that the spheres sometimes have to travel distances equivalent to 20 times the diameter before attaining a terminal velocity. They observed that the magnitude of the overshoot in the velocity decreases as the blockage ratio (ratio of

particle to cylinder diameter) increases. It was observed that at a blockage ratio of 0.25 there was a considerable enhancement in drag with the increase in Weissenberg number, but the drag enhancement disappeared upon increasing the blockage ratio to 0.5. Navez and Walters (1996) performed experiments in shear-thinning viscoelastic fluids for a blockage ratio of 0.5 and observed that the settling was dominated by the viscosity alone, and there was negligible influence of the fluid elasticity.

Huang and Feng (1995) performed numerical simulations in two-dimensional steady flows and used the Oldroyd-B model with a shear rate dependent viscosity to calculate the drag force on the cylinder as a function of the fluid rheology and the wall blockage ratio (ratio of the cylinder diameter to the spacing between walls). They observed that for unbounded flows and flows with small blockage ratios (less than 0.1), the drag on the cylinder was increased by elasticity. On the other hand, for flows with higher blockage ratios the trend was completely reversed. Increasing elasticity reduced the effect of the blocking walls. It was also observed that increased shear-thinning effects reduced the effect of the walls (Sugeng and Tanner 1986).

It is important to note that all the work done to determine the wall effects in viscoelastic fluids has been done for spheres settling in cylindrical tubes. No data is available for spheres settling in viscoelastic fluids between parallel walls (fracture walls).

4.2 EXPERIMENTAL SETUP AND PROCEDURE

Two experimental cells made of Plexiglass are used for performing the experiments. These cells are constructed such that the walls are smooth and perfectly parallel to each other. The width between the walls in the two cells is 3.6 mm and 8 mm respectively. The aspect ratio of the two cells is kept low in order to ensure that there is no effect of the walls orthogonal to the parallel walls. Figure 4.1 shows a schematic of the experimental cell.

The cell is filled with the viscoelastic fluid, and the particle is gently released in the cell through the inlet/outlet port as shown in part a) of Figure 4.2. The inlet/outlet port is then sealed with a rubber stopper, and the particle is allowed to settle until it reaches the middle of the cell (between the walls orthogonal to parallel walls). At this point, the cell is positioned vertically, and the particle is allowed to settle in the cell as shown in part b) of Figure 4.2. The settling process is recorded with a high resolution camera. Figure 4.3 shows a snapshot of a particle settling inside the experimental cell with the meter stick alongside the cell. The recorded video is then used to track the position of the particle using "Tracker 2.0" (http://www.cabrillo.edu/_dbrown/tracker/). Figure 4.4 is a snapshot from the software application showing the position of the particle being tracked at fixed time steps. This data is used to calculate the settling velocity of the particle.

The experiments are performed under a temperature controlled environment (oven). The temperature inside the oven is measured. Repeated measurements are made

as before to ensure reproducibility and to obtain error bars on each measurement. Particles of diameters varying between 1 mm to 5 mm are used in this setup.

4.3 Description and Rheology for Fluids

The fluids used for the experiments are the same as those used for measuring the settling velocities in unbounded fluids discussed in Chapter 3. The composition and rheology of the seven fluids used are discussed in details in Sections 3.2 and 3.3. Figures 3.1 through 3.7 show the steady shear-viscosity measurements with the viscosity and shear stress versus shear rate for the seven fluid mixtures. Figures 3.10 through 3.16 show the dynamic oscillatory shear measurements with the dynamic moduli versus the angular frequency. Table 3.1 shows the composition and rheological properties of the fluid mixtures.

4.4 Results for Particle Settling Between Parallel Walls

Settling velocities are experimentally measured for glass spheres settling between parallel walls. Multiple measurements are taken to get reliable averages and error bars. As discussed in Section 4.2, two experimental cells containing parallel walls are used. The spacing between the parallel walls is 3.6 mm and 8 mm respectively. Different diameter particles are used such that data points are uniformly obtained for the complete range of particle diameter to wall spacing ratio (r) varying from 0 to 1.

Figures 4.5 through 4.11 show the wall factors (F_w) from settling experiments performed in all fluid mixtures 1 through 7. It is observed that at the same value of r the wall factors are different in different fluids, which suggests that the wall factors depend on the rheology of the fluids. It is also seen that the wall factors are not a function of only the diameter to wall spacing ratio. This can be clearly observed in Figure 4.8 and Figure 4.9. We observe two different values of the wall factors at the same value of r from experiments performed in a fluid mixture using cells of different wall spacing. This suggests that, unlike Newtonian fluids, the wall factors in viscoelastic fluids are dependent on the rheology of the fluids, the particle diameter to wall spacing ratio as well as the diameter of the particle.

From Figure 4.8, it can be seen that the wall factor drops to a value below 0.46 as the ratio of particle diameter to slot with increases to 0.82. This signifies 54% reduction in the proppant settling velocity as the fracture width becomes comparable to the proppant diameter. The experimental results show that the fracture walls exert a significant retardation effect on proppant settling.

In order to examine the effect of elasticity on the wall effects, the wall factors are plotted as a function of the particle Weissenberg number for a constant value of r. Figure 4.12 shows the wall factor against We for three different values of r. It is observed that the wall factors increase with increasing Weissenberg numbers. This suggests that the effect of the confining walls decreases with increasing elasticity. It is also important to

note that for lower values of *r*, the increase of wall factors with Weissenberg numbers is not very significant. For higher values of *r* this increase is much more pronounced. This suggests that as the ratio of particle diameter to wall spacing increases, the impact of elasticity on reducing the wall effects is higher.

Balaramakrishna and Chhabra (1992) and Machac and Lecjaks (1995) presented experimental wall factors for spherical particles settling in rectangular ducts in inelastic power law fluids. Figure 4.13 shows the comparison of the experimental wall factors (in Fluids 4, 5, 6 and 7) with the predictions of correlation proposed by Machac and Lecjaks (1995). It is observed that at all values of *r* the experimental wall factors are higher than the predictions of Machac and Lecjaks (1995). The difference can be attributed to elasticity of fluids, which reduces the retardation effect of the confining walls.

An attempt is made to fit the wall factors in terms of the settling velocity under unbounded conditions and the fluid and particle properties. The following correlation is obtained using non-linear regression analysis:

$$F_w = (1-r)^p \tag{4.2}$$

Here *p* is given by:

$$p = 0.37\left(\frac{\mathrm{We}_{\infty EL}}{1+\mathrm{We}_{\infty EL}}\right)^{0.81} \mathrm{Re}_{\infty EL}^{-0.24}\, n^{0.17} \tag{4.3}$$

In Equations 4.2 and 4.3, r refers to the ratio of particle diameter to the spacing between the parallel walls. $We_{\infty EL}$ refers to the particle Weissenberg number under unconfined conditions given by:

$$We_{\infty EL} = \frac{2\lambda V_{\infty EL}}{d_p} \quad 4.4$$

Similarly $Re_{\infty EL}$ refers to the Reynolds number based on the unconfined settling velocity. Equations 4.2 and 4.3 are valid in the following range of variables:

$$0 \le r \le 1,\ 0.259 \le n \le 0.9,\ 0.22 \le We_{\infty EL} \le 7.98;\ 5\times10^{-4} \le Re_{\infty EL} \le 2.63$$

This correlation is an explicit function of the properties of the fluid and the particle and the settling velocity in the same fluid under unbounded conditions. The above correlation fits the wall factors for all the experiments very well, and the coefficient of correlation for the fit is 0.84.

4.5 Effect of Shear Thinning on Wall Factors

Let us assume that a particle diameter of 4mm and density of 2500kg/m^3 is settling in a fluid of density 1000kg/m^3 with K = 0.8 Pa.s^n, n = 0.9, λ = 0.5s. Using equations 3.13 and 4.2, the settling velocity and wall factor of particle for r varying from 0 to 1 can be calculated. Figure 4.14 shows the wall factors as a function of r. To illustrate the effect of shear thinning, the n value of the fluid is varied from 0.9 (least shear thinning) to 0.4 (most shear thinning). The wall factors for fluids with different r values are shown on the same plot. It can be observed that the wall factors are higher in fluids of lower n value suggesting that retardation effect of confining walls is reduced by shear thinning. This result is consistent with the numerical simulations of Sugeng and

Tanner (1986), Huang and Feng (1995), Missirlis et al. (2001), Song et al. (2009). Experimental results of Machac and Lecjaks (1995) for inelastic power law fluids also showed a reduction in wall retardation with increased shear thinning. We show the same behavior for spherical particles settling between parallel walls in viscoelastic fluids.

4.6 CONCLUSIONS

This chapter summarized the past work on wall effects on settling of particles in Newtonian and non-Newtonian fluids and presented experimental results on quantification of wall effects in the presence of parallel walls in VES fluids. The important conclusions from the experimental study are:

- The confining walls exert a strong retardation effect on the settling velocity of particles in viscoelastic fluids. As the particle diameter approaches the wall spacing, the settling velocity reduces considerably.

- It is observed that unlike Newtonian fluids, the wall factors in viscoelastic fluids do not depend on only the diameter to wall spacing ratio. The wall factors are observed to depend on the rheological properties of the fluid, the diameter of the particle and the particle diameter to wall spacing ratio.

- A new correlation for the wall factors in terms of the unbounded Weissenberg number and ratio of particle diameter to spacing between the walls is presented.

- Experimental results show that fluid elasticity reduces the effect of the confining walls, and this effect becomes more pronounced as the ratio of particle diameter to wall spacing increases.

- Results show that, for the same ratio of particle diameter to wall spacing, the retardation effect of confining walls is reduced with increased shear thinning behavior of fluids.

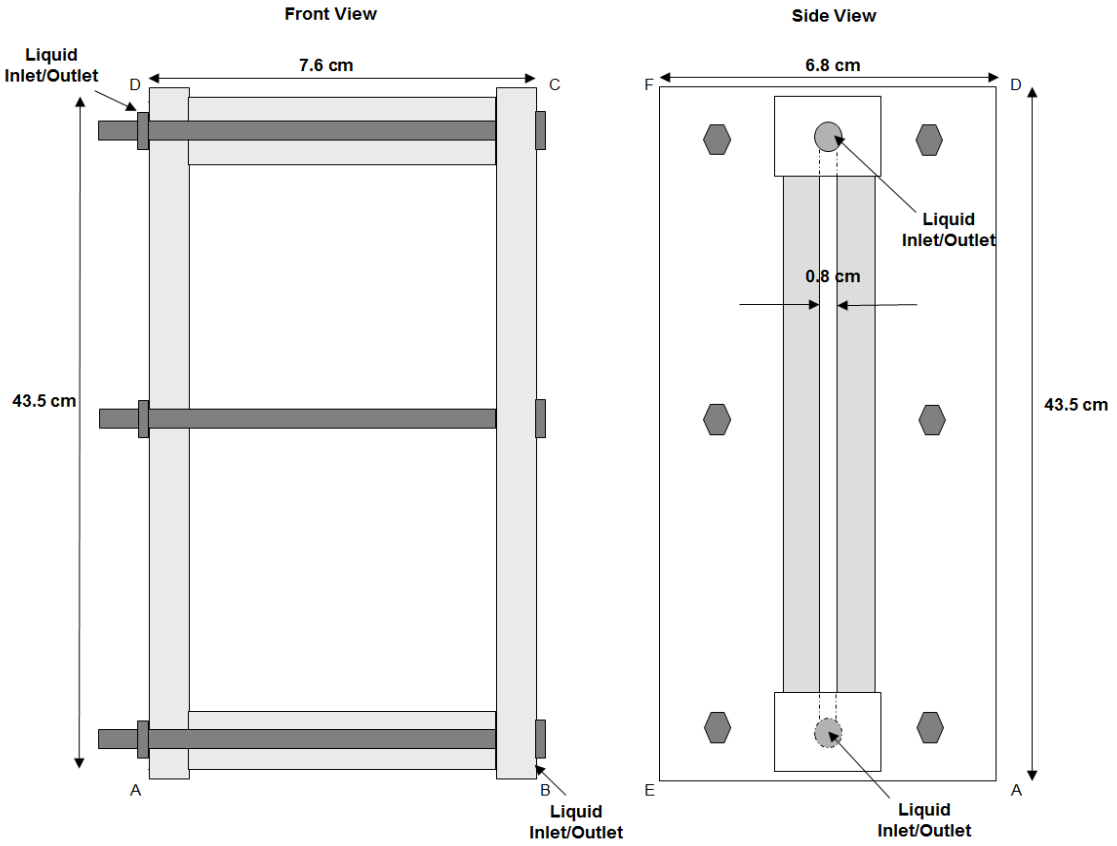

Figure 4.1: Schematic of the experimental cell for determining settling velocities between parallel walls (not to scale).

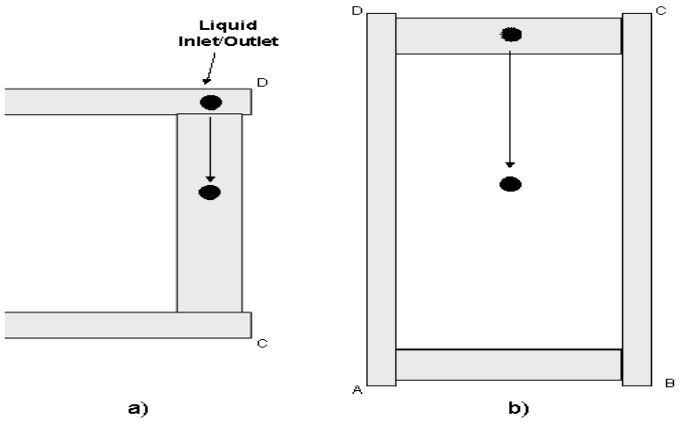

Figure 4.2: Schematic of the experimental cell illustrating the procedure for measuring the settling velocity of particles between the parallel walls.

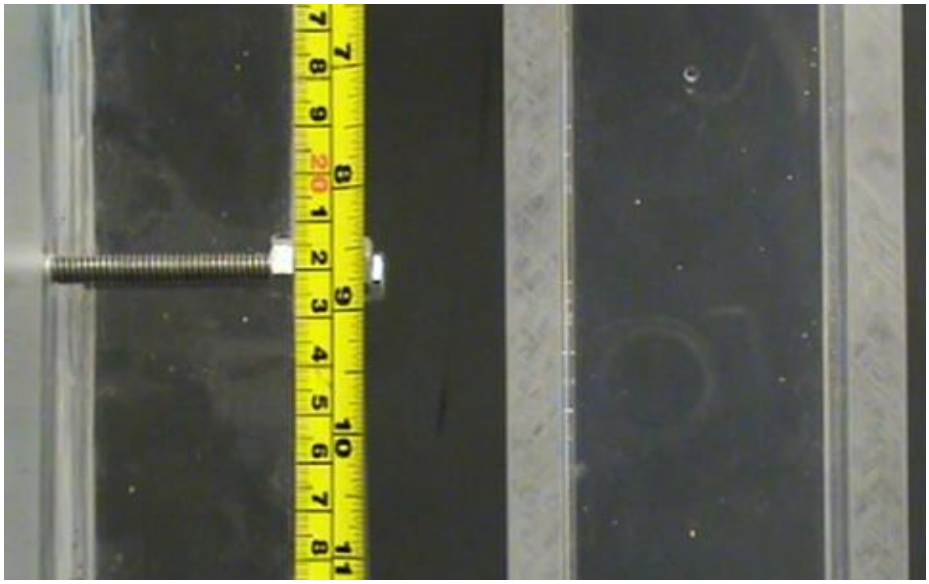

Figure 4.3: Snapshot of particle settling in the experimental cell in the VES fluid.

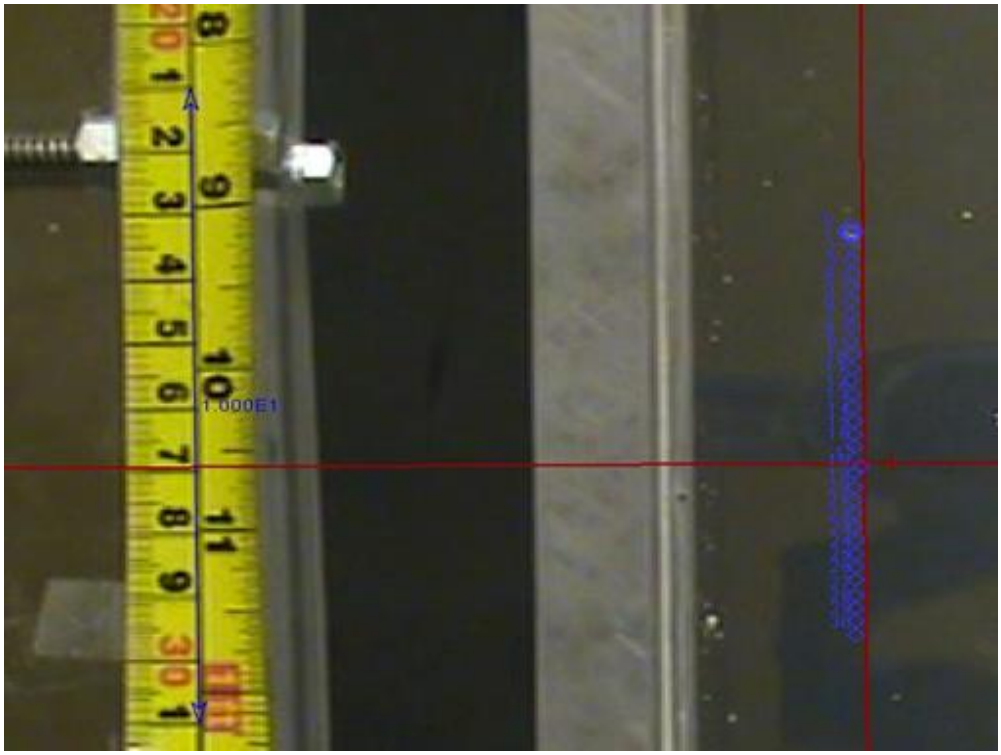

Figure 4.4: Snapshot of particle tracking in Tracker 2.0.

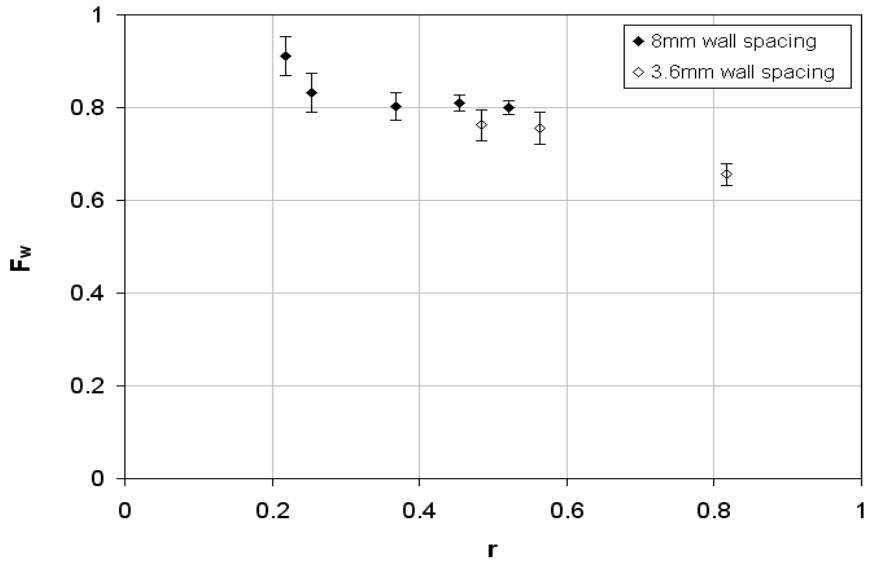

Figure 4.5: Wall factors for particles settling in Fluid 1. *r* is the ratio of particle diameter to slot width.

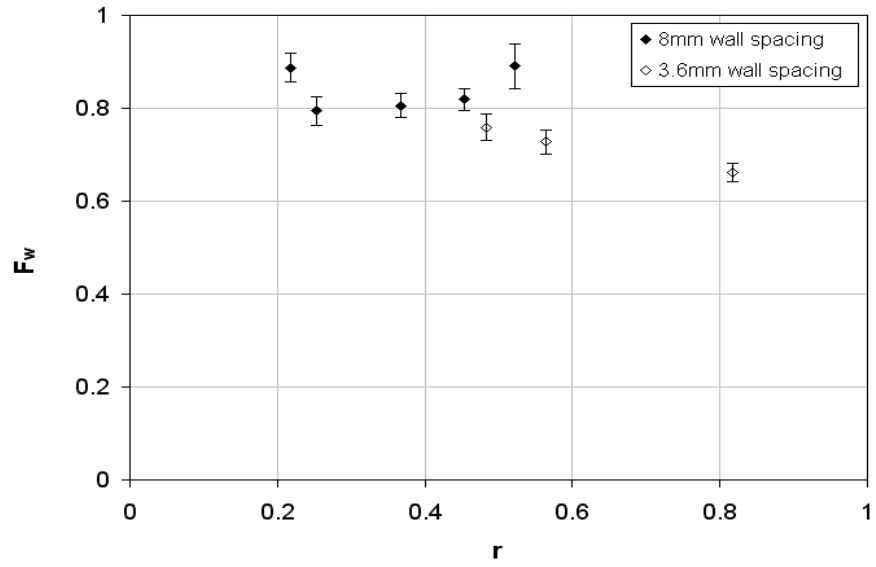

Figure 4.6: Wall factors for particles settling in Fluid 2. *r* is the ratio of particle diameter to slot width.

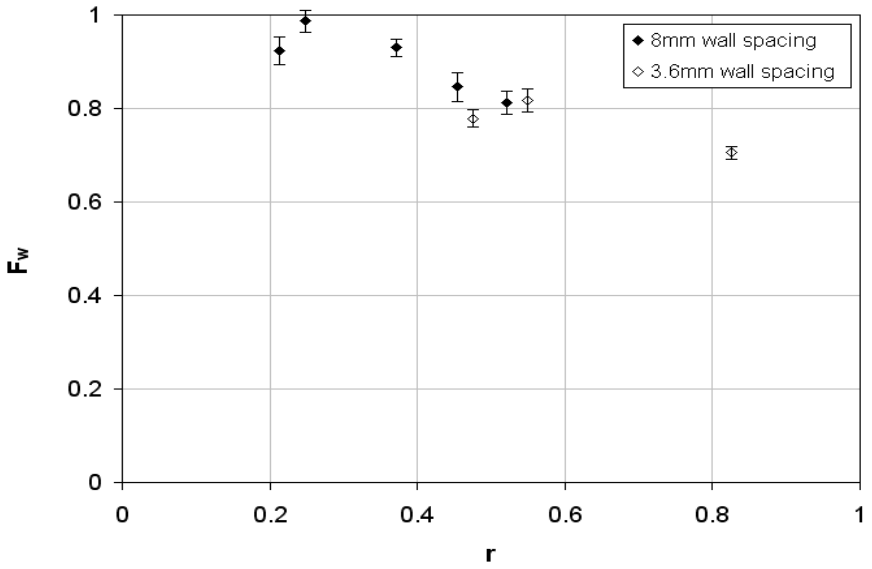

Figure 4.7: Wall factors for particles settling in Fluid 3. *r* is the ratio of particle diameter to slot width.

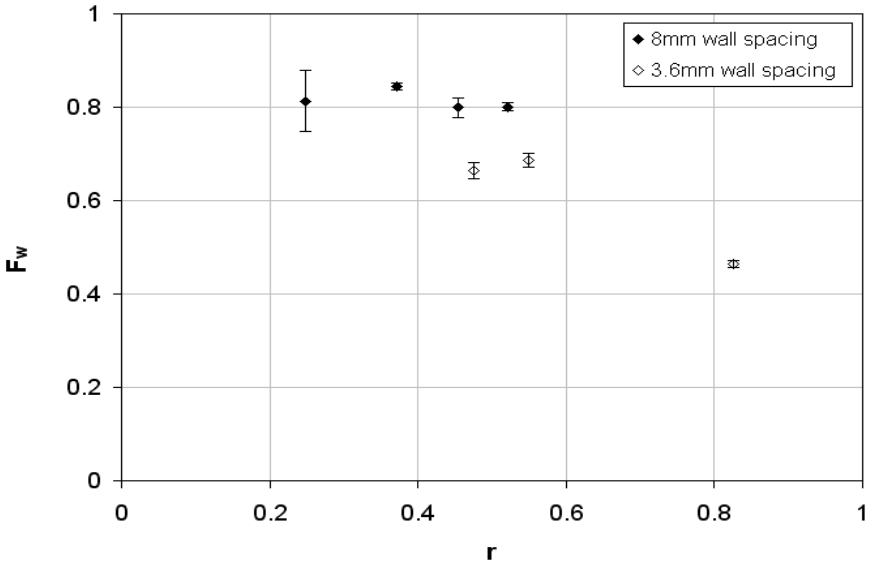

Figure 4.8: Wall factors for particles settling in Fluid 4. *r* is the ratio of particle diameter to slot width.

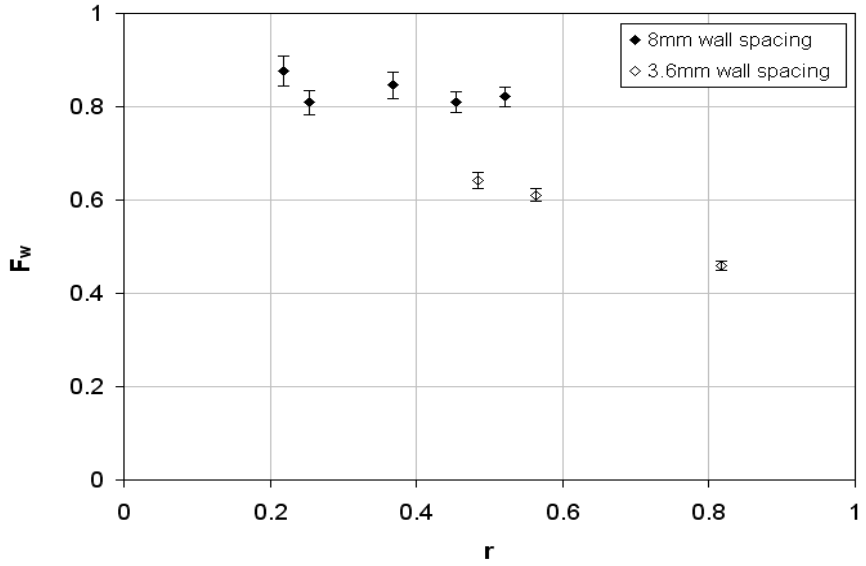

Figure 4.9: Wall factors for particles settling in Fluid 5. *r* is the ratio of particle diameter to slot width.

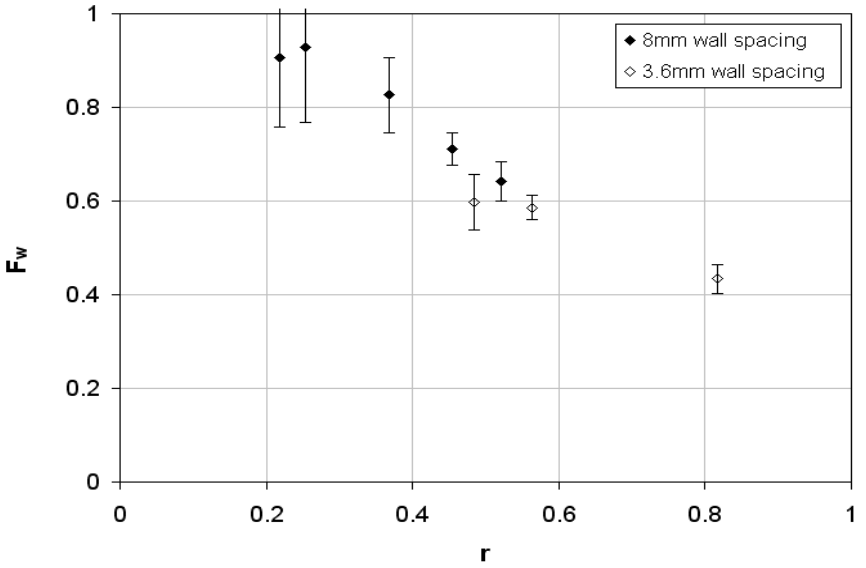

Figure 4.10: Wall factors for particles settling in Fluid 6. *r* is the ratio of particle diameter to slot width.

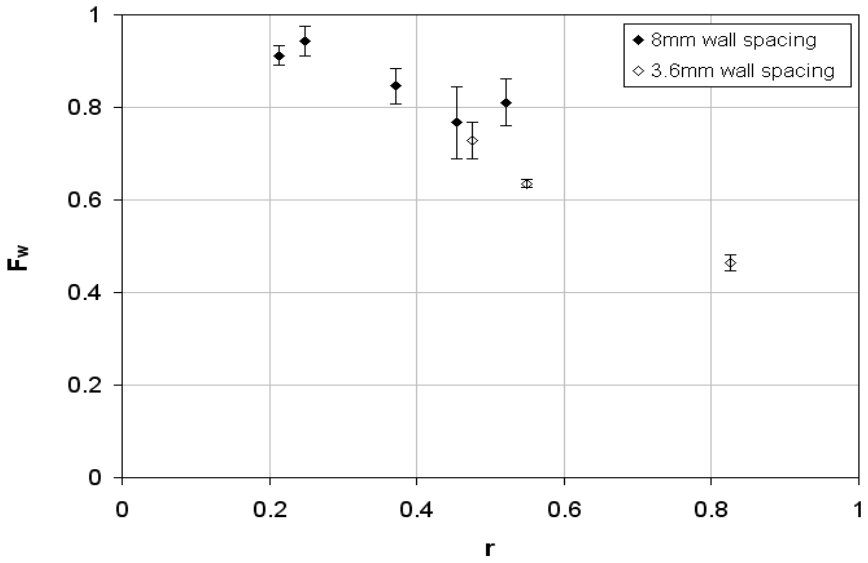

Figure 4.11: Wall factors for particles settling in Fluid 7. *r* is the ratio of particle diameter to slot width.

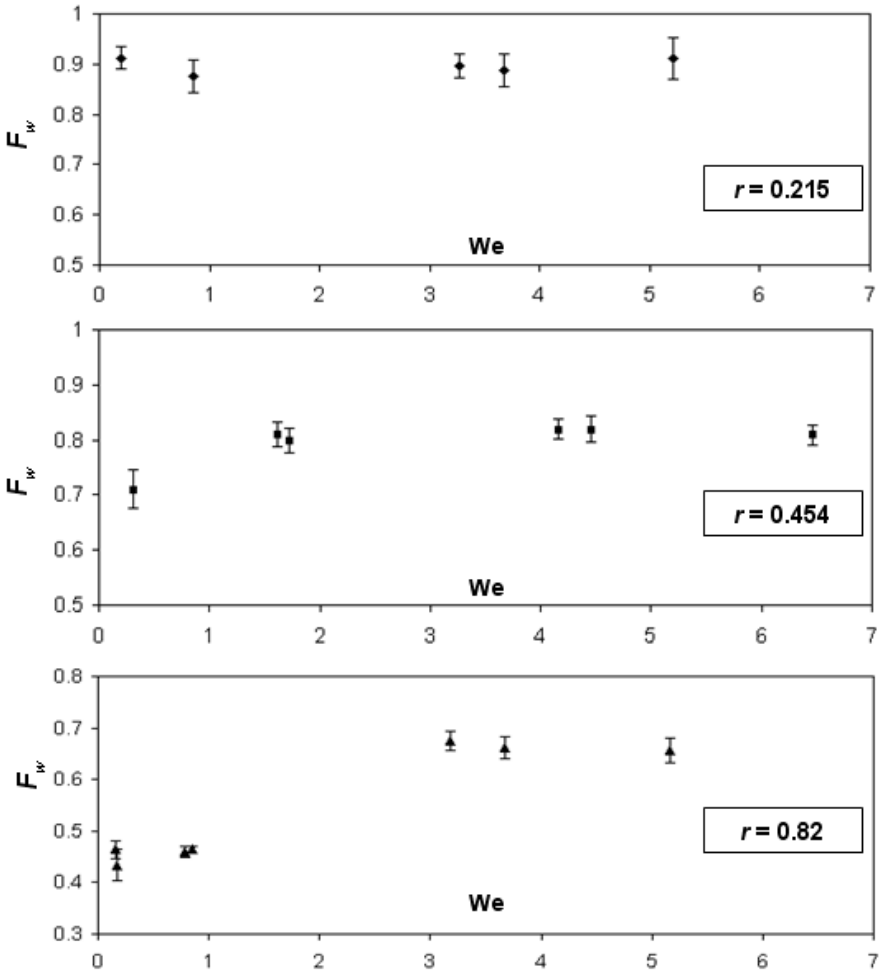

Figure 4.12: Experimentally measured wall factors against the particle Weissenberg number for three different fixed values of *r*.

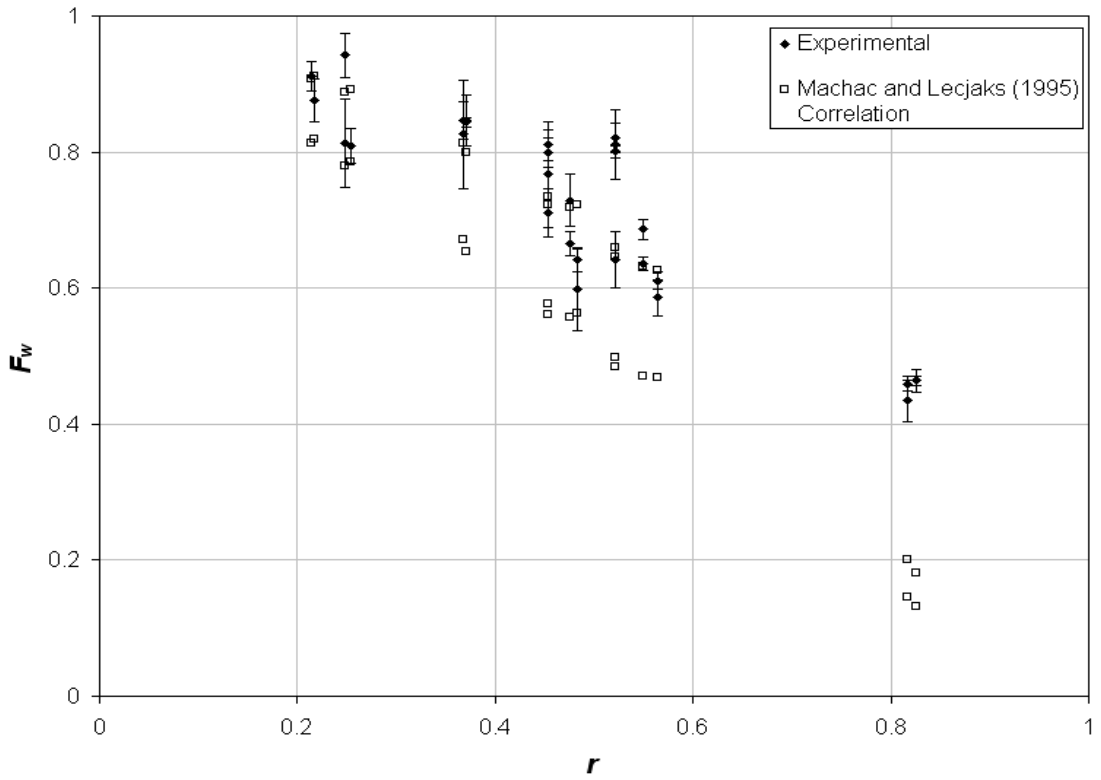

Figure 4.13: Comparison of the experimental wall factors for particles settling in Fluids 4, 5, 6 and 7 with the correlation by Machac and Lecjaks (1995).

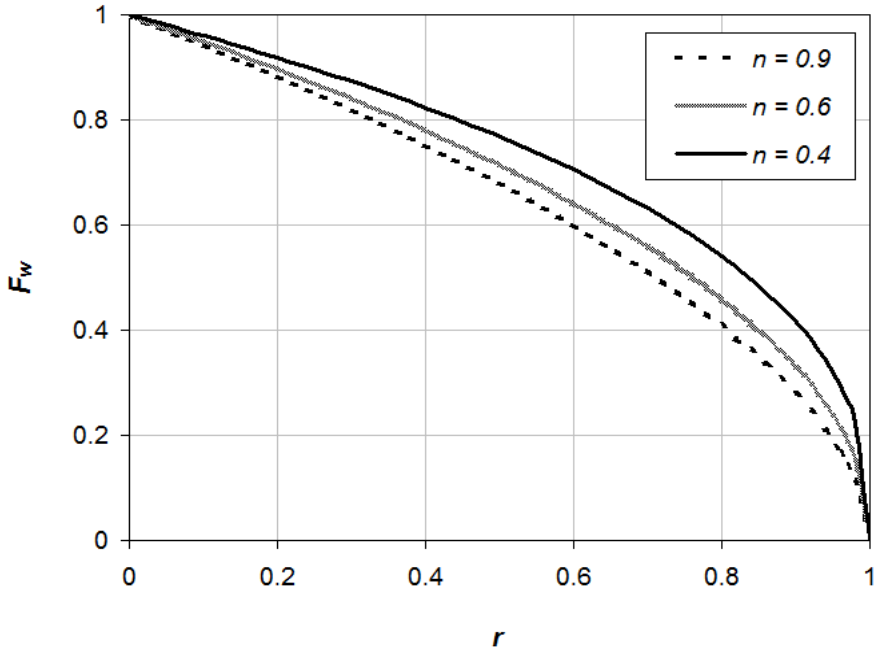

Figure 4.14: Wall factors in fluids with different n values predicted using the correlation in Equation 4.2. Wall factors decrease as the shear thinning behavior of the fluid increase.

Chapter 5: Growth of Mixing Zone in Miscible Viscous Fingering

5.1 Introduction and Past Work

Displacement of a more viscous fluid by a less viscous fluid leads to flow instabilities resulting in the formation of fingers of the less viscous fluid. The onset and evolution of instabilities is referred to as viscous fingering (Saffman and Taylor 1958; Chouke et al. 1959; Peters 1979; Homsy 1987). Viscous fingering has been a subject of extensive study over the past years because of its applications in many processes which include flow through porous media (Homsy 1987), secondary and tertiary oil recovery (Peters et al. 1987; Lake 1989; Peters and Hardham 1989; Peters and Reid 1990), proppant placement in hydraulic fractures (Liu et al. 2007) and flowback from hydraulic fractures (Pope et al. 1996). A vast body of theoretical, numerical and experimental work devoted to understanding various aspects of the instabilities is available in the literature (Zimmerman and Homsy 1992; Loggia et al. 1995; Tanveer 2000; Smirnov et al. 2005). The spreading and growth of the mixing zone is an important issue which still remains unresolved. A schematic illustrating the mixing zone is in Figure 5.1. The mixing zone is defined as the length where the local concentration of the injected fluid, c, varies from 0 (corresponding to the initial fluid) to 1 (corresponding to the injected fluid).

Several empirical models are available for the evaluation of mixing zones in unstable, miscible displacements (Koval 1963; Todd and Longstaff 1972; Fayers et al. 1994). Koval's prediction of the growth of the mixing zone in a homogenous medium is based on the following equation:

$$\frac{\partial \bar{c}}{\partial t} + U \frac{\partial}{\partial x}\left(\frac{M_e \bar{c}}{1+(M_e-1)\bar{c}} \right) = 0 \qquad 5.1$$

where $\bar{c}$ is the volume concentration of solvent averaged across the fingers, U is the total flux of fluid and M_e is the effective viscosity ratio, defined by:

$$M_e = (0.22M^{1/4} + (1-0.22))^4 \qquad 5.2$$

where M is the ratio of viscosity of displaced fluid (μ_1) to the viscosity of displacing fluid (μ_2). *Me* is the same as the Koval factor, K (Koval 1963) for a homogenous medium. The above equation was derived for hydrocarbon and solvent mixtures which follow the fourth root (or quarter power) mixing rule:

$$\frac{1}{(\mu_{mix})^{1/4}} = \frac{1-\phi}{(\mu_{HC})^{1/4}} + \frac{\phi}{(\mu_S)^{1/4}} \qquad 5.3$$

μ_{HC} is the viscosity of the hydrocarbon, μ_S is the viscosity of the solvent, μ_{mix} is the viscosity of the mixture and ϕ is the volume fraction of the solvent. The value of 0.22 was obtained by fitting the model with the recovery data of Blackwell et al. (1959). The data of Blackwell et al. (1959) was for miscible displacements in sand packs with viscosity ratios below 150. The Koval model does not have a rigorous derivation and should be considered as an ad-hoc fit to experimental data. Numerical simulations of Yang et al. (2002) and Booth (2010) are in agreement with the Koval model when the Peclet number is large and the mixing zone grows linearly. The mixing zone velocity can be defined as the rate of change of mixing zone length and is expressed by the following equation for Koval's model:

$$\frac{\Delta x}{t} = U\left(M_e - \frac{1}{M_e}\right) \tag{5.4}$$

The equation predicts that the mixing zone velocity is directly proportional to (M_e-1/M_e). The growth rate of the mixing zone agrees with the experimental observations of Wooding (1969). Yortsos and Salin (2006) used the approach by Menon and Otto (2005) and concluded that the mixing zone velocity is bounded by $(M\text{-}1)^2/(M \ln M)$. The mixing zone velocity is an integral part of design considerations for hydraulic fracturing treatments in which alternate slugs of a high viscosity and a low viscosity liquid are pumped, with one of the liquids laden with proppant (typically sand). A schematic is shown in Figure 5.2. The mixing of the two liquids is governed by the mixing zone velocity.

Experimental studies for studying viscous fingering have been performed in the past in Hele-Shaw flow cells comprising two parallel plates separated by a small gap. The cell is used to describe the two-dimensional features of flow, depth-averaged over the thin gap between the plates. Hele-Shaw cells can be constructed to have radial or rectilinear flow between the parallel plates. In this chapter, an experimental study is presented showing the mixing zone velocities in a rectilinear Hele-Shaw cell for very high viscosity ratios (up to 1225). Experiments are performed at different flow rates for injection of water into different viscosity glycerol solutions. We observe that the mixing zone velocity initially increases with viscosity ratio and reaches an asymptotic value at high viscosity ratios.

5.2 EXPERIMENTAL SETUP

Figure 5.3 shows a sketch of the Hele-Shaw cell used in the experiments. The cell is made of Plexiglass, and the flow channel is 84cm long and 5cm wide. The walls are smooth and perfectly parallel to each other with a spacing of 1mm. Figure 5.4 shows a sketch of the experimental setup. The setup consists of two 500ml Isco syringe pumps. Figure 5.5 shows one of the pumps. Pump 1 is used to fill the Hele-Shaw cell with the displaced fluid (glycerol solution), pushing the liquid against gravity with the cell kept in an inclined position (Figure 5.6). This is done to avoid any air bubbles in the cell. An accumulator with a piston is used to pump the displaced fluid to the cell. This is done to prevent the pump from coming in contact with viscous fluids.

Once the cell is filled with the displaced fluid, valve a) is switched to the other position, and the displacing fluid (water) is injected into the cell with Pump 2. A three-pronged manifold splits the displacing fluid (water) stream into three parallel streams that enters the cell from the three sides (Figure 5.7). A water-soluble dye is added to the displacing water to increase the contrast between the two liquids. The cell is kept in a horizontal plane in all the experiments to avoid any gravitational effects in the direction of flow. Upon the injection of the displacing fluid, a high definition video camera is used to record the experiment. The camera is placed over the top of the cell using a pair of tripods and is moved along the length of the cell during the experiment (Figure 5.8). A measuring scale is kept alongside the Hele-Shaw cell while recording the video.

An image analysis tool Tracker 4.0 (http://www.cabrillo.edu/~dbrown/tracker/) is used to analyze the movement of fingers and to calculate the mixing zone length as a function of time. The x-position of the finger front (where the cross-section averaged injected concentration of injected water increases to just above zero) is tracked as a function of time. The x-position of the point where the cross-section averaged injected concentration of injected water increases to one is also tracked at the same time steps. The difference between the two x-positions gives the length of the mixing zone. The measurements are discussed in details in the next sections. At least two measurements are made for each reported mixing zone length under a unique set of conditions to ensure reproducibility.

5.3 FLUID DESCRIPTION

The goal of the experiments is to measure the mixing zone velocities for displacement of water into glycerol solutions (displaced fluid). The viscosities of glycerol solutions range from 1 to 1225cp. Steady shear-viscosity measurements are made using the ARES rheometer using a double wall concentric cylinder fixture. Ten points per decade are measured. Figure 5.9 shows the viscosity of 97% glycerol solution as a function of shear rate at room temperature (22 degrees C). The solution has a constant viscosity (within 1% of the zero shear viscosity) over the complete range of shear rates. Table 1 lists the viscosity of all the glycerol solutions used in the study.

5.4 OBSERVATIONS AND RESULTS

In order to ensure the homogeneity of the Hele-Shaw cell, a unit displacement (water displacing water) is performed. The displacing water is colored with the dye and is injected at a rate of 12.35ml/min (highest injection rate in any of the subsequent experiments). Figure 5.10 shows snapshots of the displacing water front at two different times. A piston-like displacement at the interface of the two fluids is observed. This confirms that the cell walls do not cause any instability, and any finger formation is due to the viscosity contrast between the two fluids (in absence of gravity).

Displacement of the glycerol solutions is performed at three different flow rates: 12.35, 4.69 and 1.28ml/min. The mutual diffusion coefficients between distilled water and water-glycerol solutions are calculated using the relation proposed by D'Errico et al. (2004).

$$D \times 10^{9} m^{2} s^{-1} = \frac{(1.024 \pm 0.01) - (0.91 \pm 0.05) x_2}{1 + (7.5 \pm 0.3) x_2} \pm 0.004 \qquad 5.5$$

In the above equation, D is the mutual diffusion coefficient and x_2 is the mole fraction of glycerol in the water-glycerol mixture. The flow Peclet numbers (Pe) are then calculated using the following equation:

$$\mathrm{Pe} = \frac{Ub}{D} \qquad 5.6$$

U is the velocity of flow displacements, D is the diffusion coefficient and b is a characteristic length scale. For calculations, the characteristic length is taken as the gap

width of 1mm. The velocity, U, is calculated by dividing the injection rate by the cross section area of channel. Table 5.2 lists the diffusion coefficients, and the Peclet numbers at the three flow rates, for all glycerol solutions. The Peclet numbers are high ($>10^3$) for all the displacement experiments performed in this study. Based on the high Peclet numbers, it can be assumed that all the displacements are convection dominated and longitudinal diffusion can be neglected.

Figure 5.11 through Figure 5.16 show the sequential evolution of the interface at an injection rate of 4.69ml/min in 79%, 83%, 89%, 95.5%, 97% and 100% glycerol solutions respectively. As seen in these figures, initially a large number of fingers originate from the interface between the two fluids. With the progress of the displacement, the fingers become longer and wider, and their number reduces. Differences are observed in the viscous fingering patterns in different viscosity glycerol solutions at the same flow rate. At lower viscosity ratios, multiple fingers are observed to grow parallel to each other, signifying reduced shielding at low viscosity ratios (up to 80). Shielding is the process by which growth of a finger retards the growth of adjacent trailing fingers (Homsy 1987; Li et al. 2006). At higher viscosity ratios, shielding is more pronounced. An illustration of increased shielding can be observed in Figure 5.14. At the snapshot at 15s, there are two fingers close to each wall of the Hele-Shaw cell. At later times i.e. 53s it is observed that the finger closer to the wall with the scale, has retarded the growth of the finger close to the other wall.

Spreading is the mechanism by which a finger becomes wider as the displacement continues. Coalescence is the mechanism by which the tip of one finger merges into the body of another adjacent finger. Spreading and coalescence are observed in displacement is all the glycerol solutions. The degree of coalescence increases as viscosity ratio increases i.e. the fingers turn at wider angles to merge into the body of adjacent fingers. An illustration of coalescence can be observed in Figure 5.15 in snapshots at 21s and 39s. At the snapshot at 21s, two fingers in the middle of the channel are moving parallel to each other. At a later time, 39s, it is observed that the trailing finger mergers into the body of adjacent finger by turning an angle of approximately 60 degrees. Other instances of coalescence can be observed in Figure 5.16 where the finger in the middle of channel splits into two (21s), and after splitting each branch coalesces into the corresponding side finger (42s).

Tip splitting is the mechanism by which the tip of a finger splits into two or more fingers (Wooding 1969; Tan and Homsy 1988). It is observed that at low viscosity ratios (79% and 83% glycerol solution), the fingers do not exhibit prominent tips splitting features. As seen in Figure 5.11, the only tip splitting observed is shown in snapshots at 63s and 68s. The tip splits into two and both fingers continue to grow. This kind of tip splitting is referred to as even tip splitting. In the 83% glycerol solution corresponding to a viscosity ratio of 79.5 (Figure 5.12), none of the fingers split and the only phenomenon observed is merging/coalescence (Li et al. 2006). However, at higher viscosity ratios, all the dominant fingers exhibit tip splitting. At a viscosity ratio of 177.5 (Figure 5.13), the

fingers split into two, and after splitting one finger shields/retards the growth of other. This mechanism has been referred to as uneven tip splitting (Islam and Azeiz 2007). The growing finger further splits into two, and the process repeats. This observation is qualitatively consistent with the numerical simulations of Islam and Azeiz (2007). As the viscosity ratio is further increased, the tip splitting patterns become complicated with finger tips splitting into three or more fingers. Instances of finger tips splitting into three and four fingers can be observed in Figure 5.15 and Figure 5.16. In Figure 5.15, at 18s, the finger in the middle of the channel splits into three fingers, one of which grows further and shields the growth of the other two. The fingertip close to the wall at 21s splits into four fingers. One of these fingers grows and further splits into three. Similar observations are made in 100% glycerol solution (Figure 5.16) as marked in circles. To summarize, a transition from no tip splitting to prominent tip splitting is observed as the viscosity ratio between the fluids is increased.

5.4.1 Mixing Zone and Finger Tip Velocity

Using Tracker 4.0, the length of the mixing zone (as described in the schematic in Figure 5.1) is calculated at different times of evolution of the interface for all the fluid displacements. Figure 5.17 shows the mixing zone length as a function of time in 97% glycerol solution at two flow rates. A linear increase in the mixing zone length with time is observed in all the experiments. The mixing zone velocity is calculated from the slope of the straight line.

Figure 5.18, Figure 5.19 and Figure 5.20 show the mixing zone velocities in all the glycerol solutions at 12.35, 4.69 and 1.28ml/min respectively. In the three cases, a linear increase in the mixing zone velocity with viscosity ratio, up to a value of 343 is observed. Above this viscosity ratio, the mixing zone velocity plateaus. This suggests that the rate of growth of the mixing zone does not change above this viscosity ratio. This observation is not captured by the Koval's model which, as mentioned before, is an empirical fit to experimental data for viscosity ratios below 150.

Figure 5.21 shows the mixing zone velocity normalized with the injection velocities (injection rate / cross section area) at the three injection rates. It is observed that for the three injection rates the normalized mixing zone velocities converge into a single curve. This curve is a relation between the rate of growth of the mixing zone and the viscosity ratio of two fluids, in a dimensionless form. Equation 5.4 can be rearranged in the following form:

$$\left(M_e - \frac{1}{M_e} \right) = \frac{\Delta x / t}{U} \qquad 5.7$$

The right hand side of this equation is the normalized mixing zone velocity shown in Figure 5.21. Using the experimental data of the normalized mixing zone velocities, the Koval factor, M_e, is calculated from the above equation. It is compared with the Koval factor, M_e, calculated from Equation 5.2. The comparison is shown in Figure 5.22. It is observed that M_e values from the experiments are lower than those predicted from

Equation 5.2. It can also be observed that M_e calculated from the experimental data plateaus at viscosity ratios above 343 which is not captured by the Koval's formulation.

As mentioned in the Section 5.1, the value of 0.22 in Equation 5.2 was derived from fitting the experimental data of Blackwell (1959). To match our experimental data for viscosity ratios below 343, the factor ϕ i.e. the volume fraction of solvent (Equation 5.3) is adjusted. This is done on the basis that the water-glycerol mixtures obey the fourth root mixing rule. This is confirmed by the viscosity versus glycerol concentration plot from our rheological measurements i.e. the data in Table 5.1, along with a comparison from the fourth root mixing rule (Figure 5.23). A ϕ factor of 0.094 instead of 0.22 is observed to fit the mixing zone velocity data below viscosity ratios of 343 i.e. the following equation combined with Equation 5.4 are observed to fit the data:

$$M_e = (0.094M^{1/4} + (1-0.094))^4 \qquad 5.8$$

The comparison of the data and the above equation is shown in Figure 5.24. Above viscosity ratios of 343, this equation cannot be used as the experimental M_e does not change with viscosity ratio.

Figure 5.25, Figure 5.26 and Figure 5.27 show the fingertip/front velocities for water injected in all the glycerol solutions at 12.35, 4.69 and 1.28ml/min respectively. The fingertip velocities follow a trend similar to the mixing zone velocities. It is observed that fingertip velocities increase with the viscosity ratio up to a value of 343, above which

the velocities plateau. Figure 5.28 shows the relative front velocity, defined as the ratio of fingertip velocity to injection velocity (injection rate / cross section area) as a function of viscosity ratio at three injection rates. It is observed that the three curves converge, similar to observation for the mixing zone velocities.

5.4.2 Relative Finger Width

Relative finger width (RFW) is an important parameter to characterize the fluid displacement. It is defined as the area contacted by the displacing fluid to the total area behind the finger tip. Relative finger width is a measure of the sweep efficiency of the displacing fluid. To calculate the relative finger width, we use a program "ImageJ" (http://rsbweb.nih.gov/ij/). A snapshot of the displacement is taken at a specified time. The interface between the displacing and displaced fluid is outlined and the area contact by the displacing fluid is calculated. A snapshot of the outlined interface is shown in Figure 5.29. This area is divided by the total area behind the tip to calculate the RFW.

In an ideal scenario, at time, t = 0 (start of injection), the interface between the displacing and displaced fluid should be a straight line (stable interface). This would correspond to RFW = 1 at t = 0. The interface would develop instabilities at later times, resulting in reduction of RFW with subsequent injection, and development of instabilities. This is shown in the numerical simulations of Islam and Azaiez (2007). However, in the experiments we observe that at the start of injection the viscous fingers develop and propagate faster closer to the side walls of the Hele-Shaw cell. The wall

effects result in values of RFW lower than one at early times of injection. Figure 5.30 shows the relative finger width as a function of time for injection of water at 12.35ml/min in different viscosity glycerol solutions. It is observed that any time, the relative finger width reduces as the concentration (or viscosity) of glycerol increases. This suggests lower sweep in higher viscosity solutions are the same injection rate. Similar observation is made at an injection rate of 4.69 ml/min, as shown in Figure 5.31.

In the previous section, data was presented to show that the fingertip velocities are almost the same in 94%, 95.5%, 97% and 100% glycerol solutions i.e. above viscosity ratios of 343 (Figure 5.28). The data in Figures 5.30 and 5.31 show that the RFW reduces as the viscosity ratio (or glycerol concentration) is increased. The high Peclet numbers suggest that longitudinal diffusion is negligible in the displacements. Conserving the mass/volume of the injected fluid, this suggests that the thickness of the displacing water and the thickness of thin film of the displaced fluid on the walls of the cell are different during displacement in the different viscosity solutions. It has been shown that during fluid displacements, a thin film of the displaced fluid is left on the walls, in immiscible as well as miscible displacements (Bretherton 1961; Lionti-Addad and Meglio 1992; Ro and Homsy 1995; Lajeunesse et al. 1997; Lajeunesse et al. 1999; Lindner et al. 2002). In immiscible displacements, the capillary number controls the thickness of the thin film. For the motion of finite bubbles in capillary tubes, in the limit of small capillary numbers, the thickness, t, of the film for Newtonian fluids is given by (Bretherton 1961):

$$\frac{t}{R} = 0.643(3Ca)^{2/3} \qquad 5.9$$

The film thickness scales with U^{α} with $\alpha = 2/3$. U is the displacement velocity. Addition of polymers has been observed to reduce the thickness of films (Lionti-Addad and Meglio 1992; Lindner et al. 2002). Experimental studies by Lajeunesse et al. (1997, 1999) showed that the displacing fluid forms a symmetric tongue across the gap between the Hele-Shaw cells in miscible displacements, below a critical viscosity ratio and flow rate.

A mass balance approach is used to estimate the average film thickness during the fluid displacements in glycerol and PEG-PEO solutions. Assuming that the fluids are incompressible, the thickness of the water (displacing fluid) averaged over the displaced area is calculated by dividing the amount of water injected at any time by the swept area. The swept area is calculated using 'ImageJ' as mentioned previously and shown in the snapshot in Figure 5.29. The average thickness of the film is then calculated by subtracting the thickness of water from the gap width and dividing by two (assuming a symmetric tongue of displacing fluid in the gap). A schematic of the symmetric tongue is shown in Figure 5.32.

Figure 5.33 shows a plot of the average film thickness with time for displacements of different glycerol solutions at an injection rate of 12.35ml/min. The data shows that glycerol concentrations up to 89%, the average film thickness on the cell walls

does not change significantly with the glycerol concentration as well as with time. As the viscosity of the glycerol solution is increased, the average film thickness reduces with increase in glycerol concentration (or viscosity). At high glycerol concentrations the average film thickness is also observed to vary with time. For glycerol concentrations of 95.5%, 97% and 100%, the average film thickness is lower than the less concentrated glycerol solutions. Figure 5.34 shows the plot of average film thickness with time at the injection rate of 4.69ml/min. Similar to observations at the higher rate, the film thickness is observed to considerably decrease at high viscosity ratios. This reduction in film thickness explains the plateau in the mixing zone and the fingertip velocities at glycerol concentration of 94% at a constant injection rate (Figure 5.26). At the viscosity ratios above 343 (corresponding to glycerol concentration of 94%), the thickness of the tongue of displacing water increases. This reduces the propagation velocity of fingers, causing a plateau in the mixing zone and front velocities.

The effect of flow rate on the RFW and film thickness is investigated. Figure 5.35 shows the RFW with dimensionless time in the 100% glycerol solutions. The time is made dimensionless with the convective time, L/U. L is the length of the Hele-Shaw cell and U is the injection velocity. The data shows that the RFW (or sweep efficiency) reduces with the increase in injection rate of water in 100% glycerol solution. Similar observations are made in 97% and 95.5% glycerol solutions (Figures 5.36 and 5.37). However at lower viscosity ratios the flow rate does not significantly affect the relative finger width, as observed in Figures 5.38, 5.39 and 5.40 for 94%, 89% and 88.2%

glycerol solutions respectively. These observations indicate the relative finger width is reduced with increase in flow rate at higher viscosity ratios.

Figure 5.41 shows the film thickness of the 100% glycerol solutions as a function of dimensionless time at different injection rates of water. The plot shows that the film thickness is considerably reduced by an increase in the injection rate. Similar trend is observed in 97% and 95.5% glycerol solutions (Figures 5.42 and 5.43 respectively). At lower viscosity ratios, the effect of injection rate on the film thickness is not as pronounced. Figure 5.44, 5.45 and 5.46 show the film thickness at different times for different injection rates in 84%, 89% and 88.2% glycerol solutions. The film thickness is observed to be constant with time and does not change with injection rate at lower viscosity ratios.

5.5 Implications of Findings for Design of Fracture Treatments

The growth of viscous fingers and mixing zones are an integral part of design considerations for hydraulic fracturing treatments in which viscous fingers are used to carry proppant into the fracture. In reverse-hybrid fracture treatments (Liu et al. 2007), the fracture is created with a high viscosity gel-based fluid which is followed by proppant-laden low viscosity fluid. The viscous fingers formed by the low viscosity fluid carry the proppant deep into the fracture. Chapter 7 introduces a new method of proppant injection, referred to as alternate-slug fracturing, in which alternate slugs of high

viscosity and low viscosity fluids are injected into the fracture. A schematic of alternate-slug treatments is shown in Figure 5.2.

The design of these two types of fracture treatments requires us to specify the size of the viscous and non-viscous slugs. This design parameter can be determined through an accurate estimate of the velocities of viscous fingers and mixing zones. The universal relationship of the dimensionless mixing zone velocity and relative front velocity with viscosity ratio presented in Figure 5.21 and Figure 5.28 respectively, can be used in predict the mixing between these two fluids. The pumping rates and slug sizes can be determined to ensure that the two fluids do not mix completely inside the fracture. The finger velocities determine the position of viscous fingers in the direction of fracture growth. If the proppant is pumped in the less viscous fluid, the proppant distribution can be estimated from the position of viscous fingers.

For example, for typical fracture parameters shown in Table 5.3 and a pumping rate of 40bbl/min with fluid efficiency of 50%, the injection velocity in each wing of the fracture is 0.29m/s. The injection velocity is calculated by dividing the injection rate by the cross section area of fracture. For designing a reverse-hybrid fracture job, let us assume that fracture is created with a polymer pad of viscosity 500cP (at the shear rate imposed by the flow inside the fracture) which is followed by water of viscosity 1cP in the proppant stage. From Figure 5.28, the relative front velocity at a viscosity ratio of 500 is 3. The water front forming viscous fingers in the polymer will move at 0.87m/s. To

ensure the water fingertip just reaches the polymer front at the fracture tip at the end of the fracture job, the velocities suggest that the length of the polymer slug should be two times the length of water slug. Also, from Figure 5.21 the normalized mixing zone velocity is 2.5. The mixing zone will grow at a rate of 0.725m/s. For a half-fracture length of 152.4m (500ft), at the end of the fracture job mixing zone will span from x=25.4m to x=152.4m, where x is the distance from the wellbore. This is shown in the schematic in Figure 5.47. Assuming that proppant moves in the horizontal direction at the velocity of water and the polymer layers between fingers prevent proppant from settling, the proppant will be distributed in the fingers from x=25.4m to x=152.4m. From x=0 to x=25.4m, a proppant bed will form due to the high settling velocity of proppant in water. Similar observations are shown in the experiments in Chapter 7.

5.6 CONCLUSIONS

This chapter presented an experimental study to measure the mixing zone and finger velocities in rectilinear flow in a Hele-Shaw cell. Glycerol solutions with viscosities covering the entire range from 1 to 1225 cP are displaced with water at different flow rates. The main conclusions from this study are as follows:

- A systematic change in the viscous fingering patterns is observed with change in displaced fluid viscosity. At low viscosity ratios, the shielding effect is less pronounced and multiple fingers grow parallel to each other. At higher viscosity ratios, mechanisms including finger merging, coalescence and shielding are prominent.

- Tip splitting is observed to be more pronounced at higher viscosity ratios. At low viscosity ratios only one instance of tip splitting was observed. At moderate (100-300) and higher (300-1225) viscosity ratios, all the dominant fingers exhibit uneven tip splitting. At moderate viscosity ratios the finger are observed to split into two fingers whereas at higher viscosity ratios tip splitting into three or four fingers is also observed.

- All the experiments are performed at high Peclet numbers and a linear growth in the mixing zone length is observed in all the experiments. The mixing zone velocity is first observed to increase with the viscosity ratio and then reaches a constant value at high viscosity ratios (above 343). This observation is not captured by the Koval's model, which was derived using experimental data for viscosity ratios below 150.

- Plots of dimensionless mixing zone velocity versus viscosity ratio at different flow rates converge into a single curve indicating a universal relationship between these quantities.

- The fingertip velocities also increase with viscosity ratio up to a viscosity ratio of 343 above which the velocities plateau. This has not been reported in earlier studies.

- The relative finger width is observed to decrease with increase in viscosity ratio, over the entire range of viscosity ratios. The data shows a reduction in sweep efficiency with increase in viscosity ratios.

- The average thickness of the film of displaced fluid left on the walls of the cell is observed to be constant for viscosity ratios up to 343. At higher viscosity ratios, the average film thickness decreases with the viscosity ratio. This reduction in film thickness explains the observed plateau in the mixing zone and front velocities. At the viscosity ratios above 343 (corresponding to glycerol concentration of 94%), the thickness of the tongue of displacing water increases. This reduces the propagation velocity of fingers, causing a plateau in the mixing zone and front velocities.

Table 5.1: Weight percentage and viscosity of glycerol solutions.

Glycerol % by weight	Viscosity (cP)
69	19.5
79	50
83	79.5
88.2	153
89	177.5
94	343
95.5	463
97	665
100	1225

Table 5.2: Mutual diffusion coefficients and Peclet numbers for injection of water into glycerol solutions at three injection rates.

Glycerol Weight %	$D \times 10^9$ (m^2/s)	Peclet number (Pe) at water injection rate of		
		12.35 ml/min	4.69 ml/min	1.28 ml/min
79	0.153	26953	10234	2792
83	0.124	33127	12578	3431
88.2	0.089	46417	17624	4808
89	0.083	49389	18753	5116
94	0.051	81063	30779	8397
95.5	0.041	99747	37873	10332
97	0.032	129155	49039	13379
100	0.013	306837	116502	31784

Table 5.3: Fracture parameters, flow rate and fluid viscosities used for example calculation of design of reverse-hybrid treatment.

Half Length (m)	152.4
Height (m)	45.72
Width (mm)	2
Flow Rate (m^3/s)	0.10598 (40 bbl/min)
Injection Velocity (m/s)	0.29
Viscosity of Polymer Solution at the Shear Rate Imposed by Flow in the Fracture (cP)	500
Viscosity of Water (cP)	1

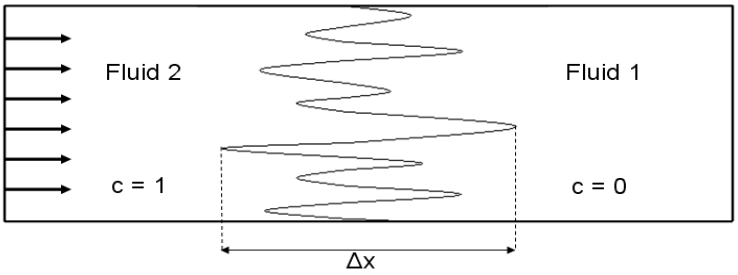

Figure 5.1: Schematic of the mixing zone. A more viscous Fluid 1 is displaced by less viscous Fluid 2 leading to the development of fingers.

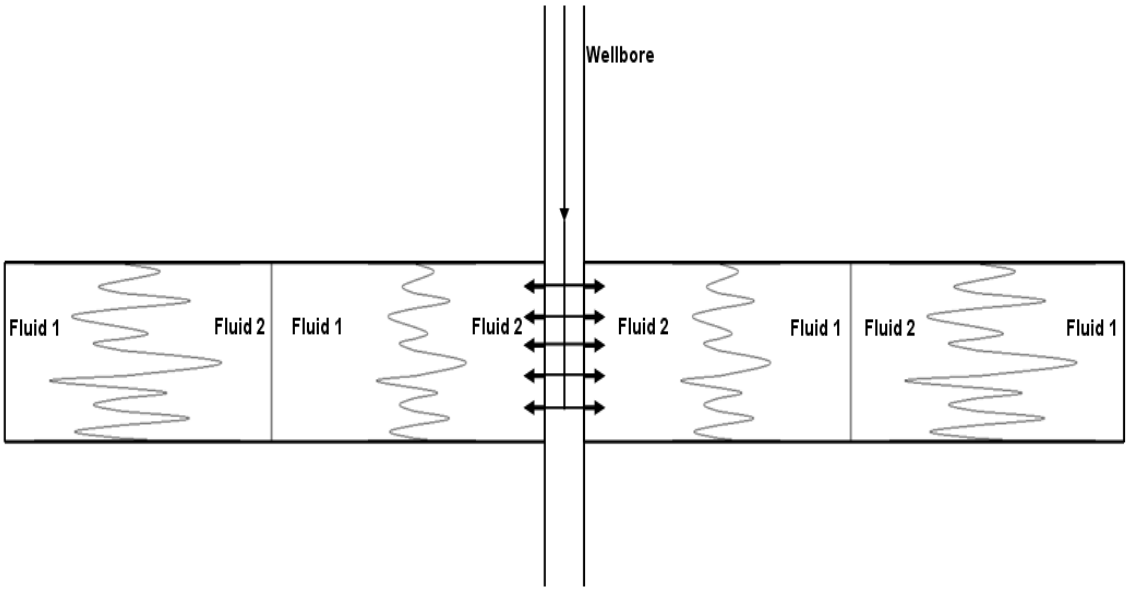

Figure 5.2: Schematic showing the injection of alternate slugs of Fluid 1 (more viscous) and Fluid 2 (less viscous) in rectilinear flow. The displacement of Fluid 2 by Fluid 1 is stable (piston-like).

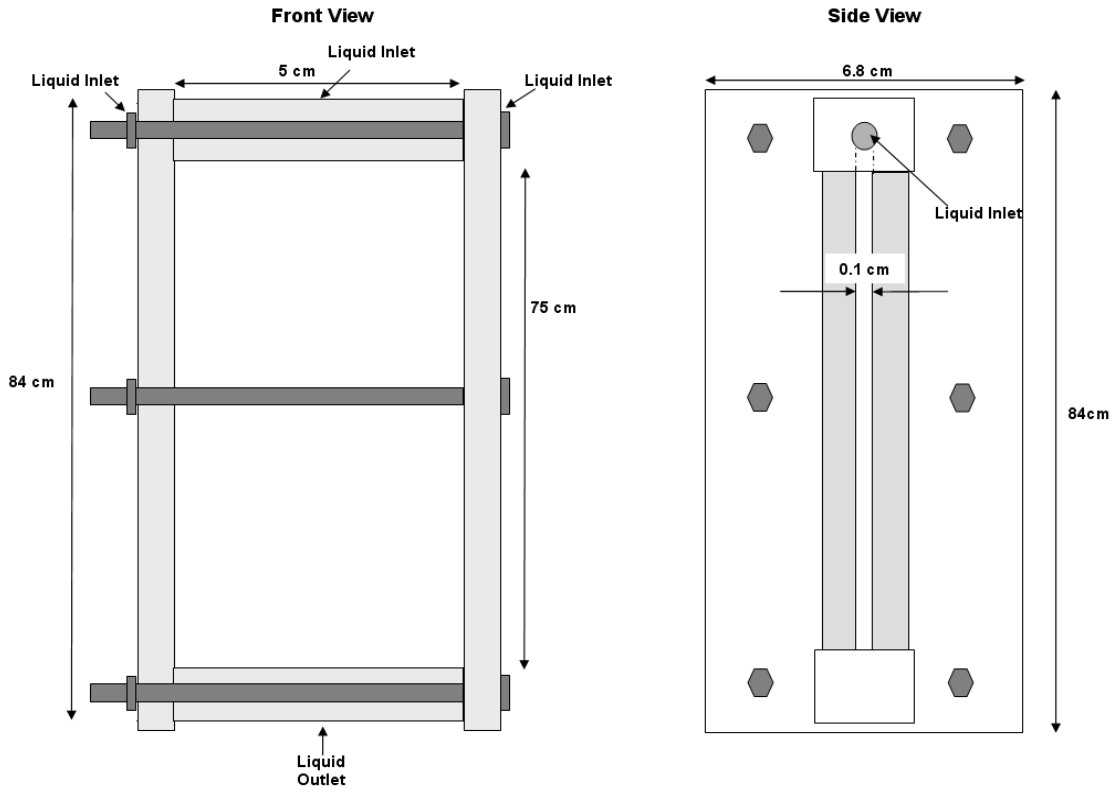

Figure 5.3: Schematic of the Hele-Shaw cell (not to scale).

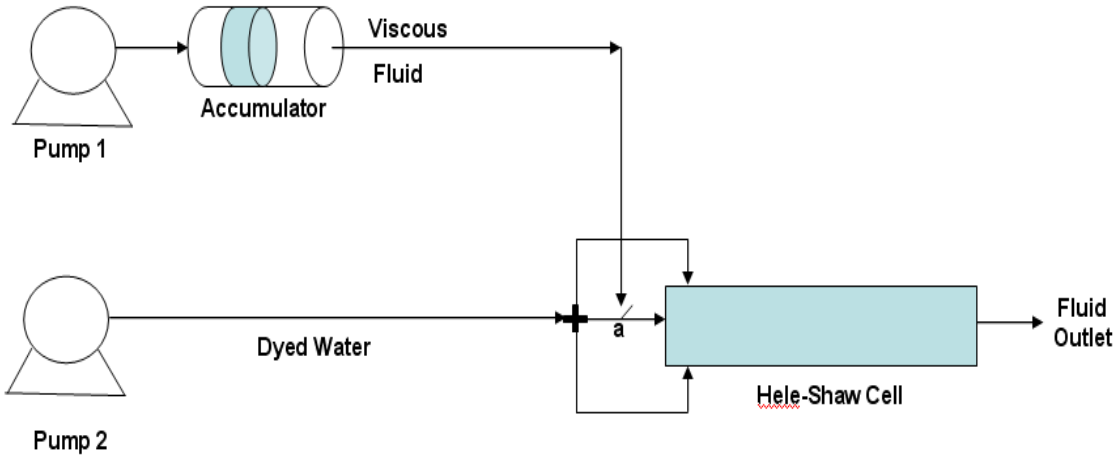

Figure 5.4: Schematic of the experimental setup.

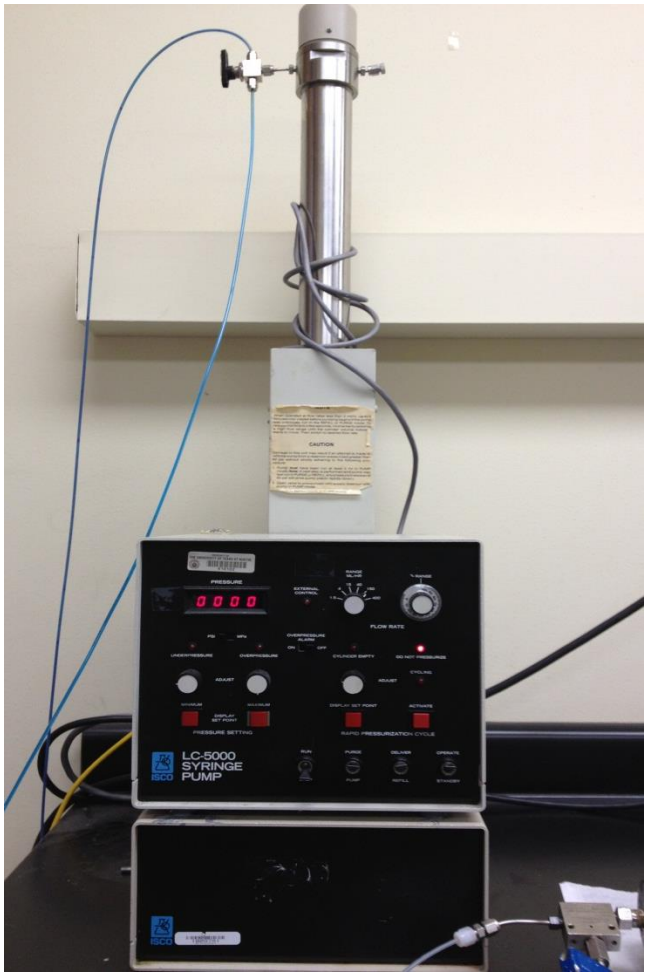

Figure 5.5: Isco syringe pump used for the viscous fingering experiments.

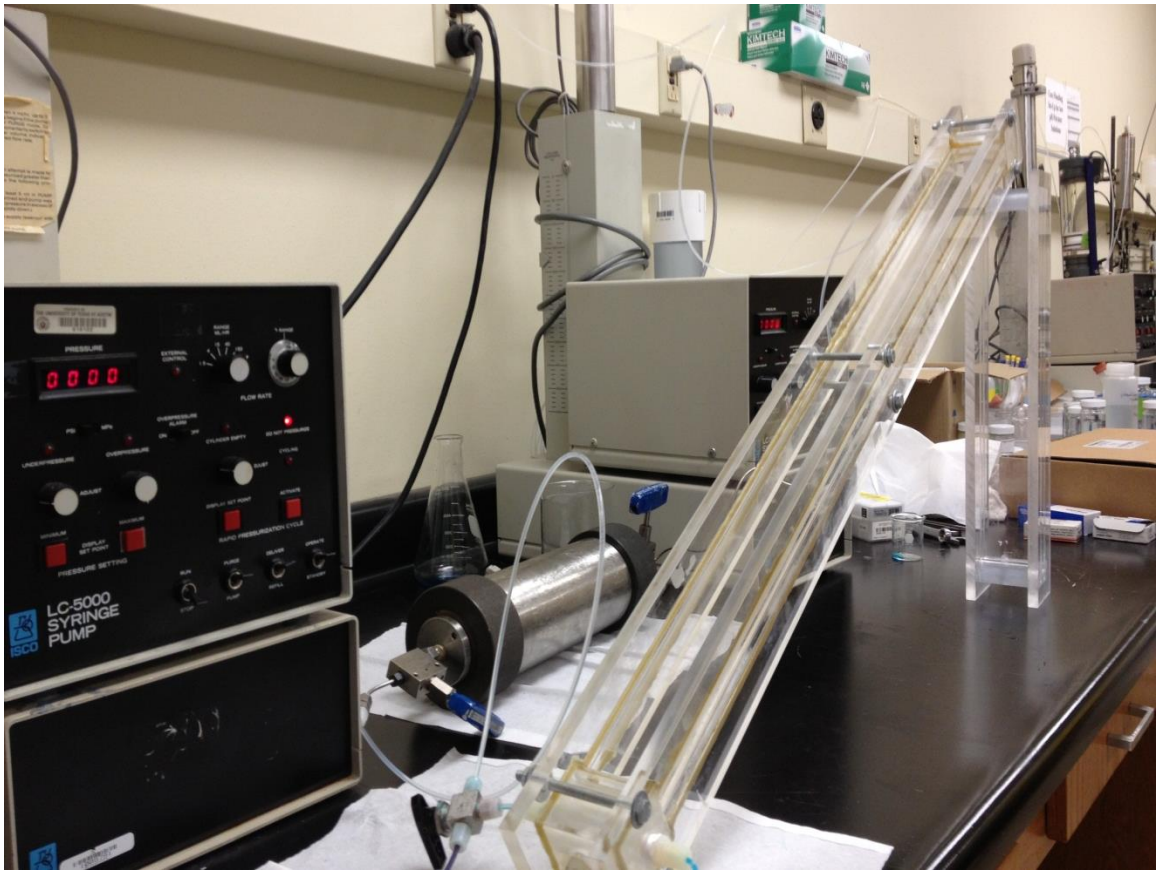

Figure 5.6: Snapshot showing the Hele-Shaw cell kept in an inclined position. The pump pushes the glycerol solution through the accumulator against gravity.

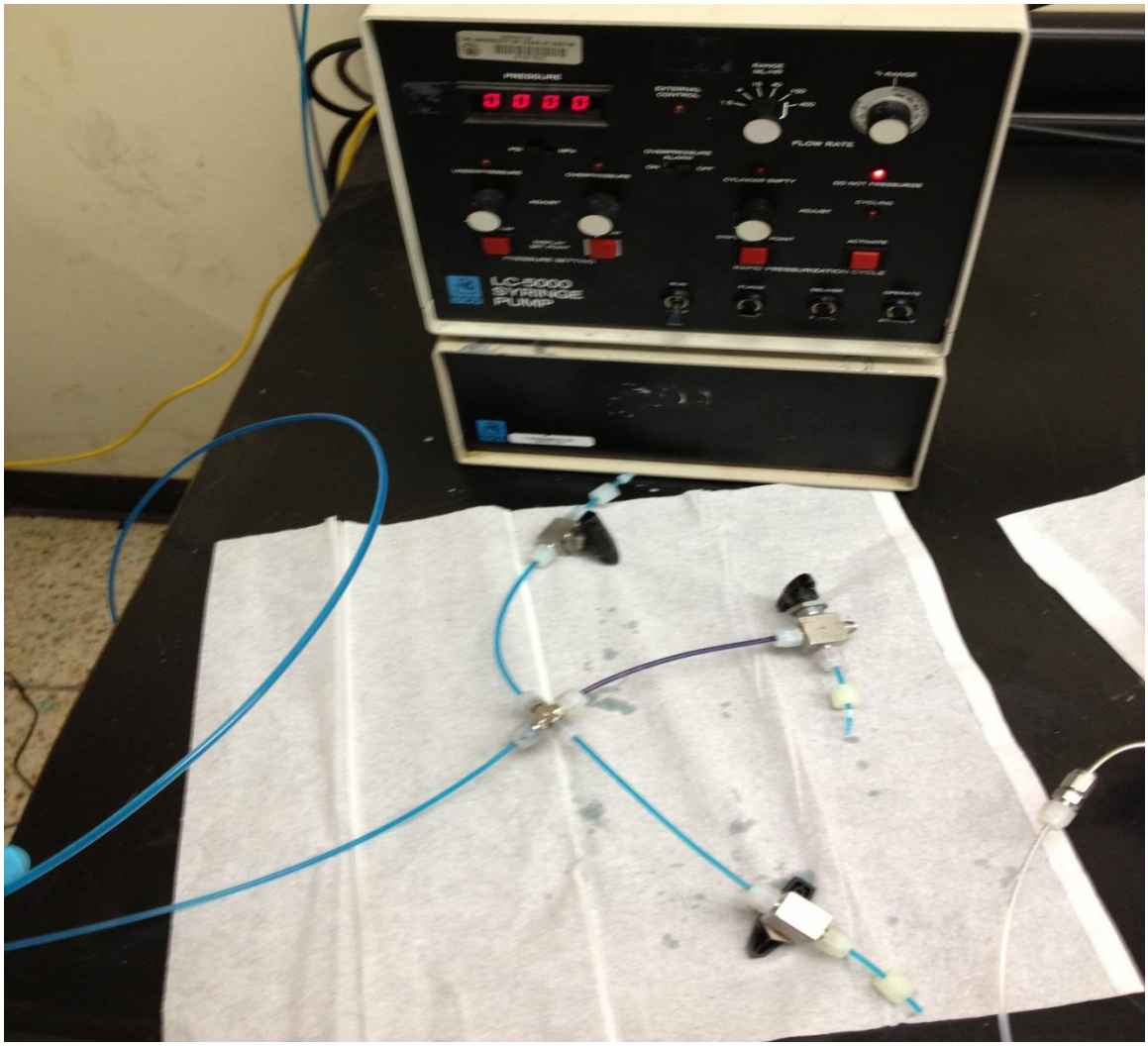

Figure 5.7: Three-pronged manifold showing the inlet from the pump divided into three streams for inlet to the Hele-Shaw cell.

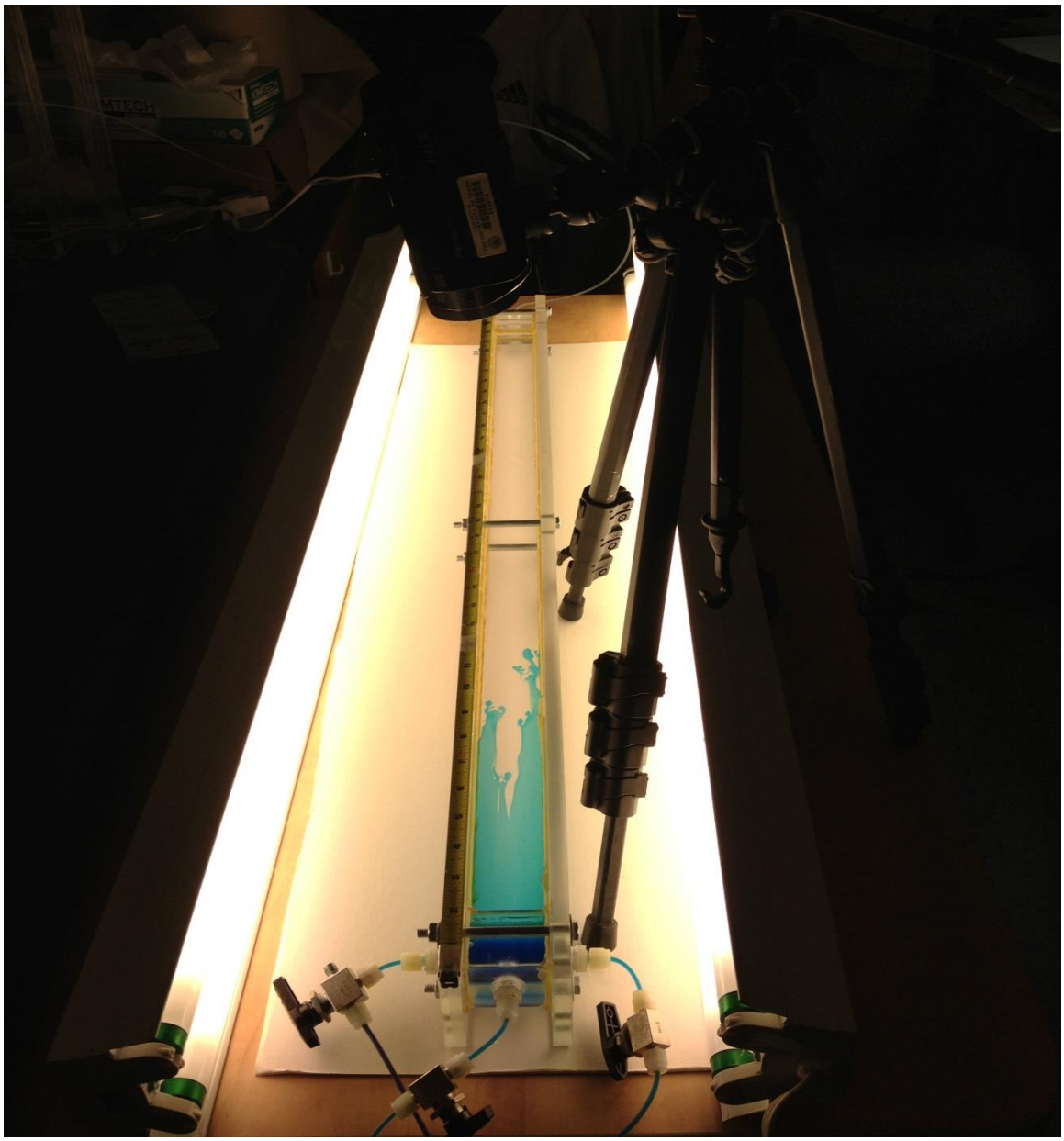

Figure 5.8: Snapshot showing the injection of dyed water into the Hele-Shaw cell from the three inlets. The experiment is recorded using a pair of tripods.

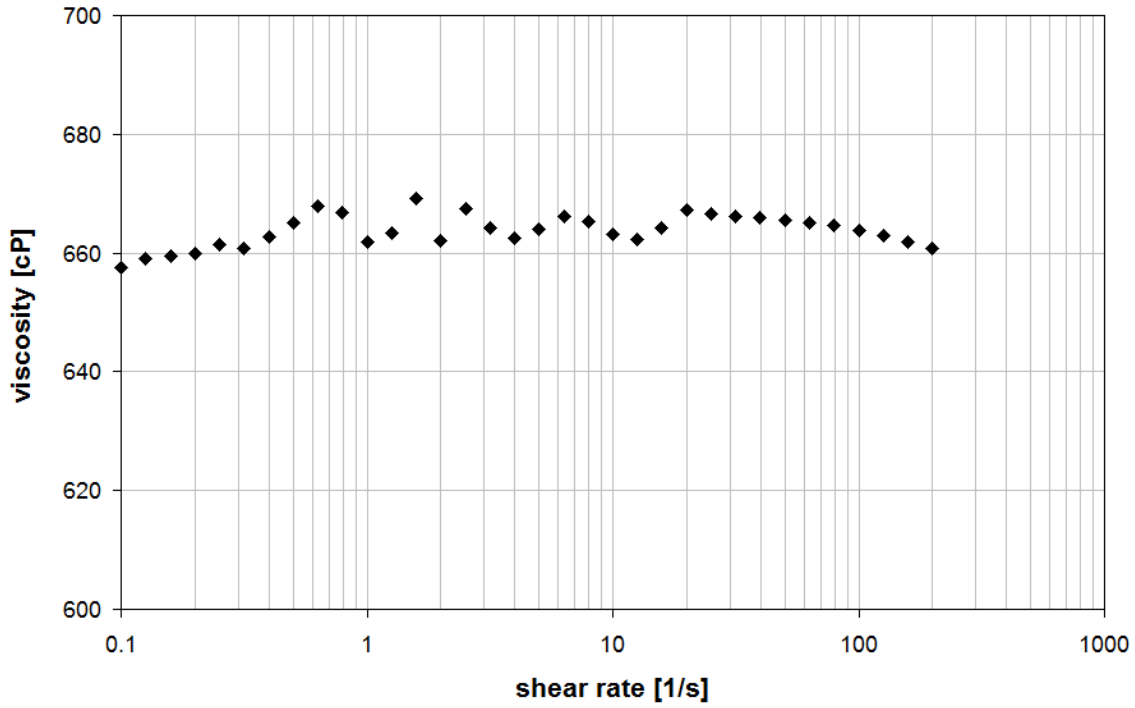

Figure 5.9: Steady shear-viscosity measurement for 97% Glycerol solution.

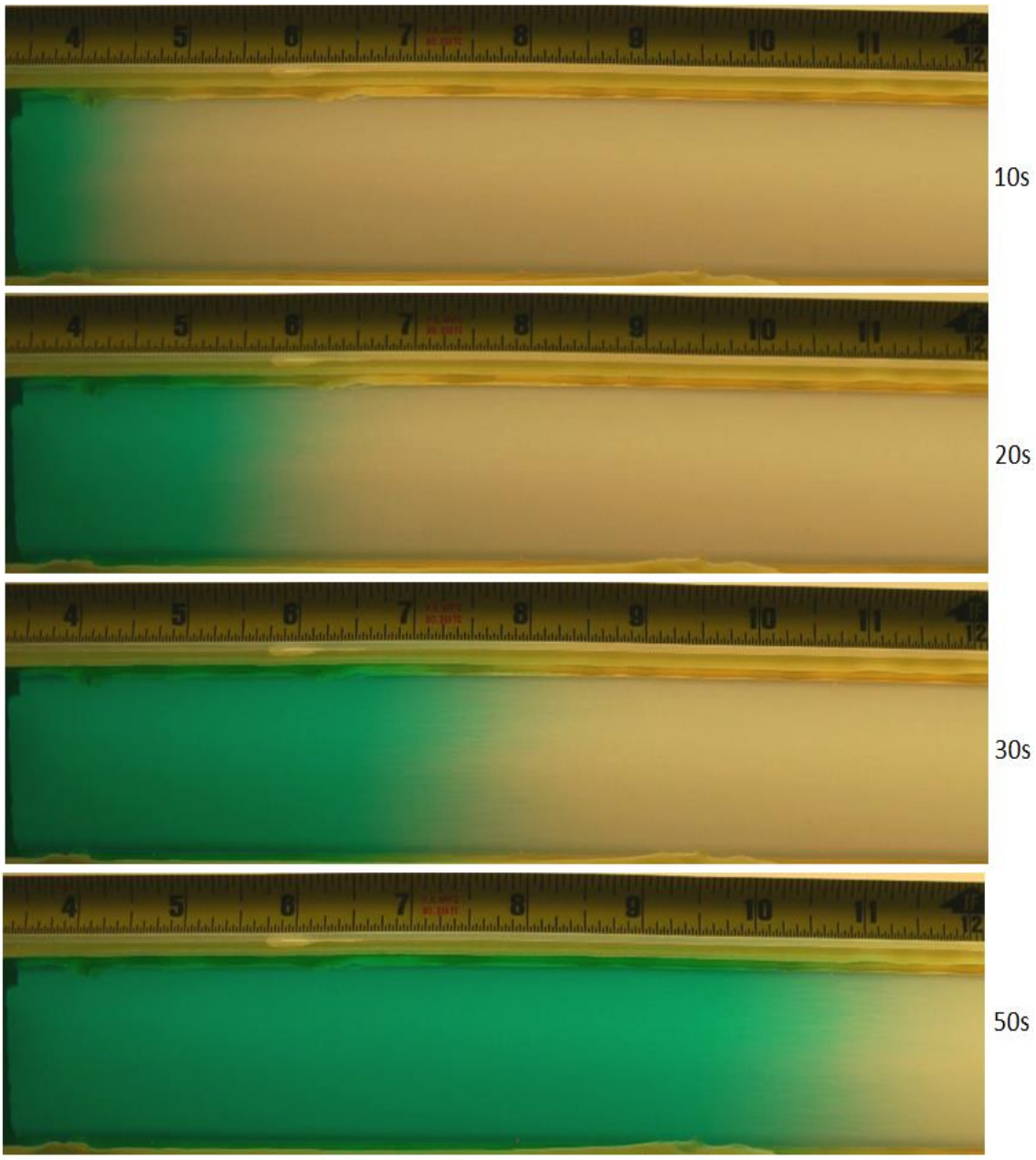

Figure 5.10: Sequential position of the interface between clear water and dyed water. Dyed water is injected into clear water at a rate of 12.35ml/min. (Viscosity Ratio, M = 1)

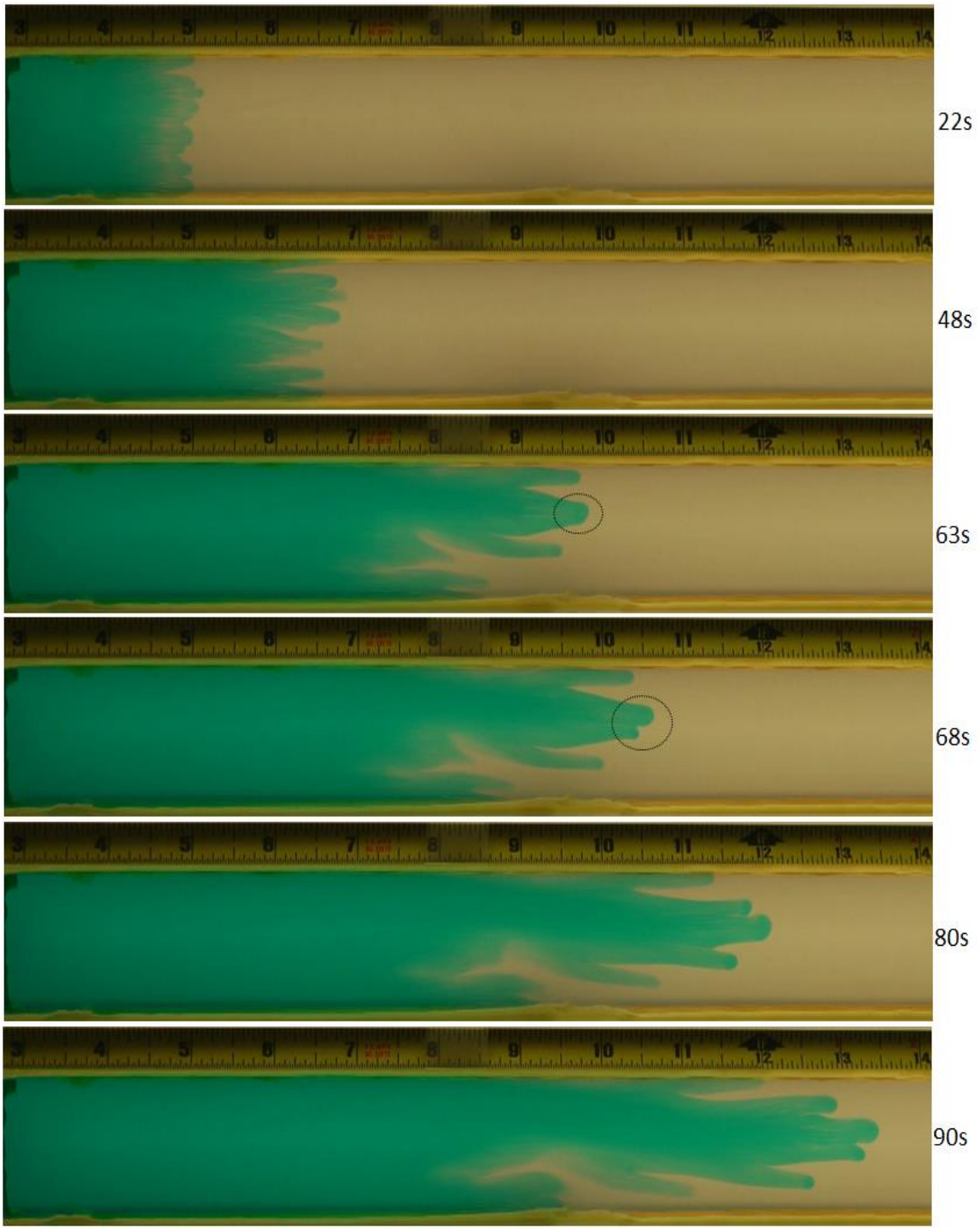

Figure 5.11: Sequential evolution of the interface between water and 79% glycerol solution. Dyed water is injected into glycerol solution at a rate of 4.69ml/min. (Viscosity Ratio, M = 50)

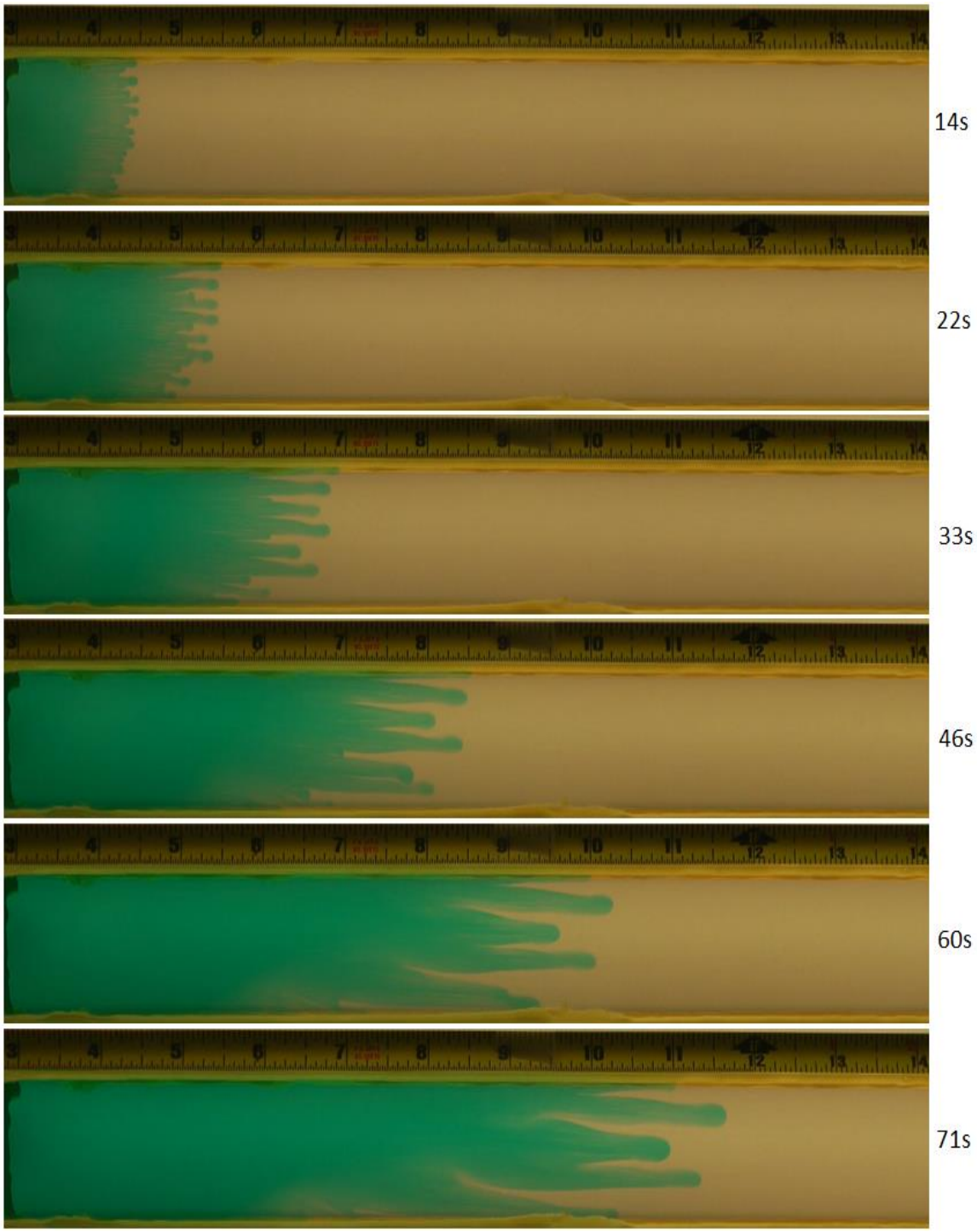

Figure 5.12: Sequential evolution of the interface between water and 83% glycerol solution. Dyed water is injected into glycerol solution at a rate of 4.69ml/min. (Viscosity Ratio, M = 79.5)

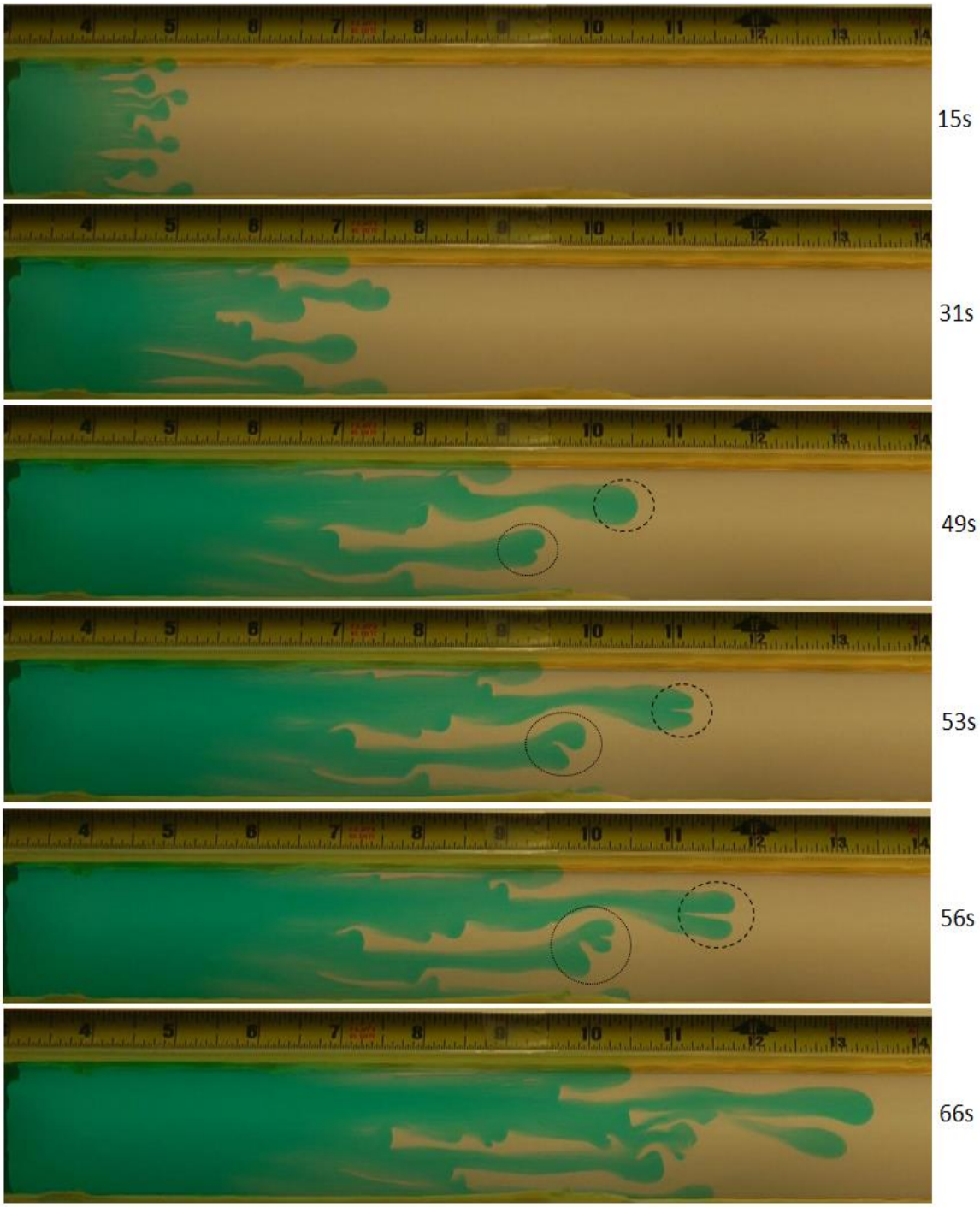

Figure 5.13: Sequential evolution of the interface between water and 89% glycerol solution. Dyed water is injected into glycerol solution at a rate of 4.69ml/min. (Viscosity Ratio, M = 177.5)

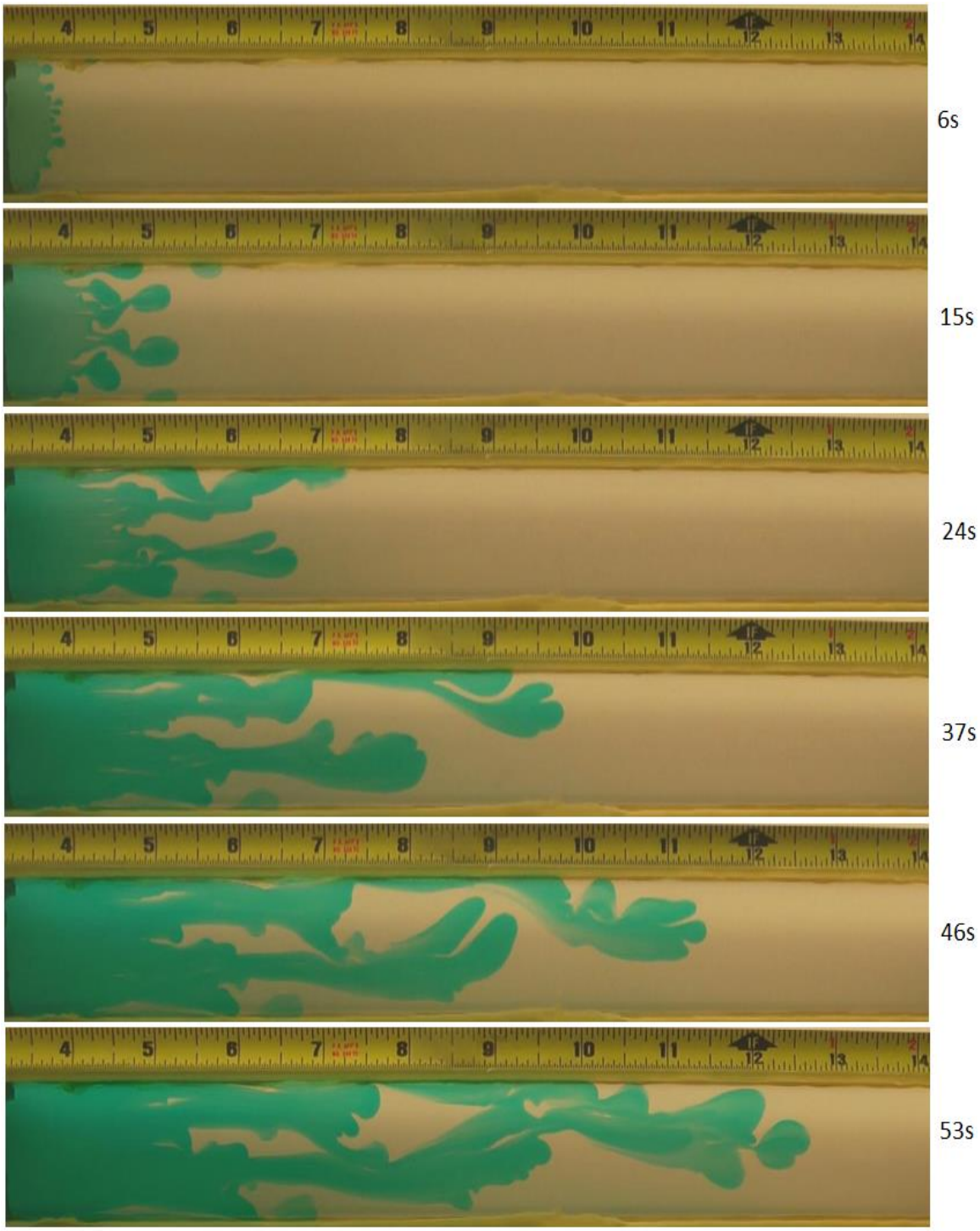

Figure 5.14: Sequential evolution of the interface between water and 95.5% glycerol solution. Dyed water is injected into glycerol solution at a rate of 4.69ml/min. (Viscosity Ratio, M = 463)

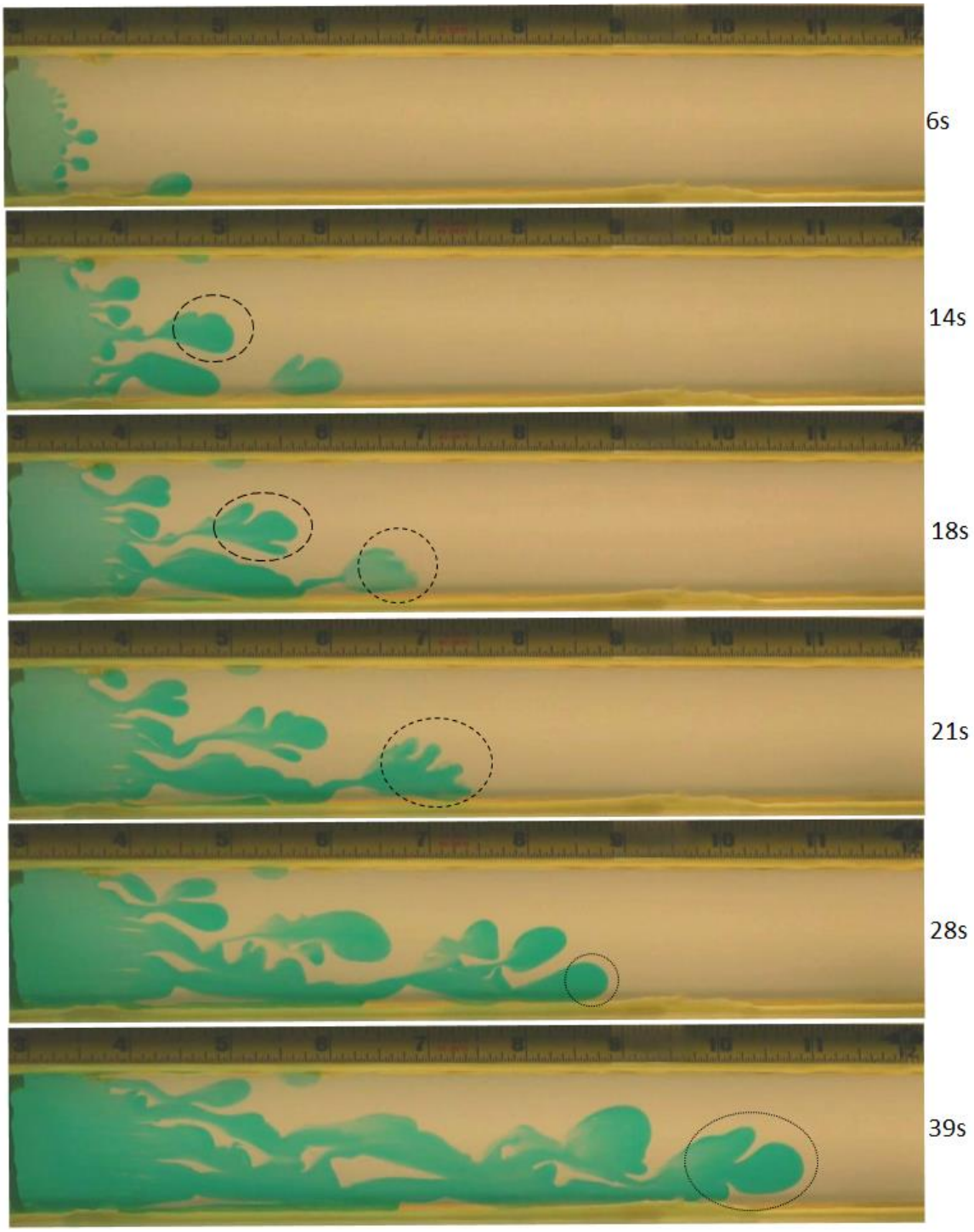

Figure 5.15: Sequential evolution of the interface between water and 97% glycerol solution. Dyed water is injected into glycerol solution at a rate of 4.69ml/min. (Viscosity Ratio, M = 665)

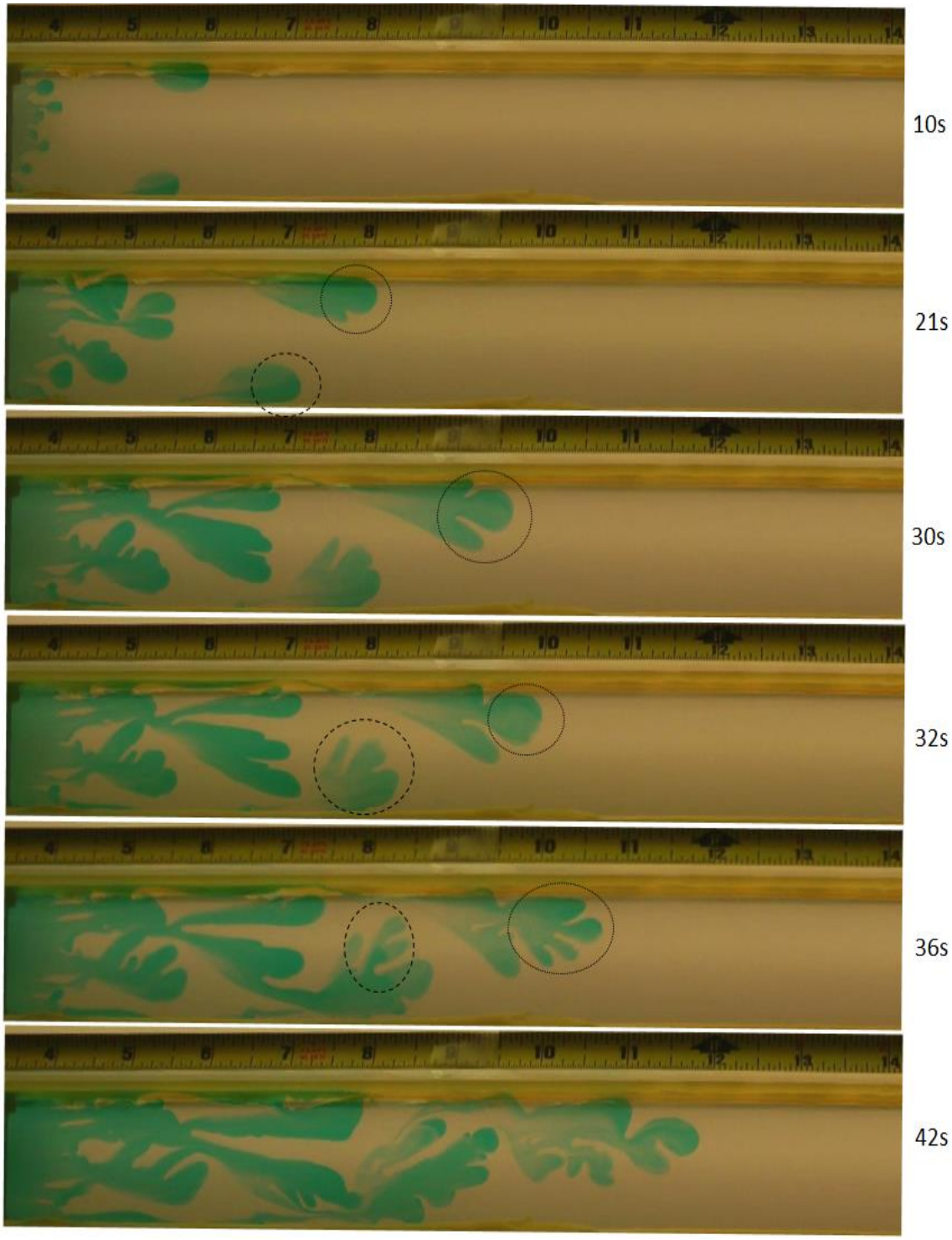

Figure 5.16: Sequential evolution of the interface between water and 100% glycerol. Dyed water is injected into glycerin at a rate of 4.69ml/min. (Viscosity Ratio, M = 1225)

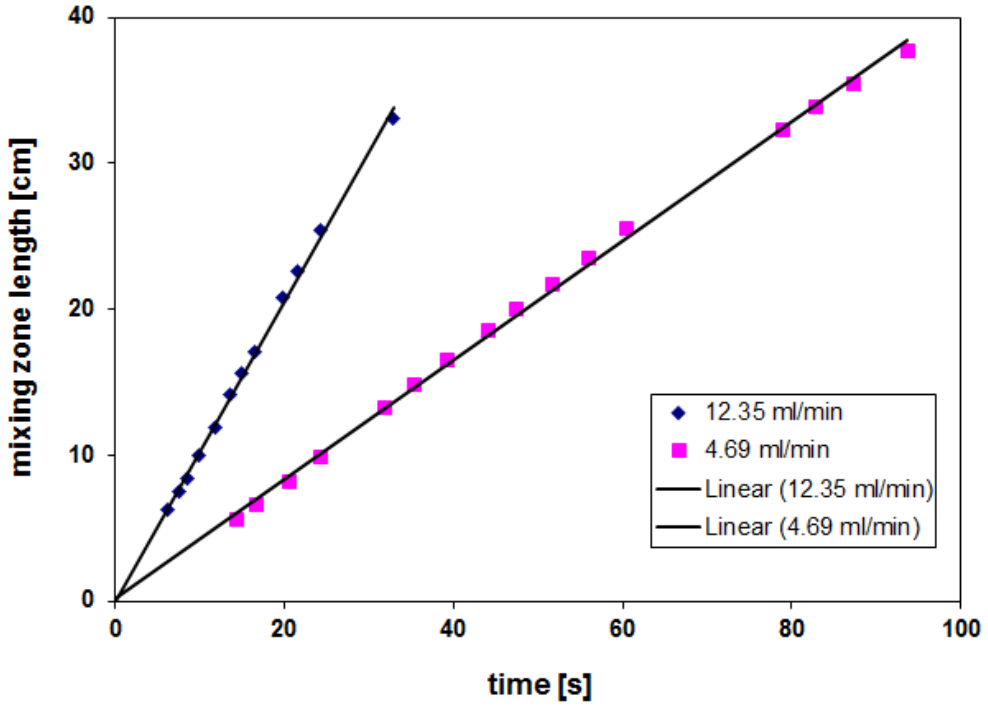

Figure 5.17: Mixing zone length as a function of time for displacement of 97% Glycerol solution with water at 12.35 and 4.69 ml/min. (Viscosity Ratio, M = 665)

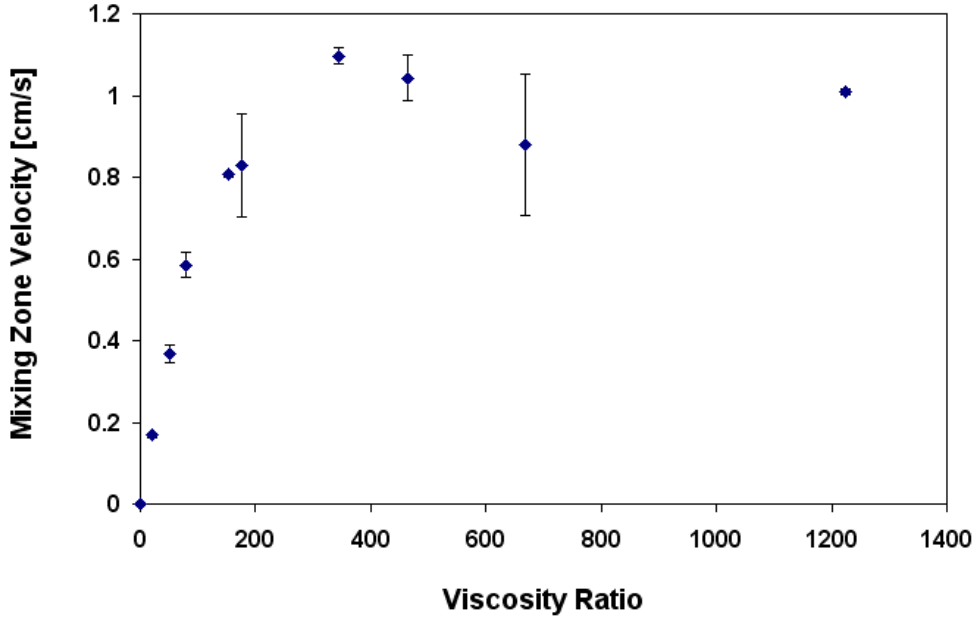

Figure 5.18: Mixing zone velocities at different viscosity ratios at an injection rate of 12.35ml/min.

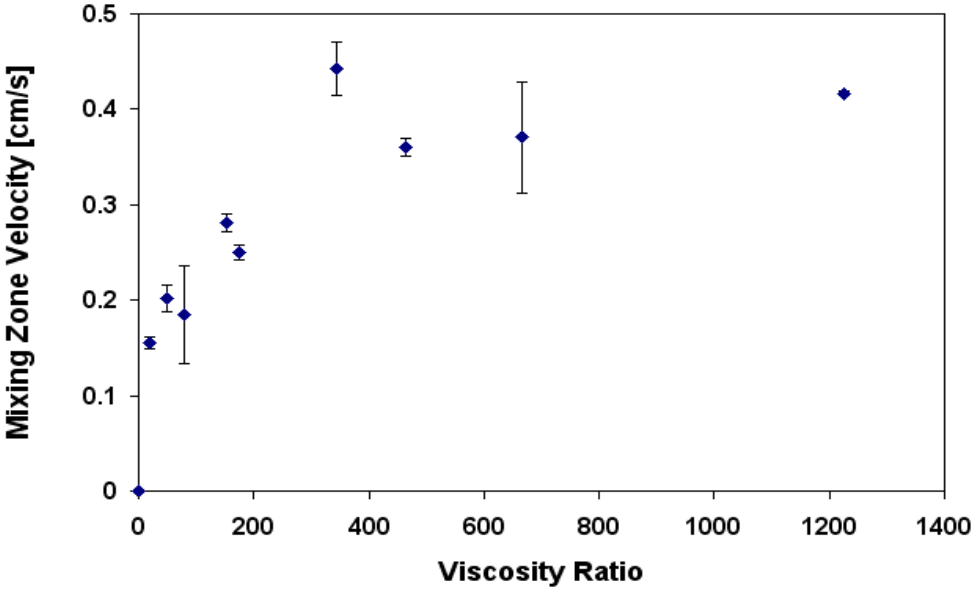

Figure 5.19: Mixing zone velocities at different viscosity ratios at an injection rate of 4.69ml/min.

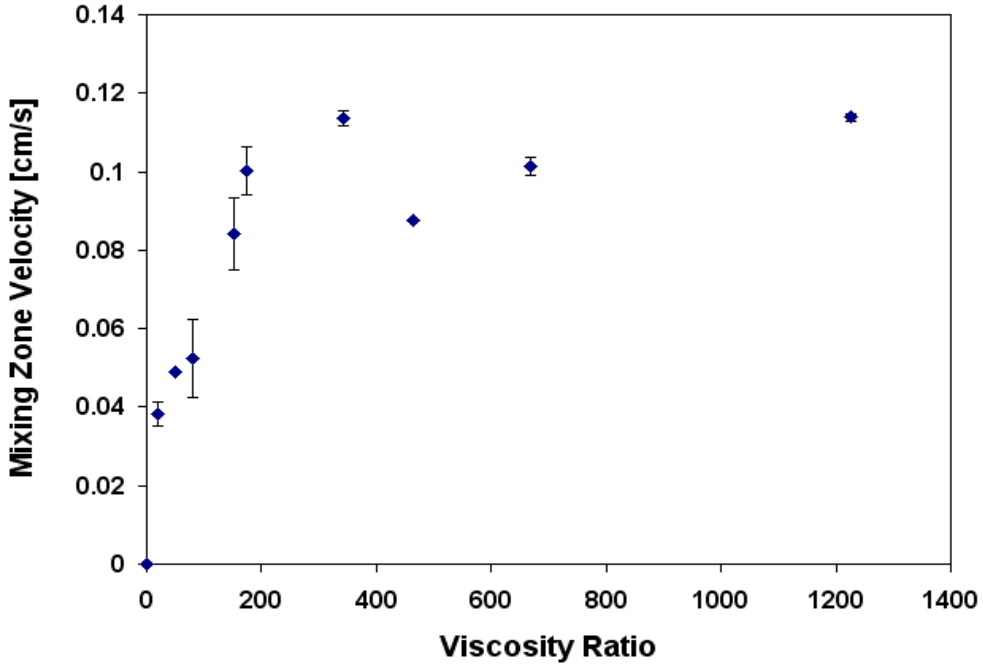

Figure 5.20: Mixing zone velocities at different viscosity ratios at an injection rate of 1.28ml/min.

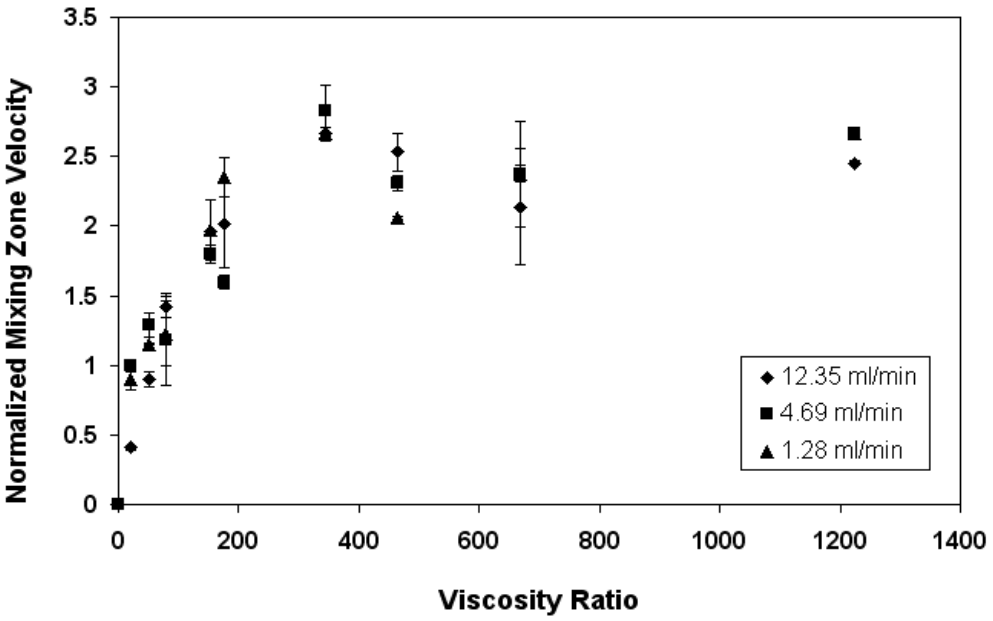

Figure 5.21: Normalized mixing zone velocities at the three injection rates for different viscosity ratios.

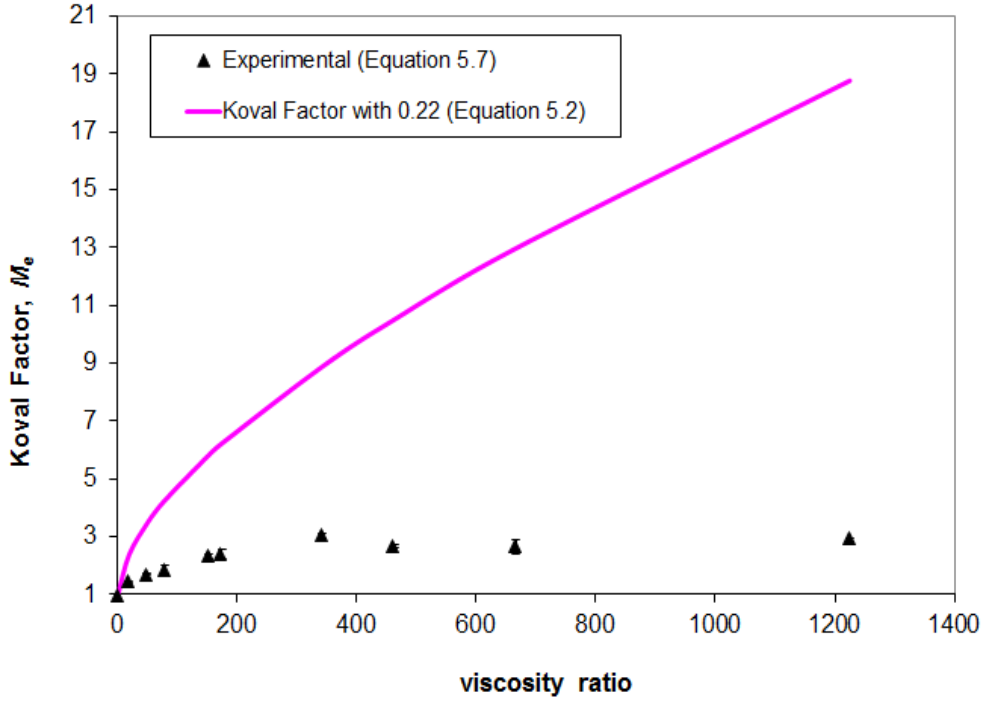

Figure 5.22: Comparison of the Koval factor from the experimental data (using Equation 5.7) and the empirical fit with 0.22 as the fitting constant (Equation 5.2).

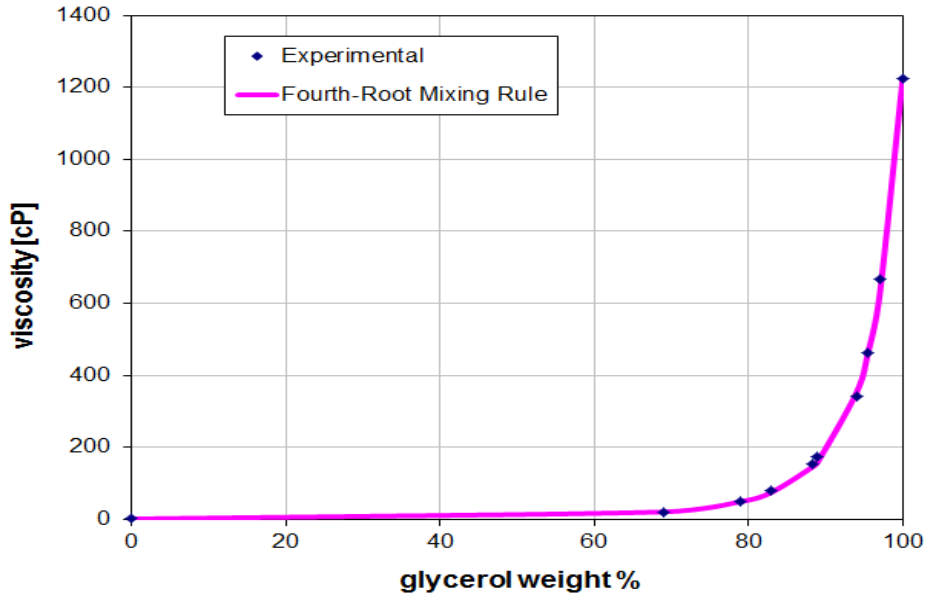

Figure 5.23: Viscosity of glycerol solutions at different concentrations. The fourth-root mixing rule (Equation 5.3) predicts the data well.

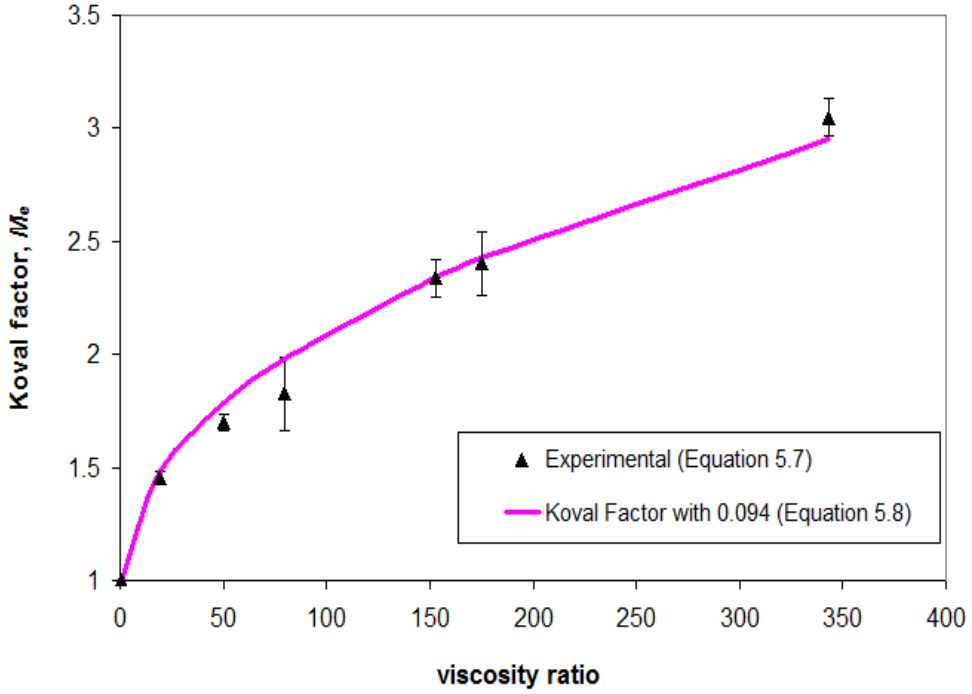

Figure 5.24: Comparison of the Koval factor from the experimental data (using Equation 5.7) with empirical fit with 0.094 as the fitting constant (Equation 5.8).

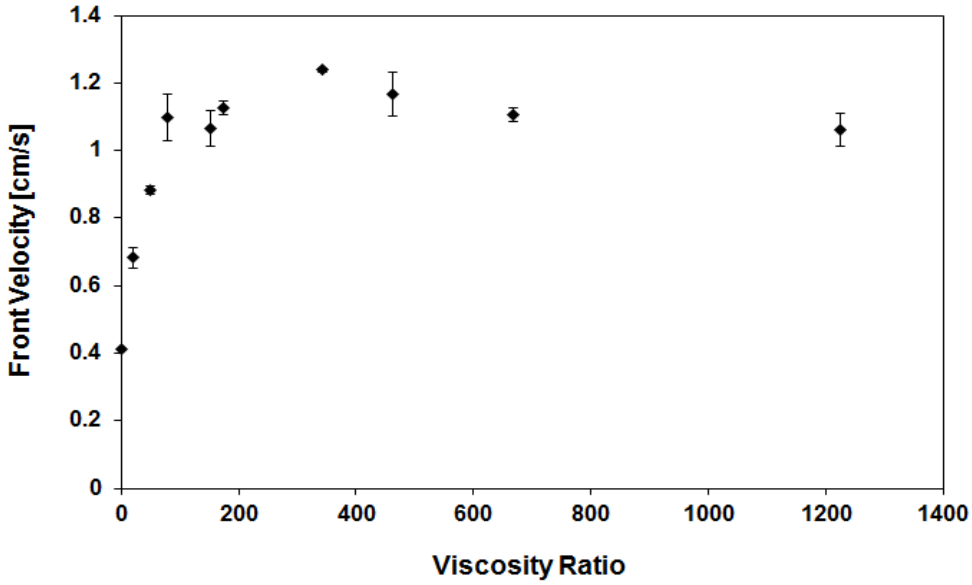

Figure 5.25: Fingertip velocities at different viscosity ratios at an injection rate of 12.34ml/min.

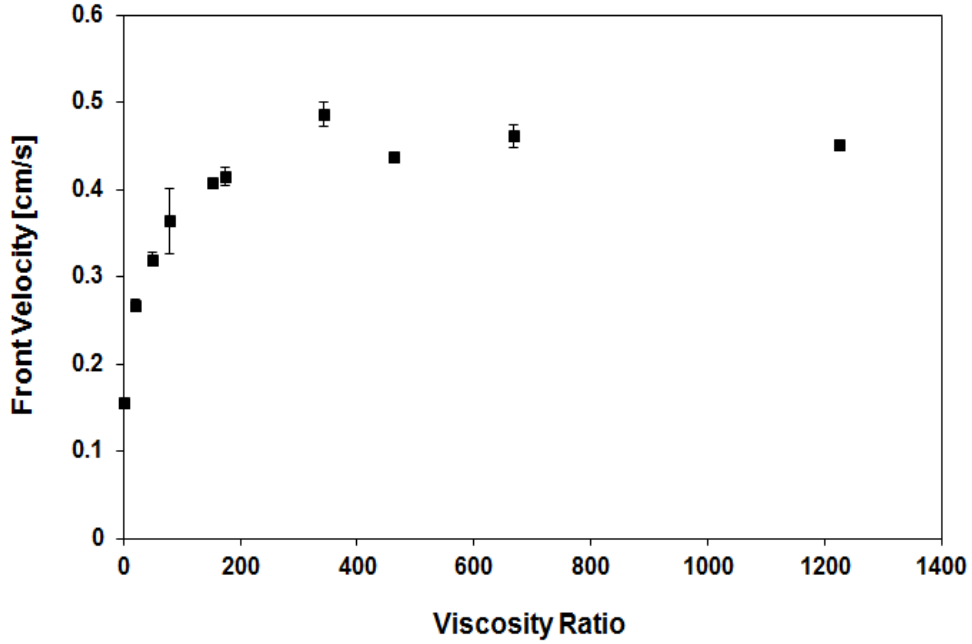

Figure 5.26: Fingertip velocities at different viscosity ratios at an injection rate of 4.69ml/min.

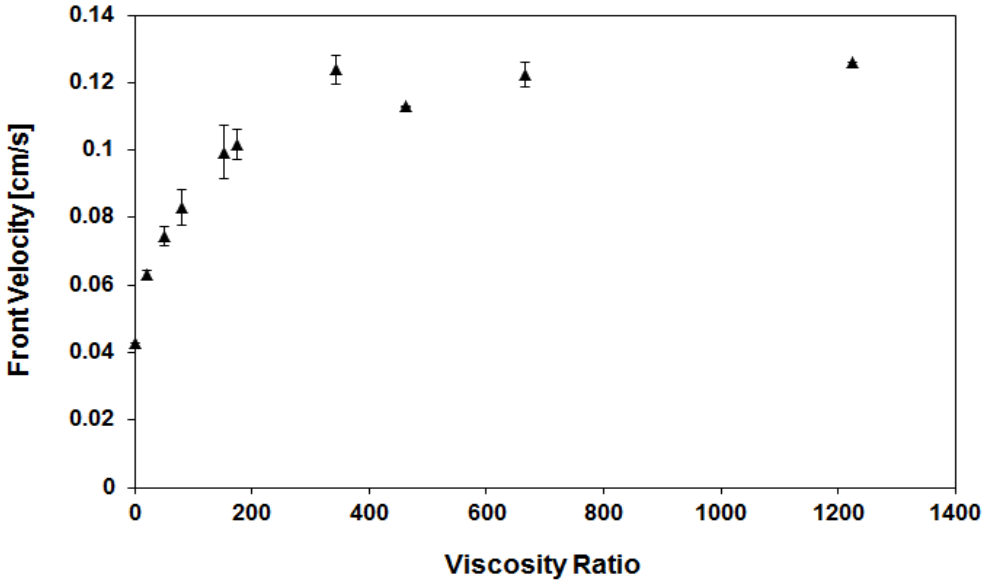

Figure 5.27: Fingertip velocities at different viscosity ratios at an injection rate of 1.28ml/min.

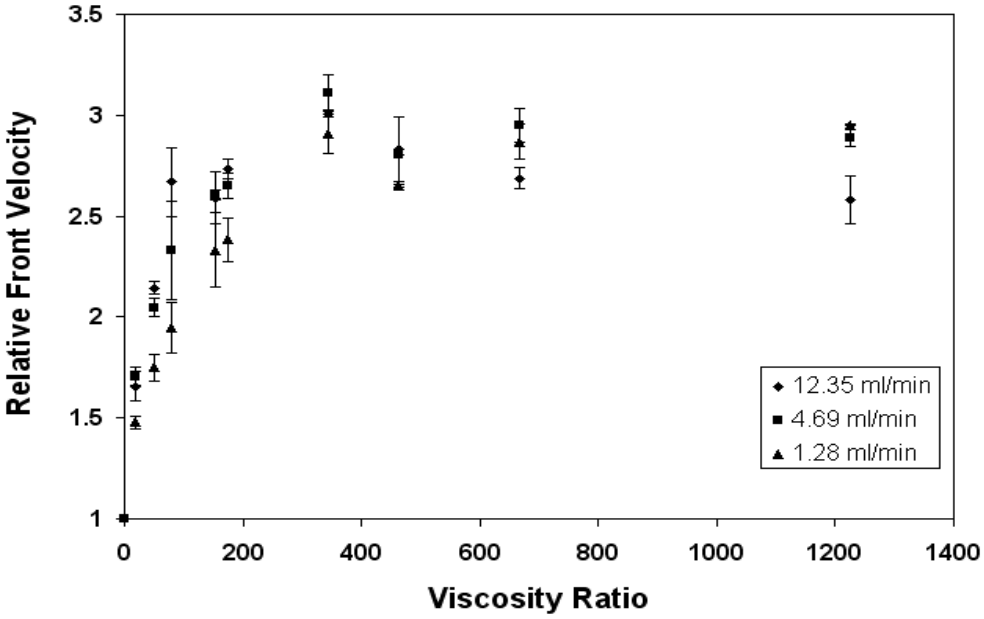

Figure 5.28: Relative front velocities in different viscosity glycerol solutions at three injection rates.

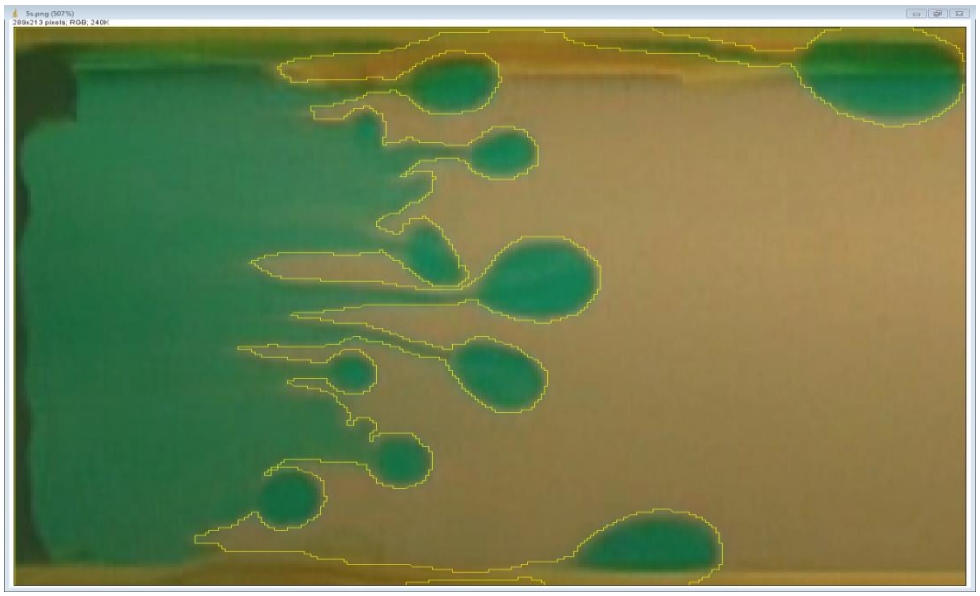

Figure 5.29: An illustration of the outlined interface between the injected dyed water and displaced glycerol solution. The area of the displacing water is calculated using ImageJ.

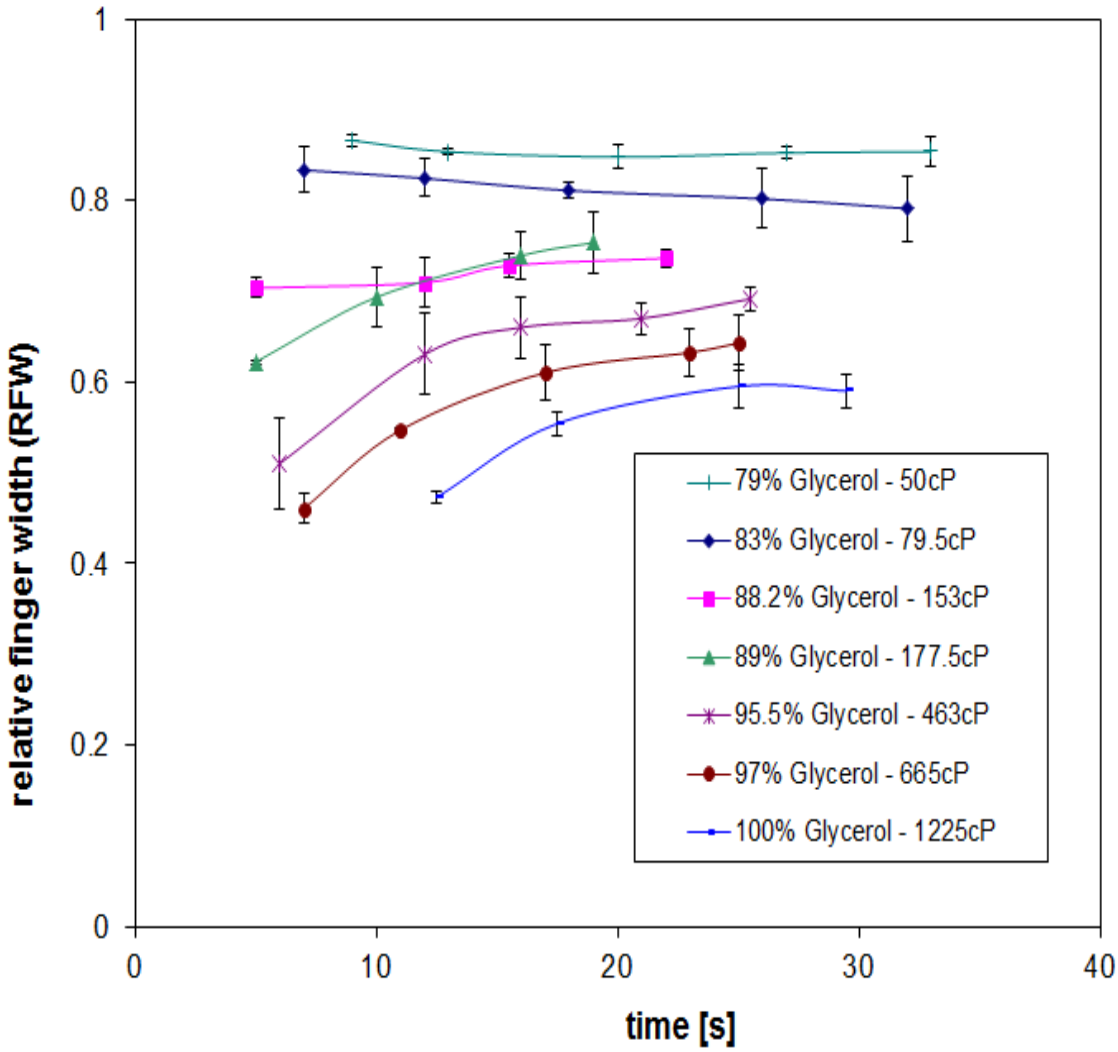

Figure 5.30: Relative finger width (RFW) as a function of time for injection of water at 12.35ml/min in different viscosity glycerol solutions.

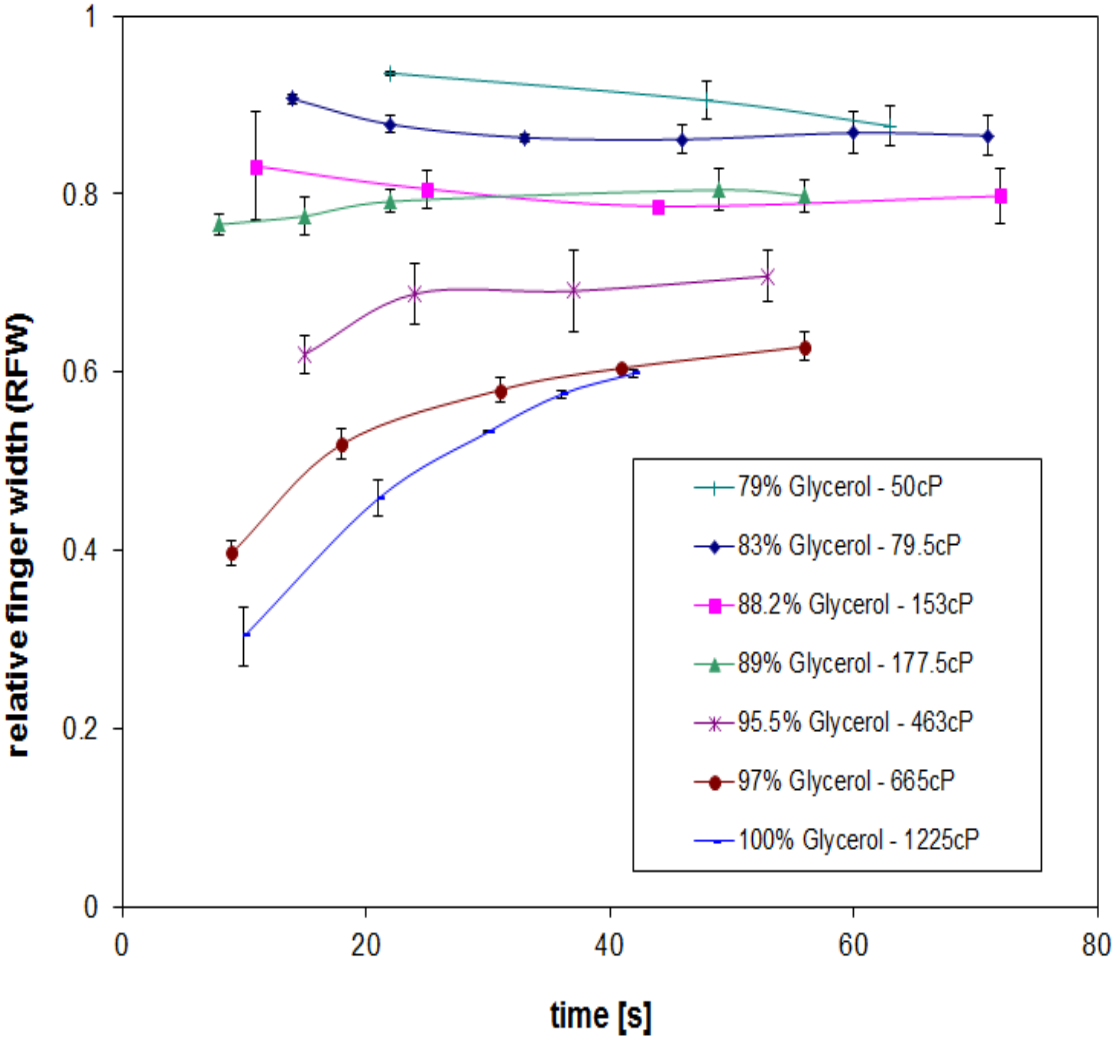

Figure 5.31: Relative finger width (RFW) as a function of time for injection of water at 4.69ml/min in different viscosity glycerol solutions.

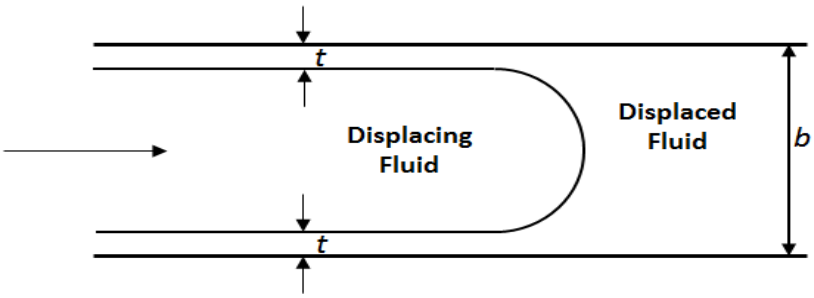

Figure 5.32: Schematic showing the symmetric tongue of the injected fluid. The thickness of the film of the displaced fluid on the walls is denoted by *t*.

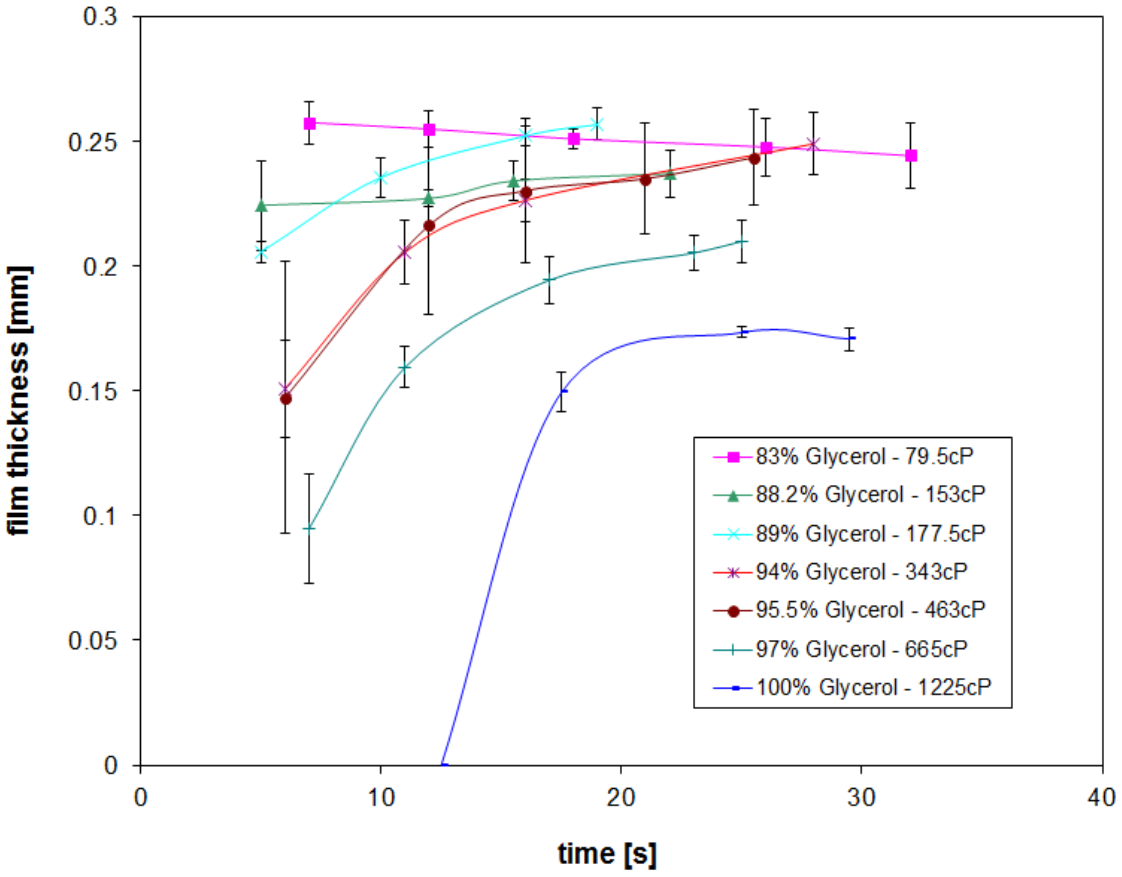

Figure 5.33: Thickness of the thin film of the displaced fluid (glycerol solutions) on the walls of Hele-Shaw cells as a function of time. The injection rate of water is 12.35ml/min.

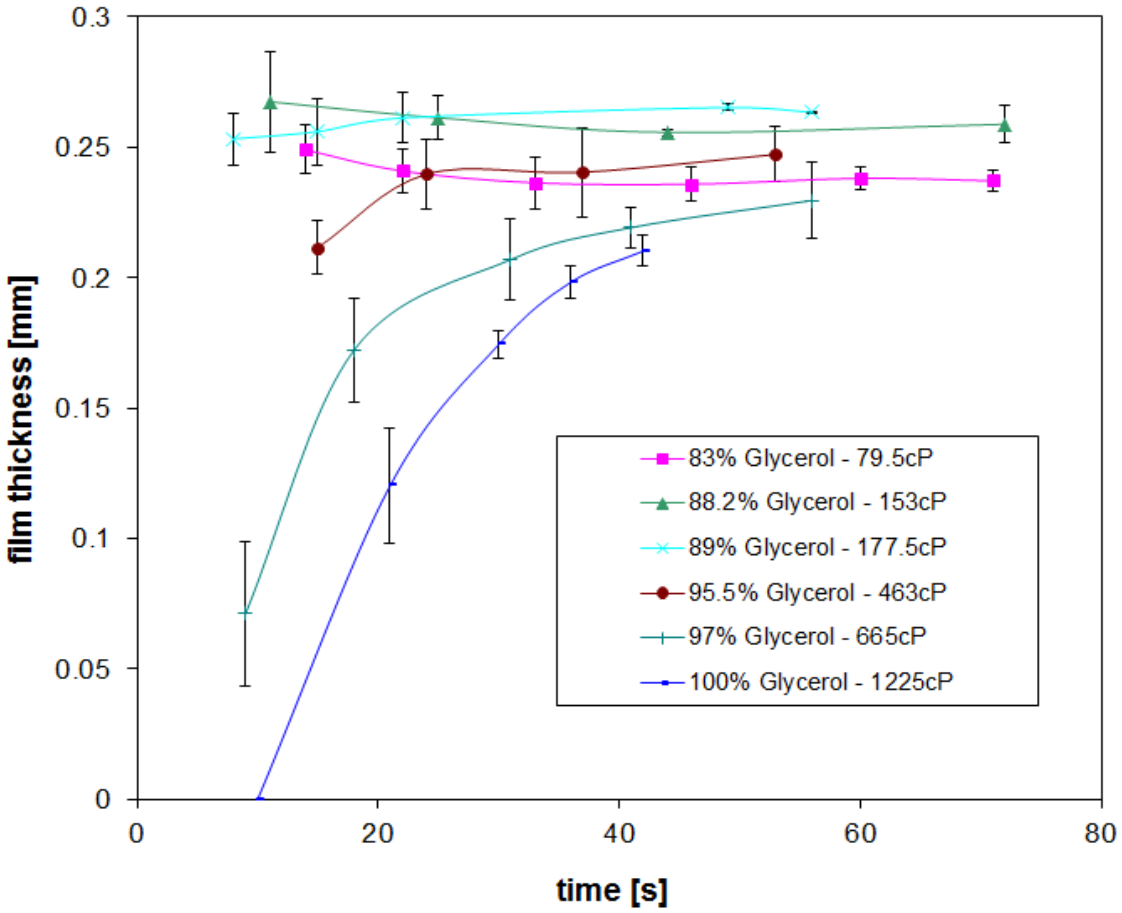

Figure 5.34: Thickness of the thin film of the displaced fluid (glycerol solutions) on the walls of Hele-Shaw cells as a function of time. The injection rate of water is 4.69ml/min.

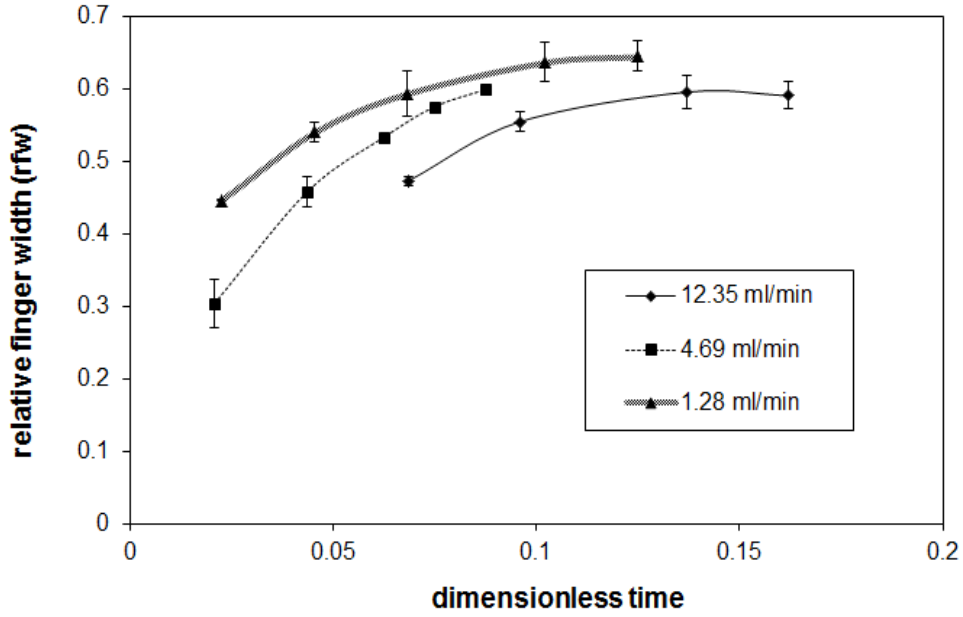

Figure 5.35: Relative finger width as a function of dimensionless time for 100% glycerol solution at different injection rates of water. (Viscosity Ratio, M = 1225)

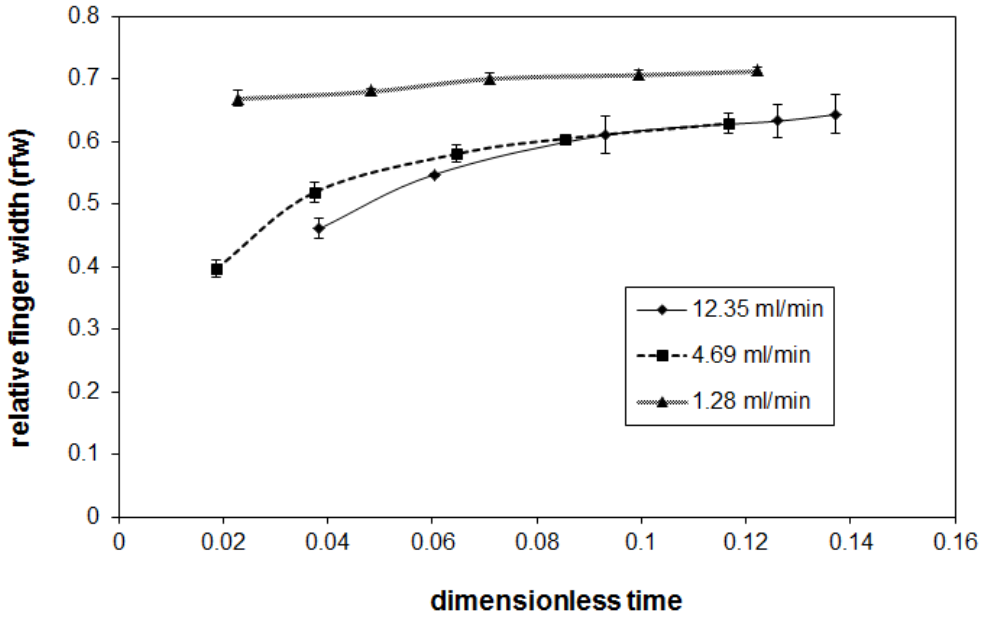

Figure 5.36: Relative finger width as a function of dimensionless time for 97% glycerol solution at different injection rates of water. (Viscosity Ratio, M = 665)

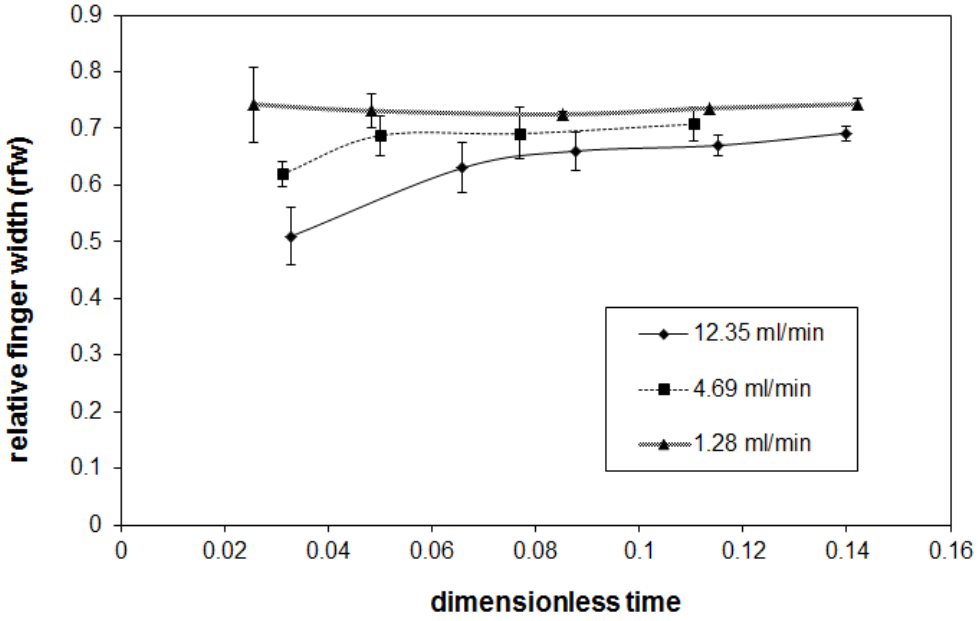

Figure 5.37: Relative finger width as a function of dimensionless time for 95.5% glycerol solution at different injection rates of water. (Viscosity ratio, M = 463)

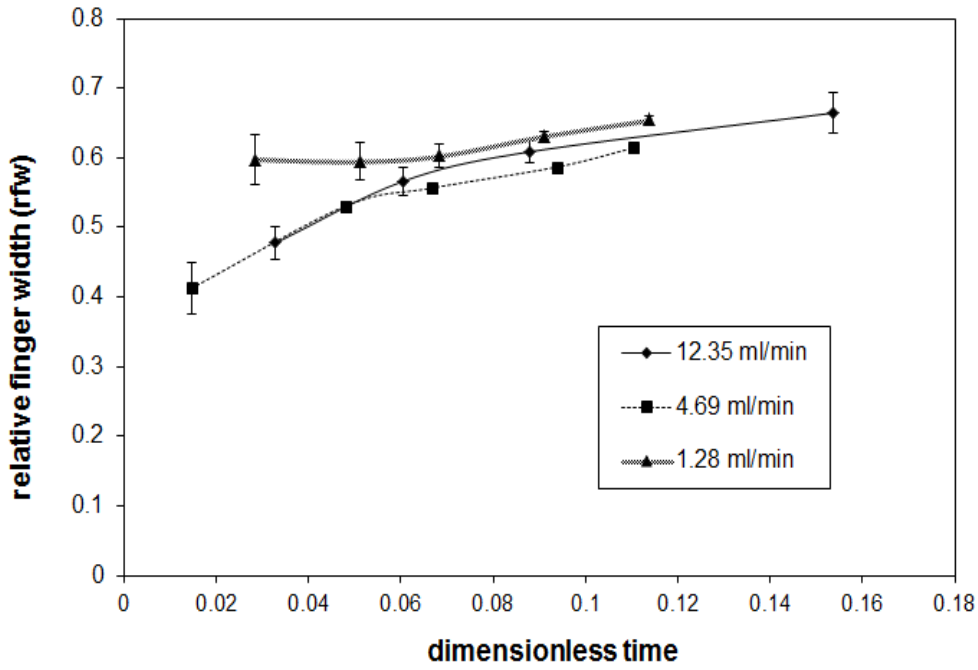

Figure 5.38: Relative finger width as a function of dimensionless time for 94% glycerol solution at different injection rates of water. (Viscosity Ratio, M = 343)

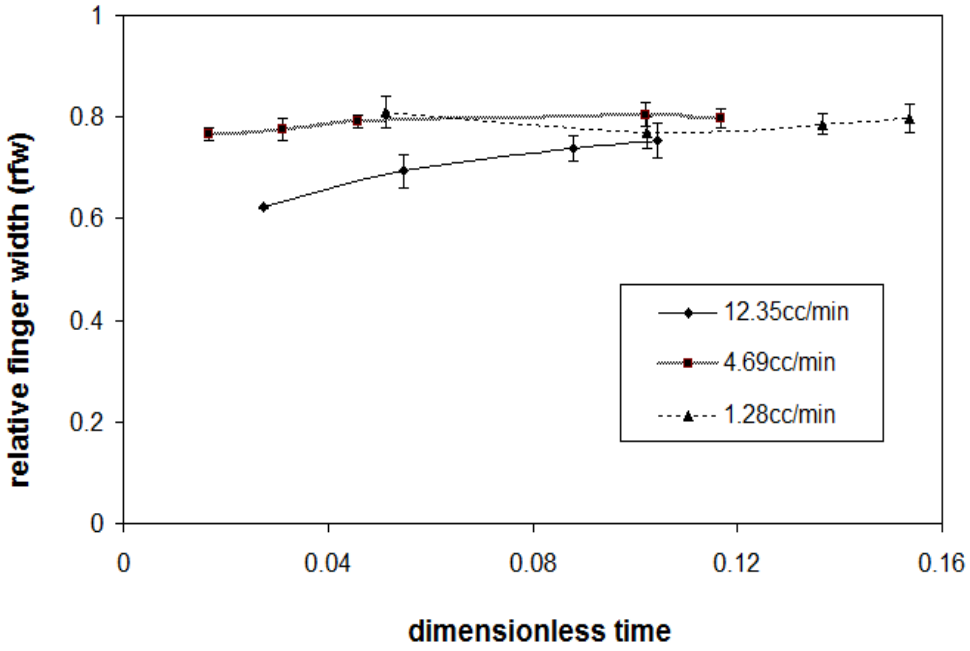

Figure 5.39: Relative finger width as a function of dimensionless time for 89% glycerol solution at different injection rates of water. (Viscosity Ratio, M = 177.5)

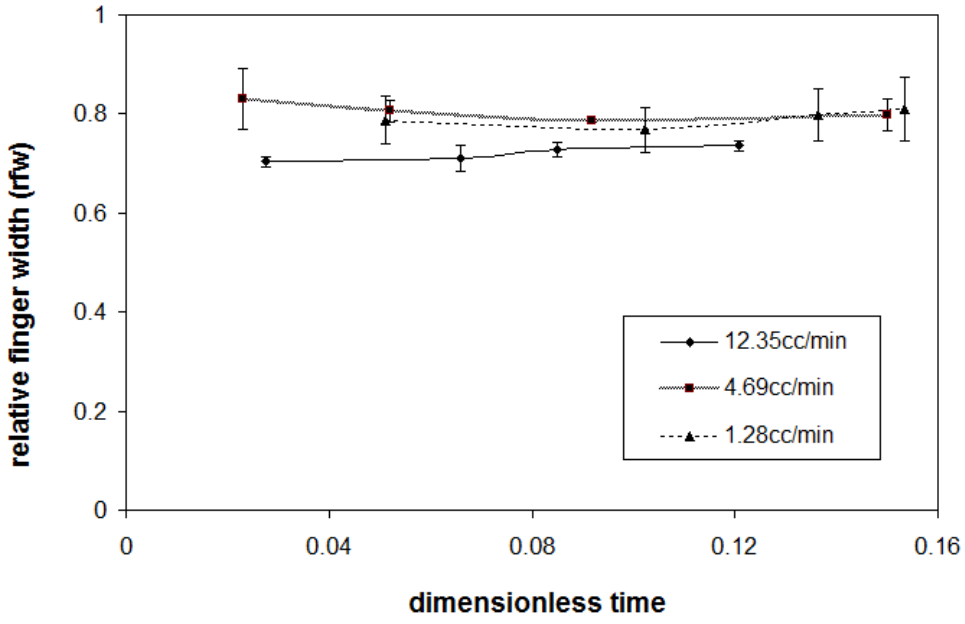

Figure 5.40: Relative finger width as a function of dimensionless time for 88.3% glycerol solution at different injection rates of water. (Viscosity Ratio, M = 153)

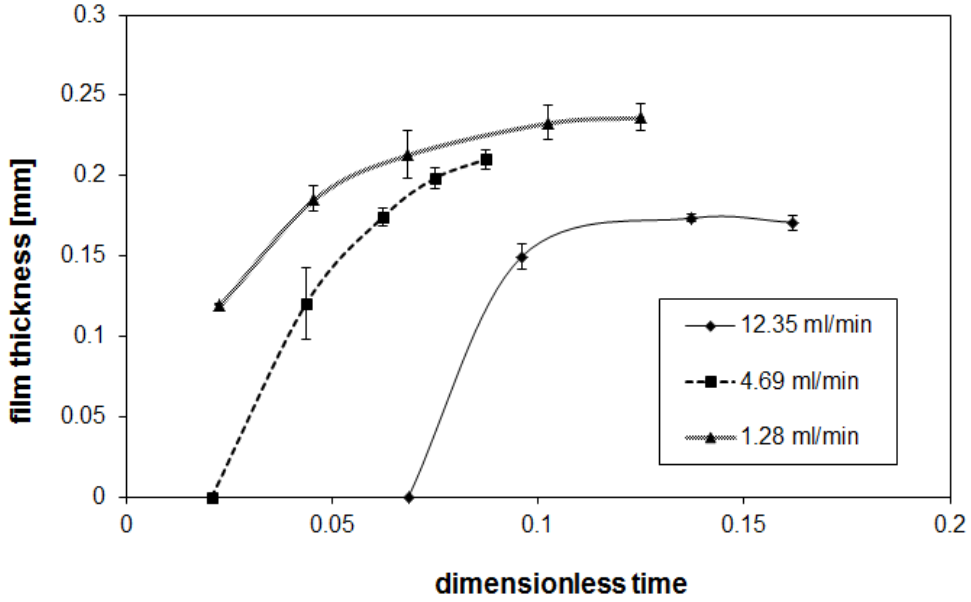

Figure 5.41: Film thickness of the film of displaced fluid as a function of dimensionless time for 100% glycerol solution at different injection rates of water. (Viscosity Ratio, M = 1225)

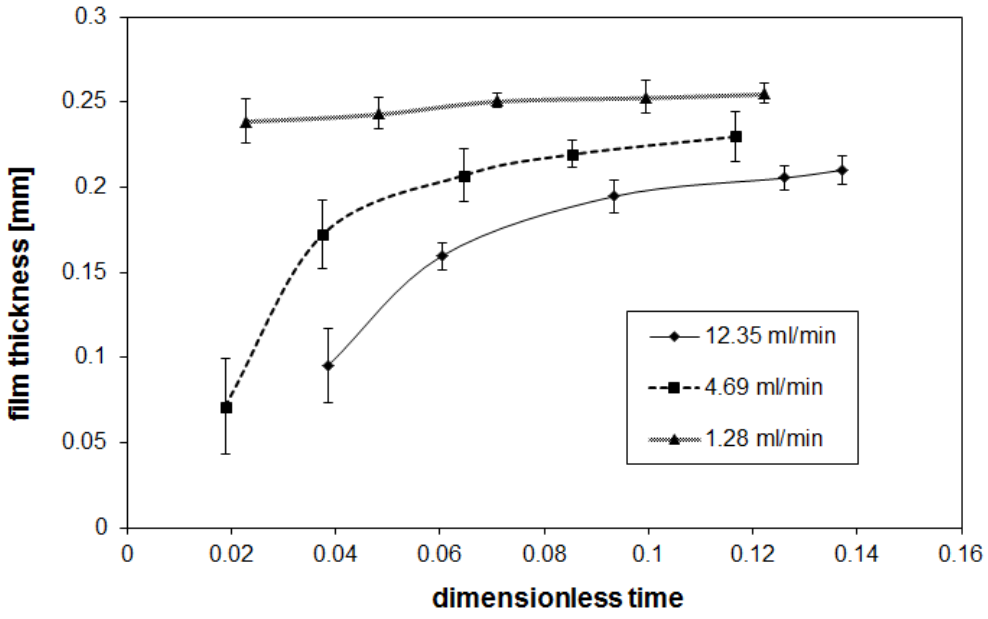

Figure 5.42: Film thickness of the film of displaced fluid as a function of dimensionless time for 97% glycerol solution at different injection rates of water. (Viscosity Ratio, M = 665)

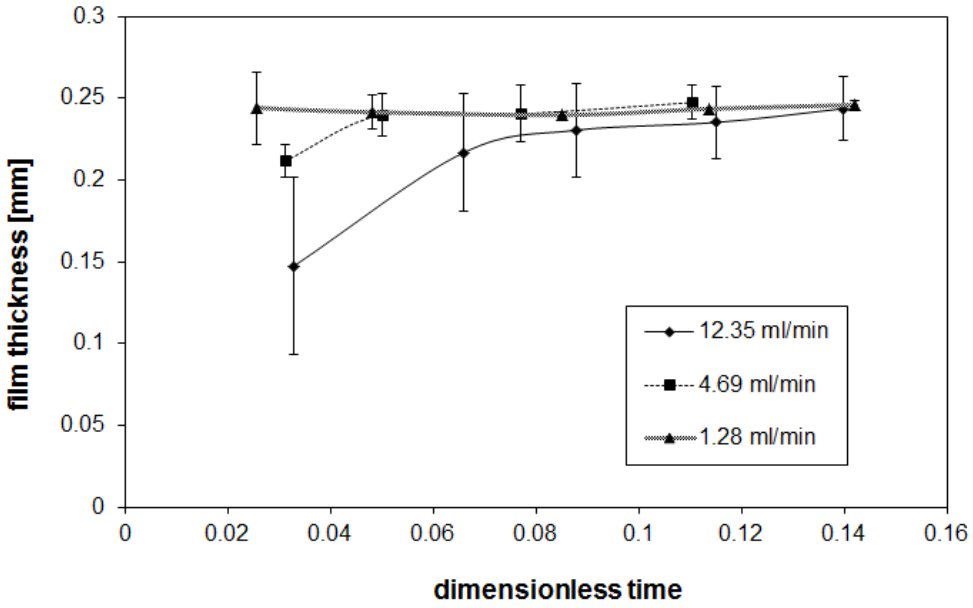

Figure 5.43: Film thickness of the film of displaced fluid as a function of dimensionless time for 95.5% glycerol solution at different injection rates of water. (Viscosity Ratio, M = 463)

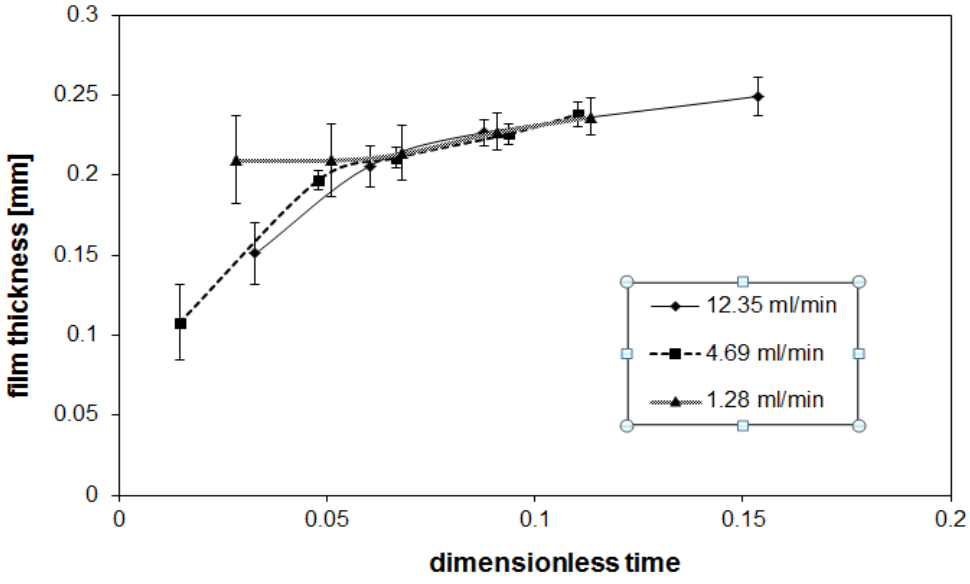

Figure 5.44: Film thickness of the film of displaced fluid as a function of dimensionless time for 94% glycerol solution at different injection rates of water. (Viscosity Ratio, M = 343)

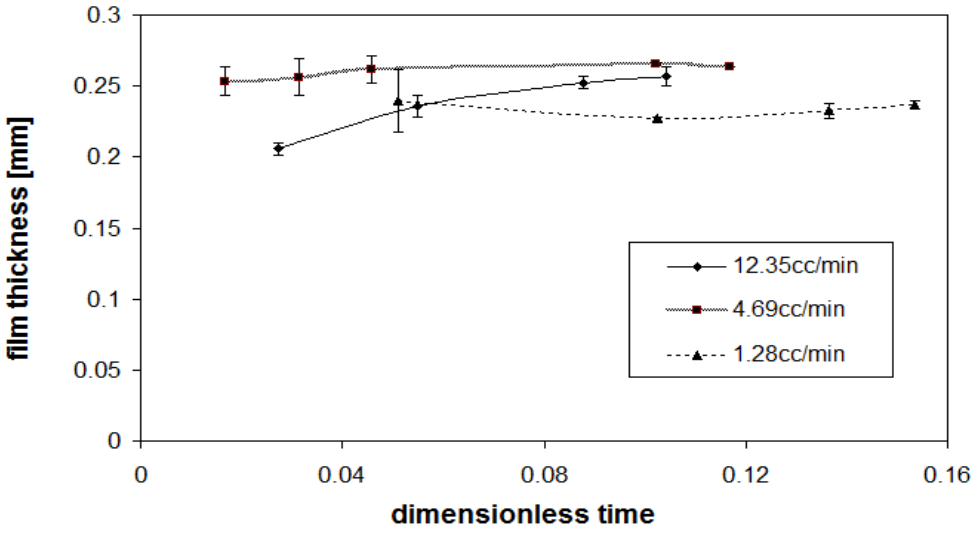

Figure 5.45: Film thickness of the film of displaced fluid as a function of dimensionless time for 89% glycerol solution at different injection rates of water. (Viscosity Ratio, M = 177.5)

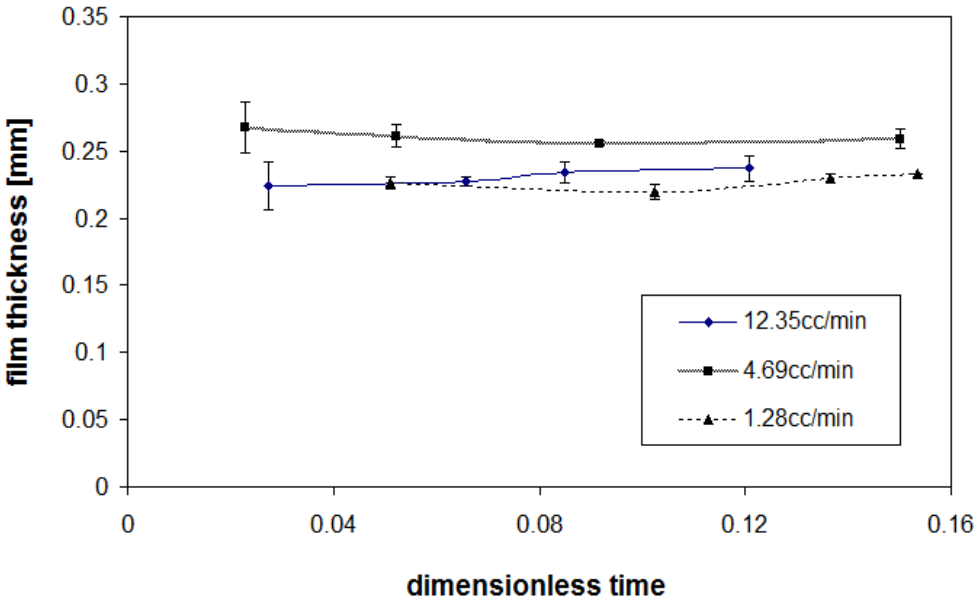

Figure 5.46: Film thickness of the film of displaced fluid as a function of dimensionless time for 88.2% glycerol solution at different injection rates of water. (Viscosity Ratio, M = 153)

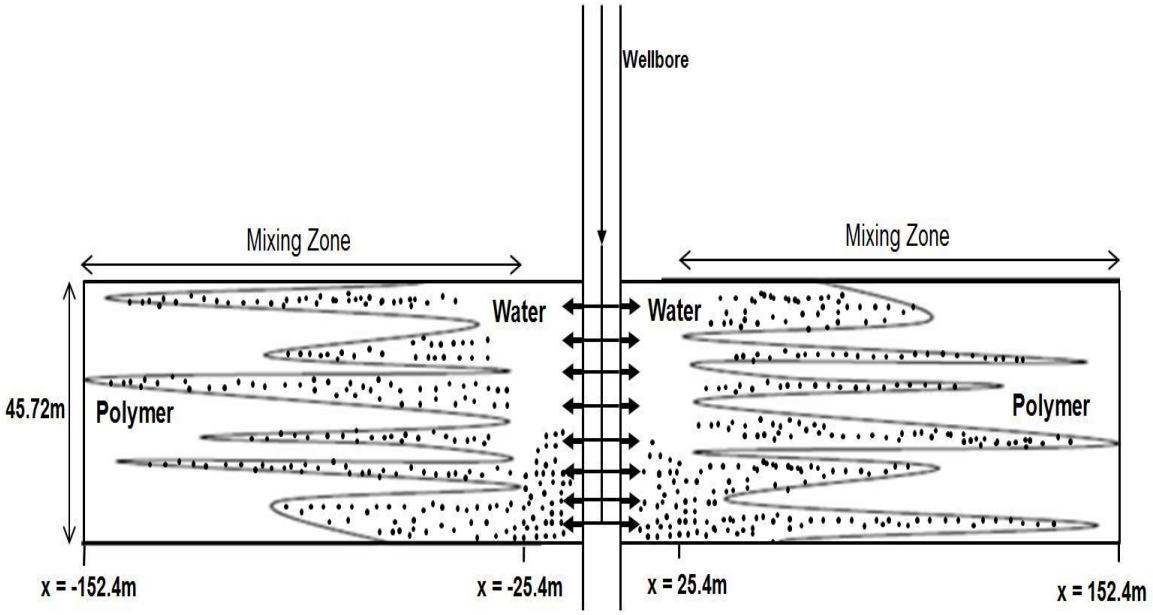

Figure 5.47: Schematic showing the viscous fingers of water in the polymer solution at the end of a reverse-hybrid fracture treatment for an example calculation. The volume of polymer slug is twice that of water. At the end of the treatment the mixing zone spreads from x=25.4m to x=152.4m in the fracture. The proppant is assumed to travel horizontally at the velocity of the fluid.

Chapter 6: Impact of Fluid Elasticity on Miscible Viscous Fingering

6.1 Introduction and Past Work

Saffman and Taylor (1958) presented theoretical solutions for the formation of viscous fingers between two Newtonian fluids in Hele-Shaw cells. The problem is a Laplacian free-boundary problem and despite of being highly non-linear, the problem has been solved numerically (Coulder 1991). In some limiting cases, analytical results have also been obtained (Howison 1986). Past work on viscous fingering in Newtonian fluids was discussed in detail in Chapter 5. Instabilities in non-Newtonian fluids are not very well understood and have not been widely studied. Patterns which are different and more complex from those in Newtonian fluids have been observed in non-Newtonian fluids (Allen and Boger 1988; Kawaguchi et al. 1997a; Kawaguchi et al. 1997b; Lindner et al. 2002; Li et al. 2006). The fluids include liquid crystals (Buka et al. 1986; Buka and Palffy-Muhoray 1987), polymer solutions (Kawaguchi et al. 1997a; Li et al. 2006; Makino et al. 1995), suspensions (Kawaguchi et al. 1997b), foams (Park and Durian 1994), gels (Lindner et al. 2000), clays (Lemaire et al. 1991) etc. A limited number of numerical studies have been conducted to determine the influence of fluid rheological properties (Sader et al. 1994) on viscous fingering patterns.

In this work, we focus on the role of fluid elasticity on viscous fingering patterns. Allen and Boger (1988) performed experiments displacing Boger fluids with Newtonian fluids and observed that the finger patterns in Boger fluids were similar to those in

Newtonian fluids with the same shear viscosity. Sader et al. (1994) pointed out that the influence of elasticity on fingering patterns depends upon the Deborah number De (defined as the ratio of fluid relaxation time, λ to fluid flow time, t_{fl}). The flow conditions under which the experiments were performed by Allen and Boger (1988) pertained to small Deborah numbers which explains the absence of fracture-like patterns. Kawaguchi et al. (1997a) performed experiments with hydroxypropyl methyl cellulose (HPMC) and observed morphological transitions from dense branching to tip-splitting and tip-splitting to skewering in high molecular weight HPMC solutions. Similar pattern transitions were not observed in low molecular weight solutions. The difference was attributed to the higher elasticity of high molecular weight solutions. Vlad and Maher (2000) observed that immiscible viscous fingers growing in Boger fluids are unstable to tip splitting at lower velocities compared to viscous fingers growing in Newtonian fluids. No fracture-like instabilities were observed. Lindner et al. (2002) performed experiments in linear Hele-Shaw cells and displaced polyethylene oxide (PEO) solution with air. They observed wider fingers than for Newtonian fluids which were attributed to higher normal stress in the PEO solutions. It was also observed that the propagation velocity of fingers did not change from that in Newtonian fluids. Mora and Manna (2010) performed a linear stability analysis of an air front pushing an Upper Convected Maxwell fluid inside a Hele-Shaw cell and showed that a unique dimensionless time parameter controls the elastic effects.

The objective of this work is to investigate the effect of elasticity on the viscous fingering patterns in miscible viscous fingering. A linear stability analysis is presented to show the impact of fluid elasticity on the stability of the interface. This is done by performing displacement experiments in linear Hele-Shaw cells by displacing aqueous Boger fluids with water. The observations are compared to those performed in Newtonian fluids (glycerol solutions), of the same viscosity, displaced with water. The comparison helps in a direct identification of the effect of fluid elasticity on flow instability.

6.2 LINEAR STABILITY ANALYSIS

To study the impact of fluid elasticity of the displaced fluid on the stability of the interface, a linear stability analysis is performed. A Newtonian fluid 1 of constant viscosity, μ_1, is separated by a viscoelastic fluid 2 of viscosity, μ_2, by a $z = 0$ in a two-dimensional rectilinear Hele-Shaw geometry. At the initial condition, t=0, fluid 1 is the domain $z < 0$ and fluid 2 in the domain $z > 0$ and the interface is moving with a constant velocity v_z=u. The interface between the fluids is perturbed slightly into a wave-like corrugation of wavelength $2\pi/n_y$ described by (Saffman and Taylor 1958):

$$z = ae^{in_y y + wt} \tag{6.1}$$

The flow of a fluid inside a rectilinear Hele-Shaw cell can be described by the following equation (Bird et al. 2007):

$$u = -\frac{b^2}{12\mu}\left(\frac{\partial p}{\partial z} + \rho g\right) \tag{6.2}$$

The equation can be rewritten as:

$$u = -\frac{k}{\mu}\left(\frac{\partial p}{\partial z} + \rho g\right) = -\nabla\Phi \tag{6.3}$$

where k denotes the permeability of the Hele-Shaw cell which is constant and equal to $b^2/12$ under laminar flow conditions. z is the direction of motion of the fluid and Φ is the velocity potential. The flow equation for the Newtonian fluid 1 can be written as:

$$u_1 = -\frac{k}{\mu_1}\left(\frac{\partial p_1}{\partial z} + \rho_1 g\right) = -\nabla\Phi_1 \tag{6.4}$$

The viscoelastic fluid is represented using a Maxwell model described by the following equation:

$$\tau_{ij} + \lambda\frac{\partial \tau_{ij}}{\partial t} = -\mu_2\dot{\gamma}_{ij} \tag{6.5}$$

The derivation of the equation was shown in Chapter 2. λ is the relaxation time of the fluid, τ_{ij} represents the stress tensor and $\dot{\gamma}_{ij}$ represents the strain rate tensor. The equation can be written in the integral form as follows (Bird et al. 1987):

$$\tau_{ij}(t) = -\int_{-\infty}^{t}\frac{\mu_2}{\lambda}\exp\left(-\frac{(t-t')}{\lambda}\right)\dot{\gamma}_{ij}(t')dt' \tag{6.6}$$

If we assume that the stress and strain rates vary with time in the same functional form as the perturbed interface (Huh and Pope 2008),

$$\tau_{ij}(y,z,t) = \tau_{ij}'(y,z)e^{wt} \tag{6.7}$$

$$\gamma_{ij}(y,z,t) = \gamma_{ij}'(y,z)e^{wt} \tag{6.8}$$

the solution of Equation 6.6 yields

$$\tau_{ij}'(y,z) = -\left(\frac{\mu_2}{1+w\lambda}\right)\dot{\gamma}_{ij}'(y,z) \tag{6.9}$$

The above equation shows that the flow equation 6.3, can be directly applied for fluid 2, except that μ is replaced by $\mu_2/(1+w\lambda)$.

$$u_2 = -\frac{k}{\mu_2/(1+\lambda w)}\left(\frac{\partial p_2}{\partial z} + \rho_2 g\right) = -\nabla\Phi_2 \tag{6.10}$$

Assuming that both the fluids are incompressible the equation of continuity can be written for each fluid as follows:

$$\nabla.u_1 = 0 \Rightarrow \nabla^2\Phi_1 = 0 \tag{6.11}$$

$$\nabla.u_2 = 0 \Rightarrow \nabla^2\Phi_2 = 0 \tag{6.12}$$

The perturbed interface velocity is given by:

$$u_1 = u + \left.\frac{\partial z}{\partial t}\right|_{z=0} = \frac{\partial\Phi_1}{\partial z} \tag{6.13}$$

Substituting Equations 6.1 and 6.13 in Equation 6.11 and solving for the velocity potential under appropriate boundary conditions, we obtain:

$$\Phi_1 = uz + \frac{aw}{n_y}e^{in_y y + wt + n_y z} + c_1 \tag{6.14}$$

where c_1 is a constant of integration. Similarly for Φ_2 we obtain:

$$\Phi_1 = uz - \frac{aw}{n_y} e^{in_y y + wt - n_y z} + c_2 \qquad 6.15$$

Now at the interface between the two miscible fluids we apply the continuity of pressure i.e. $P_1 = P_2$. The pressure continuity is an assumption for solving the analysis for a Maxwell fluid. In general, for a viscoelastic fluid there will be a normal stress jump across the interface with the normal stress higher in Fluid 2 (viscoelastic). This normal stress jump is not considered in this analysis. However, the stress jump can change the formulation of the analysis.

P_1 and P_2 from Equations 6.4 and 6.10 can be written as:

$$P_1 = -\frac{\mu_1 \Phi_1}{k} + \rho_1 gz \qquad 6.16$$

and

$$P_2 = -\frac{\mu_2 \Phi_2}{k(1+\lambda w)} + \rho_2 gz \qquad 6.17$$

Equating 6.16 and 6.17 at the interface and substituting 6.14 and 6.15:

$$-\left[\frac{\mu_1 - \left(\frac{\mu_2}{1+\lambda w}\right)}{k}\right] u + (\rho_1 - \rho_2) g - \left[\frac{\mu_1 + \left(\frac{\mu_2}{1+\lambda w}\right)}{k}\right] \frac{w}{n_y} = 0 \qquad 6.18$$

The above equation can be rewritten as:

$$\left(\frac{\mu_2}{1+\lambda w}\right)\left[\frac{w}{n_y} - u\right] + \frac{w}{n_y}\mu_1 = k(\rho_1 - \rho_2) g - \mu_1 u \qquad 6.19$$

Equation 6.19 is a quadratic in w and does not have an explicit closed form solution. In order to simplify the solution, we make an assumption that the viscosity of the displacing fluid, μ_1, is zero. This helps in a qualitative understanding of the impact of the displaced fluid elasticity on the growth of the perturbation. Substituting $\mu_1 = 0$

$$w = \frac{n_y k(\rho_1 - \rho_2)g + n_y \mu_2 u}{\mu_2 - \lambda n_y k(\rho_1 - \rho_2)g} \qquad 6.20$$

If $w < 0$ the amplitude of the perturbation is damped at an exponential rate i.e. the interface is stable. If $w > 0$ the amplitude increases at an exponential rate and the interface is unstable. To evaluate the effect of relaxation time, λ, of fluid 2 on the stability of the interface we examine the following possible cases:

Case 1: $(\rho_1 - \rho_2) > 0$

In this case the numerator in Equation 6.20 is positive. λ in the denominator appears in a negative term. As increase in λ can make the denominator negative, making the growth rate $w < 0$. Thus, an increase in the relaxation time of the displaced fluid can dampen the perturbation and provide stability to the interface.

Case 2: $(\rho_1 - \rho_2) < 0$ and $\left| n_y k(\rho_1 - \rho_2)g \right| < n_y \mu_2 u$

In this case, both the numerator and denominator in Equation 6.20 are positive and λ appears in a positive term in the denominator. The interface is always unstable. However,

an increase in λ increases the value of the denominator, reducing the growth rate of the perturbation.

Case 3: $(\rho_1 - \rho_2) < 0$ and $\left|n_y k(\rho_1 - \rho_2)g\right| > n_y \mu_2 u$

In this scenario, the numerator in Equation 6.20 is negative and λ appears in a positive term in the denominator. The interface is stable in this case. An increase in λ reduces the negative value of growth rate, *w*. However, it is important to note that growth rate will always remain negative irrespective of the value of λ.

To summarize, by assuming that the viscosity of the fluid 1 is zero, an increase in relaxation time can reduce the growth rate of the perturbation and provide stability to the interface. A complete analysis of the effect of viscosities of both fluids and relaxation time of displaced fluid would require the solution of Equation 6.19.

6.3 EXPERIMENTS

6.3.1 Description and Characterization of Fluids

The Boger fluids chosen for this study are based on the findings of Dontula et al. (1988). The fluids are prepared by adding small amounts of a high-molecular weight polymer (polyethylene oxide (PEO) with a molecular weight of 4,000,000 g/mol obtained from Aldrich) to a more concentrated aqueous solution of the same polymer but of a lower molecular weight (polyethylene glycol (PEG) with a molecular weight of 8,000

g/mol obtained from Fischer Scientific). Stock solutions of PEG were prepared by adding the oligomer to distilled water (1liter) and mixed for at least 24 hours over a magnetic stirrer. The solutions were allowed to stand for 24 hours. Different amounts of PEO were added to smaller volume of PEG solutions (400ml), and the mixture was left to mix for at least 24 hours over a magnetic stirrer. All final mixtures were colorless, odorless and transparent to the eye. Table 6.1 shows the concentrations of PEG and PEO used for preparing the two fluid mixtures used in this study.

Steady shear-viscosity measurements and dynamic oscillatory-shear measurements are made with the rheometer using a double wall concentric cylinder fixture. Figure 6.1 shows the viscosity (η) as functions of shear rate ($\dot{\gamma}$) for liquid L1. The fluid viscosity is constant (variations of viscosity are confined to 1% of the viscosity value at low shear rate). Once the PEG-PEO solution viscosity is measured, a glycerol solution is prepared, and the water weight percentage is adjusted to achieve the same viscosity. Figure 6.1 also shows the glycerol solution (88.2% by weight of glycerol). Table 6.2 shows the viscosities of the two glycerol solutions used as test fluids.

The oscillatory-shear measurements were made over a range of frequencies from 0.1 rad/s to 100 rad/s. Figure 6.2 shows the elastic modulus, G' and the viscous modulus, G'' as functions of angular frequency, ω for liquids L1 and T1. It is observed that the two fluids have similar G'' values but different G' values, suggesting that the two fluids have similar viscous properties but different elastic properties, with the polymer solution being

more elastic. The elastic and viscous moduli are simultaneously fitted to a series of Maxwell elements with relaxation times λ_k and relaxation strengths G_k, represented using the following equations (Ferry 1970):

$$G'(\omega) = \sum_{k=1}^{n_p} G_k \frac{\omega^2 \lambda_k^2}{1+\omega^2 \lambda_k^2} \tag{6.21}$$

$$G''(\omega) = \sum_{k=1}^{n_p} G_k \frac{\omega \lambda_k}{1+\omega^2 \lambda_k^2} \tag{6.22}$$

The fitting is performed by minimizing the sum of the variance measure over the frequency range.

$$\sigma^2 = \sum_{k=1}^{n_p} \left[1 - \frac{G'_{fit}(\omega)}{G'(\omega)}\right]^2 + \left[1 - \frac{G''_{fit}(\omega)}{G''(\omega)}\right]^2 \tag{6.23}$$

Figure 6.3 and Figure 6.4 show a comparison of the fit of this model with experimental data for liquids L1 and T1 respectively. Table 6.3 shows the values of relaxation times and relaxation strengths. The moduli for polymer solutions fit well with two Maxwell elements in series whereas a single Maxwell element was sufficient to fit the moduli data for glycerol solutions.

6.3.2 Experimental Setup

The experimental setup and procedure is the same as that used for measuring the mixing zone velocities in Chapter 5. Figure 6.5 shows a sketch of the Hele-Shaw cell used in the experiments. The cell is made of Plexiglass, and the flow channel is 84cm long and 5cm wide. The walls are smooth and perfectly parallel to each other with a

spacing of 1mm. Figure 6.6 shows a sketch of the experimental setup. The setup consists of two 500 ml Isco syringe pumps. Pump 1 is used to fill the Hele-Shaw cell with the displaced fluid (glycerol or PEG-PEO solution), pushing the liquid against gravity with the cell kept in an inclined position. This is done to avoid any air bubbles in the cell. An accumulator with a piston is used to pump the displaced fluid to the cell. This is done to prevent the pump syringe from coming in contact with viscous fluids.

A water-soluble dye is added to the displacing water to increase the contrast between the two liquids. The cell is kept in a horizontal plane in all the experiments to avoid any gravitational effects in the direction of flow. Upon the injection of the displacing fluid, a high definition video camera is used to record the experiment. The camera is placed over the top of the cell using a pair of tripods and is moved along the length of the cell during the experiment. A measuring scale is kept alongside the Hele-Shaw cell while recording the video. An image analysis tool Tracker 4.0 (http://www.cabrillo.edu/~dbrown/tracker/) is used to analyze the movement of the fingers and to calculate the finger velocities. Each experiment is repeated three times under a unique set of conditions to ensure reproducibility.

6.3.3 Observations and Results

In order to ensure the homogeneity of the Hele-Shaw cell a unit displacement (water displacing water) is performed. The displacing water is colored with the dye and is injected at a rate of 12.35ml/min (highest injection rate in any of the subsequent

experiments). Figure 6.7 shows snapshots of the displacing water front at four different times. The dyed water is injected from the left into the Hele-Shaw cell containing clear water. A piston-like displacement with some diffusion at the interface of the two fluids is observed. This confirms that the cell walls do not cause any instabilities and any finger formation is due to the viscosity contrast between the two fluids (in absence of gravity).

Displacement of the polymer solution, L1 and the glycerol solution, T1 is performed at three different flow rates: 12.35, 4.69 and 1.28ml/min. The mutual diffusion coefficients between distilled water and water-glycerol solutions are calculated using the relation proposed by D'Errico et al. (2004).

$$D \times 10^9 m^2 s^{-1} = \frac{(1.024 \pm 0.01) - (0.91 \pm 0.05) x_2}{1 + (7.5 \pm 0.3) x_2} \pm 0.004 \qquad 6.24$$

In the above equation, D is the mutual diffusion coefficient and x_2 is the mole fraction of glycerol in the water-glycerol mixture. The flow Pectlet numbers (Pe) are then calculated using the following equation:

$$\mathrm{Pe} = \frac{Ub}{D} \qquad 6.25$$

U is the velocity of flow displacements, D is the diffusion coefficient and b is a characteristic length scale. For calculations, the characteristic length is taken as the gap width of 1mm. The velocity, U, is calculated by dividing the injection rate by the cross section area of channel. Table 6.4 lists the diffusion coefficients, and the Peclet numbers at the three flow rates, for all glycerol solutions. The Peclet numbers are high ($>10^3$) for

the glycerol displacement experiments. The lack of data for the mutual diffusion coefficients between water and PEG-PEO solutions restricts us from calculating the Peclet numbers in displacement experiments with PEG-PEO solutions. Based on the diffusion coefficients with glycerol solutions, we assume that Peclet numbers in all the experiments are high enough for longitudinal diffusion to be neglected.

Figure 6.8 and Figure 6.9 show the sequential evolution of the interface at 12.35ml/min and 4.69ml/min in liquid L1, respectively. Figure 6.10 and Figure 6.11 show the sequential evolution of the interface at 12.35ml/min and 4.69ml/min in liquid T1, respectively. As seen in both these figures, initially a large number of fingers originate from the interface between the two fluids. With the progress of the displacement the fingers become longer and wider and their number reduces. Finger mechanisms such as shielding, spreading and coalescence (Homsy 1987) can be observed in both the fluids. Shielding is the process where a finger slightly ahead of its neighbors quickly outruns them and retards their further growth. However, the following key differences are observed in the fingering patterns between the two fluids:

(i) Tadpole-like features develop at the interface at the onset of instability in both L1 and T1. However, the necks of the tadpoles are observed to be thinner and longer in the more elastic fluid (L1).

(ii) Experiments indicate that in the fully developed regime, thinner and longer fingers form in the more elastic fluid. In the less elastic fluid it is observed that a thick finger dominates and moves through the channel.

(iii) The shielding effect is more pronounced in the less elastic fluid where the dominant finger retards the growth of the other fingers. There appears to be less competition between fingers in the more elastic fluid, and we observe multiple (3-5) thin long fingers in the fully developed regime in the more elastic fluid. An illustration of the reduced shielding effect can be observed in Figure 6.8. In the snapshots at 12s and 14.5s, we observe that the finger in closer to the wall is ahead of the finger in the middle of the channel. However, this does not slow down the growth of the middle finger as seen at later times. On the other hand, in the less elastic fluid (T1) the thick finger in the middle of the channel retards the growth of any other finger as can be observed in Figure 6.10 and Figure 6.11.

6.3.3.1Evolution of Finger Instability

To evaluate the differences in the evolution of the finger instability in the PEG-PEO and glycerol solutions, an attempt is made to compare the wave numbers and characteristic wavelengths. Figure 6.12 shows a snapshot taken at 18.5s after start of injection in Liquid L1. Water is injected at a rate of 4.69ml/min. The image has been rotated by 90 degrees. The interface between the two fluids is tracked using the software 'Plot Digitizer' shown in Figure 6.13. To eliminate the wall effects, the fingers close to the walls of the cell are not considered for the analysis. A Fourier transformation is applied to the interface, to decompose the interface into Fourier modes (Fernandez et al. 2002):

$$A(x) = \sum_{m=0}^{N/2} A_m \exp(ik_m x) \qquad 6.26$$

$A(x)$ represents the position of the interface as a function of horizontal dimension, x. m denotes the number of the Fourier mode with wave number $k_m = 2\pi m/L$. A_m denotes the amplitude of the mode k_m. L is the total length of the domain (size of the image in the x-direction) and N is the number of equally spaced points.

In order to apply the above transformation, it important that at a value of x there is a unique value of $A(x)$. This is not the case in the interface shown in Figure 6.13 because of the tadpole-like features. The interface profile is therefore modified using the MATLAB program in Appendix A and the profile is interpolated at equally spaced data points. Figure 6.14 shows the modified interface profile with the y-axis shifted. The transformation is applied to this profile. Figure 6.15 shows the plot of the amplitude pertaining to all the wavenumbers at different times. The wave number corresponding to the peak amplitude is the characteristic wave number of the growth of the instability. We observe that the wave number corresponding to the peak is the same at different times. This suggests that the characteristic wave number is the dominant wave number. Table 6.5 and Table 6.6 show the dominant wave numbers in the PEG-PEO and glycerol solutions, at three injection rates. Comparison between both pairs (liquids L1 and T1, and liquids L2 and T2) shows that dominant wave number is higher in the more elastic fluids. This suggests that fluid elasticity results in reduction in wavelength of the instabilities, causing more fingers to evolve at the interface.

6.3.3.2Finger Tip Velocity

To analyze the development of instabilities, the fingertip velocities are calculated. The distance of the tip from the inlet is calculated as a function of time. It is observed in all the displacements, that the distance of the tip from the inlet varies linearly with time. The slope of the distance-time curve gives the fingertip velocity. A relative finger velocity is defined as the ratio of fingertip velocity to the injection velocity (injection rate divided by the cross sectional area). Figure 6.16 and Figure 6.17 show the relative finger velocities as a function of the injection rate for fluids L1, T1, L2 and T2 respectively. Error bars are shown to indicate the variation observed from three different runs. From both the figures it is observed that the relative fingertip velocity is lower in the more elastic fluid.

The Deborah number, defined as the ratio of the polymer relaxation time to the flow characteristic time, is used to quantify the elastic effects. It can also be expressed as $De = \lambda \dot{\gamma}$ where $\dot{\gamma}$ is the average shear rate inside the Hele-Shaw cell. The average shear rate in the cell can be obtained as the average velocity gradient written as $\dot{\gamma} = 3U/b$ by assuming that the flow profile is parabolic (Lindner 2002), where U is the velocity of the finger and b is the gap between the parallel walls. The Deborah numbers calculated based on the fingertip velocities for the above experiments are tabulated in Table 6.7. The longest relaxation time is chosen as the characteristic relaxation time (λ) for the calculations (Bird 1987).

At the same injection rates, values of Deborah number are seen to be higher in the PEG-PEO solutions than the glycerol solutions. Also values of De $\geq$ 0.2 suggest that viscoelastic effects are dominant in the PEG-PEO solutions. This combined with the observations in Figures Figure 6.16 and Figure 6.17 lead to the conclusion that the elasticity of the fluids slows down the growth of fingers in miscible viscous fingering. The observations are in qualitative agreement with the linear stability analysis presented in Section 6.2, where it was shown that the increase in elasticity of a Maxwell fluid can lead to reduction in growth rate of the perturbation and provide stability to the interface.

6.3.3.3Relative Finger Width

Relative finger width (RFW) is defined as the area contacted by the displacing fluid to the total area behind the finger tip. Relative finger width is a measure of the sweep efficiency of the displacing fluid (Li et al. 2006). To calculate the relative finger width, a program "ImageJ" (http://rsbweb.nih.gov/ij/) is used. A snapshot of the displacement is taken at a specified time. The interface between the displacing and displaced fluid is outlined and the area contact by the displacing fluid is calculated. Figure 6.18 shows a snapshot of the area outlined in ImageJ. This area is divided by the total area behind the tip to calculate the RFW.

Figures 6.19 through 6.24 show the comparison of the relative finger widths as function of time for fluids L1 and T1, and L2 and T2 at the three injection rates. Error bars show the variation between two unique experimental runs. In an ideal scenario, at

time, t = 0, the interface between the displacing and displaced fluid should be stable. This would correspond to RFW = 1 at t = 0. The interface would develop instabilities at later times, resulting in reduction of RFW with subsequent injection and development of instabilities. This is shown in the numerical simulations of Islam and Azaiez (2007). However, in the experiments we observe that at the start of injection the viscous fingers develop and propagate faster closer to the side walls of the Hele-Shaw cell. The wall effects result in values of RFW lower than one at early times of injection.

Figure 6.19 and Figure 6.20 show that the RFWs are higher in the more elastic fluids at lower injection rates (1.28ml/min). This suggests that the sweep efficiencies are higher in the more elastic fluids at the lower injection rate. However, the trend reverses with increase in injection rate. At the injection rate of 4.69ml/min, the RFWs are higher in the less elastic fluid (Figure 6.21 and Figure 6.22). With a subsequent increase in the injection rate (12.35ml/min), the difference in the RFW values between the polymer and glycerol solutions further increases (Figure 6.23 and Figure 6.24). These observations show that with increase in injection rates, elasticity of displaced fluid causes a reduction of relative finger width and sweep efficiency. As mentioned in Table 6.7, higher Deborah numbers at higher injection rates suggest increased elastic effects with injection rate.

In section 6.3.3.2, data was presented to show that finger propagation velocity is reduced by fluid elasticity. It has also been discussed that based on the high Peclet numbers, longitudinal diffusion can be neglected. These observations lead to the

conclusion that the thickness of displaced fluid film on the walls of the Hele-Shaw cells is different in displacements in fluids of different elasticity. It has been shown that during fluid displacements, a thin film of the displaced fluid is left on the walls, in immiscible as well as miscible displacements (Bretherton 1961; Lionti-Addad and Meglio 1992; Ro and Homsy 1995; Lajeunesse et al. 1999; Lindner et al. 2002). In immiscible displacements, the capillary number controls the thickness of the thin film. For motion of finite bubbles in capillary tubes, in the limit of small capillary numbers, the thickness, t, of the film for Newtonian fluids is given by (Bretherton 1961):

$$\frac{t}{R} = 0.643(3Ca)^{2/3} \qquad 6.27$$

The film thickness scales with U^{α} with $\alpha = 2/3$. U is the displacement velocity. Addition of polymers has been observed to reduce the thickness of films (Lionti-Addad and Meglio 1992; Lindner et al. 2002). Ro and Homsy (1995) presented a theoretical analysis to calculate the film thickness immiscible displacements in Oldroyd-B and shear thinning viscoelastic fluids. It was shown that viscoelasticity reduces the thickness of film. The deviation from Newtonian fluids was attributed to normal stress effect and shear stress convection in the flow direction. The film thickness was shown to scale with U^{α} with a value of α = 4/3. Experiments by Lindner et al. (2002) for injection of air into PEO solutions observed an increase in finger width as compared to the prediction by the Saffman-Taylor solution. The finger widening was attributed to a change in the wetting film thickness. Experimental studies by Lajeunesse et al. (1997) showed that the displacing fluid forms a symmetric tongue across the gap between the Hele-Shaw cells in

miscible displacements. However, no experimental studies have been presented to study the effect of elasticity on the film thickness in miscible displacements.

A mass balance approach is used to estimate the average film thickness during the fluid displacements in glycerol and PEG-PEO solutions. Assuming that the fluids are incompressible, the thickness of the water (displacing fluid) averaged over the displaced area is calculated by dividing the amount of water injected at any time by the swept area. The swept area is calculated using 'ImageJ' as mentioned previously and shown in the snapshot in Figure 6.18. The average thickness of the film is then calculated by subtracting the thickness of water from the gap width and dividing by two (assuming a symmetric tongue of displacing fluid in the gap). A schematic of the symmetric tongue is shown in Figure 6.25.

Figure 6.26 and Figure 6.27 show the comparison of the average film thickness at different times in the polymer solutions (L1 and L2) and the glycerol solutions (T1 and T2) at an injection rate of 1.28ml/min. The data shows the film thickness is less in the more elastic fluid at the lowest injection rate. It is also observed that the average film thickness is almost constant at all times. Figure 6.28 and Figure 6.29 show the average film thickness at a higher injection rate of 4.69ml/min. The data shows a reverse in trend from the lower injection rate, showing that the film thickness is reduced due to fluid elasticity. With a further increase in injection rate to 12.35ml/min, the film thickness is observed to reduce further in the more elastic fluid (Figure 6.30 and Figure 6.31). It is

also observed that the average film thickness is not constant with time at the higher injection rates, suggesting displacement effects with increase in injection rates (Lajeunesse et al. 1999). This analysis suggests that elastic effects reduce the film thickness in miscible displacements. The elastic effects are quantified by the flow Deborah numbers (mentioned earlier in Section 6.3.3.2 and in Table 6.7). The Deborah numbers are higher at higher injection rates, leading to higher reduction in film thickness than the glycerol solutions. The results are in agreement with the theoretical analysis of Ro and Homsy (1995) and Lindner et al. (2002) for immiscible fluids.

The effect of flow rate on the RFW is investigated by plotting the RFW as a function of dimensionless time for different injection rates. The time is made dimensionless with the convective time, L/U. L is the length of the Hele-Shaw cell and U is the injection velocity. Figures 6.32 and 6.33 show the RFW for the two glycerol solutions, T1 and T2, respectively. The data show that the RFW does not change significantly with injection rate in these two glycerol solutions. Figure 6.34 and 6.35 show the RFW for the two polymer solutions, L1 and L2, respectively. In both the fluids it is observed that RFW reduces with increase in injection rates at all times. This suggests that effect of injection rate on reducing the RFW (or the sweep efficiency) is higher in more elastic fluids.

Investigation of the effect of injection rate on film thickness does not show any trend for glycerol as well as polymer solutions. Figures 6.36 and 6.37 show the film

thickness with dimensionless time in the two glycerol solutions, T1 and T2, respectively. In both the glycerol solutions, there is no clear trend of variation of film thickness with injection rate. The difference in the thicknesses at the three rates is not significant as well. Figures 6.38 and 6.39 show the film thickness with time in the two polymer solutions, L1 and L2 respectively. A greater variation in the film thickness with flow rate is observed in the polymer solutions as compared to glycerol solutions. In liquid L2, the film thickness reduces with increase in rate. The trend is not the same in liquid L1. At the highest rate in liquid L1, the average film thickness increases with time. This increase can be attributed to the three dimensional effects. We do not observe a reduction of the film thickness with increase in flow rates for Boger and Newtonian fluids, mentioned by the theoretical analysis of Ro and Homsy (1995).

6.4 Implications of Findings for Design of Fracture Treatments

In Section 5.5 in Chapter 5, we discussed the type of fracture treatments in which viscous fingers are used to transport proppant into the fracture. These include reverse-hybrid fracturing and alternate-slug fracturing. The findings from the experiments in this chapter provide further insight into design considerations of these treatments. Observations show that multiple thin fingers are formed in more elastic fluids as compared to single thick dominant finger in less elastic fluids. This suggests that more elastic gels would be more suitable for reverse-hybrid and alternate-slug fracture treatments. Multiple thin fingers will be able to transport proppant in different areas in the fracture, leading to heterogeneous proppant pack with conductive pathways for the

hydrocarbon to flow. Experimental results show that the finger velocities are reduced by the fluid elasticity. This suggests that the mixing between the slugs will be reduced when elastic gels are used. This effect will change the design pumping rate and size of the slugs in the fracture.

Using the same design criteria as used in Section 5.5 and the fracture properties as mentioned in Table 5.3, we estimate the design of the reverse-hybrid fracture treatment if an elastic polymer is used in the pad stage. The viscosity of the polymer is 500cP and the relaxation time is 0.1s. Results in Figure 6.16 and 6.17 show that the relative front velocities are reduced in the more elastic fluids, with an average reduction of 15%. The relative front velocity of water in the elastic polymer can be estimated to be 15% lower than 0.87m/s, equivalent to 0.74m/s. Given that the injection velocity of the polymer pad ahead of the water is 0.29m/s, the length of the polymer slug should be 1.55 times longer than the water slug. This will ensure that the water fingertip just reaches the polymer front at the end of the treatment. Using a polymer solution with a very low relaxation time (less elastic), the calculations in Section 5.5 showed that the polymer slug should be 2 times longer than the water slug. Thus, elasticity of the polymer changes the design of the fracture job by changing the length of the slugs of polymer and water.

6.5 CONCLUSIONS

This chapter presented an experimental study to determine the influence of elasticity on miscible viscous fingering patterns. The following are the main conclusions:

- Experimental results are presented to show that fluid elasticity of the displaced fluid changes the finger patterns in miscible viscous fingering.
- Fluid elasticity leads to the formation of thin long fingers in fully developed flow, as compared to a single thick finger in less elastic glycerol solutions with the same viscosity.
- Fluid elasticity is observed to reduce the shielding effect, resulting in the growth of multiple fingers as compared to a single thick dominant finger observed in glycerol solutions.
- Results illustrate that the dominant wave numbers are higher in more elastic fluids. Greater numbers of fingers evolve at the onset of instability in Boger fluids.
- The front velocities are observed to be lower in Boger fluids as compared to Newtonian fluids of the same viscosity.
- Results show that the relative finger widths (RFWs) are higher in the more elastic fluids at low injection rates. A transition to lower RFWs is observed at higher injection rates. This suggests that the sweep efficiencies reduce faster with injection rates in more elastic fluids.

- The displaced fluid film thickness is observed to reduce in the more elastic fluid (relative to the glycerol solution) with increase in flow rate. The observations are consistent with the analysis of Ro and Homsy (1995) for immiscible displacements in viscoelastic fluids.

Table 6.1: Concentrations and viscosities of the PEG-PEO solutions used in the experiments.

Liquid	Amount of PEG-8000, wt%	Amount of PEO-4,000,000, wt%	Viscosity, cP
L1	37.5	0.08	156
L2	37.5	0.14	176

Table 6.2: Concentrations and viscosities of glycerol solutions used in the experiments.

Liquid	Amount of Glycerin, wt%	Viscosity, cP
T1	88.2	156
T2	89	176

Table 6.3: Relaxation strengths, G_k and relaxation times, λ_k estimated using non-linear regression.

Liquid	G_k, Pa	λ_k, s
L1	70.605 0.2277	0.0022 0.096
L2	62.405 0.01079	0.0024 0.7583
T1	130.535	0.001
T2	110.42	0.00135

Table 6.4: Peclet numbers for injection of distilled water into glycerol solutions at different injection rates.

Glycerol Weight %	$D \times 10^9$ (m^2/s)	Peclet number (Pe) at water injection rate of		
		12.35 ml/min	4.69 ml/min	1.28 ml/min
88.2	0.089	46417	17624	4808
89	0.083	49389	18753	5116

Table 6.5: Comparison of the dominant wave numbers in cm^{-1} at different injection rates in Liquids L1 and T1.

Injection Rate (ml/min)	Liquid L1 37.5%PEG 0.08%PEO	Liquid T1 88.2% Glycerol
12.35	20	7
4.69	19.5	12
1.28	22	11

Table 6.6: Comparison of the dominant wave numbers in cm^{-1} at different injection rates in Liquids L2 and T2.

Injection Rate (ml/min)	Liquid L2 37.5%PEG 0.14%PEO	Liquid T2 89% Glycerol
12.35	20	19
4.69	25.5	22
1.28	31	12

Table 6.7: Flow Deborah numbers based on fingertip velocities at different injection rates.

Injection Flow Rate	12.35 ml/min	4.69ml/min	1.28ml/min
L1	21.743	7.079	1.964
T1	0.044	0.016	0.004
L2	2.985	0.958	0.241
T2	0.082	0.079	0.071

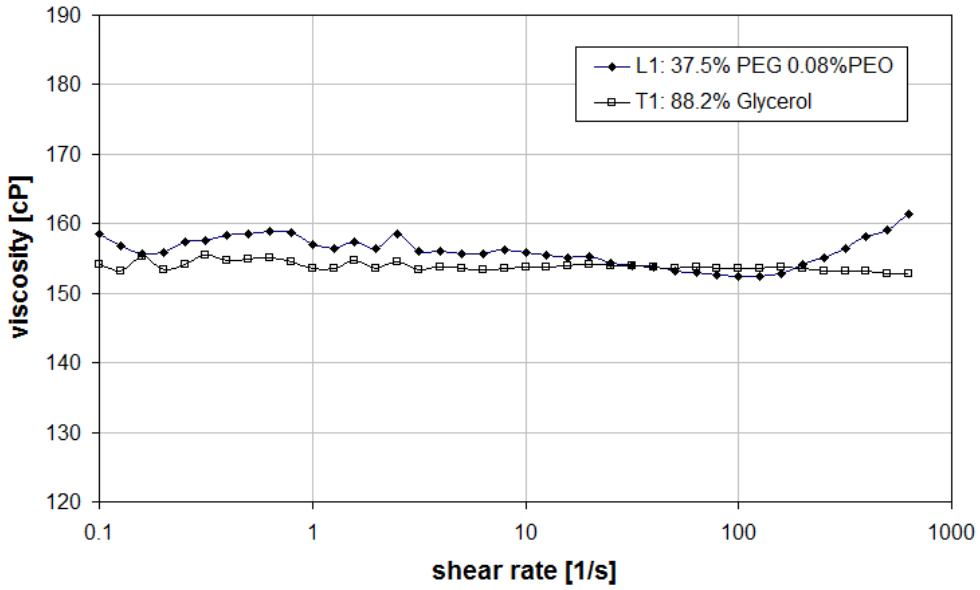

Figure 6.1: Steady shear viscosity as a function of shear rate for Liquids L1 and T1.

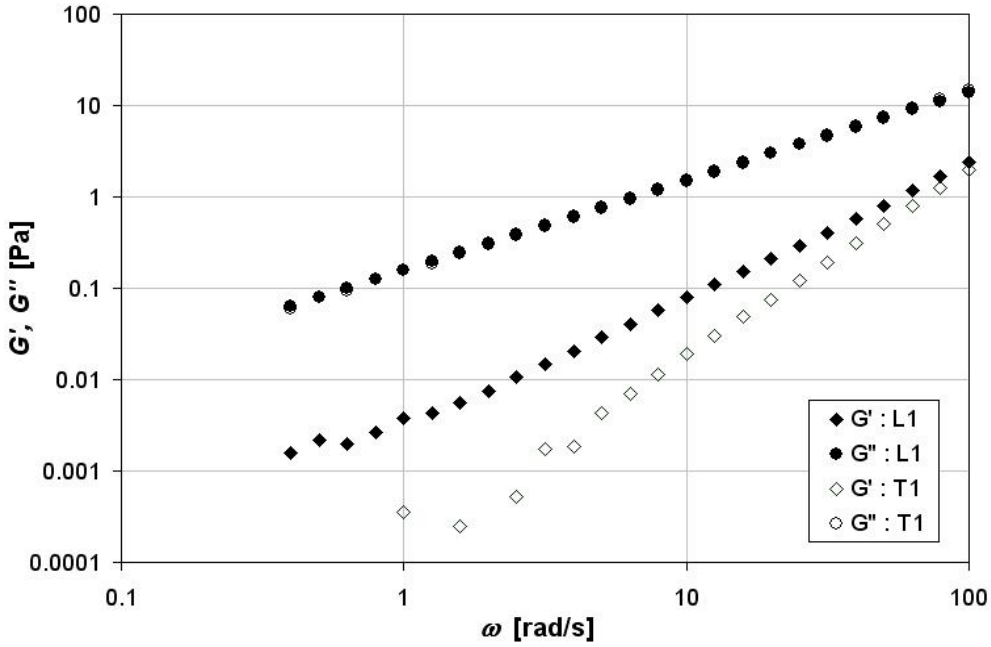

Figure 6.2: Dynamic oscillatory-shear properties of fluids L1 and T1.

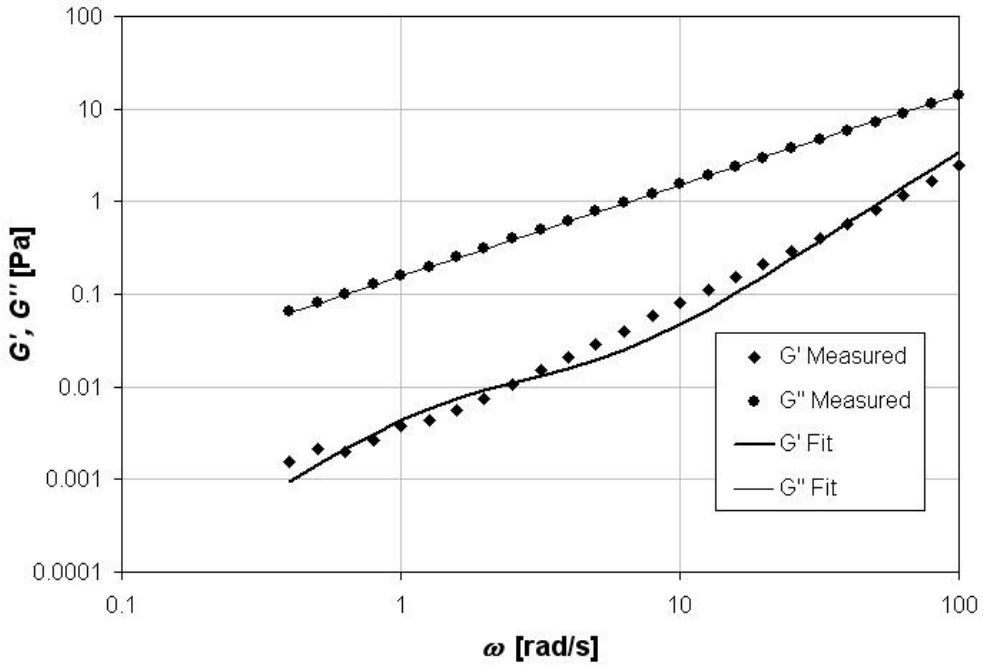

Figure 6.3: Comparison of the measured dynamic moduli with that fitted using a 2 element series Maxwell model for liquid L1.

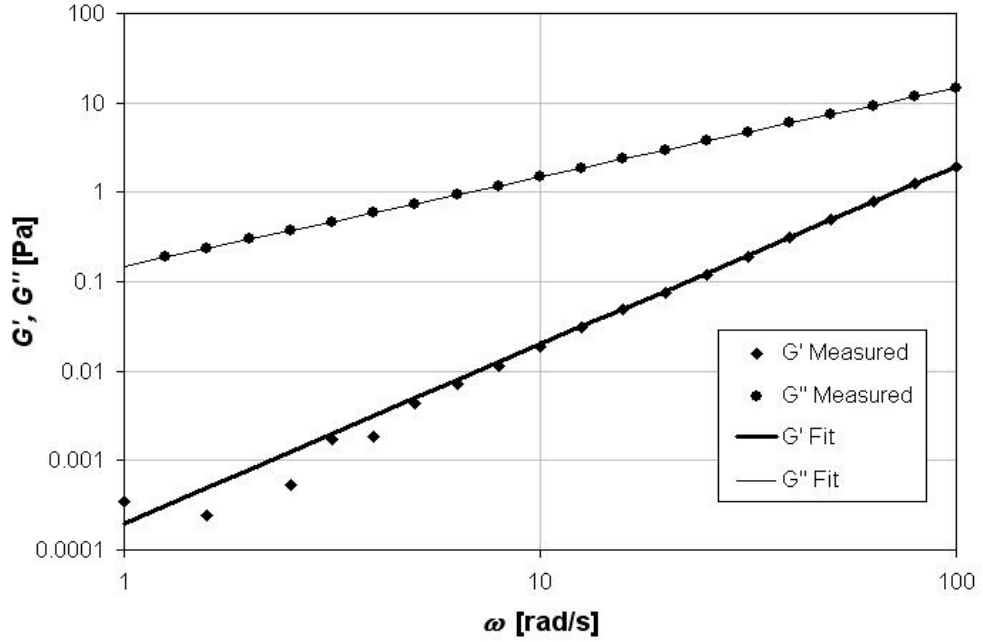

Figure 6.4: Comparison of the measured dynamic moduli with that fitted using a 1element Maxwell model for liquid T1.

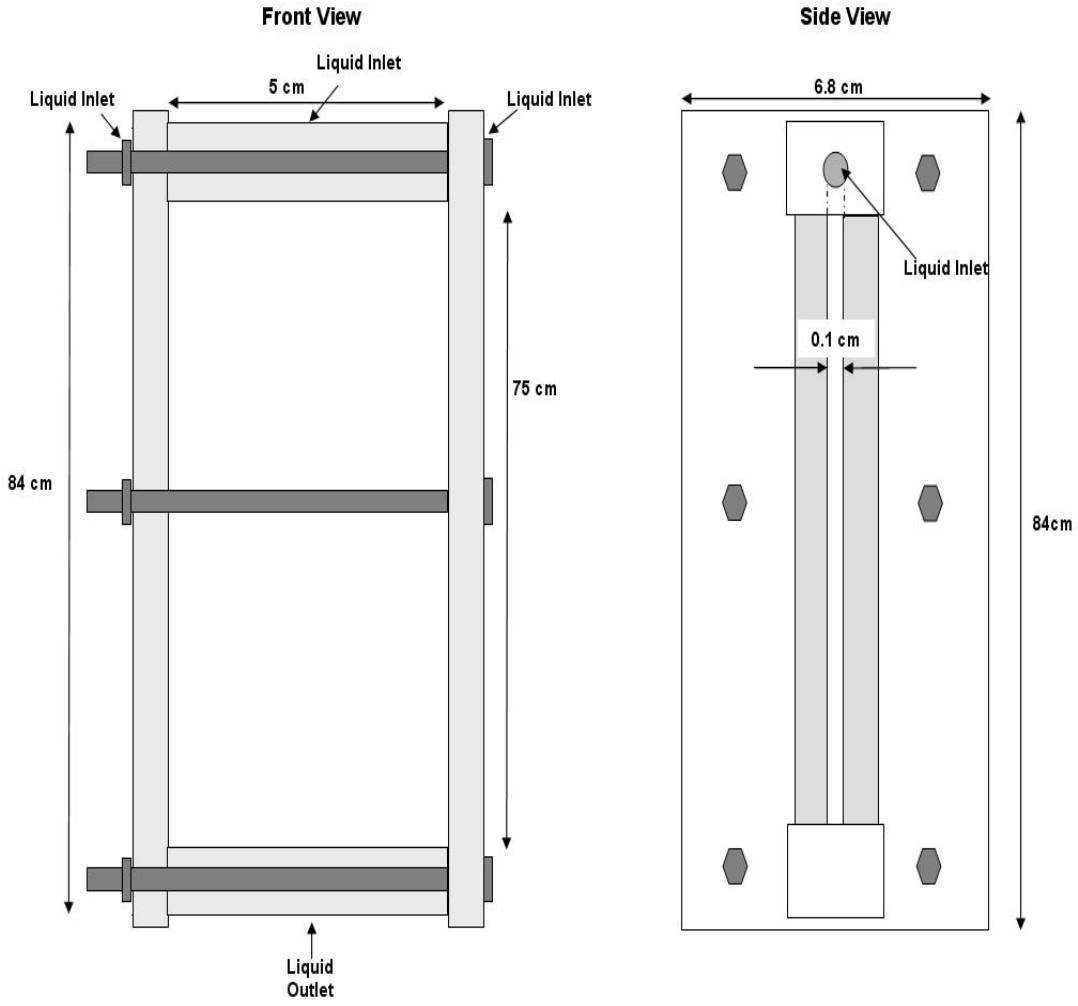

Figure 6.5: Schematic of the Hele-Shaw cell (not to scale).

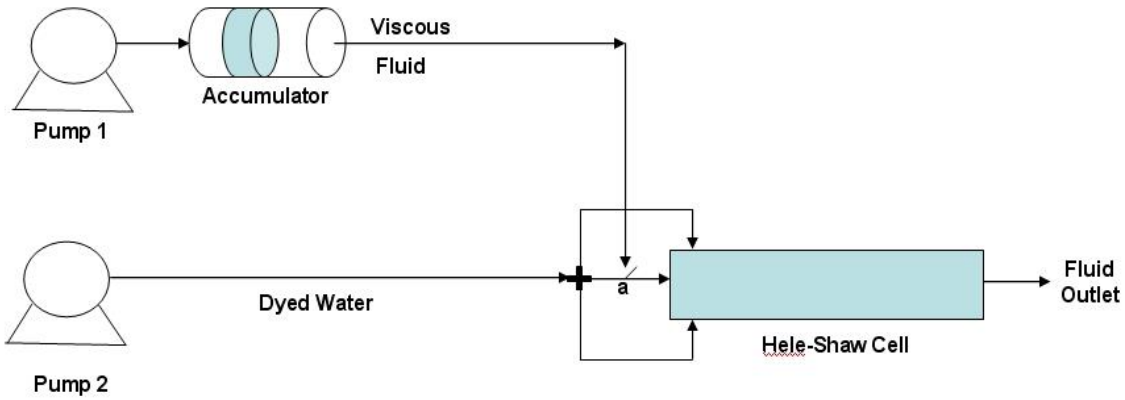

Figure 6.6: Sketch of the experimental setup showing the two pumps, with the accumulator and the Hele-Shaw cell.

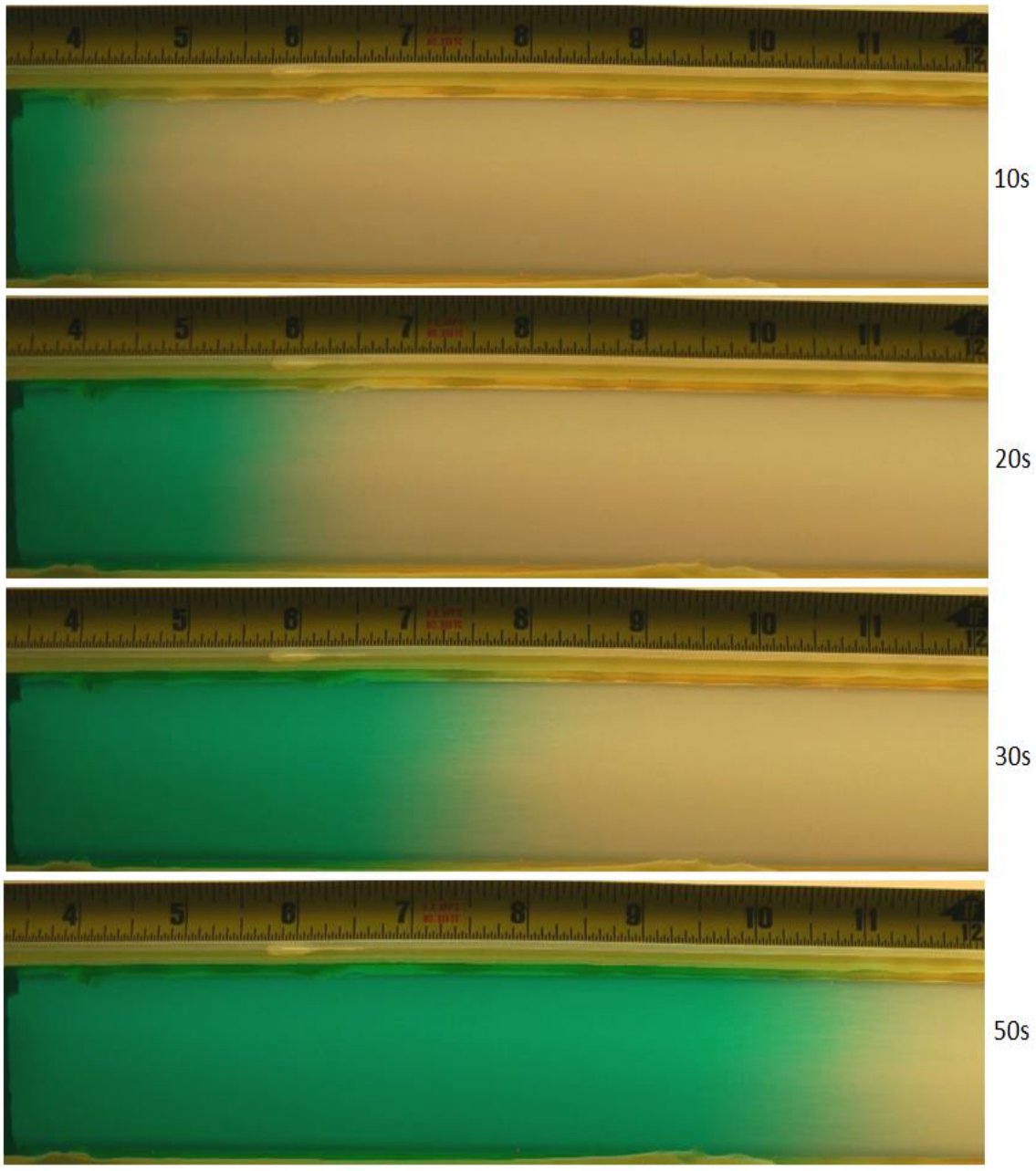

Figure 6.7: Sequential position of the interface between clear water and dyed water. Dyed water is injected into clear water at a rate of 12.35ml/min.

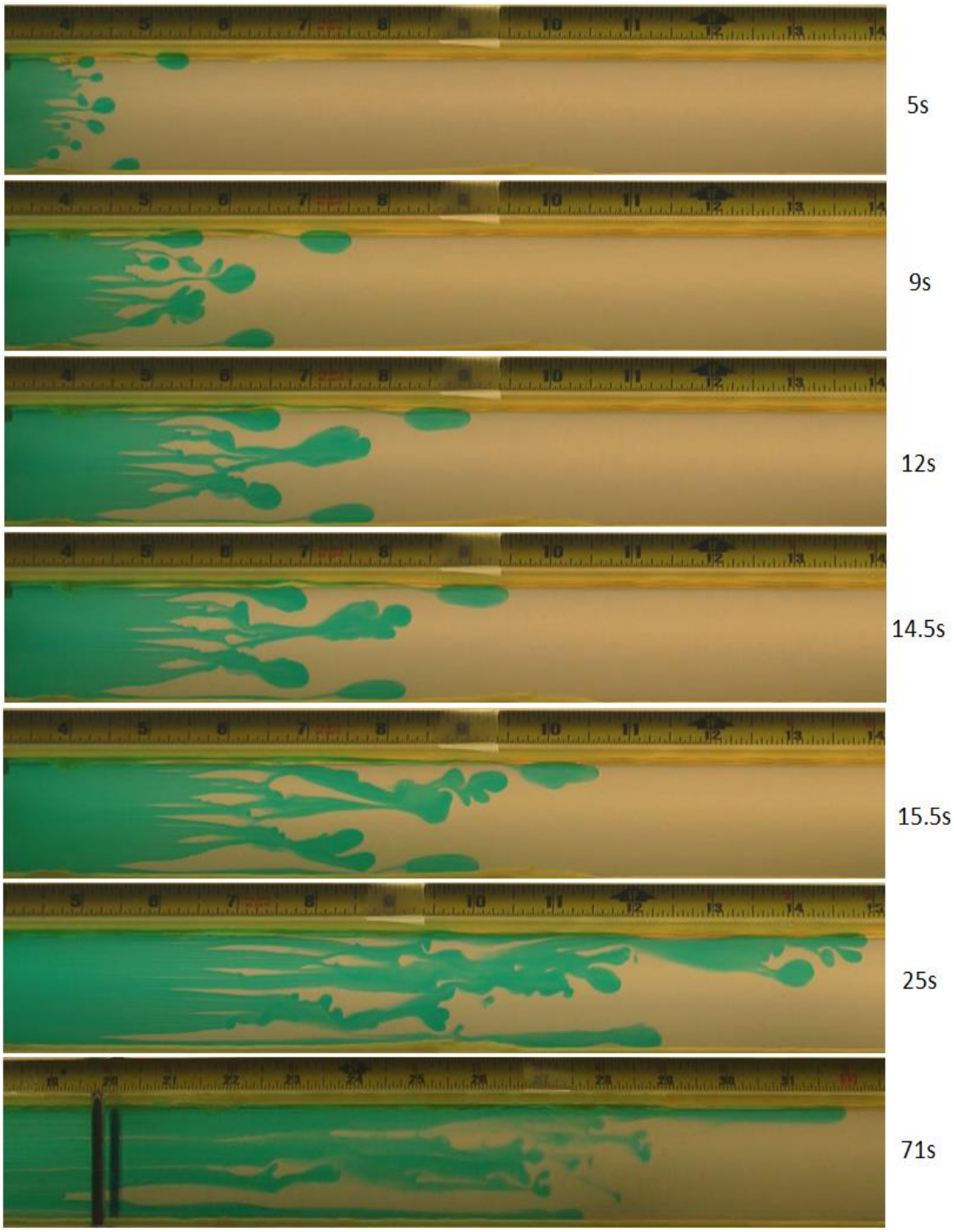

Figure 6.8: Sequential evolution of the interface between water and 37.5%PEG 0.08%PEO solution (Liquid L1). Water is injected at a rate of 12.35ml/min.

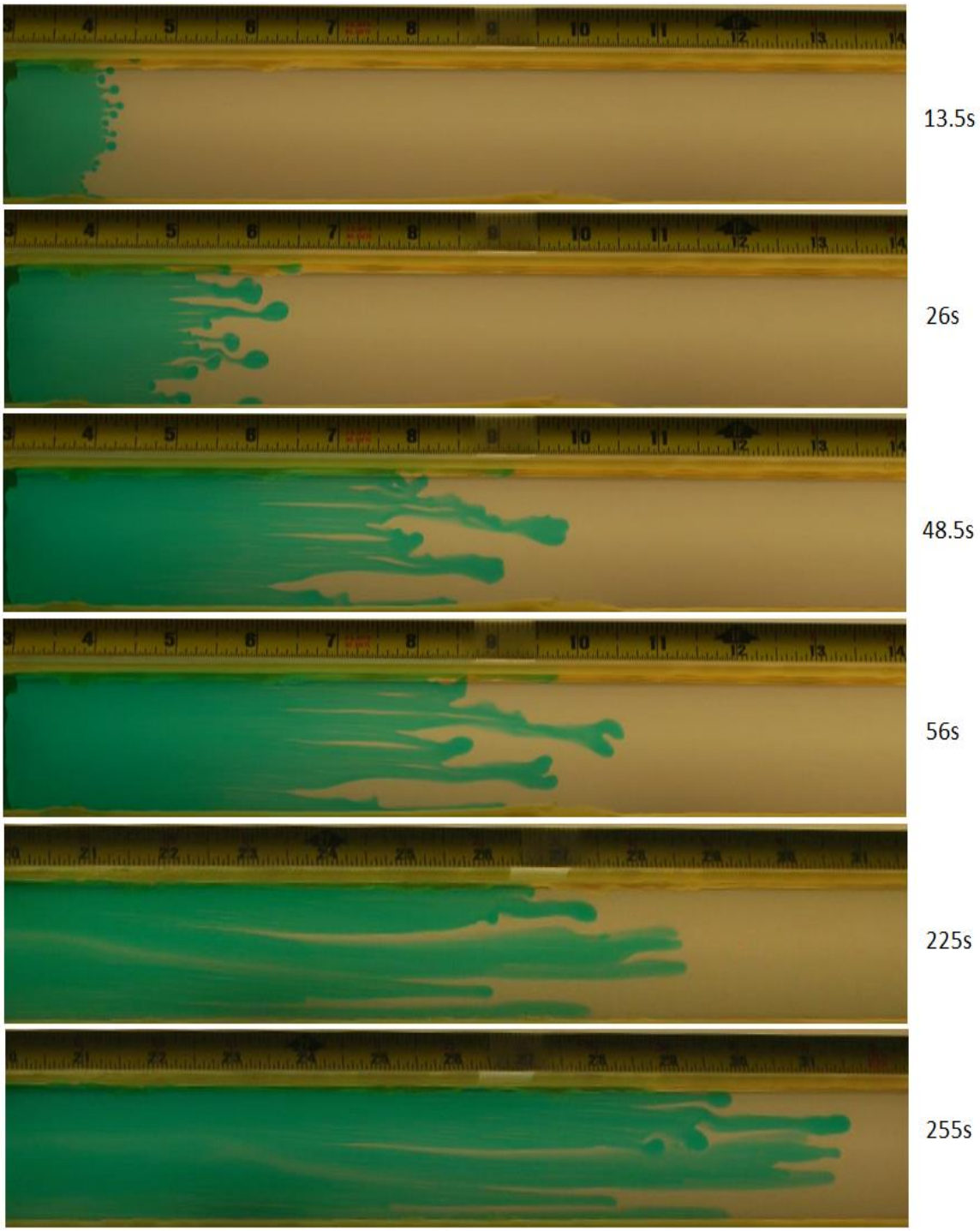

Figure 6.9: Sequential evolution of the interface between water and 37.5%PEG 0.08%PEO solution (Liquid L1). Water is injected at a rate of 4.69ml/min.

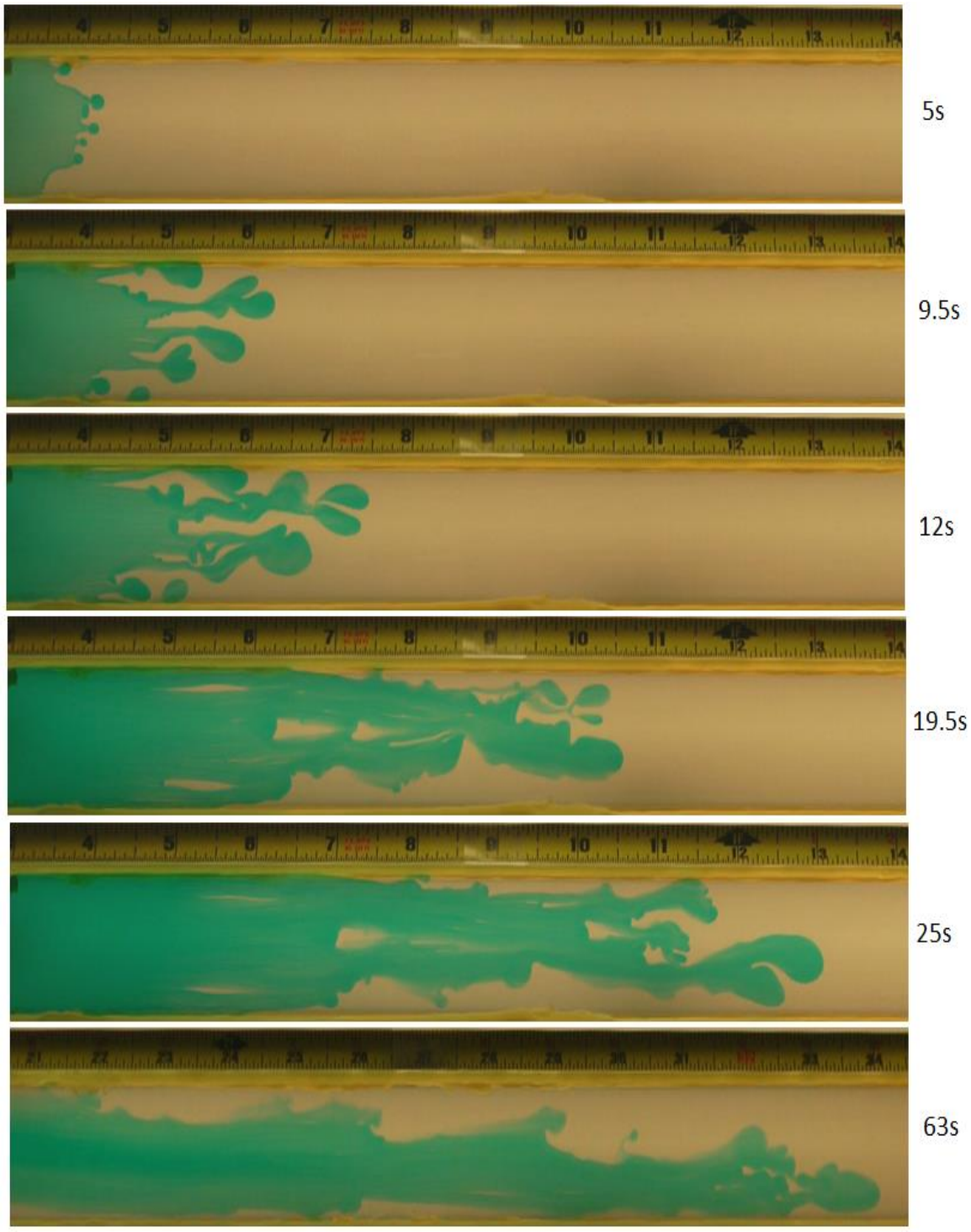

Figure 6.10: Sequential evolution of the interface between water and 88.2% glycerol solution (Liquid T1). Water is injected at a rate of 12.35ml/min.

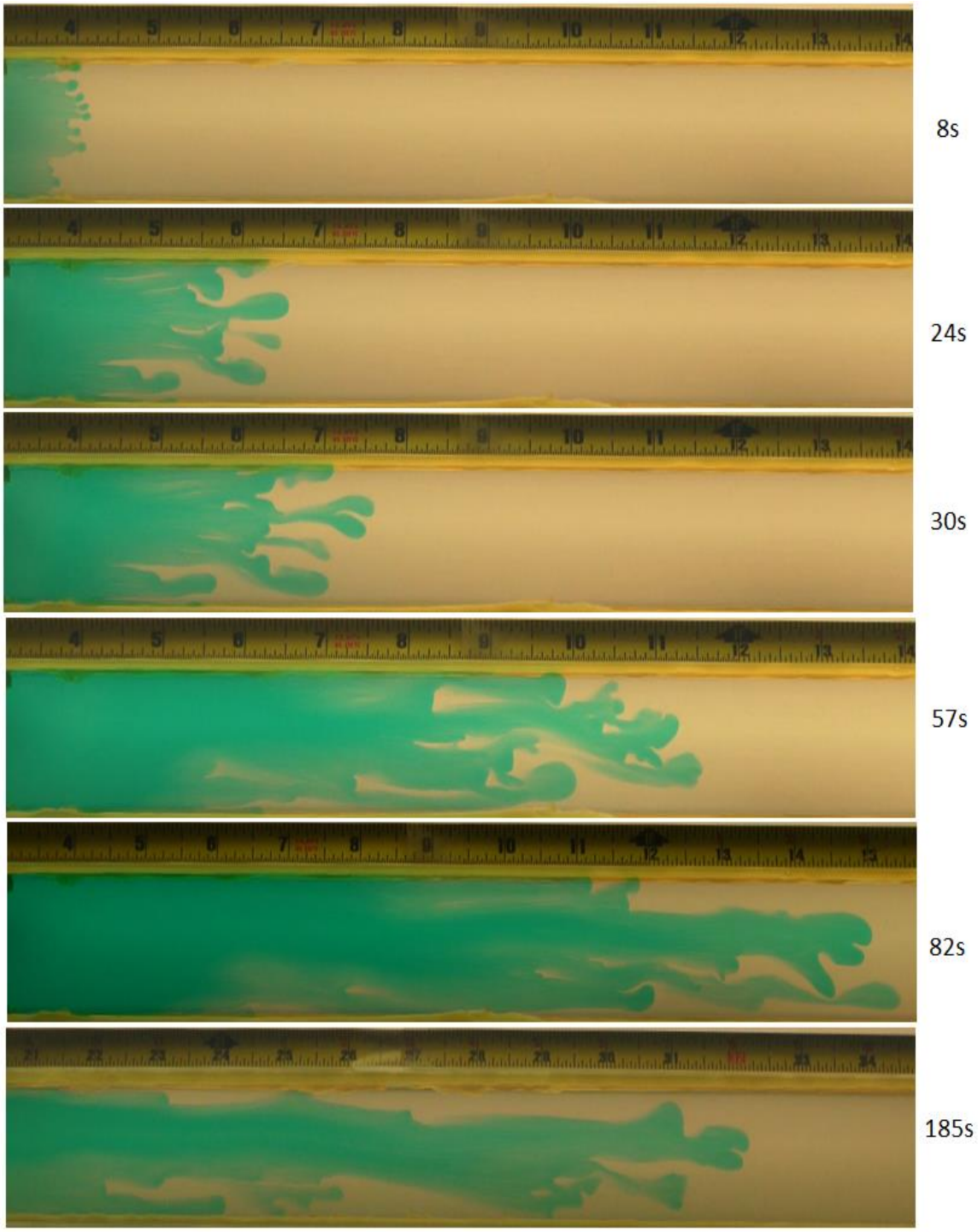

Figure 6.11: Sequential evolution of the interface between water and 88.2% glycerol solution (Liquid T1). Water is injected at a rate of 4.69ml/min.

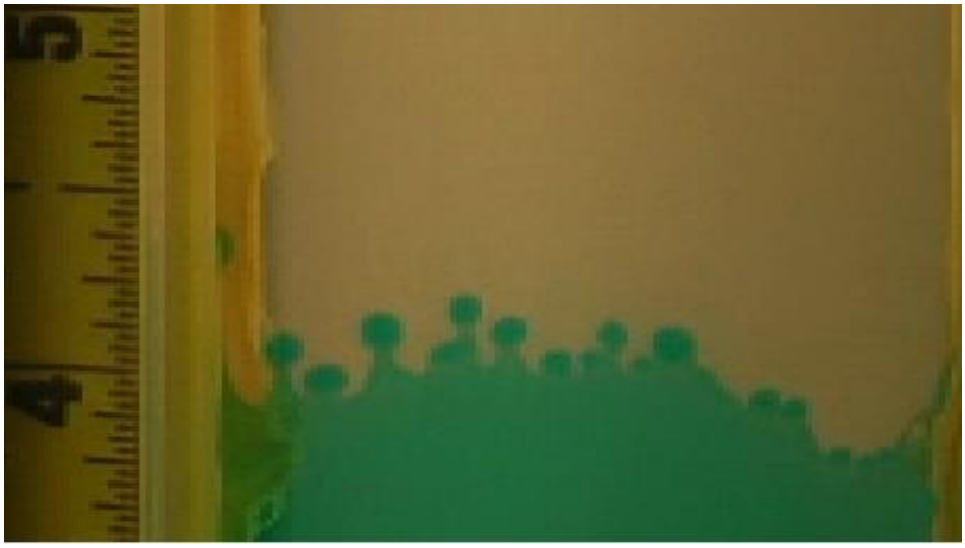

Figure 6.12: Snapshot showing the evolution of the instability for injection of water in 37.5%PEG 0.08%PEO solution (Liquid L1) at a rate of 4.69ml/min. Snapshot is taken at 18.5 seconds after starting the injection.

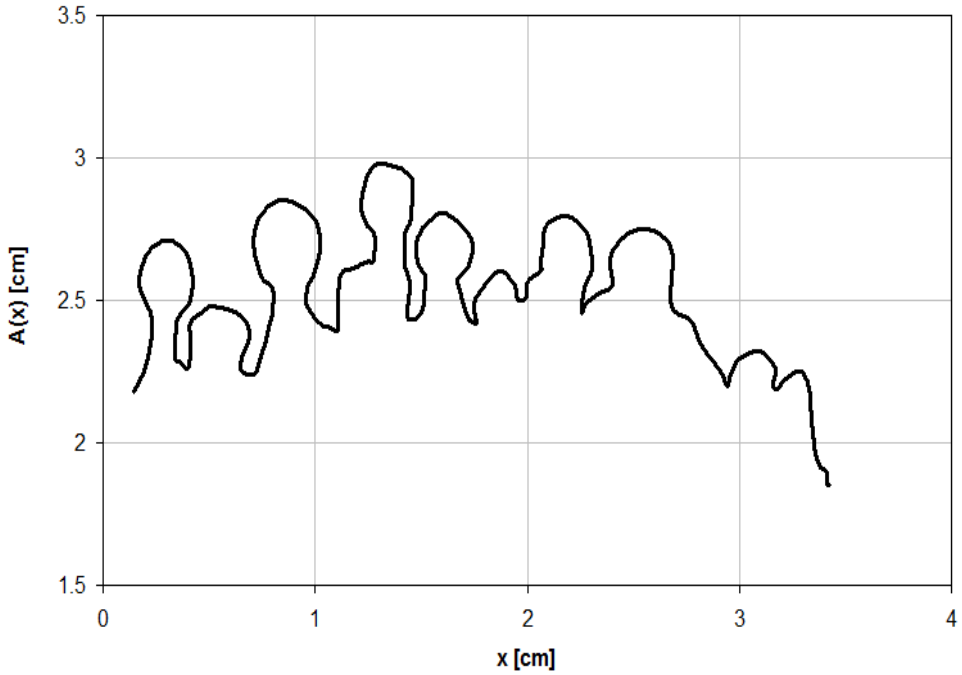

Figure 6.13: Interface between the displaced and displacing fluid tracked from Figure 6.12 using 'Plot Digitizer'.

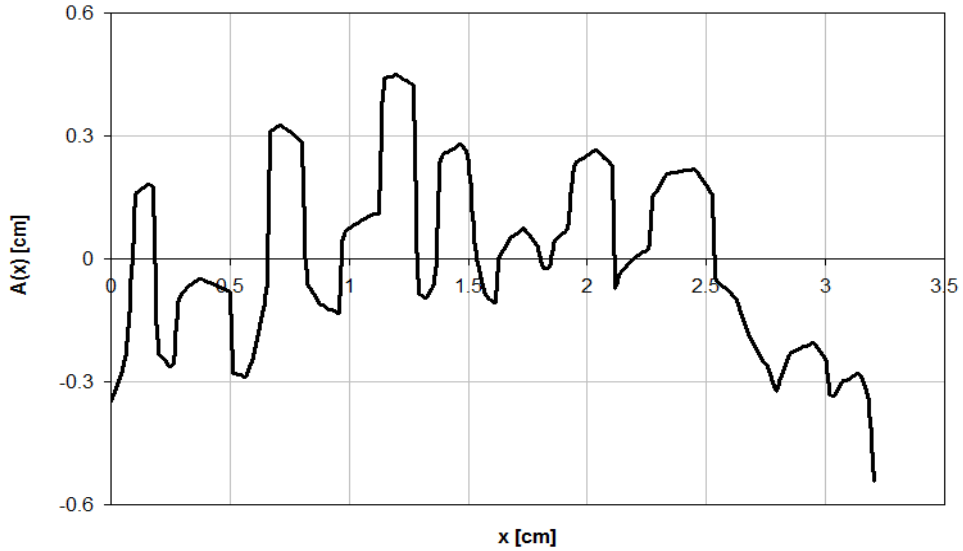

Figure 6.14: Modified profile of the interface between the two fluids to ensure that there is a unique value of A for every x.

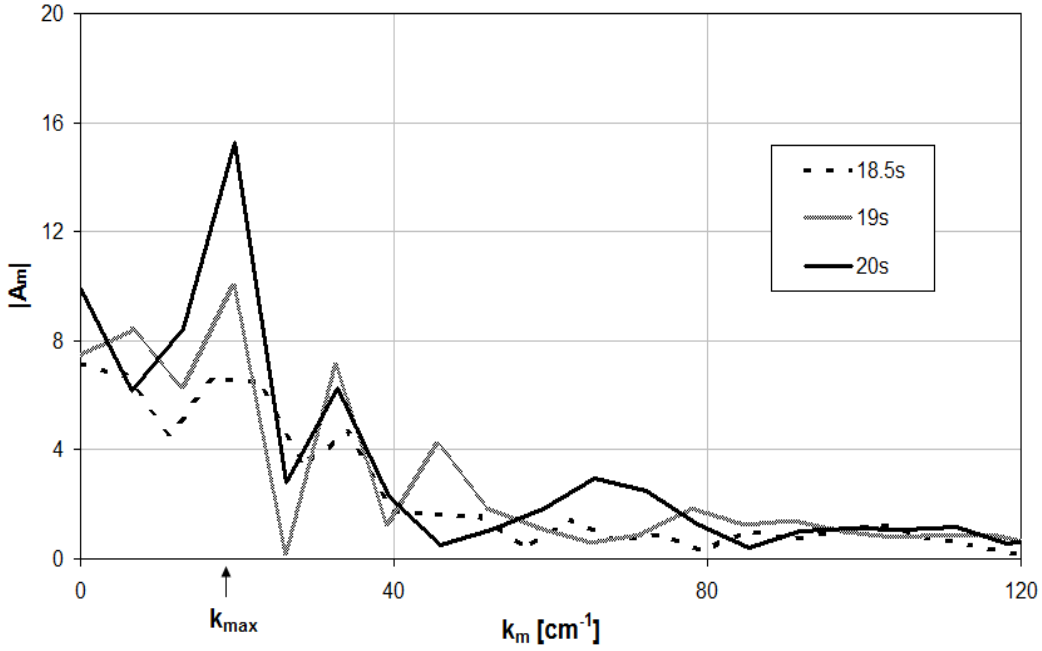

Figure 6.15: The spectrum of the wave numbers for interface evolution between water and 37.5%PEG 0.08%PEO (Liquid L1) at an injection rate of 4.69ml/min. The dominant wave number is 20 cm^{-1}.

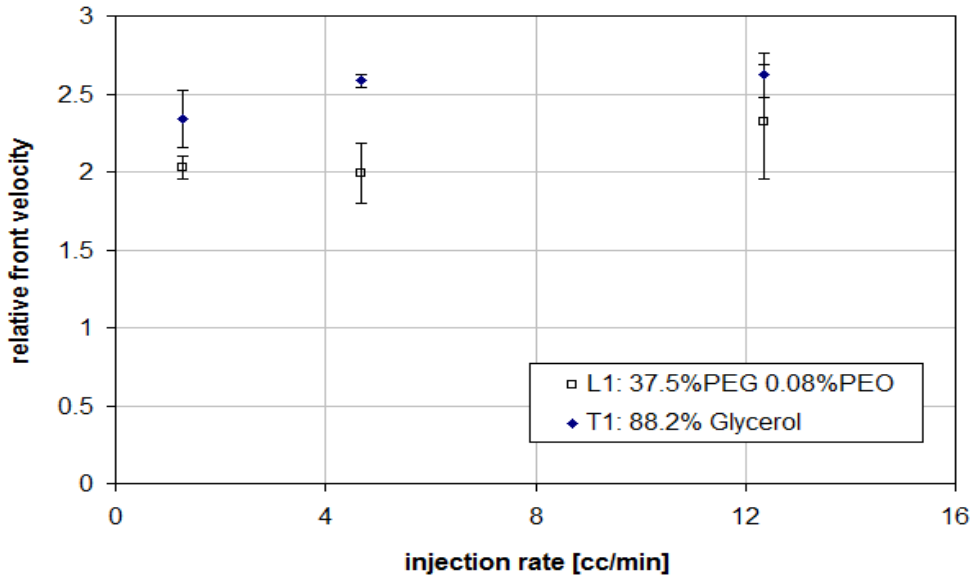

Figure 6.16: Relative front velocities (RFV) as a function of the injection rate in liquids L1 and T1.

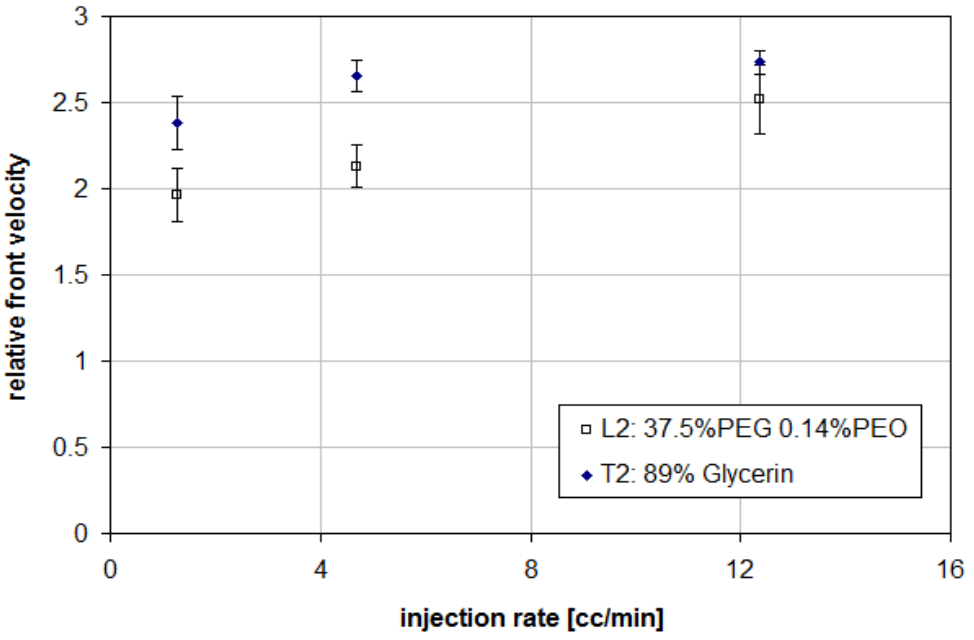

Figure 6.17: Relative front velocities (RFV) as a function of the injection rate in liquids L2 and T2.

Figure 6.18: Snapshot of the outlined interface between the displacing and displaced fluid. The area covered by the displacing fluid is calculated using ImageJ.

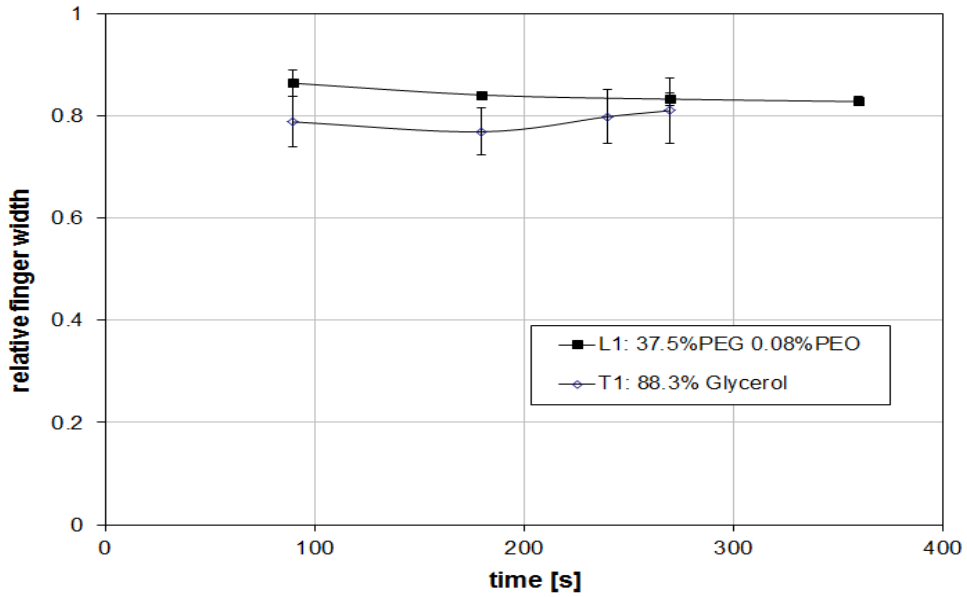

Figure 6.19: Relative finger width as a function of time at an injection rate of 1.28ml/min for liquids L1 and T1.

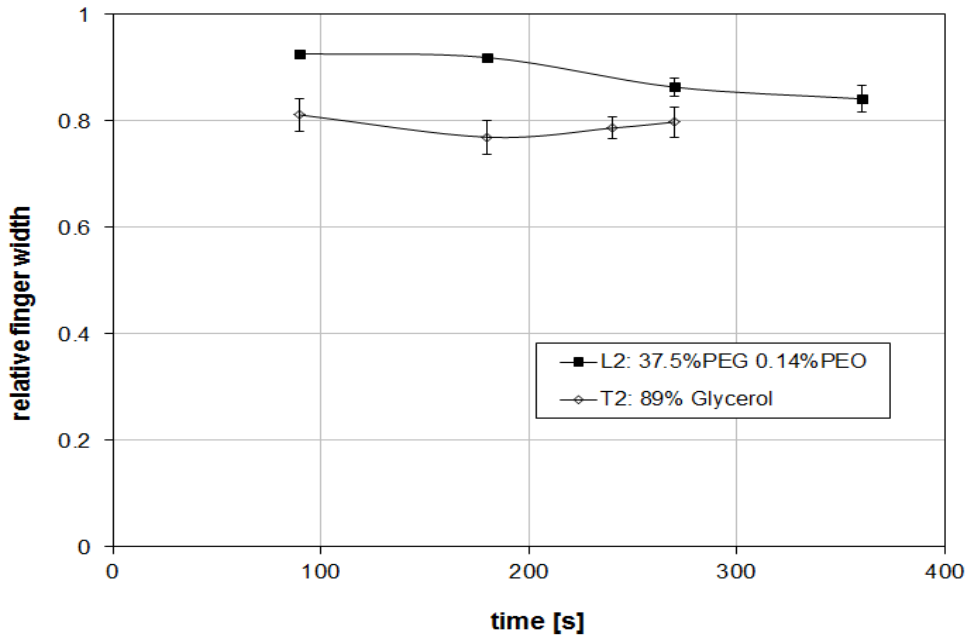

Figure 6.20: Relative finger width as a function of time at an injection rate of 1.28ml/min for liquids L2 and T2.

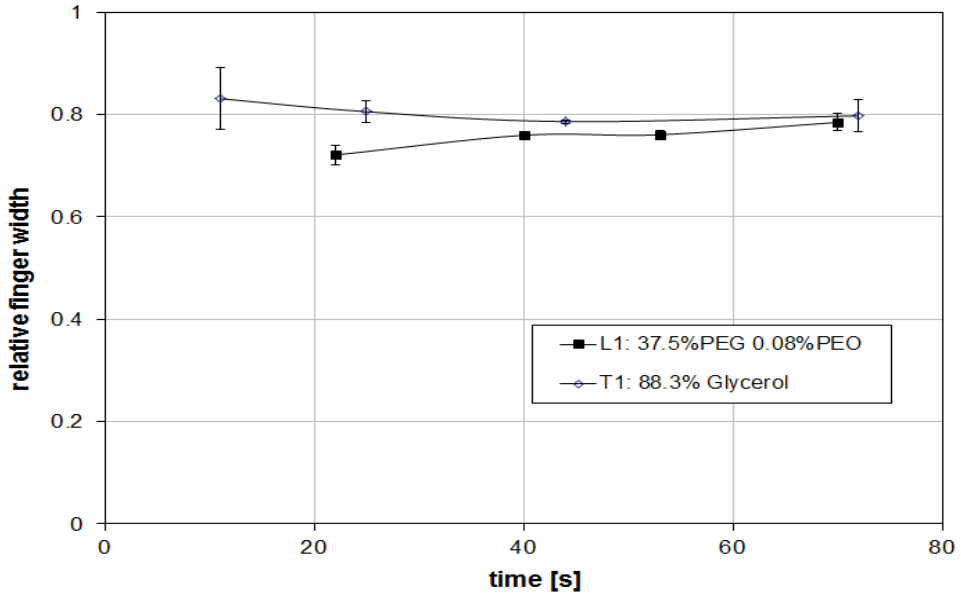

Figure 6.21: Relative finger width as a function of time at an injection rate of 4.69ml/min for liquids L1 and T1.

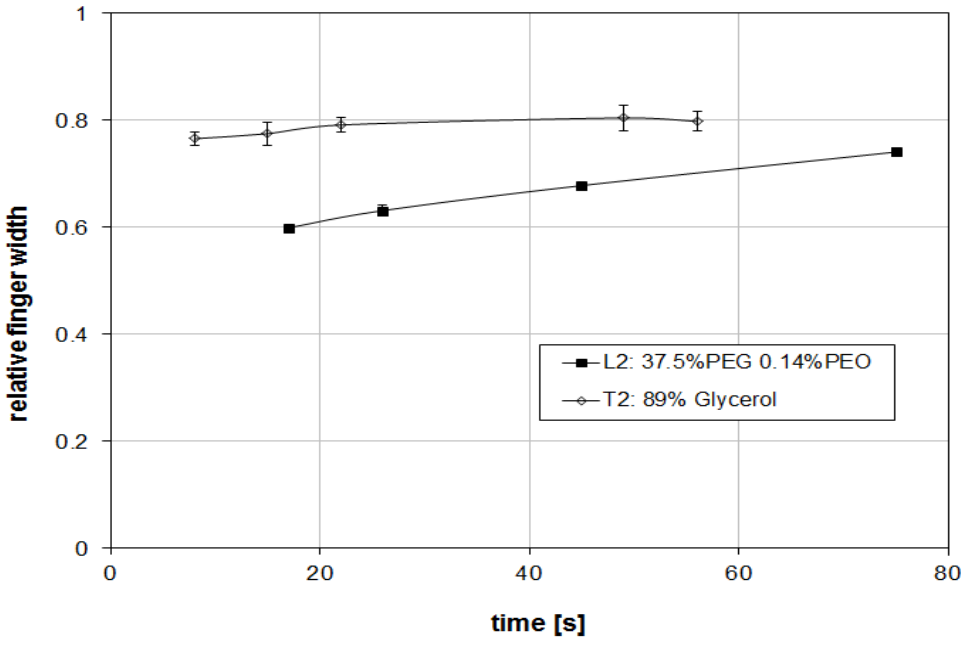

Figure 6.22: Relative finger width as a function of time at an injection rate of 4.69ml/min for liquids L2 and T2.

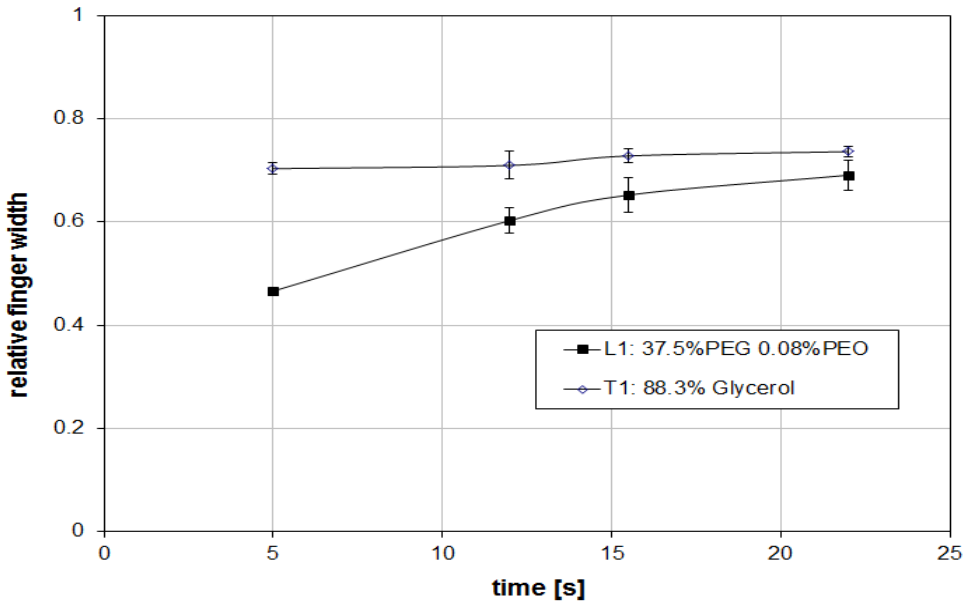

Figure 6.23: Relative finger width as a function of time at an injection rate of 12.35ml/min for liquids L1 and T1.

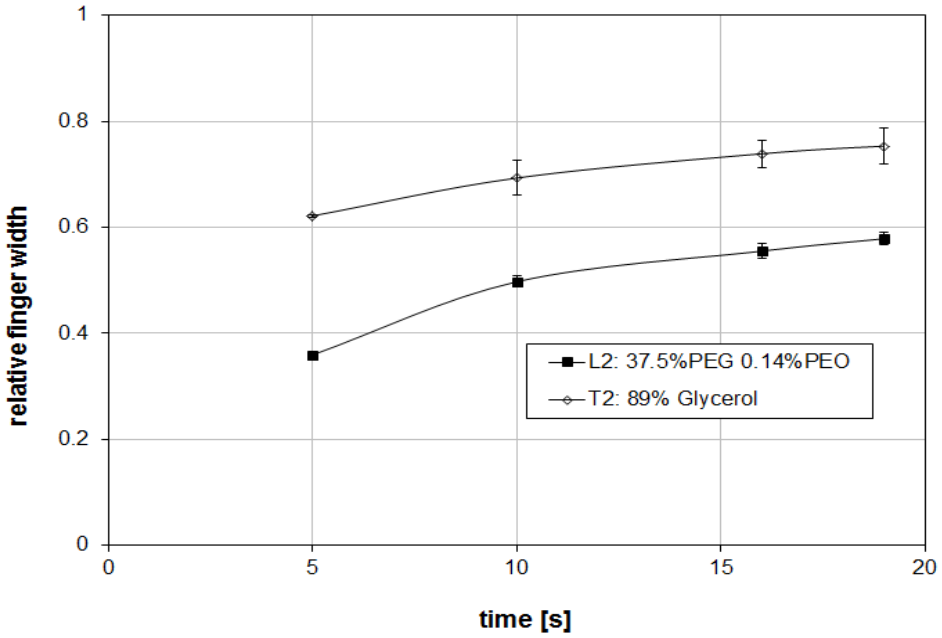

Figure 6.24: Relative finger width as a function of time at an injection rate of 12.35ml/min for liquids L2 and T2.

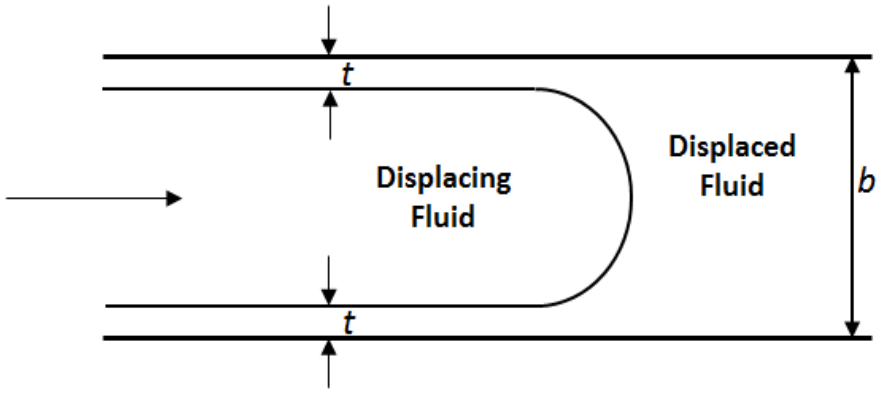

Figure 6.25: Schematic showing the symmetric tongue of the injected fluid. *t* denotes the thickness of the film of the displaced fluid on the walls.

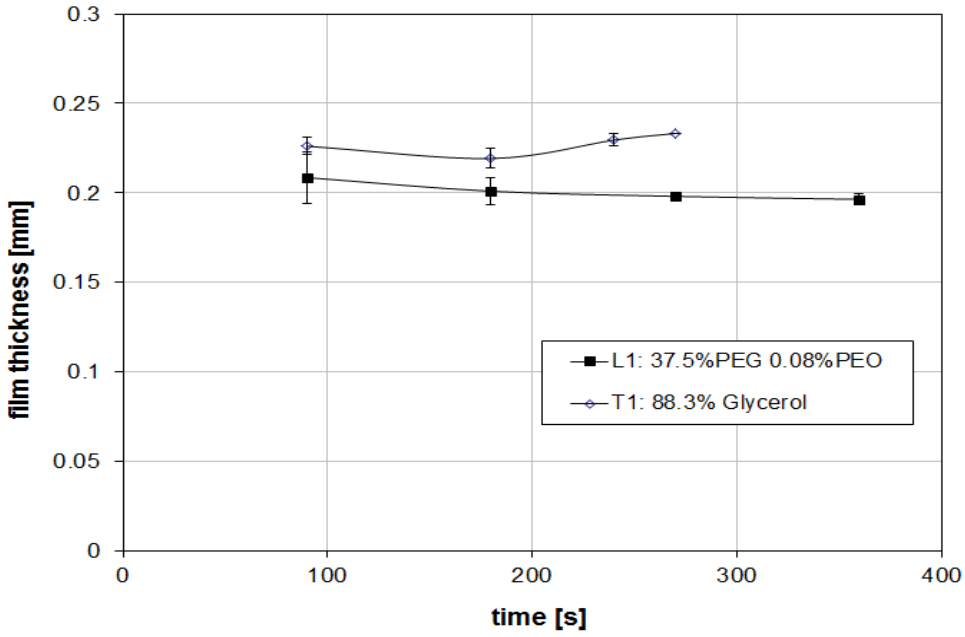

Figure 6.26: Thickness of the displaced fluid film on the walls for Liquids L1 and T1 at an injection rate of 1.28ml/min.

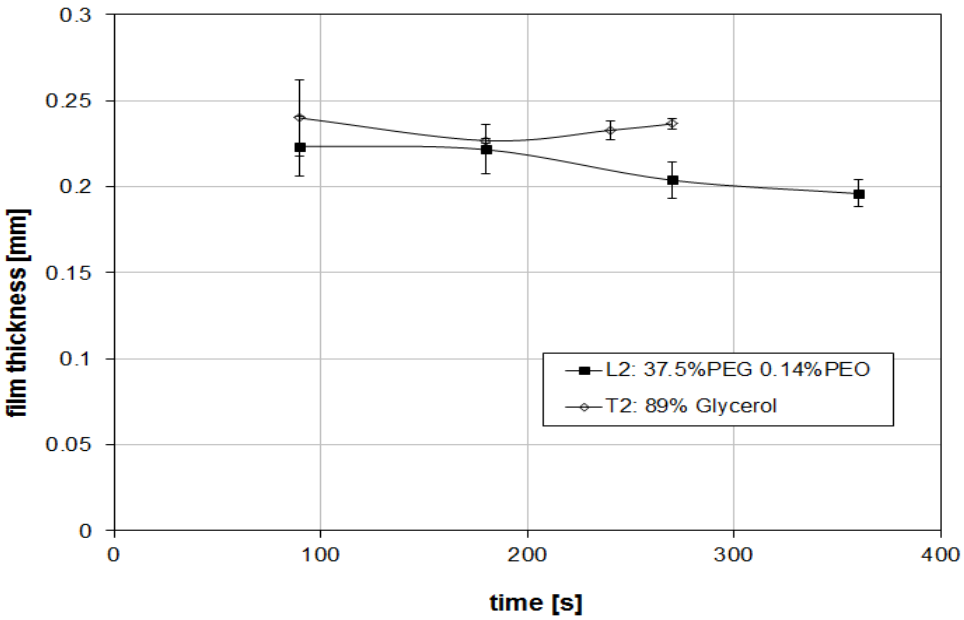

Figure 6.27: Thickness of the displaced fluid film on the walls for Liquids L2 and T2 at an injection rate of 1.28ml/min.

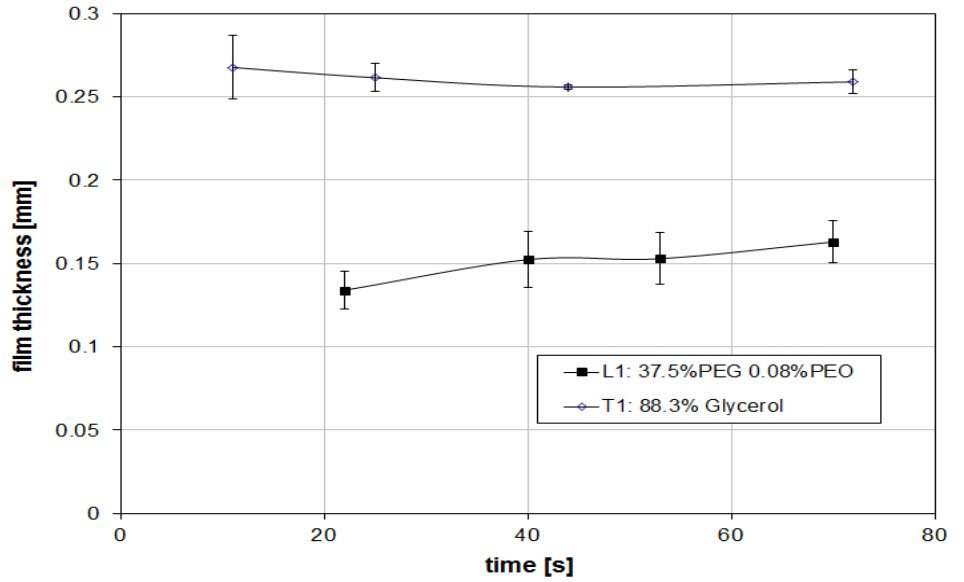

Figure 6.28: Thickness of the displaced fluid film on the walls for Liquids L1 and T1 at an injection rate of 4.69ml/min.

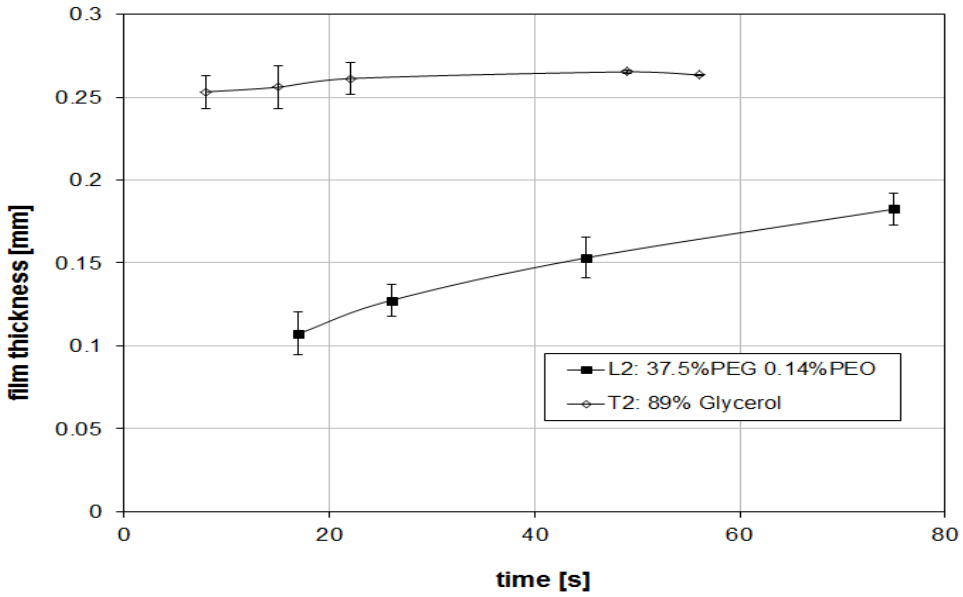

Figure 6.29: Thickness of the displaced fluid film on the walls for Liquids L2 and T2 at an injection rate of 4.69ml/min.

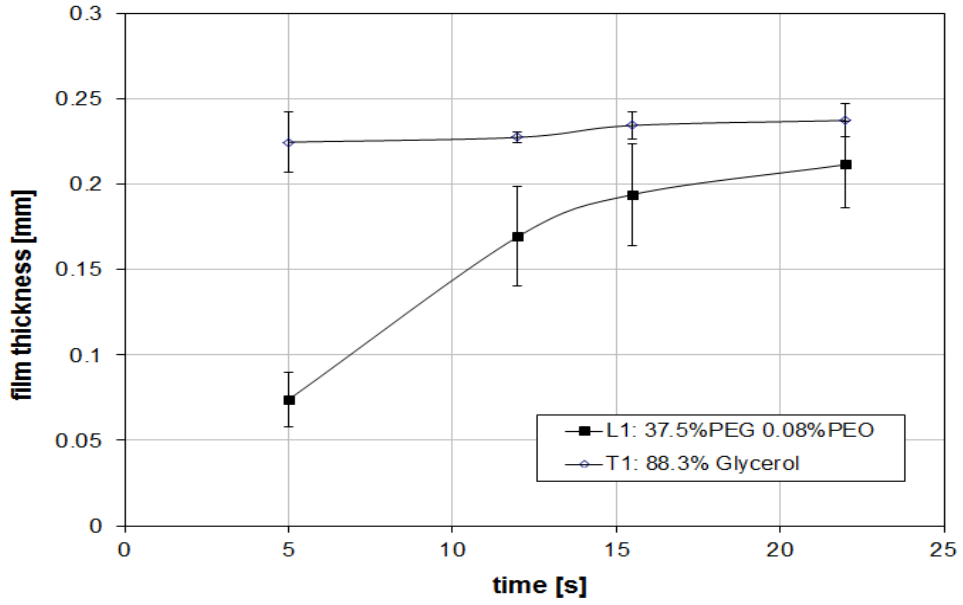

Figure 6.30: Thickness of the displaced fluid film on the walls for Liquids L1 and T1 at an injection rate of 12.35ml/min.

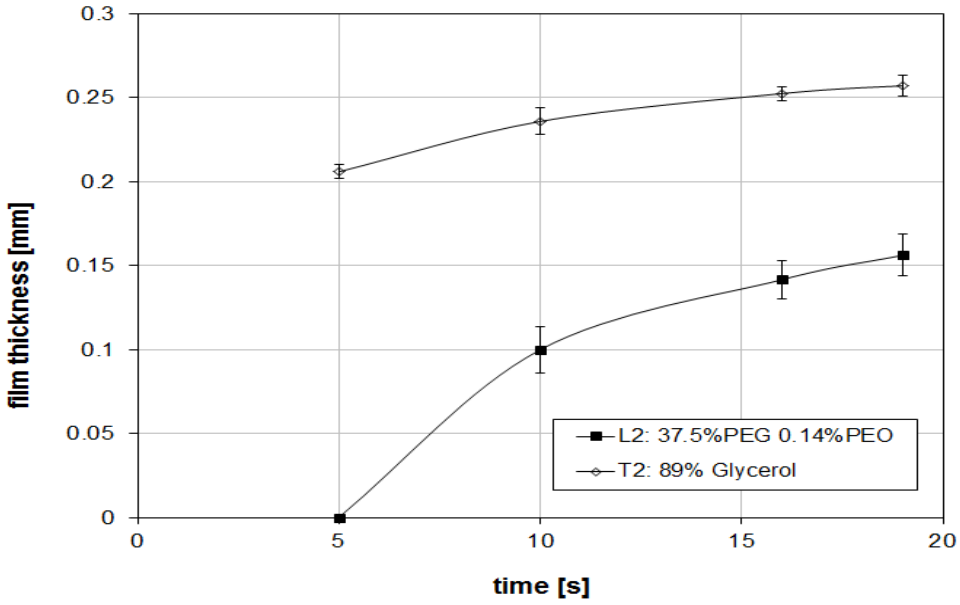

Figure 6.31: Thickness of the displaced fluid film on the walls for Liquids L2 and T2 at an injection rate of 12.35ml/min.

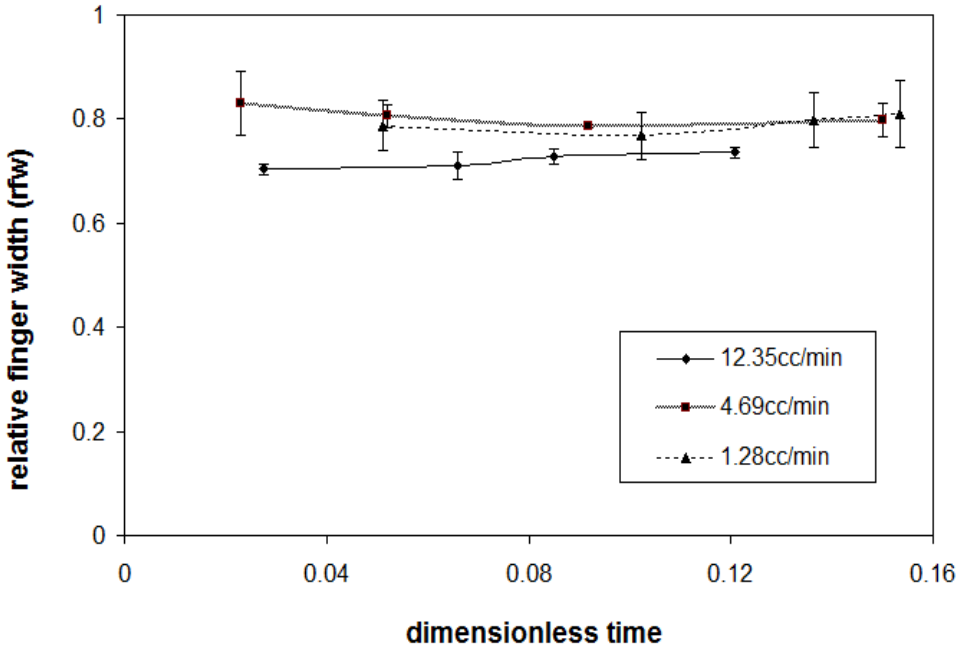

Figure 6.32: Relative finger width as a function of dimensionless time for different injection rates of water in 88.2% glycerol (T1) solution.

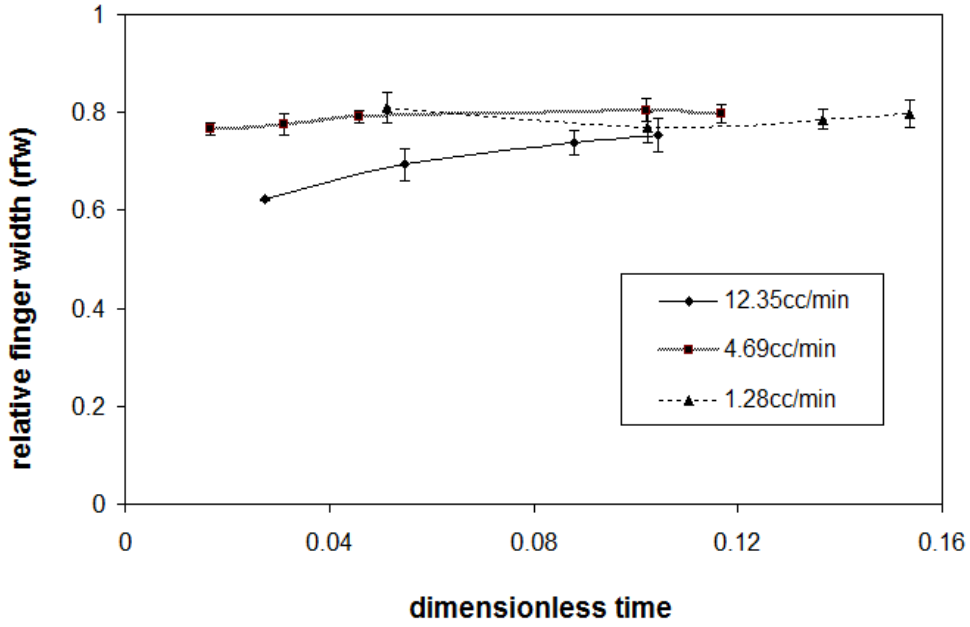

Figure 6.33: Relative finger width as a function of dimensionless time for different injection rates of water in 89% glycerol (T2) solution.

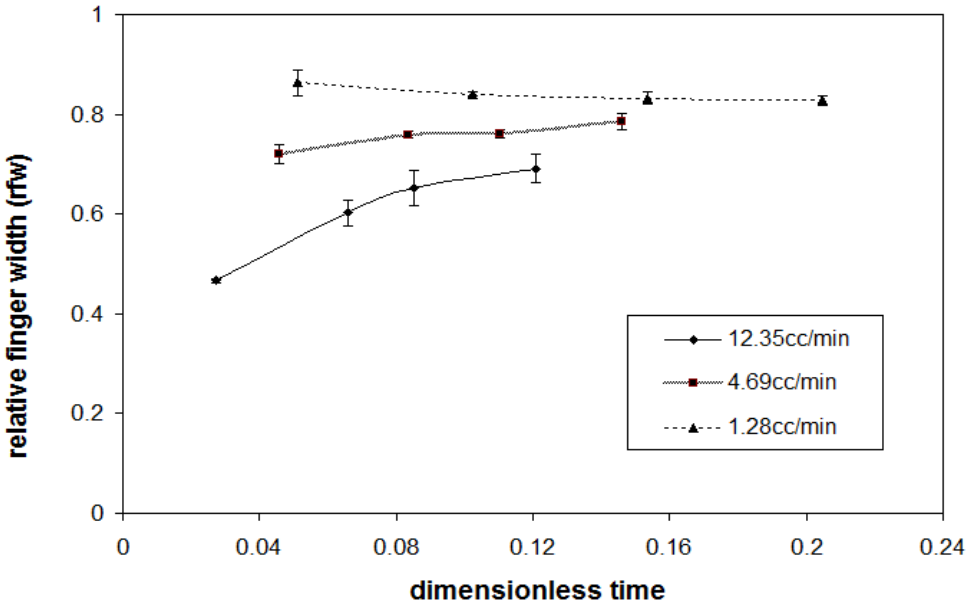

Figure 6.34: Relative finger width as a function of dimensionless time for different injection rates of water in 37.5%PEG 0.08%PEO (L1) solution.

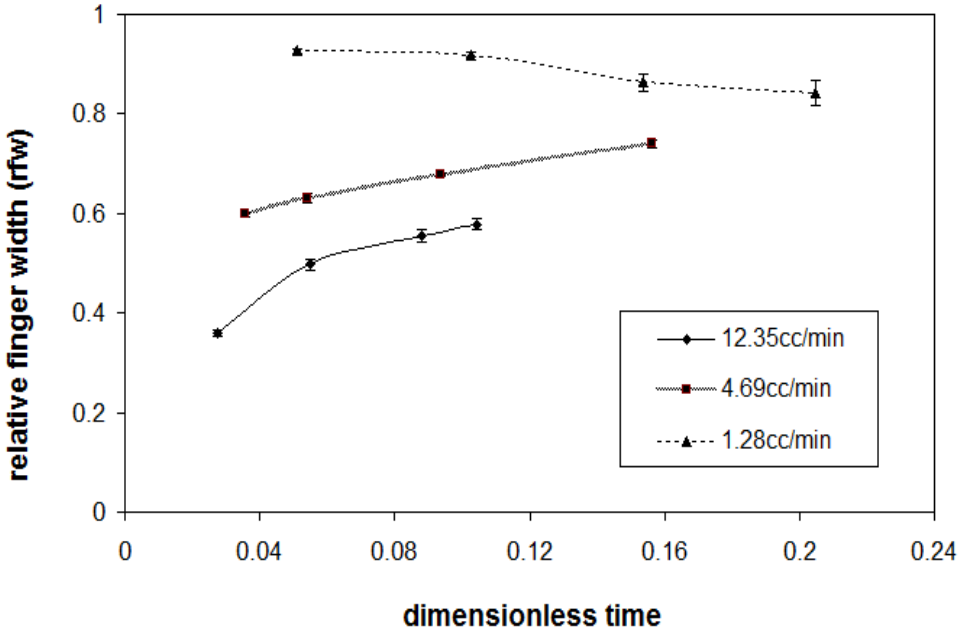

Figure 6.35: Relative finger width as a function of dimensionless time for different injection rates of water in 37.5%PEG 0.14%PEO (L2) solution.

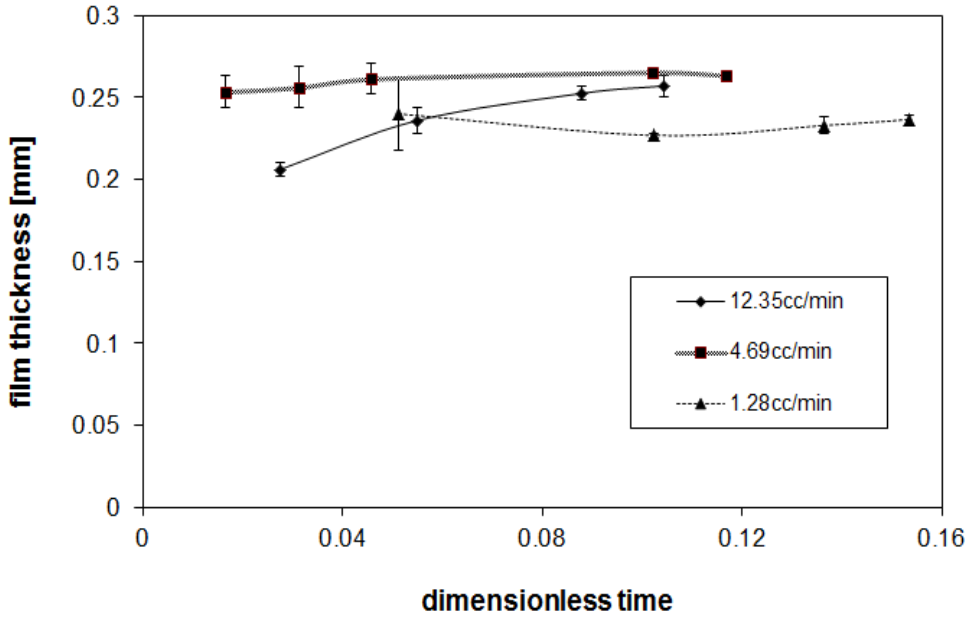

Figure 6.36: Film thickness versus dimensionless time in 88.2% glycerol (T1) solution at different injection rates.

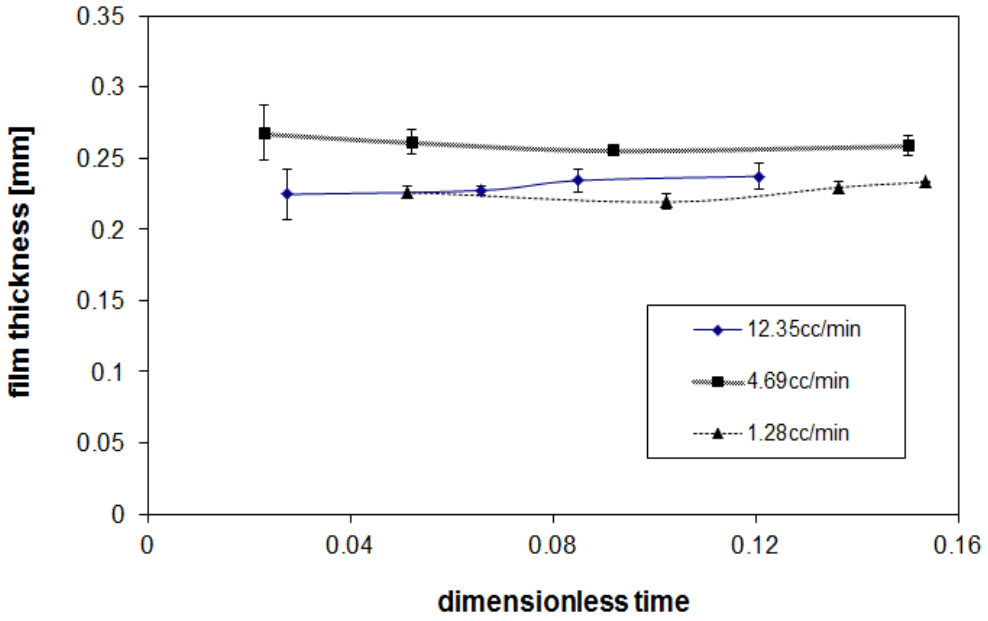

Figure 6.37: Film thickness versus dimensionless time in 89% glycerol (T2) solution at different injection rates.

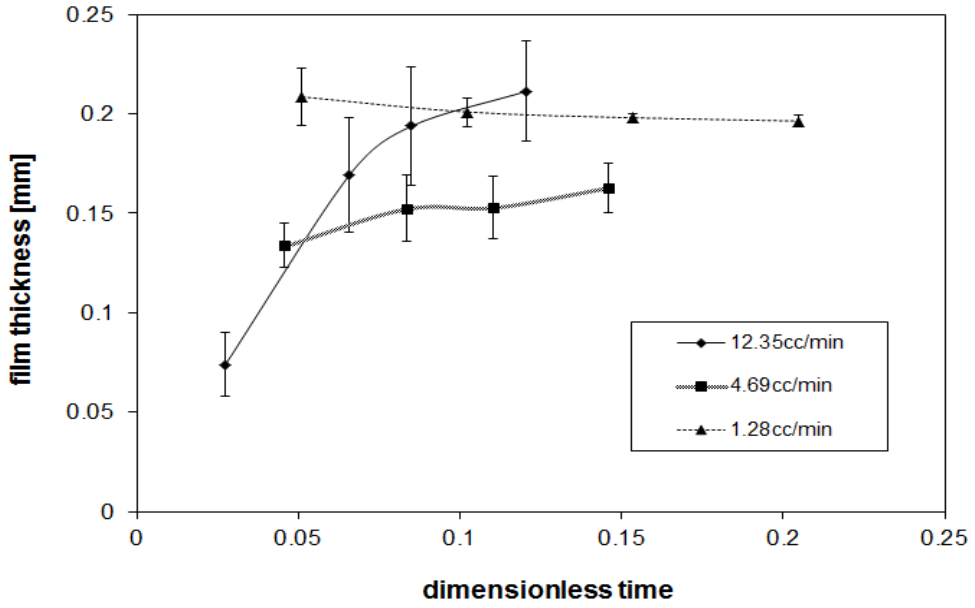

Figure 6.38: Film thickness versus dimensionless time in 37.5%PEG 0.08%PEO (L1) solution at different injection rates.

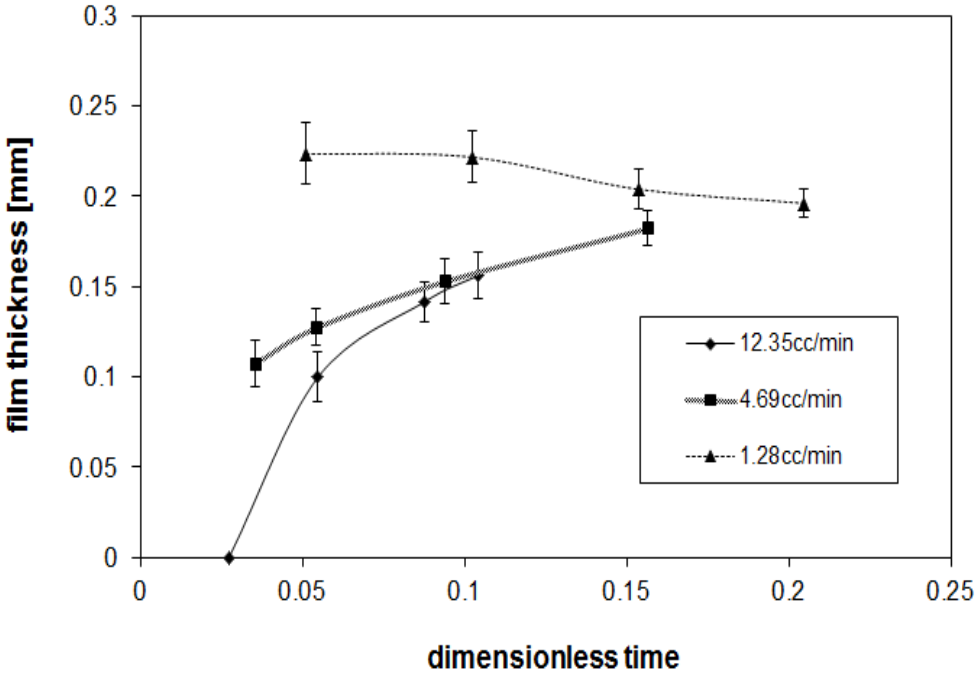

Figure 6.39: Film thickness versus dimensionless time in 37.5%PEG 0.14%PEO (L2) solution at different injection rates.

Chapter 7: Alternate-Slug Fracturing

7.1 INTRODUCTION

The productivity of fractured wells is determined by two primary factors, fracture conductivity and propped fracture length. Both of these factors are very dependent on the effective transport of proppant inside the fracture. Proppants are placed in the fracture by pumping them in the fracturing fluid. Ideally this fluid would have excellent proppant carrying abilities to keep the proppant from settling. It is desired to distribute the proppant uniformly along the length of the fracture. A typical hydraulic fracturing treatment consists of a fluid pad containing no proppant, pumped under high pressure to initiate and extend the fracture. The pad is followed by a high-viscosity fluid laden with an increasing concentration of proppant. The proppants are transported into the fracture by the high velocity of this fluid. The third stage or over-flush consists of a fluid without the proppants. The function of the over-flush is to clear the wellbore of any proppant-slurry and to displace it into the fracture. Upon the cessation of pumping, the fracture closes on the proppant pack, which provides a highly conducive pathway for the hydrocarbons to flow from the reservoir to the wellbore. For the efficient flow of hydrocarbons, it is required that the proppants be carried far into the fracture, leading to a large propped fracture length.

New fracturing techniques such as hybrid fracturing (Sharma et. al., 2004), reverse hybrid fracturing (Liu et. al., 2007) and channel (HiWAY) fracturing (Gillard et

al. 2010) have been deployed over the past few years to effectively place proppants in fractures. The goal of these methods is to generate a network of open channels within the proppant pack, providing highly conductive paths for hydrocarbons to flow from the reservoir to the wellbore. This chapter presents an experimental study on proppant placement using a new method of fracturing, referred to as Alternate-Slug fracturing, which involves alternating injections of low viscosity and high viscosity fluids into the fracture. Alternate-slug fracturing ensures deeper placement of proppants through two primary mechanisms: (a) proppant transport in viscous fingers formed by the low viscosity fluid and (b) an increase in drag force in the polymer slug leading to better entrainment and displacement of any proppant banks that may have formed. Both these effects lead to longer propped fracture length and better vertical placement of proppants in the fracture. In addition, the method offers lower polymer costs, lower pumping horsepower, smaller fracture widths, better control of fluid leakoff and less gel damage compared to conventional gel fracs.

Experiments are conducted with fluids of different viscosity and elasticity, with proppants being carried by the low viscosity fluid. It is shown that the injection rate, slug size and viscosity ratio can be used to control the geometry of the fingers created and, therefore, the proppant distribution in the fracture. The non-uniform and deeper placement of proppant in the viscous fingers leads to the creation of high permeability paths in the proppant pack.

7.2 Past Work on Proppant Placement Strategies

The conventional method of fracturing involves the use of high viscosity cross linked gels to create massive hydraulic fractures (Gidley et al. 1989). A large amount of proppants (up to 2 million pounds) are pumped with the high viscosity gels to create adequate fracture width. Cross linked gels with concentrations as high as 60 pptg have been pumped to reduce proppant settling and to minimize leak off. However, over the past two decades there has been reversal in fracturing strategies towards the use of lower viscosity fluids and less proppant mass. The primary factors leading to this reversal are the low permeability of reservoirs and/or depleted formations where fracture cleanup is difficult, poor performance of conventional fractures (less propped fractures lengths than expected/designed) and cost reduction. Slickwater fracturing involves the use of water with a small amount of friction reducer. Slickwater treatments are now widely used in tight formations where it is important to create long fracture lengths in order to maximize the contact area with the reservoir. Other methods such as hybrid fracturing, reverse-hybrid fracturing and channel fracturing have evolved over the past decade.

7.2.1 Slickwater Fracturing

Slickwater fracturing, also referred to as water-fracturing, involves the use of large volumes of water to create long fractures in low permeability formations. The fluid used is water slickened with a polyacrylamide friction reducer or a low concentration of linear gel. The slickening agents are used to lower the friction loss in the pipe during pumping. The other additives might include a scale inhibitor, oxygen scavenger,

bactericide and occasionally a surfactant. This method of fracturing is used in tight reservoirs that have low permeability and/or do not have enough pressure to clean up the gel from the fractures. Slickwater fracs have proven to be more cost effective and have shown to produce better stimulation output than the conventional crosslinked gel fracs in tight formations (Mayerhofer et al. 1997; Walker et al. 1998).

Slick water has a viscosity close to 1 cP, which is much lower than the viscosity of the conventional guar gels. Water is generally pumped at very high rates, sometimes in excess of 100 bbl/min. Due to the low viscosity and high injection rates, waterfracs provide longer fractures and may provide a more complex fracture geometry than the conventional gel fracs. It has been postulated that the complex fracture pattern provides a larger stimulated reservoir volume resulting in higher production (Mayerhofer et al. 2006). The lower viscosity also helps in better height containment making it a preferred design in situations where it is necessary to stay out of the underlying water zones.

The biggest concern with slickwater fracturing is the proppant placement/transport. The low viscosity of the slick water leads to poor proppant suspending ability. According to the Stokes law for settling, the settling velocity of proppant is higher in a low viscosity fluid. As pointed out by Palisch et al. (2010), the low viscosity does not only cause ineffective lateral placement of proppants but also leads to concerns with the vertical coverage across the pay zone(s). In order to reduce the settling velocity, low density proppants referred to as ultra-lightweight proppants have

been used in the industry (Rickards et al. 2003). The high strength and low density of these proppants make them suitable for waterfrac operations.

Palisch et al. (2010) conducted slot flow experiments to observe proppant settling in a low viscosity fluid. It was observed that the proppants settled at a short distance from the perforations and formes a dune. The dune or the proppant bed reaches an "equilibrium height" after which the particle transport is governed by fluidization and sedimentation. The equilibrium height is dependent on the fluid viscosity, fluid velocity and the proppant concentration (Kern at al. 1959). Once the equilibrium height is attained, subsequent proppant is carried further along the length of the fracture away from the perforations (Patankar et al. 2002; Handren and Palisch 2009). Figure 7.1 a), b) and c) highlight the process of bed deposition, attainment of equilibrium height and further deposition beyond the bed respectively. It has been observed that reducing the pumping rate, decreasing the concentration of proppants and using larger diameter proppants at the tail leads to higher conductivity at the top of the fracture. The larger proppant also fills up any void space created by the fluidization during the treatment.

Thus in slick-water fractures, fluidization and sedimentation of proppants has been postulated as the primary mechanism for proppant transport. The particles are moved over long distances due to the high velocity of the fluid. The distances are often more than predicted by the settling velocity of the particles. Large propped fracture lengths using slick water fracs have been observed in the field (Leonard et al. 2007)

demonstrating that proppants are carried large distances by the mechanisms mentioned above.

7.2.2 Hybrid Fracturing

Hybrid fracturing technique involves the use of slick water as well as gel-based fluid for fracture creation. Slick water is pumped first to create adequate fracture length and width. This is followed by a cross-linked gel pad and then the proppant stage containing proppant laden in gels. Gels carry the proppant more efficiently into the fracture which allows for a more uniform and consistent distribution of proppant prior to fracture closure. Hybrid fracturing combines the benefits and advantages of both conventional gel and water frac treatments and has been employed in tight gas plays over the past years. Rushing and Sullivan (2003) presented a study of various stimulation treatments in the Bossier tight gas sand play and compared the performance of hybrid fracs with water fracs. Using pressure transient analysis, they observed that hybrid fracs generated longer effective fracture half-lengths and larger effective fracture conductivities than conventional water fracs. It was suggested that the design of hybrid fracs need to be optimized in order to ensure higher average conductivities consistently.

Sharma et al. (2004) analyzed a comprehensive data set for the Bossier formation. They presented production data showing the higher production rates obtained from the hybrid fracs as compared to conventional crosslinked gel fracs as well as water fracs. From the pressure build and production data, they observed that the effective propped

fracture half-lengths for hybrid fracs (220 ft) were lower than the created fracture half-lengths indicated by the microseismic data (400-500 ft). However, the effective propped fracture half-lengths were higher than those obtained from either crosslinked gel/sand or waterfrac treatments (100-150 ft) illustrating the effectiveness of hybrid fractures.

7.2.3 Reverse-Hybrid Fracturing

In an unstable displacement of a more-viscous fluid by a less-viscous fluid, the less viscous fluid tends to form fingers into the flow-channel. This method of fracturing uses the phenomenon of viscous fingering to efficiently place proppants in the fracture. Ely et al. (1993) developed a technique, termed "pipelining", which used viscous fingering between the high-viscosity, cross-linked pad and a much lower viscosity, proppant-laden linear gel to transport proppants. They used this technique to selectively place proppants in the zone of interest in the presence of a hydraulic fracture that extends below and above the zone. The following criteria have been laid out for the technique to successful:

- The viscosity of the cross-linked gel should be 30-50 times the viscosity of the proppant laden fluids for the fingers to form.
- The cross-linked pad fluid should be designed to main sufficient viscosity at the downhole conditions throughout the job. This is important to ensure the formation of viscous fingers and to minimize proppant settling.
- The width of the fracture in the zone of interest should be sufficient enough to make use of differential viscosity. For this to occur, it is important that the zone of

interest has a Young's modulus lower than that of the underlying and overlying rocks.

- Only the zone of interest should be perforated. The technique has a very limited chance of success in open hole completions.
- Forcing the closure of the fracture by flowing it at a minimum rate of 1 bpm is recommended to minimize proppant settling and ensure that proppant stays in the pay zone.

They presented case histories to justify the above mentioned criteria for the use of this fracturing technique. It was shown that this fracturing technique can be very efficient for stimulating thin producing intervals within a thick rock section or in close proximity to water or gas zones.

Liu et al. (2007) revisited this method of fracturing and presented an experimental study to determine the effect of various factors which affect the performance of treatments involving viscous fingering for proppant placements. They referred to these treatments as reverse-hybrid fractures (RHF), since the sequence of fluid injection is reverse to what is used in hybrid fractures. Experiments showed that the amount of the gel injected ahead of the slick water should be sufficient (more than a quarter of the expected fracture volume) to ensure that the gel layers form effective barriers for proppant settling. As the concentration of the gel is increased, there is a significant reduction in the settling of proppants. Increasing the gel volume to be equal to the volume of the fracture does not significantly hinder the proppant settling, even though it increases

the chemical costs. High injection rates and high mobility ratios are favorable for the formation of viscous fingers and the transport of proppant along the length of the fracture. Experiments on cells with rough walls showed that slick water tends to flow along the wider channels of the fracture and pushes or squeezes the guar gels into the narrower regions of the fracture. These gel layers can suspend more proppants and make more proppant accumulate above the narrower part of the fracture, forming a proppant pack. Narrow and non-uniform fracture widths can result in non-uniform proppant packs, and this can be an important mechanism of proppant retention in water fracs done in hard rocks.

Based on this extensive experimental study, the following criteria have been laid out for selecting potential candidate wells for RHFs:

- Wells with laminated sands with non-uniform stress profiles. The laminated sands allow the effective propagation of gel layers, which lead to better proppant placement.
- Formations with high elastic moduli (hard rocks) that can tolerate non-uniform proppant packs.
- Wells that show poor response to gel fracs because of the gel-induced damage. The advantage of placing the proppant in slick water is that the proppant pack is not embedded in the gel since it is packed in slick water.
- Wells in which tip screen-out is not a big issue. Because the proppant is being placed in a low-viscosity fluid, high injection rates need to be maintained to avoid a drop in net pressure.

- Formations in which excessive height growth is a concern. This method of fracturing can help in placing proppants within the zone of interest.
- Formations with high leakoff that preclude the use of slickwater.

7.2.4 Channel Fracturing

Introduced by Gillard et al. (2010), the channel fracturing technique involves intermittent pumping of proppant-laden and proppant-free gelled fluid at a high frequency. The goal is to generate a network of open channels within the proppant pack, providing highly conductive paths for hydrocarbons to flow from the reservoir to the wellbore. A schematic of the channel fracturing pumping schedule is shown in Figure 7.2

The pumping schedule comprises of a pad stage followed by the proppant stages. Instead of continuous injection of proppant, as is done in a conventional fracturing treatment and shown by the bold line in the figure, the proppant is added in short pulses separated by pulses of clean fluid. The last stage of the pumping schedule, referred to as the tail-in-stage, comprises of the continuous addition of proppant in order to ensure a uniform and stable connection of the fracture with the wellbore. Another important feature of the channel fracturing technique is the heterogeneous perforation scheme which consists of clusters of perforations separated by non-perforated intervals. This is done to ensure the formation of heterogeneous proppant distribution inside the fracture.

In order to minimize the dispersion of proppant in the treating equipment, wellbore and the fracture reservoir, a degradable fibrous material is added to the proppants. Experimental study has been performed in a 0.3inch slot and 0.78inch diameter 108ft long pipe (Gillard et al. 2010), and the proppant concentration at the inlet and outlet was recorded using a X-ray registration system. It is shown that addition of fibers reduces the settling, ensures the integrity of proppant slugs and reduces dispersion. Field scale measurements based on the hydrostatic pressure measurements show that a proppant pulse of 15 seconds injected in 8860 ft tubing was observed to have duration of 20 seconds at the end of the tubing, showing that addition of fibers to proppants minimizes dispersion.

Channel fracturing has been implemented in various fields in the past years and has shown better performance than other fracturing techniques. Seven wells treated with channel fracturing in Argentina's Loma La Lata field rendered 53% higher initial production than eight offset wells treated conventionally (Gillard et al. 2010). Projections show 15% increase in the hydrocarbon recovery over 10 years as compared to conventionally treated wells. Results from 13 wells (153 stages) treated in the Stud Horse Butte (SHB) area of the Jonah field show a 10% increase in initial gas production and a 17% increase in a projected 10 year recovery as compared to conventional fracturing treatments (Johnson et al. 2011). It was also observed that the fracture net pressures were reduced by 34% using channel fracturing. This reduction in net pressures can be favorable for reducing screen outs and reducing vertical growth of fractures. Rhein et al.

(2011) reported hydrocarbon production increases ranging between 32% and 68% from channel fracturing as compared to slickwater and hybrid fracturing in horizontal wells in the Hawkville field in Texas. Numerical simulations indicated an increase in the area of contact with the reservoir and enhanced connectivity between the wellbore and reservoir. Medvedev et al. (2013) presented large-scale slot flow laboratory experiments to show that fibers help in keeping the alternate slugs of proppants intact inside the fracture. It was also shown that proppant settling is reduced with the addition of fibers in the fluid. Fracture conductivity experiments with proppant clusters showed that conductivities with dispersed clusters of proppant are orders of magnitude higher than that of a uniform proppant pack.

7.3 Experimental Methods

A fracture cell (Hele-Shaw cell) made of Plexiglass is used for the experiments. The walls are smooth and perfectly parallel to each other. The cell is 84cm long, 8cm wide and has a wall spacing of 2mm. Figure 7.3 shows a sketch of one of the fracture cells. Figure 7.4 shows a sketch of the experimental setup. The setup consists of a Moyno pump (Figure 7.5) whose discharge is divided into two lines via a three-way valve (v). Stream A pushes the piston in an accumulator containing the more viscous fluid. Stream B enters a custom-made blender used for pumping the slurry of water mixed with proppants.

The blender is made out of a 3 inch diameter PVC pipe. It consists of a piston that is pushed with the water from the pump. On the other side of the piston, water is mixed with proppant and is continuously stirred with a high speed rotor powered by an electric motor. Figure 7.6 shows the blender along with the direction of movement of piston and the direction of movement of proppants. Figure 7.7 shows the electric motor used to power the rotor. The liquid mixed with proppant comes out through a hole in the piston connected to a pipe. The pipe comes out of the blender through the end cap (Figure 7.8 and Figure 7.9). This custom designed apparatus allows us to inject a relatively homogeneous low viscosity proppant laden fluid into the cell and to minimize the effect of proppant settling in the flow lines. Figure 7.10 illustrates black ceramic proppants being pumped along with a polymer solution using the mixer.

The discharge from the accumulator and blender are connected to the inlet end of the fracture cell via a three-way valve. The valve can be switched to inject either the fluid from the accumulator or the blender into the cell. The cell is kept on a table such that the walls are perpendicular to the ground.

7.4 PROPPANT TRANSPORT EXPERIMENTS

In this section, experimental results to illustrate the transport of proppants using alternate-slug fracturing are presented. Experiments are also performed showing proppant transport using other methods such as conventional fracturing, slickwater fracturing,

hybrid fracturing and reverse hybrid fracturing. The visualization helps present a direct comparison between the different proppant transport strategies.

It is important to consider the scaling relations that allow us to apply the lab findings to the field. The factors that can be controlled to ensure proper scaling are: the dimensions of fracture cell, injection rate, proppant size and proppant density. In our experiments, the dimensions of the cell (discussed in a previous section) are selected such that the length to height ratio of the fracture (approximately equal to 10) is in the same range as those in the field. In the field, a typical fracture length is 500ft and the height is 50 ft. For the dimensions of the fracture cell it is best to make the following dimensionless numbers as close to the field conditions as possible:

$$\mathrm{Re} = \frac{Uw\rho_f}{\mu} \tag{7.1}$$

$$\frac{t_{adv}}{t_{set}} = \frac{L}{H}\frac{V_s}{U} \tag{7.2}$$

In the above equations, U is the fluid horizontal flow velocity in the fracture, w is the fracture (cell) width, ρ_f is the density of fluid, μ is the viscosity of fluid, L and H are the length and height of the fracture (cell) respectively, and V_s is the settling velocity of proppant particles.

Matching the fluid Reynolds number (Re) in the fracture and the ratio t_{adv}/t_{set}, the ratio of advective time to settling time of proppant, allows us to properly scale the lab

observations to the field. t_{adv}/t_{set} can be understood as the ratio of time the particle takes to move a unit distance in the horizontal direction to that in the vertical direction. The ratio helps in comparing the proppant locations in the fracture cell and a real fracture, and is the most important for designing the proppant transport experiments.

Table 7.1 shows a comparison of the dimensions and flow rate between a field scale fracture and our fracture cell. Assuming an injection rate of 40 bbl/min and fluid efficiency of 50%, the Reynolds number at the field scale is 57.96. In the lab scale experiments, we need to use fluids with same viscosity and density as those used in the field. The horizontal velocity required to attain the same Reynolds number is 0.29m/s. In a cell that is 0.84m long, it is impossible to attain the same velocity with proppant laden fluids. The maximum flow rate we could attain in the experiments without exceeding the pressure rating of the fracture cell is 5.9cc/s. This is equivalent to a Reynolds number of 7.38. The difference in Reynolds numbers between the field and lab scale is a limitation of the experiment. However, it is important to note that the main goal of the experiments is to observe proppant transport. Therefore, the more important scaling parameter is t_{adv}/t_{set} which scales the trajectory of proppant particles.

The experiments are performed with two types of proppant, 80/100 mesh sand (specific gravity 2.65) and 30/60 mesh ceramic proppants (specific gravity 3.25). Table 7.1 shows the comparison of the two types of proppant in the experimental cell to the field scale fracture with 20/40mesh sand. It is observed that the value of t_{adv}/t_{set} with

80/100 mesh sand is very close to the field scale value. This justifies the use of 80/100 mesh sand under our experimental conditions to simulate field scale proppant transport. The value of t_{adv}/t_{set} with 30/60mesh ceramic proppant is much higher than the field value. This suggests that the proppant settling effects (vertical motion of proppants) will be amplified in the experiments with ceramic proppants.

7.4.1 Proppant Transport Experiments with Sand

Sand grade 'F-95' obtained from 'Ottawa Foundry Sands' is used for the experiments. The sand is sieved to obtain the 80/100mesh fraction. The specific gravity of the sand grains is 2.65.

7.4.1.1Water Fracturing

To demonstrate proppant transport using water fracturing, the fracture cell is filled with water. Dyed water (1200ml) with 120g sand is loaded in the blender, and the slurry is injected into the cell at a rate of 5.9cc/s. The concentration of the slurry is approximately 3ppg (pounds per gallon of water). Figure 7.11 shows the sequential snapshots of the movement of water and sand in the fracture. The snapshots highlight the poor proppant transport capability of water. As soon as the sand enters the fracture, it settles down forming a bed. The height and the length of the proppant bed grow over time with subsequent sand injection by mechanisms of fluidization and sedimentation. Similar observations have been highlighted by Palisch et al. (2010). In this experiment, we observe that the propped fracture is almost a quarter of the total fracture length after pumping one pore volume of water into the fracture.

7.4.1.2Hybrid Fracturing

This type of treatment involves the creation of the fracture with water followed by proppant laden gel pad. To demonstrate the proppant transport using hybrid fracturing, the experiment is performed with a 1% PEO solution. PEO is chosen for the experiment because it is optically transparent and is easy to clean as compared to guar-based gels. The polymer has a molecular weight of 4,000,000. It is added to distilled water over a magnetic stirrer in batches of 500ml and stirred for 24 hours for complete hydration and dissolution. Figure 7.12 shows the viscosity of 1% PEO solution as a function of shear rate. The PEO solution is shear thinning and has a low shear viscosity of 1340cP.

The fracture cell is filled with dyed water. Approximately 1200ml of 1% PEO solution laden with 120g sand is loaded in the blender. The blender is kept at an inclination of 45 degrees (as shown in Figure 7.10) with sand flowing in the direction of gravity. The flow rate from the pump is set at 5.9cc/s. The concentration of proppants flowing out of the blender is approximately 3ppg (pounds of sand per gallon of fluid). The solution laden with sand is pumped into the cell.

Figure 7.13 shows sequential snapshots of sand laden polymer solution injected into the fracture. The figure highlights the advantage of using a high viscosity fluid for efficient proppant transport. We observe that sand is properly suspended in the polymer solution with minimal settling. The sand is distributed uniformly through the height of the fracture. It is also interesting to observe the mixing between the injected polymer solution

and the dyed water initially in the cell. This mixing leads to sand particles being transported in the water.

7.4.1.3Reverse Hybrid Fracturing

As described in the Section 7.2, in reverse-hybrid fracture treatment the fracture is created with a high viscosity fluid which is followed by injection of low-viscosity proppant-laden fluid. In the experiment, the fracture cell is filled with 1% PEO solution. Dyed water (approximately 1200ml) with 120g sand is loaded in the blender, and the slurry is injected into the cell. Figure 7.14 shows a snapshot of the injection of water in the cell. The injection rate of water is the same as in the other experiment, equal to 5.9cc/s. The water fingers through the polymer solution and carries the sand much further down the length of the fracture than in water fracturing. Due to the high viscosity of the polymer solution, the proppant remains suspended in the finger for a long time. Proppant is placed deeper into the fracture as a result of faster propagation in viscous fingers. On subsequent injection of water, a proppant bed forms near the injection point as the proppant settles fast in water. Upon the formation of the proppant bed, further transport of proppant in the fracture occurs by fluidization and sedimentation similar to that observed in water fracturing.

7.4.1.4Alternate-Slug Fracturing

In this method of fracturing, a high viscosity proppant-free fluid and a low viscosity proppant-laden fluid are injected alternately (in slugs) into the fracture. Experiments are performed to observe the proppant distribution in the fracture using this

method. Figure 7.15 shows sequential snapshots from a video shot for such an experiment. The fracture cell is filled with 1%PEO solution. Proppant-laden water and proppant-free PEO solution are then pumped alternately at an injection rate of 5.9cc/s by switching valve (v) alternately in Figure 7.4.

The water, along with proppant, fingers through the polymer solution. Sand particles are carried in the fingers (similar to observations in reverse-hybrid fracturing). At the same time, some sand settles near the injection port forming a proppant bed. A slug of proppant-free polymer solution follows the water (shown in Figure 7.15(iii)). The polymer solution exerts an increased drag force due to its high viscosity and sweeps the particles away from the bed. This is seen by the reduction in height of the proppant bed and the transport of particles further down the length of fracture. The advantage of injecting the slug of polymer is to more effectively transport the particles from proppant bed deeper into the fracture.

The proppant-laden water is then injected again after the polymer as shown in Figure 7.15(iv). The water fingers through the previous polymer slug and carries more proppant particles in the fingers. Proppant particles also settle down near the injection port increasing the height of the proppant bed there. This is again followed by a slug of polymer that sweeps the particles (Figure 7.15(v)) into the fracture. A reduction in height of the proppant bed from Figure 7.15(iv) to (v) can be observed. At this stage it is also observed that proppant particles are carried through the length of the fracture and are

distributed heterogeneously across the height of the fracture, providing better vertical coverage of proppant than in the other methods. Figure 7.19(vi) shows the injection of the next slug of water with sand. It will be advisable to end the treatment with a water-sand slug to ensure good contact between the wellbore and the fracture.

7.4.2 Proppant Transport Experiments with Ceramic Proppants

The ceramic proppant of size 30/60 mesh are obtained from "Carbo Ceramics". The density of the proppant measured using displacement of water is 3.25 g/cc. As mentioned before, the vertical motion (settling) of proppant will be amplified as compared to horizontal motion of proppant based on the dimensionless parameter t_{adv}/t_{set}. The experiments are nevertheless useful for demonstrating the advantages of alternate-slug fracturing.

7.4.2.1Conventional Fracturing

This type of treatment involves the use of a high viscosity fluid (usually uncrosslinked or crosslinked gel) laden with proppant. To demonstrate proppant transport using a high viscosity fluid, an experiment is performed with 1% polyethylene oxide (PEO) solution. The solution is shear thinning and has a low shear viscosity of 1340cP.

The fracture cell is filled up with the PEO solution. The same solution (approximately 1200ml) along with 25g of proppant is loaded in the blender. The blender is kept at an inclination of 45 degrees (as shown in Figure 7.10) with the proppant flowing in the direction of gravity. The pump flow rate is set at 5.9cc/s. The

concentration of proppant flowing out of the blender is approximately 1ppg (pounds of proppant per gallon of fluid). The solution laden with proppant is pumped into the cell. The snapshots from the experiment are shown in Figure 7.16. The figure highlights the advantage of using a high viscosity fluid for efficient proppant transport. The viscosity of the PEO solutions results in good suspension of proppant. The proppant are transported through the length of the fracture. Due to their high density and relatively larger size, proppant particles settle as they move along the length of the fracture, forming a bed. It is important to mention that crosslinked gels can have viscosities higher than the 1% PEO solution used in this experiment, and they can suspend proppant for a longer time.

7.4.2.2Water Fracturing

To demonstrate proppant transport using water fracturing, the fracture cell is filled with clear water and dyed water with proppant is injected into the cell. Figure 7.17 shows the snapshots of the movement of water and proppant in the fracture. The injection rate is 5.9cc/s, the same as in the previous experiment. The snapshots highlight the poor proppant transport capability of water. The proppant settles down quickly forming a bed, similar to observations from experiments with sand. The height and the length of the proppant bed grow over time with injection of subsequent proppant by mechanisms of fluidization and sedimentation. Similar observations have been highlighted by Palisch et al. (2010). In this experiment, we observe that the propped fracture is less than a quarter of the total fracture length after pumping one pore volume of water into the fracture.

7.4.2.3Reverse Hybrid Fracturing Treatment

In the experiment, the fracture cell is filled with a 1% PEO solution and dyed water with proppant is injected into the cell. Figure 7.18 shows a snapshot of the injection of water in the cell. The injection rate of water is the same as in the other experiment, equal to 5.9cc/s. The water fingers through the polymer solution and carries the proppant much further down the length of the fracture than in water fracturing. Due to the high viscosity of the polymer solution, the proppant remains suspended in the finger for a long time. Proppant are placed deeper into the fracture as a result of faster propagation in viscous fingers. On subsequent injection of water, a proppant bed forms near the injection point as the proppant settles fast in water. Upon the formation of the proppant bed, further transport of proppant in the fracture occurs by fluidization and sedimentation similar to that observed in slickwater fracturing.

7.4.2.4Alternate-Slug Fracturing

Figure 7.19 shows snapshots from a video shot for alternate-slug fracturing, in which slugs of ceramic proppant laden water and 1% PEO solution are injected alternately. The fracture cell is filled with 1%PEO solution. Proppant-laden water and PEO solution are then pumped alternately at an injection rate of 5.9cc/s by switching valve (v) alternately in Figure 7.4.

The observations are similar to alternate-slug experiments performed with 80/100 mesh sand as described in Section 7.4.1.4. The water, along with proppant, fingers

through the polymer solution. Proppant particles are carried in the finger. At the same time some proppant particles settle near the injection port forming a proppant bed. The water is followed by a slug of proppant-free polymer solution at the same injection rate (shown in Figure 7.19(ii)). The polymer solution exerts an increased drag force due to its high viscosity and sweeps the particles away from the bed. This is seen by the reduction in height of the proppant bed and the transport of particles further down the length of fracture. The proppant-laden water is then injected again after the polymer as shown in Figure 7.19 (iii). The water fingers through the previous polymer slug and carries more proppant particles in the fingers. Proppant particles also settle down near the injection port increasing the height of the proppant bed there. This is again followed by a slug of polymer that sweeps the particles (Figure 7.19(iv)) into the fracture. A reduction in height of the proppant bed from Figure 7.19 (iii) to Figure 7.19 (iv) can be observed. At this stage it is also observed that proppant particles are carried through the length of the fracture and are distributed heterogeneously across the height of the fracture, providing better vertical coverage of proppants than in the other methods. Figure 7.19 (v) and (vi) show the injection of the next slug of water and polymer solution respectively.

7.5 Design of Alternate-Slug Fracturing Treatments

The experiments in Section 7.4 highlight the advantage of using alternate-slug fracturing over other methods discussed previously. Alternate-slug fracturing takes advantage of viscous fingering to place proppant deep in the fracture, as well as high drag force of high viscosity polymer solutions. Both the effects help in carrying the proppant

to longer distances in the fracture and distribute them better vertically in the fracture. Other advantages of this method of fracturing over conventional gel fracturing include lower polymer costs, reduced gel damage and lower pumping horsepower as less amount of polymer is used. This method of fracturing will also result in longer created fracture lengths and reduced fracture widths as compared to conventional fracturing. Better control on fluid leakoff as compared to slickwater fracturing is obtained, reducing the risk of tip screenouts.

The design of alternate-slug fracture treatments requires designing the injection rates, slug sizes and proppant concentration. To determine the injection rates and slug sizes it is important to know the effect of factors such as viscosity, elasticity, and flow rate on the growth of viscous fingers and mixing of fluids. Studies presented in Chapter 5 and 6 determine the effect of these factors. In Chapter 5, we studied that mixing zone and finger velocity do not increase linearly with viscosity ratio but plateau above viscosity ratios of 343. Dimensionless plots in Figures 5.21 and 5.28 can be used to calculate mixing zone velocities and finger velocities respectively at any injection rate and viscosity ratio. These plots can be inputted into a fracture simulator to calculate fluid distribution inside the fracture. An example calculation to determine the length of slugs is shown below.

For the design of the alternate-slug treatment, let us assume that polymer of viscosity M cP (at the shear rate imposed by the flow inside the fracture) and water of

viscosity 1 cP are pumped alternately into the fracture. The viscosity ratio between the two fluids is *M*. At a constant injection/pumping rate in the fracture, let the injection velocity be *U*. (The injection velocity is calculated by dividing the injection rate by the cross section flow area of fracture.) Figure 7.20 shows the dimensionless plot of the relative front velocity versus viscosity ratio. This is the same plot as shown in Figure 5.28 in Chapter 5. At any viscosity ratio, *M*, the relative front velocity can be read from the plot as *x*. This implies that at an injection velocity of *U*, the water fingertip water will move a velocity *xU*. Figure 7.21 shows the dimensionless plot of the normalized mixing zone velocity versus viscosity ratio. This is the same plot as shown in Figure 5.21 in Chapter 5. At any viscosity ratio, *M*, the normalized mixing zone velocity can be read from the plot as *y*. This implies that an injection velocity of *U*, the mixing zone is growing at velocity *yU*. This is illustrated in the schematic in Figure 7.22, which shows a slug of polymer pumped into the fracture followed by a slug of water. The polymer front is moving at a velocity *U* ahead of the water fingertip at one given time.

To minimize mixing between every alternate water slug, it is required that the water fingertip should just be able to catch up with the polymer front at the end of pumping. If the polymer slug is pumped for time t_1 and following water slug is pumped for time t_2, the above condition requires:

$$U \times (t_1 + t_2) = x \times U \times t_2 \qquad 7.3$$

The above equation can be rearranged to write:

$$t_1 = \frac{(x-1)}{x}(t_1 + t_2) \tag{7.4}$$

$$t_2 = \frac{(t_1 + t_2)}{x} \tag{7.5}$$

Equations 7.4 and 7.5 can be used to calculate the time (or volume) for each slug to be pumped.

To illustrate the design a vertical facture in a vertical well with fracture parameters mentioned in Table 7.2 is considered. A pumping rate of 40bbl/min with fluid efficiency of 50% is selected. The injection velocity in each wing of the fracture is 0.29m/s. Let the viscosity of polymer, *M*, be 200cP (at the flow shear rate in the fracture). At a viscosity ratio of 200,

$x = 2.7$ (from Figure 7.20)

$y = 2.2$ (from Figure 7.21)

From Equations 7.4 and 7.5,

$t_1 = 0.63\ (t_1+t_2)$

$t_2 = 0.37\ (t_1+t_2)$

The above equations suggest $t_1 = 1.7t_2$. This suggests that the polymer slug ahead of the water slug should be 1.7 times longer than the water slug for the water fingertip to just catch up with the polymer front at the end of pumping.

If the fracturing treatment consists of injection of one slug of polymer followed by one slug of water i.e. a reverse-hybrid treatment, the length of the mixing zone can be calculated using x, y values, fracture parameters and flow rates. Figure 7.23 shows a schematic illustrating the length of the mixing zone and length where the cross-section averaged concentration of injected water is one, inside one wing of the fracture. Up to distance of 28.2m away from the wellbore, the cross-section (or height) averaged concentration of water is one. This suggests that there will be a proppant bank due to high proppant settling rates in water up to distance of 28.2m away from the wellbore. From a distance of 28.2m to 152.4m there will be viscous fingers with polymer layers in between which can suspend proppant due to the high viscosity of polymer.

If the fracture treatment involves pumping 3 slugs of polymer and 3 slugs of water alternately, there will be three mixing zones. The schematic in Figure 7.24 shows the length of the fluid distributions inside the fracture. Each mixing zone is 41.4m long. The assumption in the calculation is that once the trailing polymer slug is injected behind the water slug, the fingers of water move at the velocities equal to injection velocity i.e. the mixing zone does not grow any further. Further work needs to be done to address the growth of the fingers and mixing zone in alternate injection, once the water is further displaced by the polymer. The trailing polymer slug pushes the water in a piston-like fashion and therefore the growth rates will be slower than the mixing zone and fingertip velocity predictions we obtain from Figures 7.20 and 7.21. However, the growth velocities can be greater than the injection velocity, unlike what is assumed in this

example calculation.

In Chapter 6, we discovered that fluid elasticity retards the growth of viscous fingers. In other words, this would reduce mixing between the slugs. It was also found that fluid elasticity leads to formation of multiple thin fingers as compared to a single thick dominant finger in a less elastic fluid. This suggests that more elastic gels will be more useful in alternate-slug fracturing as proppant can be placed in multiple fingers providing better proppant height distribution and heterogeneity in the proppant pack.

7.6 CONCLUSIONS

In this chapter an experimental study is presented to introduce a new method of proppant injection referred to as Alternate-Slug Fracturing. The method involves alternate injection of slugs of proppant-laden low viscosity fluid and proppant-free high viscosity fluid. Proppant transport experiments are performed in a fracture cell to illustrate mixing of fluids and proppant distribution using alternate-slug fracturing. The observations are compared to other methods of fracturing including conventional fracturing, slickwater fracturing and reverse-hybrid fracturing. The main conclusions are as follows:

- Alternate-slug fracturing can potentially provide better distribution of proppant throughout the fracture when compared with slick water or gel fracturing, as it takes advantage of viscous fingering for deeper placement of proppant as well as viscous sweeps to move any proppant banks that may have formed.

- The velocity of injected low viscosity fluid increases as it the interface breaks down into fingers. The high horizontal velocity thus exerts an increased drag on proppant particles, carrying them deeper in the fracture.

- The trailing slug of polymer exerts higher drag force on the settled proppant particles (banks) and pushes them deeper into the fracture.

- This method of proppant injection lowers the risk of tipscreen outs as compared to slickwater and reverse-hybrid fracturing. The alternating polymer slug will be able to maintain a wider fracture width because of its high viscosity.

- Design of alternate-slug fracture treatments requires understanding of mixing of fluids as a function of injection rate, viscosity and elasticity of fluids. Experimental studies in Chapters 5 and 6 address these fundamental issues.

- More elastic gels are more suitable for alternate-slug fracturing treatments as fluid elasticity leads to formation of multiple thin fingers. The multiple fingers will help place proppant heterogeneously in the fracture.

Table 7.1: Dimensions and flow rate comparison of field scale fracture and experimental fracture cell.

	Field Scale	**Flow Cell**
Length (m)	152.4	0.84
Height (m)	45.72	0.08
Width (mm)	2	2
Flow Rate (m^3/s)	0.10598 (40 bbl/min)	5.9×10^{-6}
Viscosity (cP)	10	10
Density of Fluid (kg/m^3)	1000	1000
Horizontal Velocity (m/s)	0.289	0.0369
Channel Reynolds Number (Re)	**57.96**	**7.38**
t_{adv}/t_{set}	**0.74** (20/40 mesh sand)	**2.04** (80/100 mesh sand)
t_{adv}/t_{set}	**0.74** (20/40 mesh sand)	**11.12** (30/60 mesh ceramic proppant)

Table 7.2: Typical fracture parameters used for illustrating an example for design of Alternate-Slug fracture treatments.

Half Length (m)	152.4
Height (m)	45.72
Width (mm)	2
Flow Rate (m^3/s)	0.10598 (40 bbl/min)
Injection Velocity (m/s)	0.29
Viscosity of Polymer Solution at the Shear Rate Imposed by Flow in the Fracture (cP)	200
Viscosity of Water (cP)	1

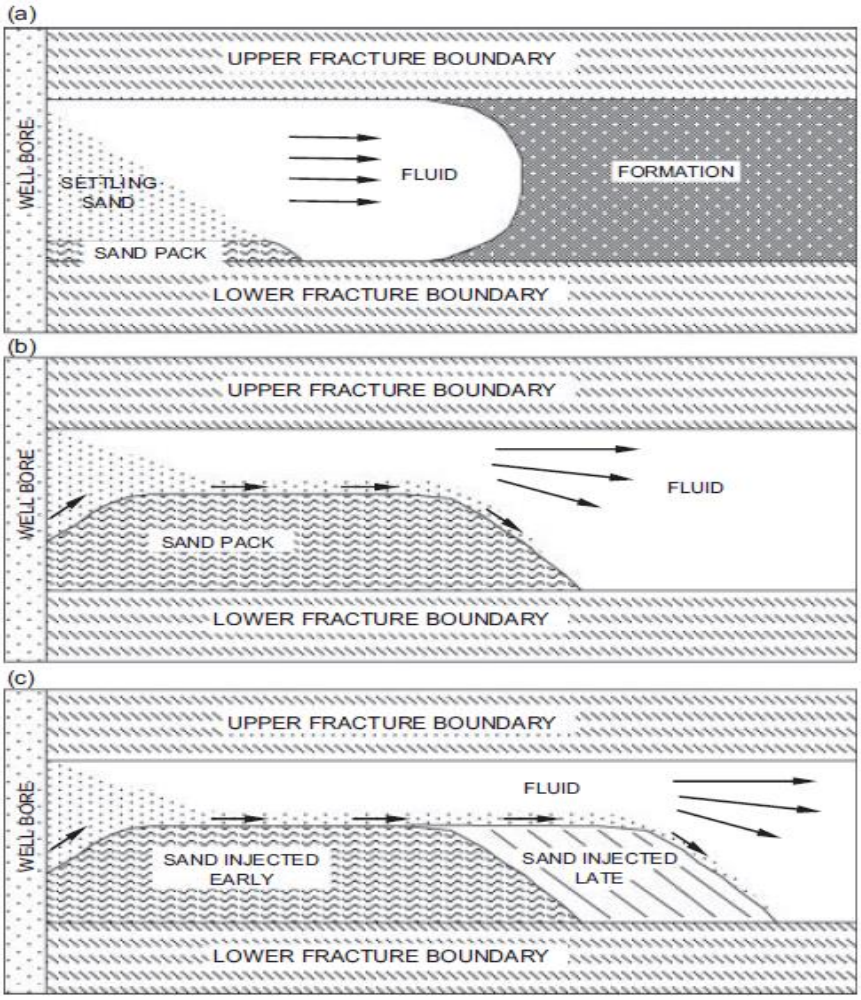

Figure 7.1: Schematic of sequence of proppant deposition in slickwater fracturing (after Kern et al. 1958).

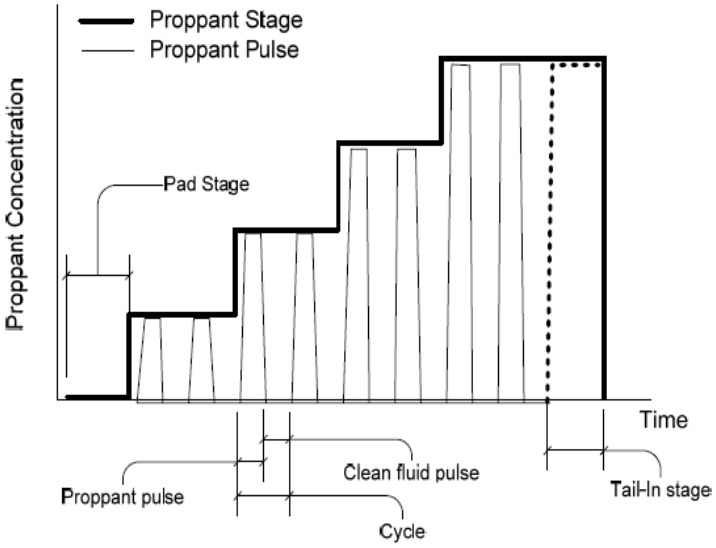

Figure 7.2: Pumping schedule for conventional and channel fracturing treatments (from Gillard et al. 2010).

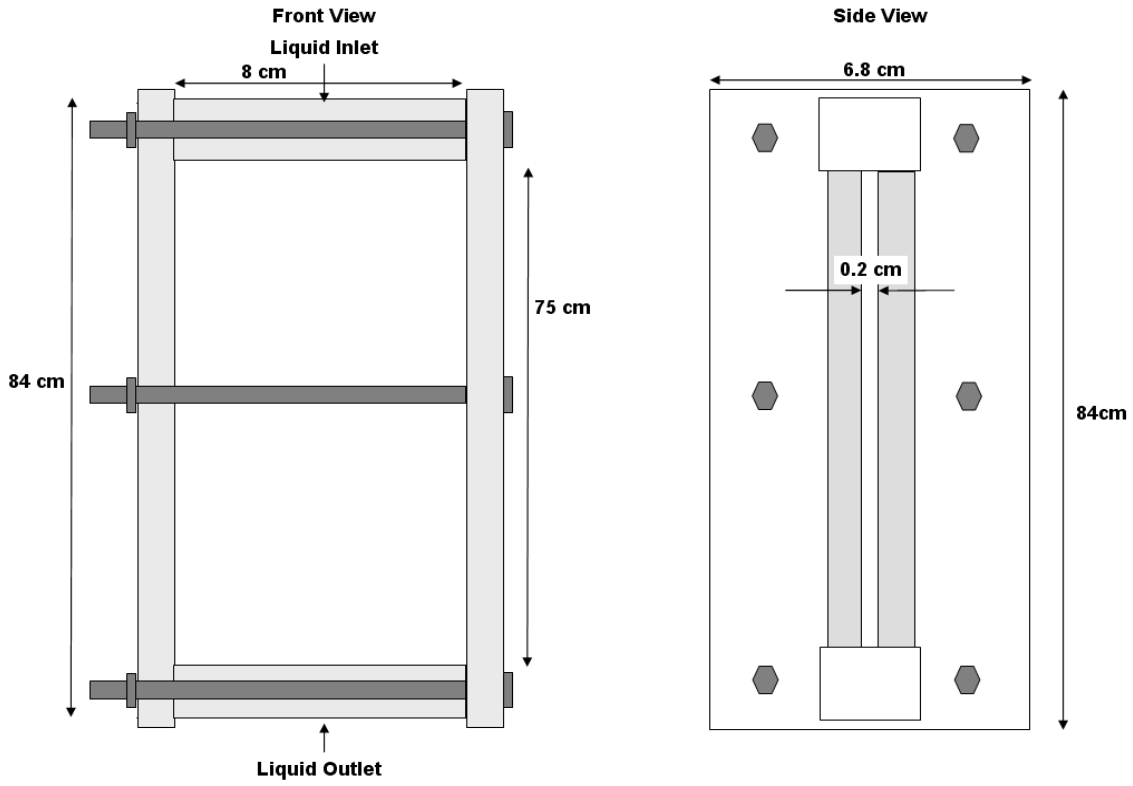

Figure 7.3: Schematic of the fracture cell.

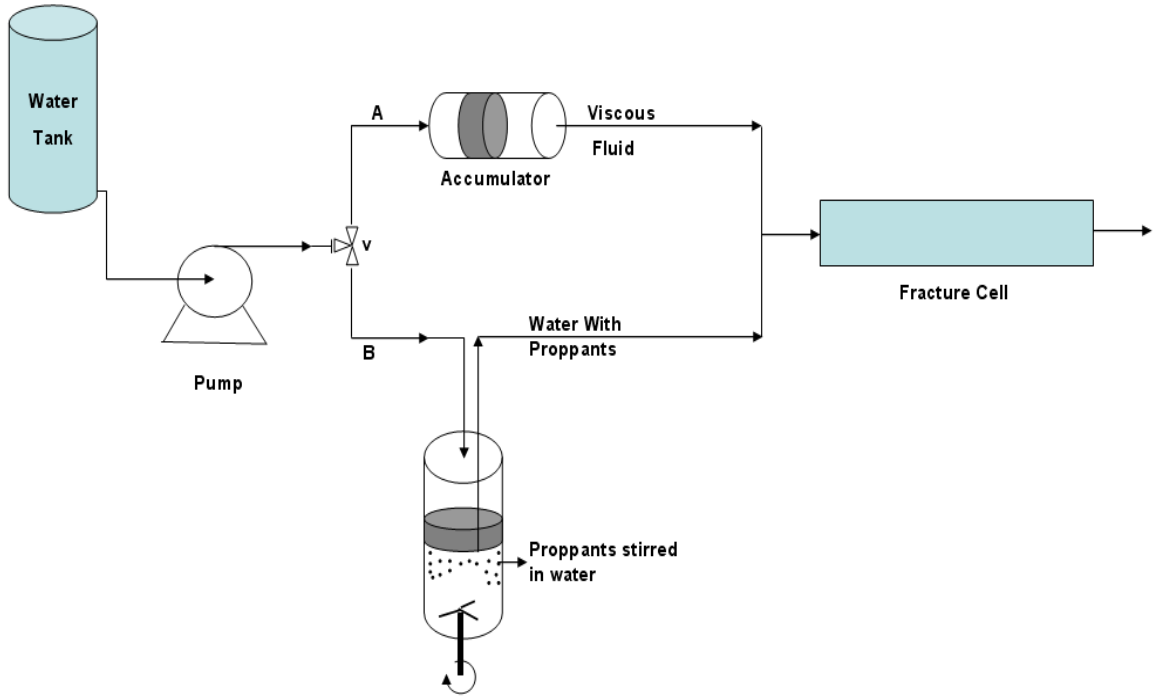

Figure 7.4: Sketch of the experimental setup.

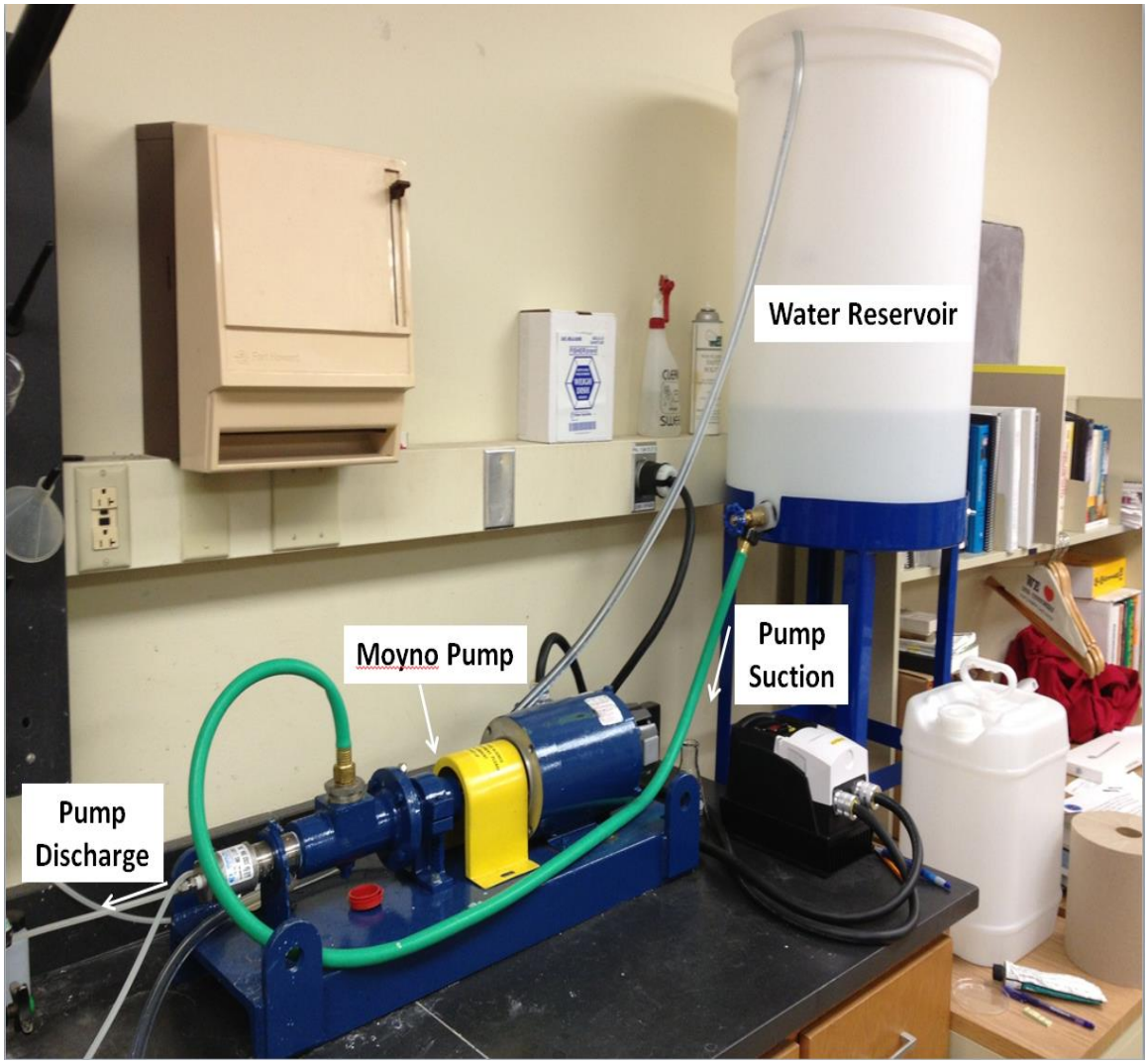

Figure 7.5: Snapshot showing the Moyno pump along with the water reservoir for the suction to the pump.

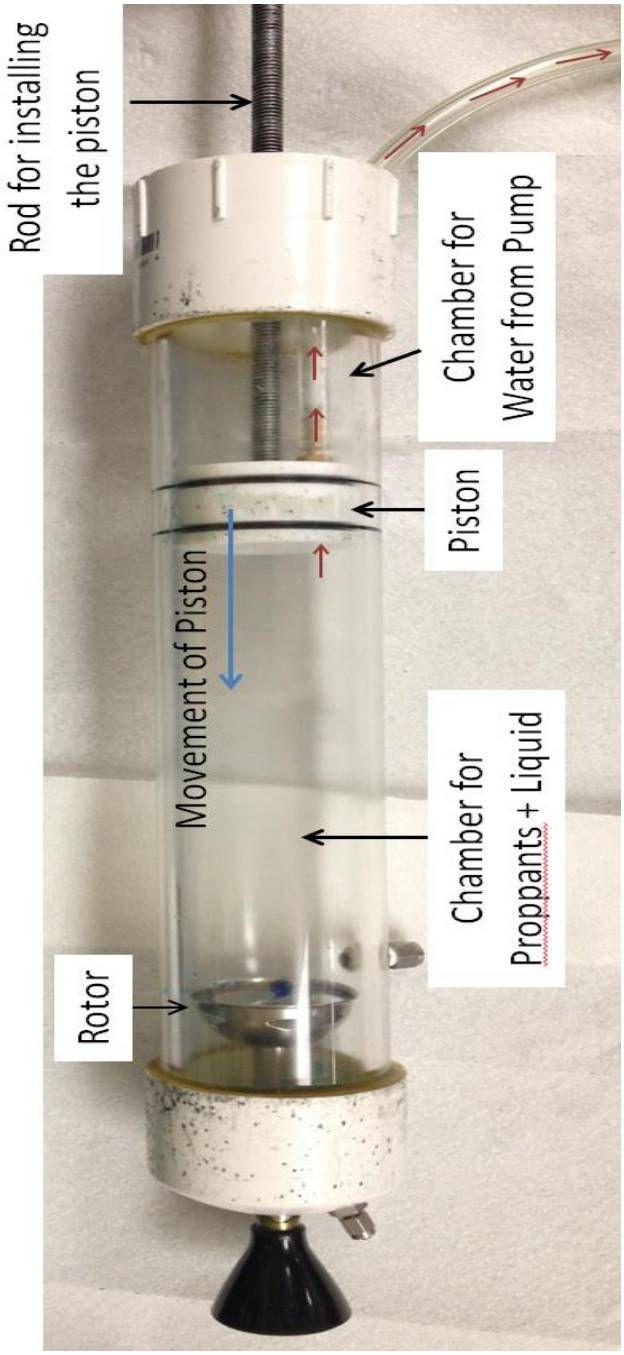

Figure 7.6: Illustration of the custom made blender for pumping proppant slurry. The blue arrow shows the direction of movement of the piston which is pushed by water. The red arrows show the direction of movement of proppant slurry through the hole in the piston and the tubing.

Figure 7.7: Electric motor connected to the rotor on one side of the blender.

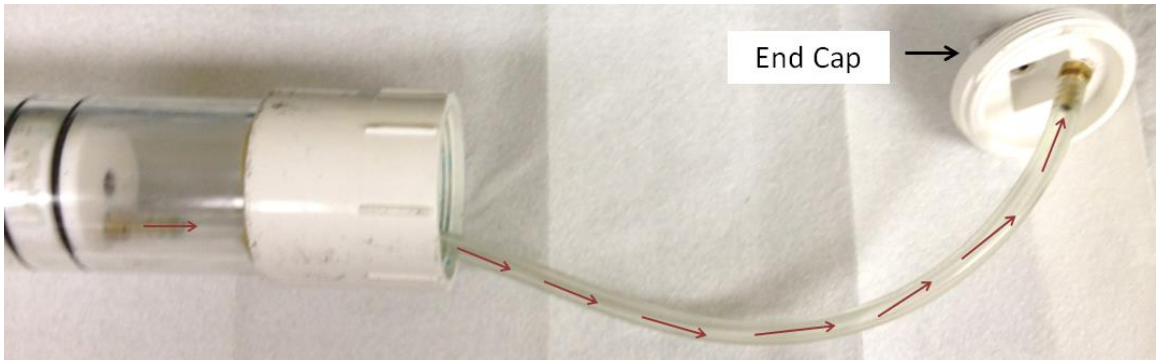

Figure 7.8: Illustration of the tubing connecting the piston to the end cap, transporting proppants along with liquid.

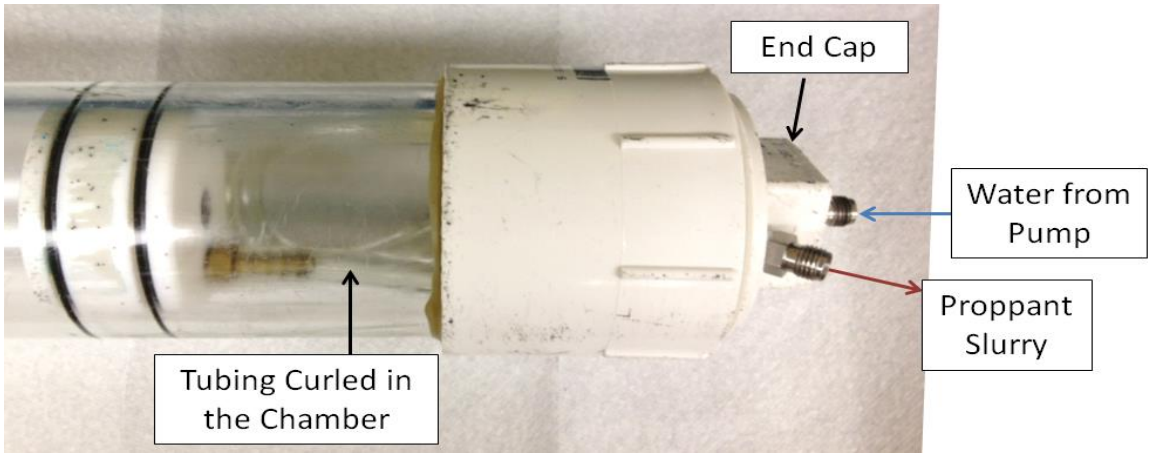

Figure 7.9: Snapshot showing the end cap connected to the PVC pipe with the tube curled in the chamber.

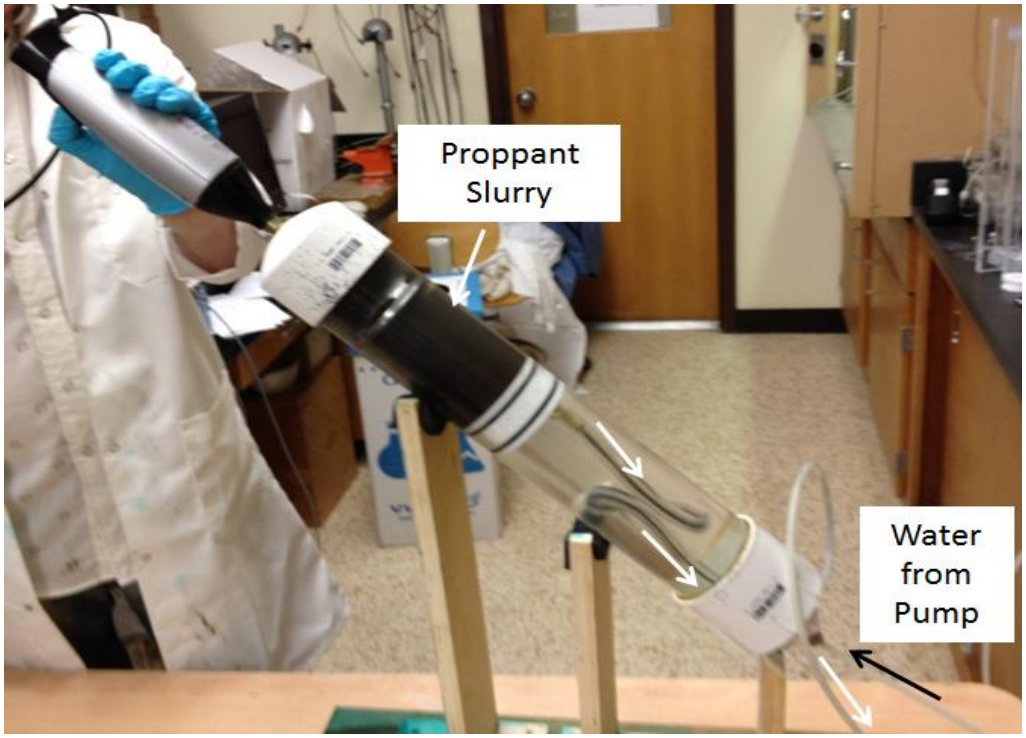

Figure 7.10: Illustration of the blender being used to pump proppants (black) in a polymer solution. The black arrow indicates the direction of injection of water from the pump pushing the piston upwards. White arrows shows the proppant slurry pumped our through the piston, tubing and the end cap.

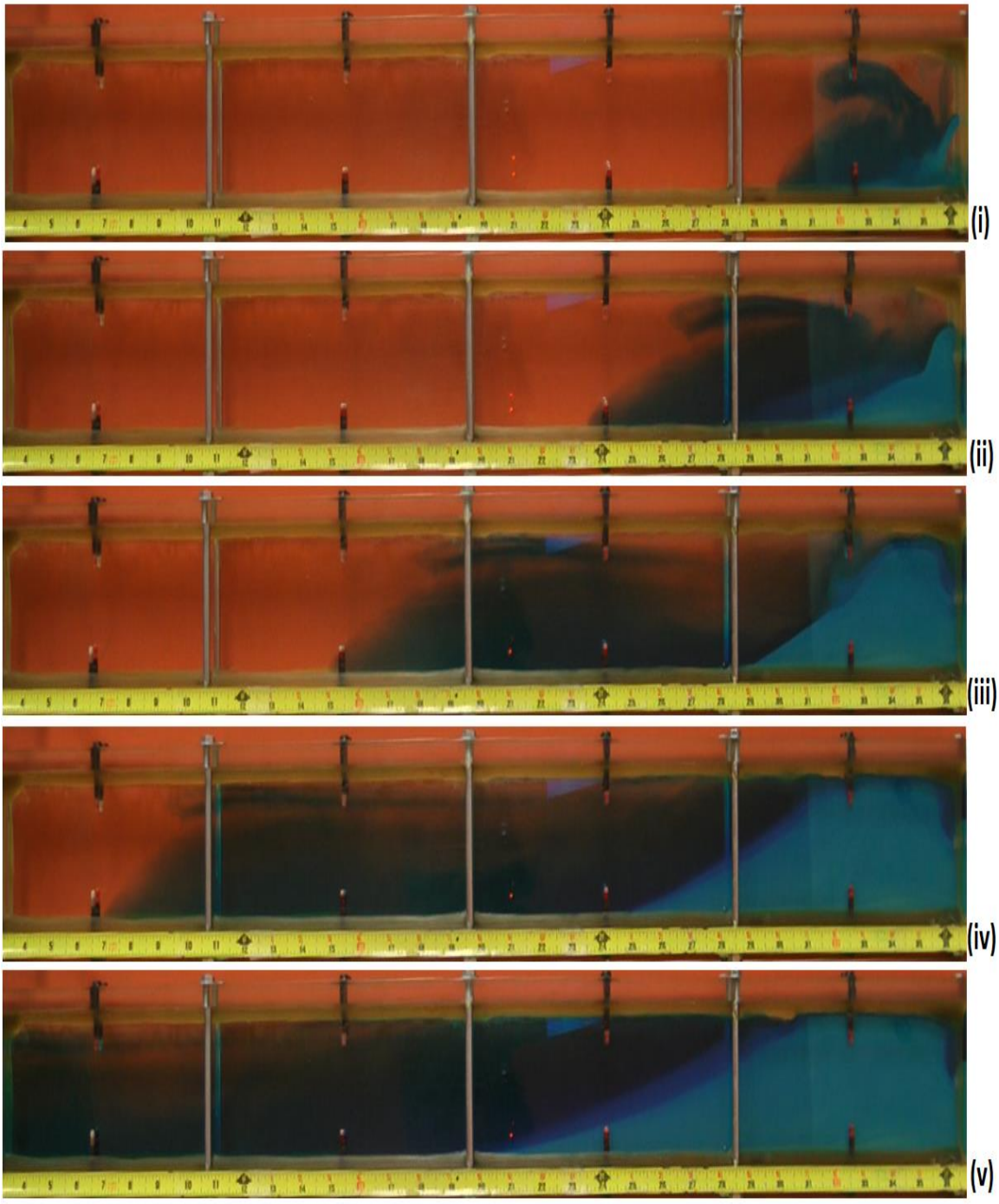

Figure 7.11: Sequential snapshots showing the injection of water along with sand in the cell. The cell is initially filled with clear water and blue dyed water with white sand is injected.

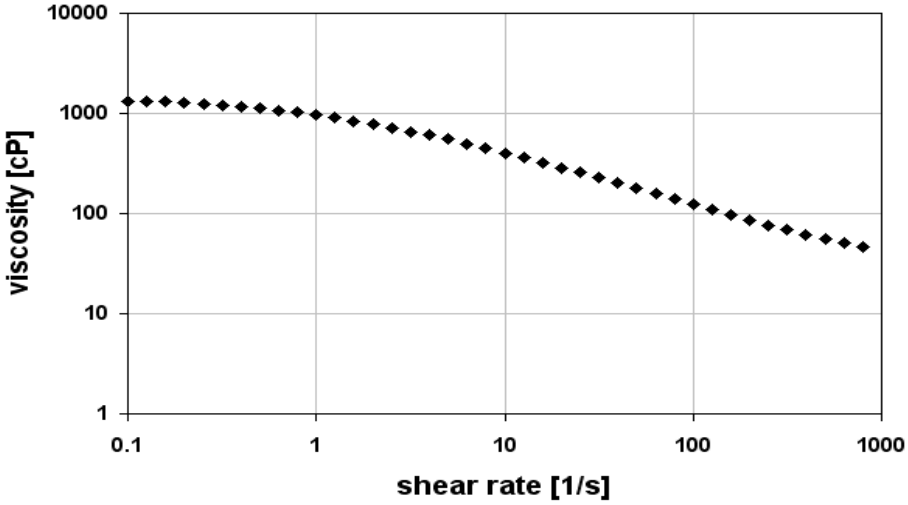

Figure 7.12: Viscosity versus shear rate for 1 % polyethylene oxide (PEO) solution.

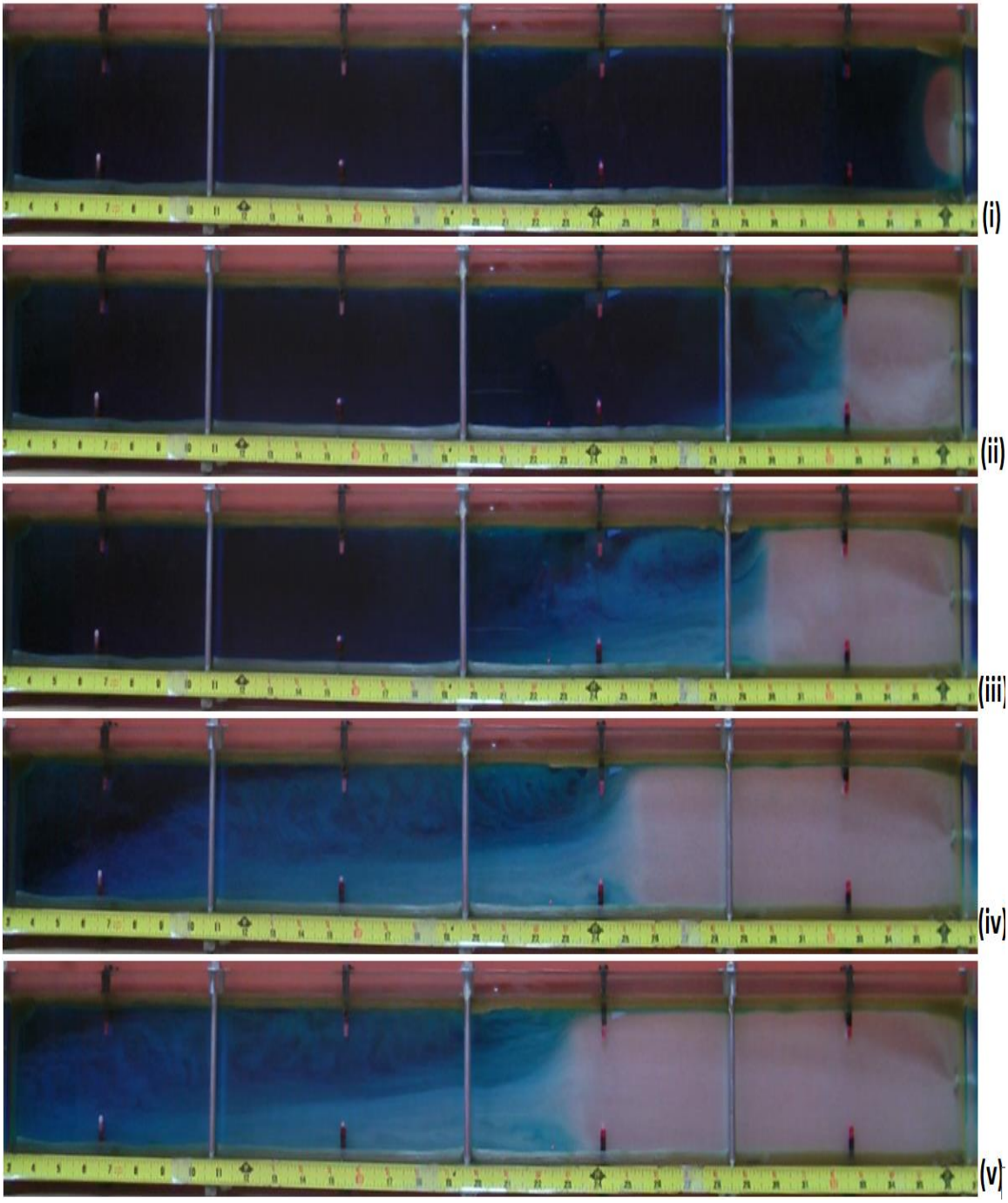

Figure 7.13: Sequential snapshots showing the injection of sand in 1% polyethylene oxide solution in the cell. The cell is initially filled with the blue dyed water and the injected polymer solution is clear.

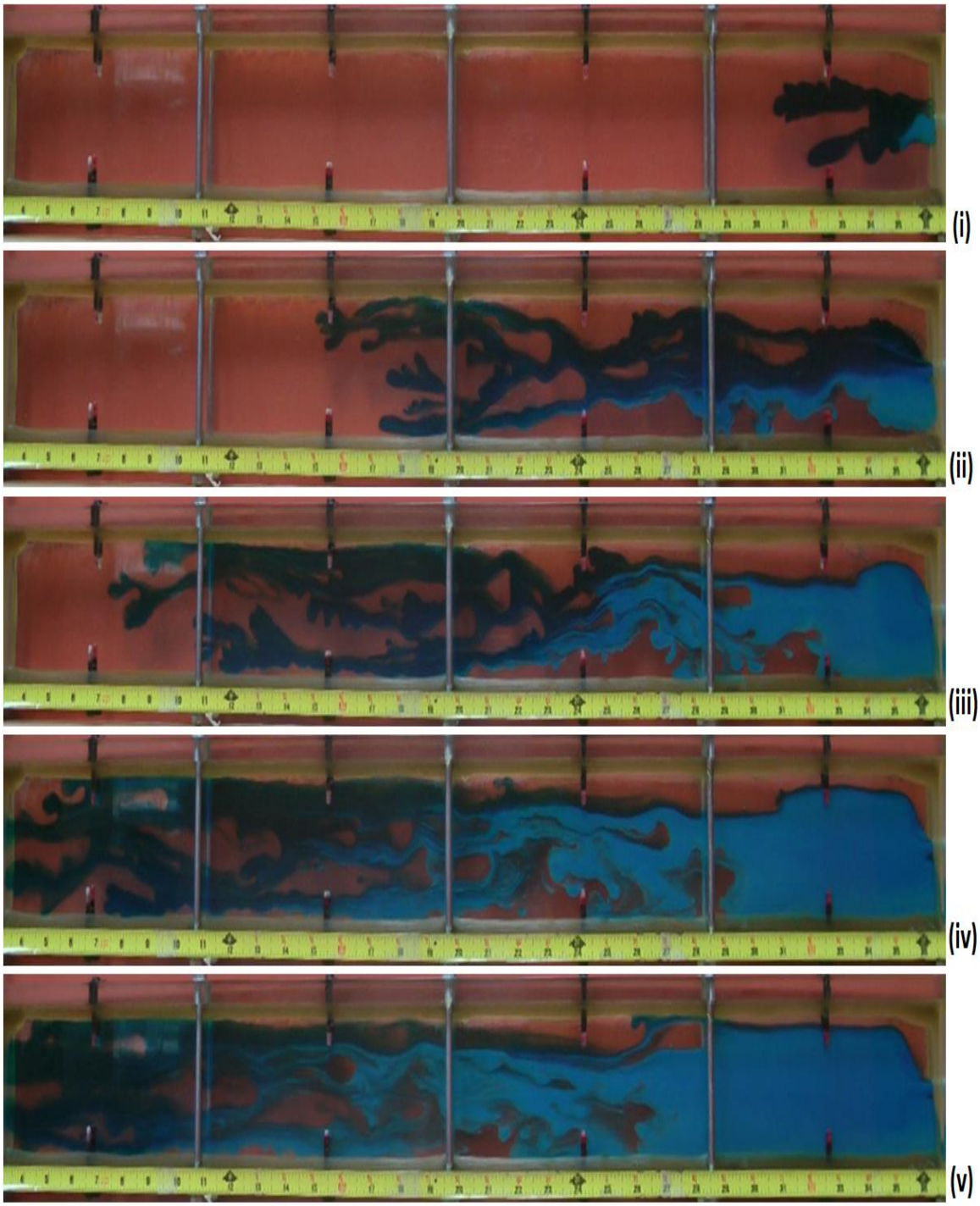

Figure 7.14: Sequential snapshots illustrating the reverse-hybrid fracturing treatment. Dyed water along with land is injected into a cell containing 1% polymer (PEO) solution.

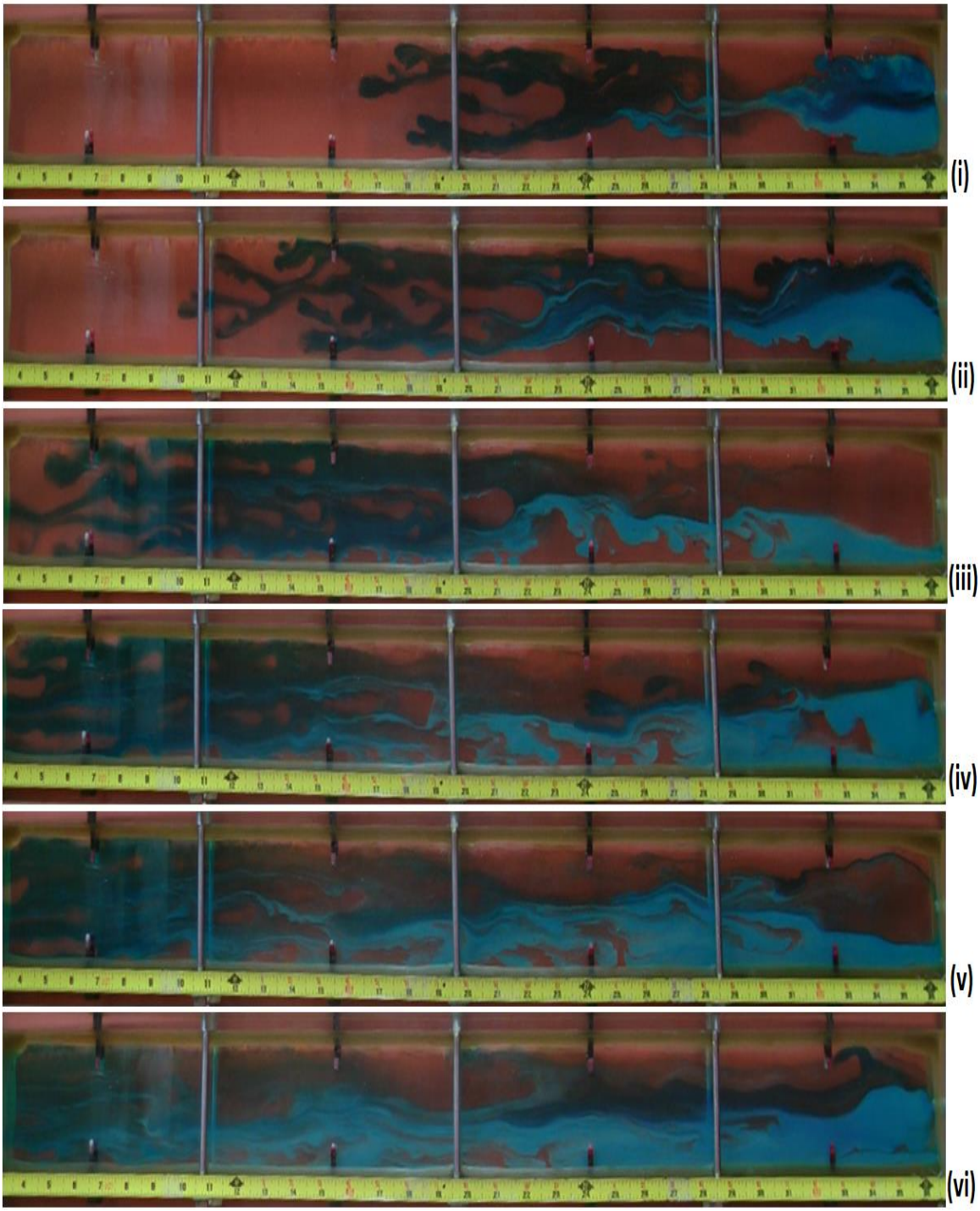

Figure 7.15: Sequential snapshots illustrating the alternate-slug fracturing treatment. Sand-laden water (dyed) and proppant-free 1% polyethylene oxide solution (clear) are injected alternately into the fracture cell.

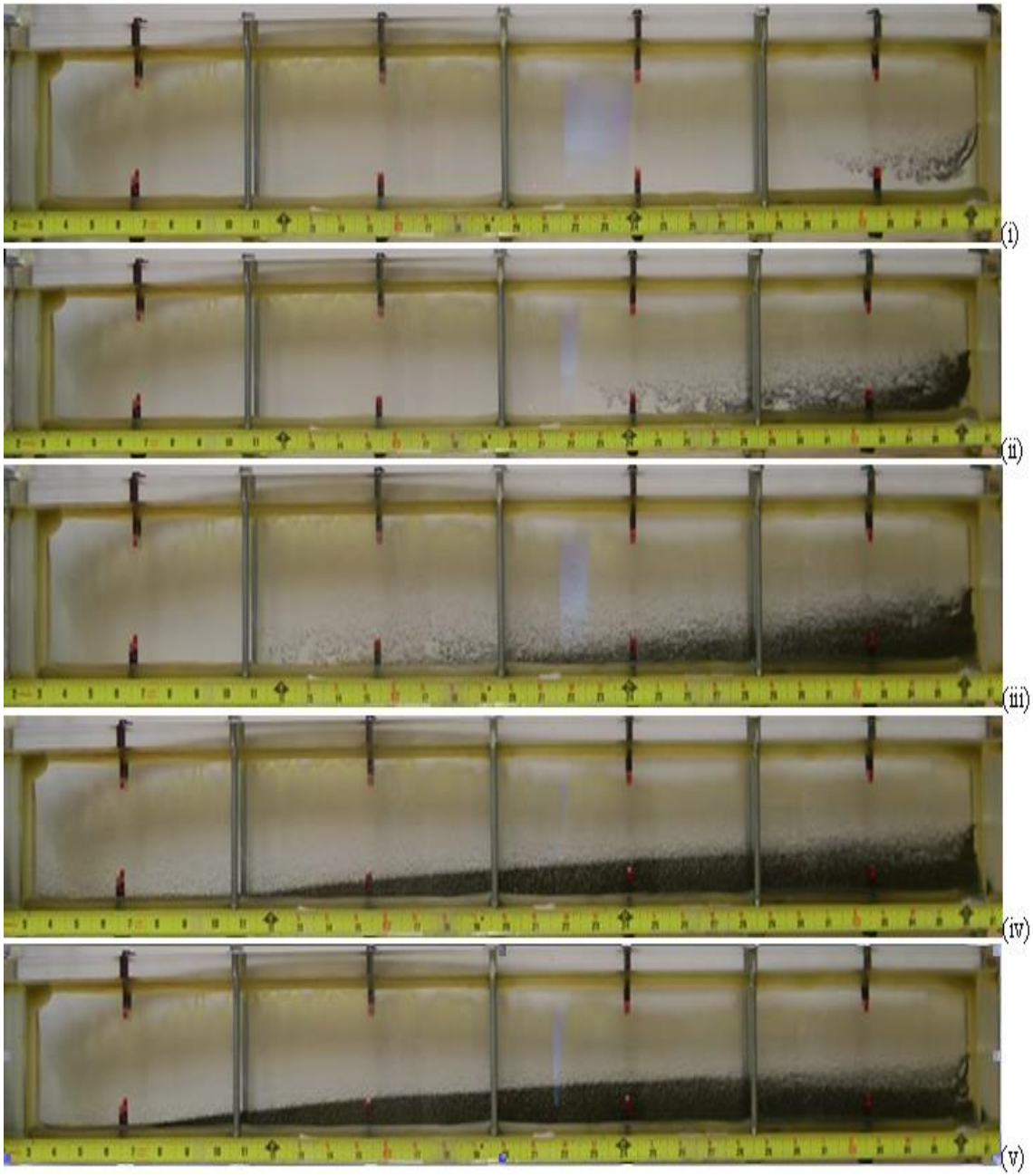

Figure 7.16: Sequential snapshots showing the injection of 1% polyethylene oxide solution along with ceramic proppant in the cell. The cell is initially filled with the same polymer solution.

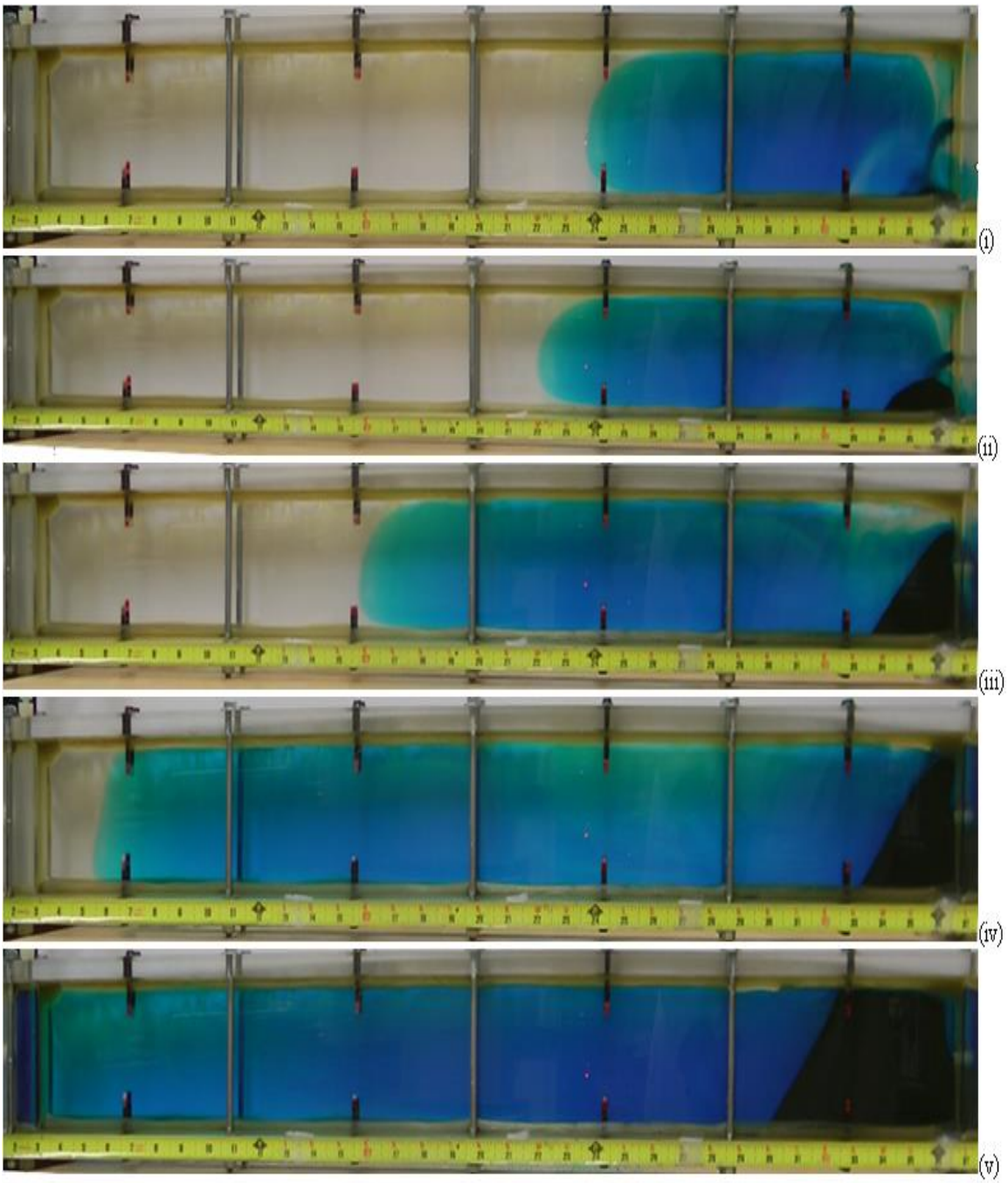

Figure 7.17: Sequential snapshots showing the injection of water along with ceramic proppant in the cell. The cell is initially filled with clear water and dyed water with proppant is injected.

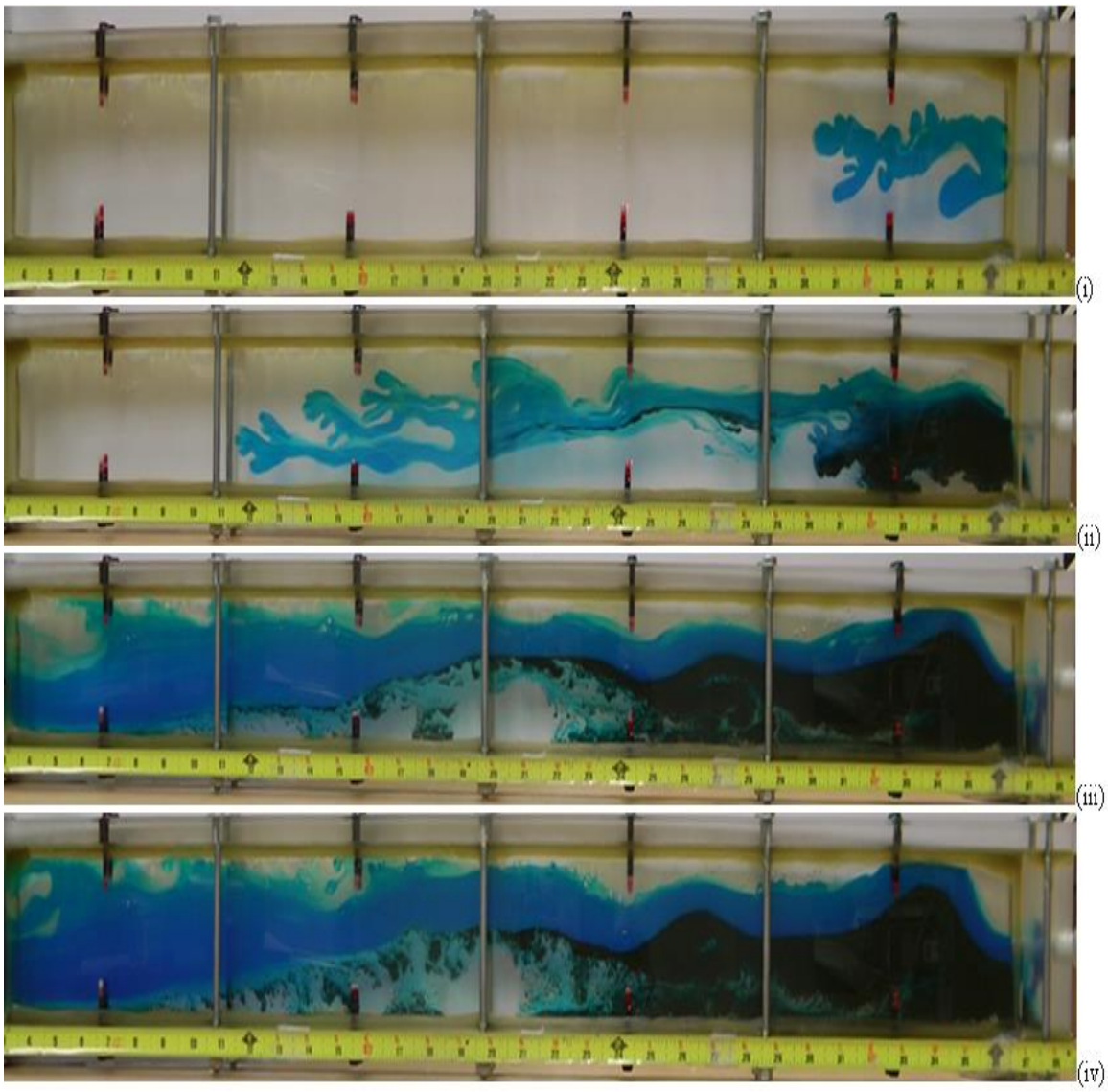

Figure 7.18: Sequential snapshots illustrating the reverse-hybrid fracturing treatment. Water along with ceramic proppant is injected into a cell containing 1% polymer (PEO) solution.

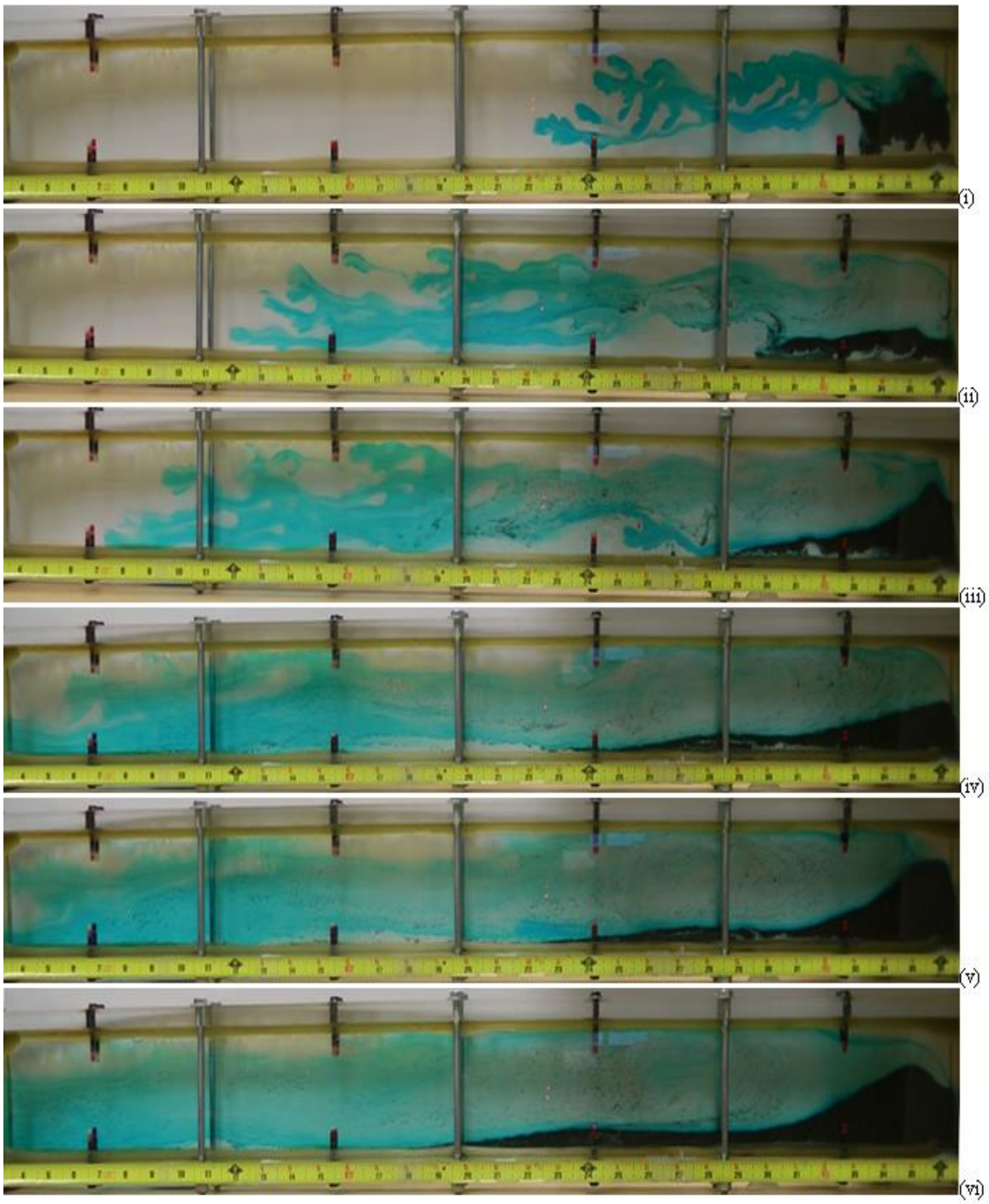

Figure 7.19: Sequential snapshots illustrating the alternate-slug fracturing treatment. Proppant-laden water (dyed) and proppant-free 1% polyethylene oxide solution are injected alternately into the fracture cell.

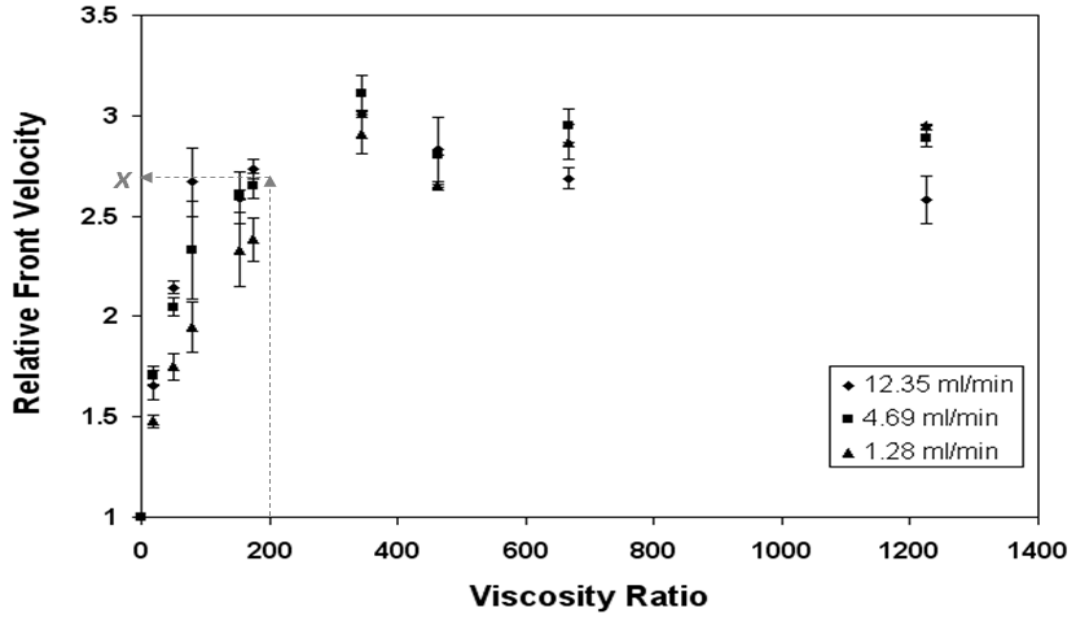

Figure 7.20: Relative front velocity as a function of viscosity ratio. The figure is same as Figure 5.22 in Chapter 5. Relative front velocity is the velocity of the fingertip/finger front divided by the injection velocity.

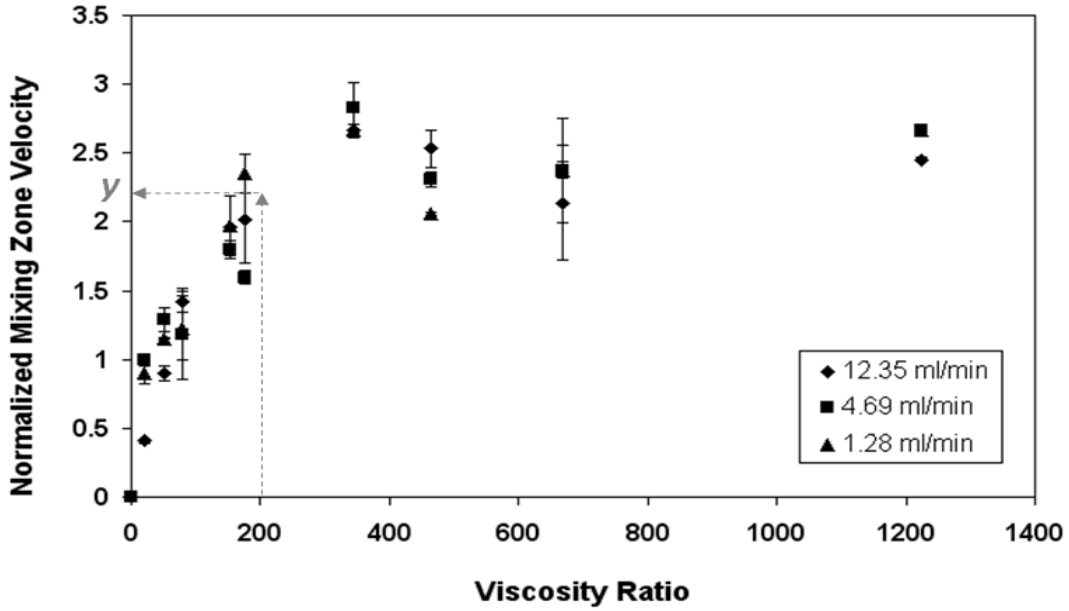

Figure 7.21: Relative front velocity as a function of viscosity ratio. The figure is same as Figure 5.17 in Chapter 5. Normalized mixing zone velocity is the velocity of the mixing zone divided by the injection velocity.

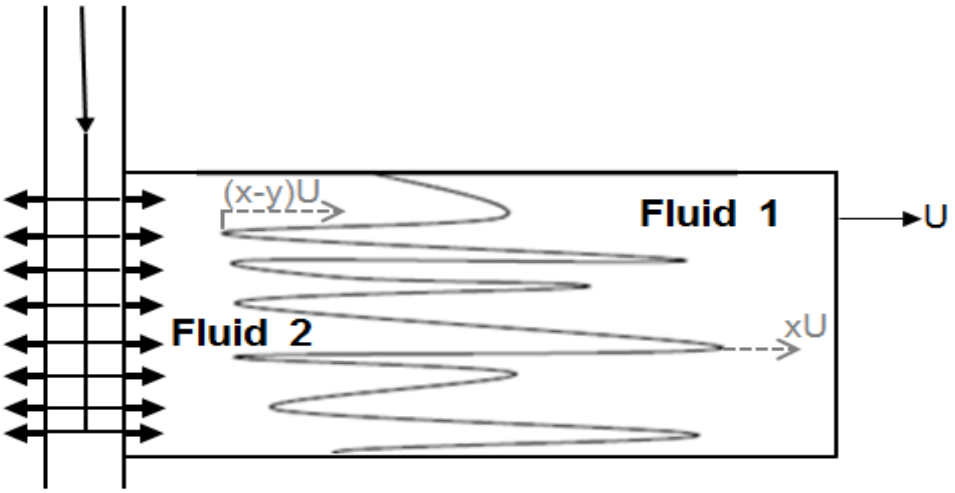

Figure 7.22: Schematic showing the movement of the fluid fronts in one wing of a vertical fracture. The more viscous fluid 1 is injected first at velocity, *U* followed by a less viscous fluid 2 at the same injection rate. The finger tip and the mixing zone move at different velocities.

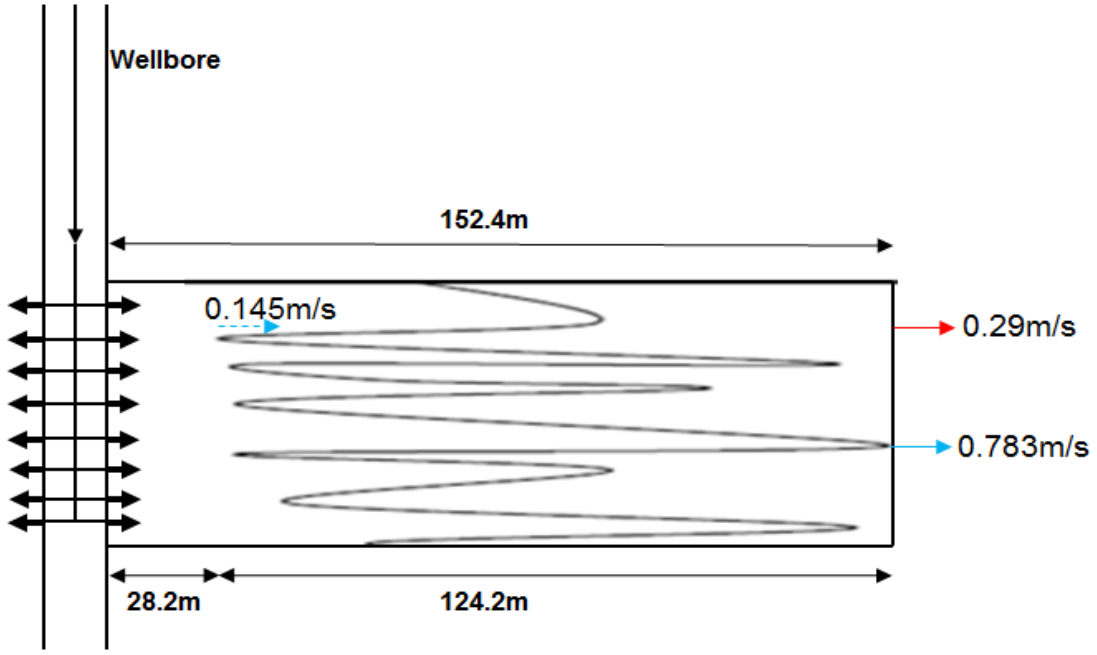

Figure 7.23: Schematic showing the distances covered by the fingertip and mixing zone in one wing of the fracture at the end of the reverse-hybrid fracture treatment. The treatment consists of only one slug of polymer followed by one slug of water. The length of the mixing zone is 124.2m.

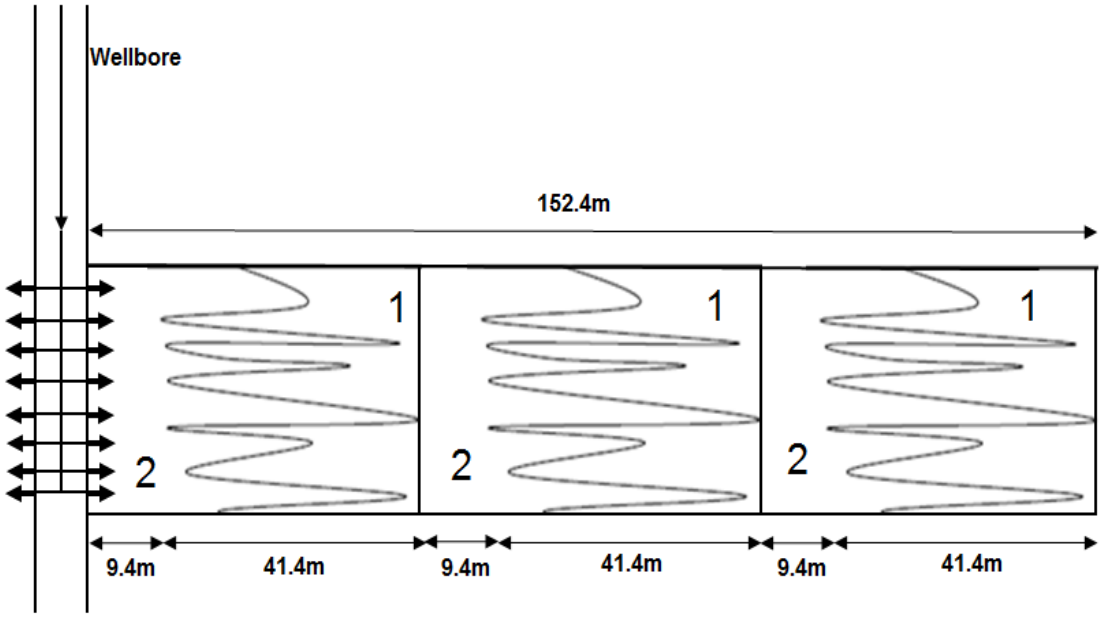

Figure 7.24: Schematic showing the distances covered by the fingertip and mixing zone in one wing of the fracture at the end of an alternate-slug fracture treatment. The treatment involves 3 slugs of polymer and water each. '1' denotes the polymer and '2' denotes water.

Appendix A

The following is the MATLAB code used for the image analysis for calculating the dominant wave number. The coordinates of the interface at a given time are inputted into the code.

```
data = [0.155684    2.29694
0.203584    2.38201
0.191609    2.45493
0.215559    2.56431
0.203584    2.61292
0.143709    2.67368
0.131734    2.73445
0.131734    2.80737
0.191609    2.86813
0.263458    2.88029
0.359257    2.85598
0.371232    2.73445
0.359257    2.64938
0.311358    2.62507
0.299383    2.49139
0.311358    2.46708
%% Copy all the (x,y) coordinates of the interface in this matrix
    ];

xdata = data(:,1);ydata = data(:,2);
L =  max(xdata) - min(xdata);
N = length(xdata)
x1data = xdata +(10^-6)*rand(length(xdata),1);
y1data = ydata;
xmid = zeros(N-1,1);
ymid = zeros(N-1,1);

for i = 1:N-1
    xmid(i) = (x1data(i+1)+x1data(i))/2;
    ymid(i) = (y1data(i+1)+y1data(i))/2;
end

xnew = x1data(1);
ynew = y1data(1);
for i = 1:N-1
    xnew = [xnew;xmid(i);x1data(i+1)];
    ynew = [ynew;ymid(i);ydata(i+1)];
end
Xdata= x1data; Ydata= y1data; %%%after random addition to xdata

x1data= xnew;
```

```
y1data= ynew;
N = length(x1data);
for i = 1:N-1
    xmid(i) = (x1data(i+1)+x1data(i))/2;
    ymid(i) = (y1data(i+1)+y1data(i))/2;
end

xnew = x1data(1);
ynew = y1data(1);
for i = 1:N-1
    xnew = [xnew;xmid(i);x1data(i+1)];
    ynew = [ynew;ymid(i);y1data(i+1)];
end

x1data = xnew; y1data= ynew;  %%%interpolated xdata after 2 random
additions

m = 0;
x2data = [];
y2data = [];
for i = 1:length(x1data)
    if( m < x1data(i)|| y1data(i) < y1data(i-1))
        x2data = [x2data; x1data(i)];
        y2data = [y2data; y1data(i)];
        m = x1data(i);
    end
end
Nw = length(x2data);
m = max(x2data)+10;
x3data = [];
y3data = [];
for i = 1:Nw
    if( m > x2data(Nw-i+1))
        x3data = [x2data(Nw-i+1); x3data];
        y3data = [y2data(Nw-i+1); y3data];
        m = x2data(Nw-i+1);
    end
end
figure;
plot(xdata,ydata,'r'); hold on;
plot(x1data,y1data,'*');

figure;
plot(x1data,y1data,'r');hold on;
plot(x2data,y2data,'g');
plot(x3data,y3data);

x3new = x3data -min(x3data);  %%% shifting to origin
xi = 0:max(x3new)/((length(x3new)-1)):max(x3new);
yi = interp1(x3new,y3data,xi);
figure;
plot(xdata-min(xdata),ydata,'r');hold on;
```

```
plot(x3new,y3data);
plot(xi,yi,'o');
yj = yi- sum(yi)/length(yi);

finding_max=1;      %finding all maxima and minima
maxima_x=[];
maxima_y=[];
maxima_counter=[];
minima_x=[];
minima_y=[];
minima_counter=[];
minima_counter(1)=1;  %first point is always the minima
minima_x(1)=xi(1);
minima_y(1)=yj(1);
m=1;
n=1;
for i=1:numel(xi)-1
    if (finding_max==1 && yj(i)>yj(i+1))
        maxima_x(m)=xi(i);
        maxima_y(m)=yj(i);
        maxima_counter(m)=i;
        finding_max=0;
        m=m+1;
    else
        if(finding_max==0 && yj(i)<yj(i+1))
            minima_x(n+1)=xi(i);
            minima_y(n+1)=yj(i);
            minima_counter(n+1)=i;
            finding_max=1;
            n=n+1;
        end
    end
end
minima_counter(n+1)=numel(xi);
max_ally=max(yj);

for i=1:numel(minima_counter)-1;
    first_coordinate=minima_counter(i);
    last_coordinate=minima_counter(i+1);
    local_max_y(i)=max(yj(first_coordinate:last_coordinate));
    for j=first_coordinate:last_coordinate
        yjnew(j)=yj(j)+max_ally-local_max_y(i);
    end

end
yjnew2 = yjnew- sum(yjnew)/length(yjnew);
xinew=xi(1:numel(yjnew2));


figure;
plot(xi,yj);
```

```
hold on;
plot(xinew,yjnew,'r');

NFFT1=100;
NFFT2=100;

waveno1 = fft(yj,NFFT1);
waveno2=fft(yjnew2,NFFT2);

figure
plot(2*pi*(0:29)*numel(xi)/(max(xi)*NFFT1),abs(waveno1(1:30)));
hold on
plot(2*pi*(0:29)*numel(xinew)/(max(xinew)*NFFT2),abs(waveno2(1:30)),'r'
);


xaxis=(2*pi*(0:29)*numel(xinew)/(max(xi)*NFFT2))';
yaxis=(abs(waveno2(1:30)))';
```

Glossary

A	Area of cross section (m^2)
$A(x)$	Position of the interface between the fluids (cm)
b	Spacing between walls of Hele-Shaw cell
$\bar{c}$	Dimensionless volume concentration of solvent averaged across fingers
C_D	Drag coefficient
C_{D0}	Drag coefficient in the Stokes region
$C_{D\infty}$	Drag coefficient in the Newton's region
d_p	Particle diameter (m)
D	Diffusion coefficient ($m^{2/}s$)
De	Deborah number
$E(t)$	Relaxation modulus (Pa)
F	Force (N)
F_w	Wall factor
g	Acceleration due to gravity (m/s^2)
G^*	Dynamic modulus (Pa)
G'	Elastic modulus (Pa)
G''	Viscous modulus (Pa)
G_0	Plateau modulus (Pa)
G_k	Relaxation strength, Pa
H	Height of fracture or fracture cell (m)
k	Spring constant of the spring (Pa)

k_m	Wave number (cm^{-1})
K	Flow consistency index ($Pa.s^n$)
L	Length of fracture or fracture cell (m)
M	Viscosity ratio of two fluids
M_e	Effective viscosity ratio of two fluids (or the Koval factor)
n	Power-law index or flow behavior index.
n_y	Wave number (1/m)
N_d	Dimensionless group defined by Darby (2001) (Equation 3.11)
p	Coefficient in the correlation for calculating wall factors in viscoelastic fluids (Equation 4.3)
Pe	Pectlet number
r	Ratio of the particle diameter to spacing between parallel walls
Re	Reynolds number for flow of fluid
$Re_{\infty EL}$	Reynolds number based on unconfined settling velocity in viscoelastic fluid
$Re_{\infty INEL}$	Reynolds number based on the inelastic settling velocity under unconfined conditions
Re_{PL}	Reynolds number for a sphere falling in a power law liquid
t	time (s)
t_{adv}	Advective time for motion of particle (s)
t_{set}	Settling time of particle (s)
u	Flow velocity in a Hele-Shaw cell, (m/s)

U	Total flux or the horizontal velocity of fluid (m/s)
V or V_s	Settling velocity of a particle (m/s)
$V_{\infty INEL}$	Settling velocity in an inelastic fluid under unconfined conditions (m/s)
$V_{\infty VE}$	Settling velocity in a viscoelastic fluid under unconfined conditions (m/s)
V_x	Velocity of fluid in x-direction (m/s)
w	Growth rate of the interface (1/s)
We	Weissenberg number based on settling velocity of particle
$We_{\infty EL}$	Weissenberg number of the particle settling in an unbounded elastic fluid
$We_{\infty INEL}$	Dimensionless number relating the relaxation time to particle diameter and unbounded settling velocity
$X(n)$	Drag correction factor
x	Notation for the relative front velocity, used in the design calculations in Chapter 7.
y	Notation for the normalized mixing velocity, used in the design calculations in Chapter 7.
z	Location of the interface between two fluids (m)
α,β,b,k	Parameters defined by Renaud et al. (2004) (Equations 3.7 – 3.10)
$\dot{\gamma}$	Shear rate (1/s)
Δx	Length of mixing zone (m)
ε	Strain (shear or elongation) in the Maxwell element
η	Viscosity of the fluid (Pa.s)

λ	Relaxation time of the fluid (s)
μ	Viscosity of fluid (Pa.s)
μ_1	Viscosity of displaced fluid (cP)
μ_2	Viscosity of displacing fluid (cP)
μ_{HC}	Viscosity of hydrocarbon phase (cP)
μ_{mix}	Viscosity of solvent (mixture)
μ_S	Viscosity of solvent (cP)
ρ	Density of the fluid (kg/m^3)
ρ_1	Density of the displacing fluid (kg/m^3)
ρ_2	Density of the displacing fluid (kg/m^3)
ρ_f	Density of the liquid (kg/m^3)
ρ_p	Density of the particle (kg/m^3)
σ	Stress in the Maxwell element (Pa) (or Variance for fitting moduli data)
σ'	Component of stress in-phase with strain (Pa)
σ''	Component of stress out-of-phase with strain (Pa)
τ	Shear stress (Pa)
ϕ	Volume fraction of solvent (injected fluid)
Φ	Velocity potential (m^2/s)
χ	Ratio of the surface area to projected area of a particle
ω	Angular frequency (rad/s)

References

Acharya, A. R. 1988. Viscoelasticity of Crosslinked Fracturing Fluids and Proppant Transport. *SPE Production Engineering* 3: 483-488.

Acharya, A., Mashelkar, R.A., and Ulbrecht, J. 1976. Flow of Inelastic and Viscoelastic Fluids Past a Sphere, Part II: Anomalous Separation in the Viscoelastic Fluid flow. *Rheologica Acta* 15: 471-478.

Allen, E. and Boger, D. V. 1988. The Influence of Rheological Properties on Mobility Control in Polymer-Augumented Waterflooding. Paper SPE 18097 presented at the SPE Annual Technical Conference and Exhibition, Houston, Texas, 2-5 October.

Asadi, M., Conway, M. W. and Barree, R. D. 2002. Zero Shear Viscosity Determination of Fracturing Fluid: An Essential Parameter in Proppant Transport Characterizations. Paper SPE 73755 presented at the SPE International Symposium and Exhibition on Formation Damage Control, Lafayette, Louisiana, 20-21 February.

Balaramakrishna, P.V. and Chhabra, R.P. 1992. Sedimentation of a Sphere Along the Axis of a Long Square Duct Filled with Non-Newtonian Fluids. *The Canadian Journal of Chemical Engineering* 70: 803-807.

Bird, R.B. 1976. Useful non-Newtonian Models. *Annual Review of Fluid Mechanics* 8: 13.

Bird, R.B., Armstrong, R.C. and Hassanger, O. 1987. *Dynamics of Polymeric Liquids Vol. 1: Fluid Dynamics*, second edition, John Wiley & Sons, New York.

Bird, R.B., Stewart, W.E. and Lightfoot, E.N. 2007. *Transport Phenomena,* Revised Second edition, John Wiley & Sons, New York.

Bisgaard, C. 1983. Velocity Fields Around Spheres and Bubbles Investigated by Laser-Doppler Anemometry. *Journal of Non-Newtonian Fluid Mechanics* 12 (3): 283-302.

Blackwell, R.J., Rayne, J.R. and Terry, W.M. 1959. Factors Influencing the Efficiency of Miscible Displacement. *Transactions AIME* 216: 1-8.

Bohlin, T. 1960. On the Drag on a Sphere Moving in a Viscous Fluid Inside a Cylindrical Tube. *Trans Royal Institute of Technology Stockholm* 155: 1-63.

Booth, R.J.S. 2010. On the Growth of the Mixing Zone in Miscible Viscous Fingering. *Journal of Fluid Mechanics* 655: 527-539.

Bretherton, F.P. 1961. The Motion of Long Air Bubbles in Tubes. *Journal of Fluid Mechanics* 10: 166-188.

Broadbent, J.M. and Mena, B. 1974. Slow Flow of an Elastico-Viscous Fluid Past Cylinders and Spheres. *Chemical Engineering Journal* 8: 11-19.

Brule, B. H. A. A. V. D. and Gheissary, G. 1993. Effects of Fluid Elasticity on the Static and Dynamic Settling of a Spherical Particle. *Journal of Non-Newtonian Fluid Mechanics* 49: 123-132.

Buka, A. and Palffy-Muhoray, P. 1987. Stability of Viscous Fingering Patterns in Liquid Crystals. *Physical Review A* 36: 1527-1529.

Buka, A., Kertesz, J. and Vicsek, T. 1986. Transitions of Viscous Fingering Patterns in Nematic Liquid Crytals. *Nature* 324: 424-425.

Bush, M. B. and Phan-Thien, N. 1984. Drag Force on a Sphere in Creeping Motion Through a Carreau Model Fluid. *Journal of Non-Newtonian Fluid Mechanics* 16 (3): 303-313.

Carreau, P.J., DeKee, D. and Chhabra, R.P. 1997. *Rheology of Polymeric Systems*, Hanser, Munich.

Chhabra, R.P. 1996. Wall Effects on Terminal Velocity of Non-Spherical Particles in Non-Newtonian Polymer Solutions. *Powder Technology* 88: 39-44.

Chhabra, R. P. 2002. Wall Effects on Spheres Falling Axially in Cylindrical Tubes. In *Transport Processes in Bubbles Drops and Particles*, 2nd edition, Chapter 2, DeKee, D. and Chhabra, R. P., Eds., Taylor & Francis, New York.

Chhabra, R.P. 2007. *Bubbles, Drops and Particles in Non-Newtonian Fluids*, second edition, Boca Raton, Florida: Taylor & Francis.

Chhabra, R. P. and Uhlherr, P.H.T. 1980. Creeping Motion of Spheres Through Shear-Thinning Elastic Fluids Described by the Carreau Viscosity Equation. *Rheologica Acta* 19 (2): 187-195.

Chhabra, R. P., Tiu, C. and Uhlherr, P. H. T. 1981. A Study of Wall Effects on the Motion of a Sphere in Viscoelastic Fluids. *Canadian Journal of Chemical Engineering* 59: 771-775.

Chhabra, R. P., Uhlherr, P. H. T. and Boger, D. V. 1980. The Influence of Fluid Elasticity on the Drag Coefficient for Creeping Flow Around a Sphere. *Journal of Non-Newtonian Fluid Mechanics* 6(3-4): 187-199.

Cho, Y.I., Harnett, J.P., and Lee, W.Y. 1984. Non-Newtonian Viscosity Measurements in the Intermediate Shear Rate Range With the Falling-Ball Viscometer. *Journal of Non-Newtonian Fluid Mechanics* 15: 61-74.

Chouke, R.L., Van Meurs, P. and Van Der Poel, C. 1959. The Instability of Slow, Immiscible, Viscous Liquid-Liquid Displacements in Permeable Media. *Petroleum Transactions AIME* 216: 188-194.

Clift, R., Grace, J.R., and Weber, M.E. 1978. *Bubbles, Drops and Particles.* Academic Press, New York.

Coulder, Y. 1991. Growth Patterns: From Stable Curved Patterns to Fractal Structures. In *Chaos, Order and Patterns.* R. Artuso, P. Cvitanovic and G. Casati, Plenum.

D'Errico, G., Ortona, O., Capuano, F. and Vitagliano, V. 2004. Diffusion Coefficients for the Binary System Glycerol + Water at 25° C. A Velocity Correlation Study. *Journal of Chemical and Engineering Data* 49 (6): 1665-1670.

Dallon, D.S. 1967. A Drag Coefficient Correlation for Spheres Settling in Ellis Fluids. Ph.D. Dissertation, University of Utah, Salt Lake City, Utah.

Dantas, T. N. C., Santanna, V. C., Neto, A. A. D. and Moura M. C. P. A. 2005. Hydraulic Gel Fracturing. *Journal of Dispersion Science and Technology* 26: 1-4.

Darby, R. 2001. *Chemical Engineering Fluid Mechanics*. Second edition, Marcel Dekker, New York.

Dazhi, G., and Tanner, R.I. 1984. The Drag on a Sphere in a Power Law Fluid. *Journal of Non-Newtonian Fluid Mechanics* 17: 1-12.

Delshad, M., Kim, D. H., Magbagbeola, O. A., Huh, C., Pope, G. A. and Tarahhom, F. 2008. Mechanistic Interpretation and Utilization of Viscoelastic Behavior of Polymer Solution for Improved Polymer-Flood Efficiency. Paper SPE 113620 presented at the SPE Improved Oil Recovery Symposium, Tulsa, Oklahoma, 19-23 April.

Dontula, P., Macosko, C.W. and Scriven, L.E. 1988. Model Elastic Liquids with Water-Soluble Polymers. *AIChE* 44 (6): 1247-1255.

Ely, J.W., Hargrove, J.S., Wolters, B.C. and Kromer, J.C. 1993. Pipelining: Viscous Fingering Prop Fracture Technique Finds Wide Success in Permian and Delaware Basins. Paper SPE 26528 presentted at the SPE Annual Technical Conference and Exhibition, Houston, Texas, 3-6 October.

Faxen, H. 1922. Der Widerstand gegen die Bewegung einer starren Kugel in einer zähen Flüssigkeit, die zwischen zwei parallelen ebenen Wänden eingeschlossen ist. *Annalen der Physics* 68: 89-119.

Fayers, F.J., Jouaux, F. and Tchelepi, H.A. 1994. An Improved Macroscopic Model for Viscous Fingering and its Validation for 2D and 3D Flows – I. Non-Gravity Flows. *In Situ* 18: 43-78.

Fernandez, J., Kurowski, P., Petitjeans, P., and Meiburg, E. 2002. Density-Driven Unstable Flows of Miscible Fluids in a Hele-Shaw Cell. *Journal of Fluid Mechanics* 451: 239-260.

Ferry, J. D. 1970. *Viscoelastic Properties of Polymers*, second edition, John Wiley & Sons Inc., USA.

Ford, J.T., Oyeneyin, M.B., Heriot-Watt, U., Gao, E., Williamson, R.S., and Peel, L.C. 1994. The Formulation of Milling Fluids for Efficient Hole Cleaning: An Experimental Investigation. Paper SPE 38819 presented at the European Petroleum Conference, London, U.K, October 25-27.

Gidley, J.L., Holditch, S.A., Nierode, D.E. and Veatch Jr., R.W. 1989. Recent Advances in Hydraulic Fracturing, SPE Monograph Series Vol. 12, Richardson, TX: Monograph Series.

Gillard, M., Medvedev, O., Pena, A., Medvedev, A., Penacorada, F. and d'Huteau, E. 2010. A New Approach to Generating Fracture Conductivity. Paper SPE 135034 presented at the SPE Annual Technical Conference and Exhibition, Florence, Italy, 20-22 September.

Graham, D.I., and Jones, T.E.R. 1994. Settling and Transport of Spherical Particles in Power-Law Fluids at Finite Reynolds Number. *Journal of Non-Newtonian Fluid Mechanics* 54: 465-488.

Gupta, D. V. S. 2009. Unconventional Fracturing Fluids for Tight Gas Reservoirs. Paper SPE 119424 presented at the SPE Hydraulic Fracturing Technology Conference, Houston, Texas, 19-21 January.

Gupta, D.V.S., and Tudor, E. H. 2005. Method for Fracturing Subterranean Formations, US Patent No. 6,875,728.

Gupta, D.V.S., Leshchyshyn, T.T., and Hlidek, B.T. 2005. Surfactant Gel Foam/Emulsions: History and Field Application in the Western Canadian Sedimentary Basin. Paper SPE 97211 presented at the SPE Annual Technology Conference and Exhibition, Dallas, Texas, October 9-12.

Handren, P. and Palisch, T. 2009. Successful Hybrid Slickwater-Fracture Design Evolution: An East Texas Cotton Valley Taylor Case History. *SPE Productions and Operations*, August: 415-423.

Hawkins, G.W. 1988. Laboratory Study of Proppant-Pack Permeability Reduction Caused by Fracturing Fluids Concentrated During Closure. Paper SPE 18261 presented at the SPE Annual Technical Conference and Exhibition, Houston, Texas, 2-5 October.

Homsy, G.M. 1987. Viscous Fingering in Porous Media. *Annual Review of Fluid Mechanics* 19: 271-311.

Howison, J.D. 1986. Fingering in Hele-Shaw Cells. *Journal of Fluid Mechanics* 167: 439-453.

Huang, P. Y., and Feng, J. 1995. Wall Effects on the Flow of Viscoelastic Fluids Around a Circular Cylinder. *Journal of Non-Newtonian Fluid Mechanics* 60: 179-198.

Huh, C. and Pope, G.A. 2008. Residual Oil Saturation From Polymer Floods: Laboratory Measurements and Theoretical Interpretation. Paper SPE 113417 presented at the SPE/DOE Improved Oil Recovery Symposium, Tusla, Oklahoma.

Islam, M.N. and Azaiez, J. 2007. New Viscous Fingering Mechanisms at High Viscosity Ratios and Peclet Number Miscible Displacements. *Journal of Porous Media* 10(4): 357-375.

Johnson, J., Turner, M., Weinstock, C., Pena, A., Laggan, M., Rondon, J. and Lyapunov, K. 2011. Channel Fracturing – A Paradigm Shift in Tight Gas Stimulation. Paper SPE 140549 presented at the SPE Hydraulic Fracturing Technology Conference and Exhibtion, The Woodlands, Texas, 24-26 January.

Jones, W. M., Price, A. H. and Walters, K. 1994. The Motion of a Sphere Falling Under Gravity in a Constant Viscosity Elastic Liquid. *Journal of Non-Newtonian Fluid Mechanics* 53: 175-196.

Kawaguchi, M., Makino, K. and Kato, T. 1997a. Viscous Fingering Patterns in Polymer Solutions. *Physica D* 109: 325-332.

Kawaguchi, M., Makino, K. and Kato, T. 1997b. Viscous Fingering Patterns of Silica Suspensions in Polymer Solutions: Effects of Viscoelasticity and Gravity. *Physica A* 246: 385-398.

Kelessidis, V.C., and Mpandelis, G. 2004. Measurements and Prediction of Terminal Velocity of Solid Particles Falling Through Stagnant Pseudoplastic Liquids. *Powder Technology* 147: 117-125.

Kern, P.R., Perkins, T.K., and Wyant, R.E. 1959. The Mechanics of Sand Movement in Fracturing. *Journal of Petroleum Technology* 11 (7): 55-57.

Khan, A.R., and Richardson, J. F. 1987. The Resistance to Motion of a Solid Sphere in a Fluid. *Chemical Engineering Science* 62: 135-150.

Kim, D. H., Lee, S., Ahn, C. H., Huh, C. and Pope, G. A. 2010. Development of a Viscoelastic Property Database for EOR Polymers. Paper SPE 129971 presented at the SPE Improved Oil Recovery Symposium, Tulsa, Oklahoma, 24-28 April.

Koval, E.J. 1963. A Method for Predicting the Performance of Unstable Miscible Displacement in Heterogeneous Media. *SPE Journal* 3: 145-155.

Lajeunesse, E., Martin, J., Rakotomalala, N. and Salin, D. 1997. 3D Instability of Miscible Displacements in a Hele-Shaw cell. *Physical Review Letters* 79: 5254-5257.

Lajeunesse, E., Martin, J., Rakotomalala, N., Salin, D. and Yortsos, Y.C. 1999. Miscible Displacements in a Hele-Shaw Cell at High Rates. *Journal of Fluid Mechanics* 398: 299-319.

Lake, L.W. 1989. *Enhanced Oil Recovery*, Englewoods Cliff, NJ: Prentice-Hall.

Leitzell, J. R. 2007. Viscoelastic Surfactants: A New Horizon in Fracturing Fluids for Pennsylvania. Paper SPE 111182 presented at the SPE Eastern Regional Meeting, Lexington, Kentucky, 17-19 October.

Lemaire, E., Levitz, P., Daccord, G. and Van Damme, H. 1991. From Viscous Fingering to Viscoelastic Fracturing in Colloidal Fluids. *Physical Review Letters* 67: 2009-2012.

Leonard, R., Woodroof, R., Bullard, K., Middlebrook, M. and Wilson, R. 2007. Barnett Shale Completions: A Method of Assessing New Completion Strategies. Paper SPE 110809 presented at the SPE Annual Technical Conference and Exhibition, Anahein, California, 11-14 November.

Li, H., Maini, B. and Azaiez, J. 2006. Experimental and Numerical Analysis of the Viscous Fingering Instability of Shear-Thinning Fluids. *Canadian Journal of Chemical Engineering* 84: 52-62.

Lindner, A., Coussot, P. and Bonn, D. 2000. Viscous Fingering in a Yield Stress Fluid. *Physical Review Letters* 85: 314-317.

Lindner, A., Bonn, D., Poire, E.C., Amar, M.B. and Meunier, J. 2002. Viscous Fingering in Non-Newtonian Fluids. *Journal of Fluid Mechanics* 469: 237-256.

Lionti-Addad, S., Di Meglio, J.M. 1992. Stabilization of Aqueous Foam by Hydrosoluble Polymers. 1. Sodium dodecyl sulfate-poly(ethylene oxide) system. *Langmuir* 8: 324-327.

Liu, Y. and Sharma, M. M. 2005. Effect of Fracture Width and Fluid Rheology on Proppant Settling and Retardation: An Experimental Study. Paper SPE 96208 presented at the SPE Annual Technical Conference and Exhibition, Dallas, Texas, 9-12 October.

Liu, Y., Gadde, P. B. and Sharma, M. M. 2007. Proppant Placement Using Reverse-Hybrid Fracs. *SPE Productions & Operations* August: 348-356.

Loggia, D., Rakotomalala, N., Salin, D. and Yortsos, Y.C. 1995. Evidence of New Instability Thersholds in Miscible Fluid Flows. *Europhysics Letters* 32: 633-638.

Machac, I, Cakl, J., and Lecjaks, Z. 1987. Fall of Spheres Through Non-Newtonian Liquids in Transition Region. Proceedings of CHISA Congress, Prague, The Czech Republic.

Machac, I., and Lecjaks, Z. 1995. Wall Effect for a Sphere Falling Through a Non-Newtonian Fluid in a Rectangular Duct. *Chemical Engineering Science* 50(1): 143-148.

Makino, K., Kawaguchi, M., Aoyama, K. and Kato, T. 1995. Transition of Viscous Fingering Patterns in Polymer Solutions. *Physics of Fluids* 7: 455-457.

Mathis, S. P., Pitoni, E., Ripa, G., Ferrara, G., Conte, A. and Ruzic, M. 2002. VES Fluid Allows Minimized Pad Volumes and Viscosity to Optimize Frac-Pack Geometry: Completion Type Evolution in Barbara Field, Central Adriatic Sea. Paper SPE 78317 presented at the SPE European Petroleum Conference, Aberdeen, Scotland, 29-31 October.

Mayerhofer, M.J., Richardson, M.F., Walker Jr., R.N., Meehan, D.N., Oehler, M.W. and Browning Jr., R.R. 1997. Proppants? We Don't Need No Proppants. Paper SPE 38611 presented at the SPE Annual Technical Conference and Exhibition, San Antonio, Texas, 5-8 October.

Mayerhofer, M.J., Lolon, E.P., Youngblood, J.E. and Heinze, J.R. 2006. Integration of Microseismic Fracture Mapping Results With Numerical Fracture Network Production Modeling in the Barnett Shale. Paper SPE 102013 presented at the SPE Annual Technical Conference and Exhibition, San Antonio, Texas, 24-27 September.

McKinley, G. H. 2002. Steady and Ttransient Motion of Spherical Particles in Viscoelastic Liquids. In *Transport Processes in Bubbles, Drops and Particles*, ed. DeKee, D. and Chhabra, R.P. Chapter 14, second edition, Taylor & Francis, New York.

Medvedev, A., Yudina, K., Panga, M.K., Kaemer, C.C. and Pena, A. 2013. On the Mechanisms of Channel Fracturing. Paper SPE 163836 presented at the SPE Hydraulic Fracturing Technology Conference, The Woodlands, Texas, 4-6 February.

Menon, G. and Otto, F. 2005. Dynamic Scaling in Miscible Viscous Fingering. *Communications in Mathematical Physics* 257: 303-317.

Michaelides, E.E. 2002. Analytical Expressions for the Motion of Particles. In *Transport Processes in Bubbles Drops and Particles*, 2nd edition, Chapter 2, DeKee, D. and Chhabra, R. P., Eds., Taylor & Francis, New York.

Michaelides, E.E. 2003. Hydrodynamic Force and Heat/Mass Transfer from Particles, Bubbles and Drops – The Freeman Scholar Lecture. *Journal of Fluids Engineering (AMSE)* 125: 209-238.

Missirlis, K.A., Assimacopoulos, D., Mitsoulis, E., and Chhabra, R.P. 2001. Wall Effects for Motion of Spheres in Power-Law Fluids. *Journal of Non-Newtonian Fluid Mechanics* 96 (3): 459-471.

Miyamura, A., Iwasaki, S., and Ishii, T. 1981. Experimental Wall Correction Factors of Single Solid Spheres in Ttriangular and Square Cylinders, and Parallel Plates. *International Journal of Multiphase Flow* 7: 41-46.

Mora, S. and Manna, M. 2010. Saffman-Taylor Instability of Viscoelastic Fluids: From Viscous Fingering to Elastic Fractures. *Physical Review E* 81: 026305.

Navez, V. and Walters, K. 1996. A Note on Settling in Shear-Thinning Polymer Solutions. *Journal of Non-Newtonian Fluid Mechanics* 67: 325-334.

Palisch, T.T., Vincent, M.C. and Handren, P.J. 2010. Slickwater Fracturing: Food for Thought. *SPE Productions and Operations* August: 327-344.

Park, S.S. and Durian, D.J. 1994. Viscous and Elastic Fingering Instabilities in Foam. *Physical Review Letters* 72: 3347-3350.

Patankar, N.A., Joseph, D.D., Wang, J., Barree, R., Conway, M. and Asadi, M. 2002. Power Law Correlations for Sediment Transport in Pressure Driven Channel Flows. *International Journal of Multiphase Flow* 28 (8): 1269-1292.

Peters, E.J. 1979. Stability Theory and Viscous Fingering in Porous Media. PhD Dissertation, University of Alberta, Alberta, Canada.

Peters, E.J. and Hardham, W.D. 1989. A Comparison of Unstable Miscible and Immiscible Displacements. Paper SPE 19640 presented at SPE Annual Technical Conference and Exhibition, San Antonio, Texas, October 8-11.

Peters, E.J. and Reid, C.A. 1990. A Microcomputer-Based Imaging System for the Visualization of Fluid Displacements. *Journal of Petroleum Technology* May: 558-563.

Peters, E.J., Broman, J.A. and Broman Jr., W.H. 1987. Computer Image Processing: A New Tool for Studying Viscous Fingering in Corefloods. *SPE Reservoir Engineering* November: 720-728.

Pope, D.S., Leung, L.K., Gulbis, J. and Constein, V.G. 1996. Effects of Viscous Fingering on Fracture Conductivity. *SPE Production & Facilities* 11(4): 230-237.

Renaud, M., Mauret, E., and Chhabra, R.P. 2004. Power-Law Fluid Flow Over a Sphere: Average Shear Rate and Drag Coefficient. *The Canadian Journal of Chemical Engineering* 82: 1066-1070.

Rhein, T., Loayza, M., Kirkham, B., Oussoltsev, D., Altman, R., Viswanathan, A., Pena, A., Indriati, S., Grant, D., Hanzik, C., Pittenger, J., Tabor, L., Makarychev-Mikhailov, S. and Mikhaylov, A. 2011. Paper SPE 145403 presented at the SPE Annual Technical Conference and Exhibtion, Denver, Colorado, 30 October – 2 November.

Ribeiro, L.H. and Sharma, M.M. 2012. Multiphase Fluid-Loss Properties and Return Permeability of Energized Fracturing Fluids. *SPE Productions & Operations* 27 (3): 265-277.

Rickards, A.R., Brannon, H.D., Wood, W.D. and Stephenson, C.J. 2003. High Strength, Ultra-Lightweight Proppant Lends New Dimensions to Hydraulic Fracturing Applications. Paper SPE 84308 presented at the SPE Annual Technical Conference and Exhibition, Denver, Colorado, 5-8 October.

Ro., J.S. and Homsy, G.M. 1995. Viscoelastic Free Surface Films: Thin Film Hydrodynamics of Hele-Shaw and Dip Coating Flows. *Journal of Non-Newtonian Fluid Mechanics* 57: 203-225.

Rushing, J.A. and Sullivan, R.B. 2003. Evaluation of a Hybrid Water-Frac Stimulation Technology in the Bossier Tight Gas Sand Play. Paper SPE 84934 presented at the SPE Annual Technical Conference and Exhibition, Denver, Colorado, 5-8 October.

Sader, J. E., Chan, D. Y. C. and Hughes, B. D. 1994. Non-Newtonian Effects on Immiscible Viscous Fingering in a Radial Hele-Shaw Cell. *Physical Review E* 49: 420-432.

Saffman, P. G. and Taylor, G. I. 1958. The Penetration of a Fluid Into a Porous Medium or Hele-Shaw Cell Containing A More Viscous Liquid. *Proceedings of Royal Society of London A* 245: 312-329.

Samuel, M., Card, J. C., Nelson, E. B., Brown, J. E., Vinod, P. S., Temple, H. L., Qu, Q. and Fu, K. 1997. Polymer-Free Fluid for Hydraulic Fracturing. Paper SPE 38622 presented at the SPE Annual Technical Conference and Exhibition, San Antonio, Texas, 5-8 October.

Shah, S.N. 1982. Proppant Settling Correlations for Non-Newtonian Fluids. *SPE Journal* 22 (2): 164-170.

Shah, S.N. 1986. Proppant-Settling Correlations for Non-Newtonian Fluids. *SPE Production Engineering Journal* 1 (6): 446-448.

Shah, S.N., Fadili, Y.E., and Chhabra, R.P. 2007. New Model for Single Spherical Particle Settling Velocity in Power Law (Visco-Inelastic) Fluids. *International Journal of Multiphase Flow* 33: 51-66.

Sharma, M.M., Gadde, P.B., Sullivan, R., Sigal, R., Fielder, R., Copeland, D., Griffin, L. and Weijers, L. 2004. Slick Water and Hybrid Fracs in the Bossier: Some Lessons Learnt. Paper SPE 89876 presented at the SPE Annual Technical Conference and Exhibition, Houston, Texas, 26-29 September.

Sigli, D. and Coutanceau, M. 1977. Effect of Finite Boundaries on the Slow Laminar Isothermal Flow of a Viscoelastic Fluid Around a Spherical Obstacle. *Journal of Non-Newtonian Fluid Mechanics* 2: 1-21.

Smirnov, N.N., Nikitin, V.F., Maximenko, A., Thiercelin, M. and Legros, J.C. 2005 Instability and mixing flux in frontal displacement of viscous fluids from porous media. *Physics of Fluids* 17: 08412.

Song, D., Gupta, R.K., and Chhabra, R.P. 2009. Wall Effects on a Sphere Falling in Quiescent Power Law Fluids in Cylindrical Ttubes. *Industrial & Engineering Chemistry Research* 48: 5854-5856.

Sugeng, F., and Tanner, R.I. 1986. The Drag on Spheres in Viscoelastic Fluids With Significant Wall Effects. *Journal of Non-Newtonian Fluid Mechanics* 20: 281-292.

Tanveer, S. 2000. Surprises in viscous fingering. *Journal of Fluid Mechanics* 409: 273-308.

Todd, M.R. and Longstaff, W.J. 1972 The Development, Testing, and Application of a Numerical Simulator for Predicting Miscible Flood Performance. *Journal of Petroleum Technology* 24: 874-882.

Tripathi, A., and Chhabra, R.P. 1995. Drag on Spheroidal Particles in Dilatant Fluids. *AIChE* 41 (3): 728-731.

Tripathi, A., Chhabra, R.P., and Sundararajan, T. 1994. Power-Law Fluid over Spheroidal Particles. *Industrial & Engineering Chemistry Research* 33: 403-410.

Tullock, D.L., Phan-Thien, N. and Graham, A.L. 1992. Boundary Element Simulations of Spheres Settling in Circular, Square and Triangular Ducts. *Rheologica Acta* 31: 139-150.

Uhlherr, P.H.T., Le, T.N. and Tiu, C. 1976. Characterization of Inelastic Power-Law Fluids Using Falling Sphere Data. *Canadian Journal of Chemical Engineering* 54: 497-502.

Vlad, D.H. and Maher, J.V. 2000. Tip-Splitting Instabilities in the Channel Saffman-Taylor Flow of Constant Viscosity Elastic Fluids. *Physical Review E* 61: 5439-5444.

Walker Jr., R.N., Hunter, J.L., Brake, A.C., Fagin, P.A. and Steinsberger, N. 1998. Proppants, We Still Don't Need No Proppants – A Perspective of Several Operators. Paper SPE 49106 presented at the SPE Annual Technical Conference and Exhibition, New Orleans, Louisiana, 27-30 September.

Walters, K. and Tanner, R. I. 1992. The Motion of a Sphere through an Elastic Fluid. In *Transport Processes in Bubbles, Drops and Particles*, ed. Chhabra, R. P. and DeKee, D., Chapter 3, Hemisphere, New York.

Wooding, R.A. 1969. Growth of Fingers at an Unstable Diffusing Interface in a Porous Medium or Hele-Shaw Cell. *Journal of Fluid Mechanics* 39: 477-495.

Yang, Z.M., Yortsos, Y.C. & Salin, D. 2002. Asymptotic Regimes in Unstable Miscible Displacements in Random Porous Media. *Advances in Water Resources* 25: 885-898.

Yortsos, Y.C. and Salin, D. 2006. On the Selection Principle for Viscous Fingering in Porous Media. *Journal of Fluid Mechanics* 557: 225-236.

Zapryanov, Z., and Tabakova, S. 1999. *Dynamics of Bubbles, Drops and Rigid Particles*. Kluwer Academic Publishers, Dordrecht, The Netherlands.

Zhang, K. 2002. Fluids for Fracturing Subterranean Formations.U.S. Patent No. 6,468,945.

Zimmerman, W.B. and Homsy, G.M. 1991. Viscous Fingering in Miscible Displacements: Unification of Effects of Viscosity Contrast, Anisotropic Dispersion, and Velocity Dependence of Dispersion on Nonlinear Finger Propagation. *Physics of Fluids A* 4: 2348-2359.

Web References

Software package ‘Tracker’ <http://www.cabrillo.edu/_dbrown/tracker/>2012.

Software package ‘ImageJ’ < http://rsb.info.nih.gov/ij/>

Software package ‘Plot Digitizer’ < http://plotdigitizer.sourceforge.net/>